



**HAL**  
open science

# Polarisation resolved photoluminescence in van der Waals heterostructures

Sangjun Park

► **To cite this version:**

Sangjun Park. Polarisation resolved photoluminescence in van der Waals heterostructures. Condensed Matter [cond-mat]. Institut Polytechnique de Paris, 2022. English. NNT: 2022IPPAX041 . tel-03714563

**HAL Id: tel-03714563**

**<https://theses.hal.science/tel-03714563>**

Submitted on 5 Jul 2022

**HAL** is a multi-disciplinary open access archive for the deposit and dissemination of scientific research documents, whether they are published or not. The documents may come from teaching and research institutions in France or abroad, or from public or private research centers.

L'archive ouverte pluridisciplinaire **HAL**, est destinée au dépôt et à la diffusion de documents scientifiques de niveau recherche, publiés ou non, émanant des établissements d'enseignement et de recherche français ou étrangers, des laboratoires publics ou privés.



INSTITUT  
POLYTECHNIQUE  
DE PARIS

NNT : 2022IPPAX041

Thèse de doctorat



# Polarization resolved photoluminescence in van der Waals heterostructures

Thèse de doctorat de l'Institut Polytechnique de Paris  
préparée à l'École polytechnique

École doctorale n°626 École doctorale de l'Institut Polytechnique de Paris (EDIPP)  
Spécialité de doctorat: Physique de la matière condensée

Thèse présentée et soutenue à Palaiseau, le 14 Juin 2022, par

**SANGJUN PARK**

Composition du Jury :

Luca Perfetti Professeur, Laboratoire des Solides Irradiés (LSI), École polytechnique, Palaiseau, France	Président
Abhay Shukla Professeur, L'Institut de Minéralogie, de Physique des Matériaux et de Cosmochimie (IMPMC), Sorbonne Université, Paris, France	Rapporteur
Johann Coraux Directeur de recherche, Institut Néel, CNRS (UPR 2940)/Université Grenoble Alpes, Grenoble, France	Rapporteur
Julien Chaste Chargé de Recherche, Centre de Nanosciences et de Nanotechnologies (C2N), CNRS (UMR 9001)/Université Paris-Saclay, Palaiseau, France	Examineur
Fabian Cadiz Professeur Assistant, Laboratoire de Physique de la Matière Condensée (PMC), École polytechnique, Palaiseau, France	Directeur de thèse
Fausto Sirotti Directeur de Recherche, Laboratoire de Physique de la Matière Condensée (PMC), CNRS (UMR 7643)/École polytechnique, Palaiseau, France	Directeur de thèse
Alistair Rowe Chargé de Recherche, Laboratoire de Physique de la Matière Condensée (PMC), CNRS (UMR 7643)/École polytechnique, Palaiseau, France	Invité

*Dedication*





# Acknowledgements

First of all, I very much appreciate the jury, who evaluated and gave me priceless comments on my thesis and the audience of my thesis defense.

I cannot begin to express my thanks to my supervisors, Fabian Cadiz and Fausto Sirotti. You are something more than thesis supervisors for me. Your research guidance, mindset, attitude, and teamwork were incredible, which you showed and taught me. I feel fortunate to get this chance to experience and learn from you. I'm deeply indebted to Alistair Rowe and Agatha Ulibarri, (I would say) my co-co-supervisor and a best friend working together on the optical experiment. I am also sorry that I distracted you a lot in the lab. I would like to say  $F_2A_2$  (Fabian Cadiz, Fausto Sirotti, Alistair Rowe, and Agatha Ulibarri) is everything in my five years of French Lab life. You were supervisors, family, friends, neighborhoods, counselors. . . for me, literally everything, and still, you are.

I would also like to extend my deepest gratitude to my M2 internship supervisor Daniel Paget (with Fabian Cadiz), who taught me the optics and spectroscopy experiment for the very first time in PMC. I was slow and inexperienced, but you patiently waited and explained to me.

I also wish to thank EPS group members for creating an enjoyable and encouraging environment to produce a lot of positive externalities in research and life. I'd like to acknowledge Gookbin Cho and PMC lab members for all the enjoyable moments.



# Contents

<b>1</b>	<b>Introduction</b>	<b>4</b>
1.1	General introduction . . . . .	5
1.2	2D materials . . . . .	7
1.3	Transition metal dichalcogenides (TMDs) . . . . .	8
1.3.1	Atomic structure . . . . .	8
1.3.2	Strongly bound excitons in 2D . . . . .	10
1.3.3	The role of the spin-orbit interaction on the optical selection rules . . . . .	12
1.3.4	Valley polarization and coherence . . . . .	15
1.4	Fabrication and synthesis . . . . .	16
1.4.1	Bottom-up approach: Large-area synthesis . . . . .	16
1.4.2	Top-down approach: practical methods for vertical heterostructures . . . . .	17
1.5	Suppression of dielectric disorder by hBN encapsulation . . . . .	20
1.6	Conclusions . . . . .	21
<b>2</b>	<b>Sample preparation &amp; experimental methods</b>	<b>23</b>
2.1	Mechanical exfoliation . . . . .	23
2.1.1	Process . . . . .	24
2.1.2	Characterization of TMD monolayers . . . . .	32
2.1.3	Vacuum annealing . . . . .	35
2.1.4	Fabrication of contacted devices . . . . .	37
2.2	Polarization-resolved $\mu$ -photoluminescence spectroscopy . . . . .	38
2.2.1	Setup . . . . .	38
2.2.2	Alignment . . . . .	43
2.2.3	Polarization resolved spectroscopy . . . . .	46
2.2.4	Imaging . . . . .	48
2.3	Conclusions . . . . .	51

<b>3</b>	<b>Demonstration of spin/valley pumping of resident electrons in WS<sub>2</sub> monolayers</b>	<b>53</b>
3.1	Observed excitonic complexes at T = 20 K . . . . .	54
3.1.1	PL spectra at T = 20 K . . . . .	54
3.1.2	Power dependence . . . . .	56
3.2	Demonstration of optical spin/valley pumping . . . . .	57
3.3	Demonstration of a dynamical spin/valley polarization of the resident electrons . . . . .	59
3.3.1	Trion (T <sub>1</sub> and T <sub>2</sub> ) emission intensity under circular and linear excitation . . . . .	59
3.3.2	TRPL: investigation of build-up and recombination under circular/linear excitation . . . . .	60
3.3.3	Qualitative explanation for the dynamical polarization of resident electrons . . . . .	62
3.3.4	Dynamic valley polarization under resonance excitation of the excited excitonic states . . . . .	64
3.4	Conclusions . . . . .	66
<b>4</b>	<b>Exciton physics under high excitation fluences in MoSe<sub>2</sub> monolayers</b>	<b>69</b>
4.1	Peak identification & polarization-resolved spectra . . . . .	70
4.1.1	Experimental results . . . . .	70
4.1.2	Identification of the trion type . . . . .	71
4.1.3	A negligible circular polarization for both trion and exciton . . . . .	73
4.2	Power dependent excitation: sublinear behavior of PL at high excitation powers . . . . .	75
4.2.1	The estimation of the doping level . . . . .	76
4.2.2	Effective temperature of the trion and exciton . . . . .	77
4.3	Imaging of the Halo: Laser-induced local heating of trions and excitons . . . . .	79
4.3.1	Experimental results . . . . .	79
4.3.2	A role of the hot exciton formation in the exciton and trion profiles . . . . .	80
4.3.3	The origin of the halo at high excitation powers . . . . .	82
4.3.4	Seebeck drift: Modeling for the halo based on the thermal gradient . . . . .	83
4.3.5	Exciton (X <sup>0</sup> ) resonant excitation . . . . .	85
4.4	Conclusions . . . . .	87
<b>5</b>	<b>Visualizing positively &amp; negatively charged excitonic species and the dynamical valley polarization of resident carriers in MoS<sub>2</sub> monolayers</b>	<b>89</b>
5.1	Fabrication and characterization of the MoS <sub>2</sub> charge tunable device . . . . .	90
5.2	Observing excitonic Rydberg states . . . . .	93
5.3	Visualization of excitonic complexes while electrically controlling the doping state . . . . .	94
5.3.1	Experimental results . . . . .	94
5.3.2	The fine structure of the negatively charged trion (T <sub>1</sub> and T <sub>2</sub> ) . . . . .	95

5.3.3	PL asymmetry in the $V_g$ response and $X'^+$ emission . . . . .	96
5.3.4	Estimation of doping level at $V_g = +30$ V and $V_g = -20$ V . . . . .	98
5.4	Circular & linear polarization in the different doping regimes . . . . .	100
5.4.1	Experimental results . . . . .	100
5.4.2	$X'^0$ and $X''^0$ emission states . . . . .	101
5.4.3	Negatively charged trions ( $T_1$ and $T_2$ ): very large valley polarization . . . . .	102
5.5	Demonstration of optically induced dynamical valley polarization of resident carriers (n- and p- types) .	104
5.5.1	Experimental results . . . . .	104
5.5.2	Model : dynamical valence valley polarization . . . . .	104
5.6	Conclusions . . . . .	106
<b>6</b>	<b>Conclusions and perspectives</b>	<b>109</b>
<b>A</b>	<b>Appendix</b>	<b>113</b>
A.1	Before/after laser irradiation in MoSe <sub>2</sub> monolayer . . . . .	113
A.2	Before/after laser irradiation in MoSe <sub>2</sub> monolayer . . . . .	113
A.3	Optical components (for $\mu$ -PL) . . . . .	113
A.4	PT100 temperature table (annealing chamber) . . . . .	116
<b>B</b>	<b>Résumé en français</b>	<b>117</b>

# Chapter 1

## Introduction

In this thesis, I have studied the excitonic spin/valley physics of transition metal dichalcogenide monolayers (MLs) through a polarization-resolved optical pumping technique.

**Chapter 1** briefly introduces the general interest in current industrial semiconductor technology and research fields of 2D materials. We will discuss details of 2D semiconducting transition metal dichalcogenides (TMDs) and focus on their optical properties: chiral optical selection rules and excitonic behaviors.

**Chapter 2** introduces our sample fabrication method (mechanical exfoliation) to obtain high optical quality hBN-encapsulated TMDs and the experimental setup (polarization-resolved micro-PL microscope) with a closed cycle He cryostat. The key features of our experimental setup allow us to study spin/valley polarization dynamics of 2D-TMDs by exploiting the chiral optical selection rules through the polarization resolving technique (circular/linear). Also, our hyperspectral imaging makes it possible to study the excitonic transport of TMDs, which can also be polarization-resolved.

**Chapter 3** introduces the cryogenic temperature experiments on polarization-resolved micro-PL in hBN encapsulated  $WS_2$  monolayer. We successfully resolved the different excitonic species, which are narrow in PL due to the hBN encapsulation, and demonstrated their spin/valley polarization. Especially, we resolved the trion fine structure which consists on a doublet separated by  $\Delta E(T_1-T_2) \sim 6$  meV and observed  $\sim 80$  % ( $\sim 18$  %) degree of circular polarization for the  $T_1$  ( $T_2$ ). We also have demonstrated that an optically induced dynamical valley polarization of resident electrons can be established. We observed a strong spin-dependent PL intensity for the  $T_1$ , which exhibits a ratio  $R = I^\sigma/I^\pi = 1.9$ . To interpret these experimental observations, we have proposed a simple bi-molecular model for the trion formation, which depends on the laser polarization due to the dynamical polarization of resident electrons.

**Chapter 4** introduces exciton physics under high excitation fluences in  $MoSe_2$  monolayer at low temperatures.

We focused on the information that can be extracted under high-density laser irradiations. We revealed the appearance of a halo for trions at high excitation powers and built a model to interpret the halo formation by using the steady-state drift-diffusion equation which includes the Seebeck drift induced by a thermal gradient.

**Chapter 5** introduces polarization-resolved micro-PL experiments in a MoS<sub>2</sub> charge tunable device. This device allows us to change the doping level of the sample between n, p, and neutral regimes. In that way, one can visualize and study both negatively and positively charged exciton species in one sample. We demonstrated that the optically induced dynamical valley polarization of resident carriers (for both n- and p- types) is also detectable in PL in Mo-based TMD MLs.

The main results obtained during my thesis work are summarized in the **Chapter 6 - Conclusions and perspectives** along with the foreseen developments of this activity in the short and medium term.

## 1.1 General introduction

The importance of the semiconductor industry has been continuously increasing and widely affecting the broad field of science and technology development since the first invention of the transistor [1]. Complex and massive systems have been based on transistor developments which would not have been possible with the electron tube. Computers, state-of-the-art integrated transistors, are an essential component for every activity of humanity from our daily life to frontier technologies. Automatized systems for massive production, technology and objects which require a higher precision are produced by increasing transistors density. Likely, this level of science and technology dependence on machines will not decrease.

In 1952, Geoffrey W.A. Dummer proposed the first idea of the integrated circuit to print electronic components on a semiconducting wafer. In 1958, this idea was realized by Jack. S. Kilby: he invented the first integrated circuit made of 6 transistors. This integrated circuits (IC) innovation opened dramatic progress of computer development. This progress made the new paradigm of the integrated circuit more solid, which has grown rapidly and still so.

As predicted by Gordon E. Moore, the performance of integrated circuits (IC) has doubled every two years exponentially since the 1970s. As shown in Fig. 1.1, the exponential growth still holds, but we must prepare to face the end of the paradigm for several reasons.

So far, people have developed IC technology by reducing their size down to the nanometer limit. In about 50 years, the precision of the technology was reduced from tens of micrometer to a few nm scales. In 1972, INTEL started an IC production with a 10  $\mu$ m process and now produces a computer CPU with a 10 nm process and Advanced Micro Devices (AMD) with a 7 nm one. Foundry companies adapted 4 nm processes for mobile application processors (APs) in 2022 and are testing 3 nm processes for massive production this year. We may expect that the silicon industry and IC paradigm get close to a physical limit once we consider that the lattice constant of the

crystalline silicon is 2.35 Å. For instance, one must have a facility of massive production to control 4 ~ 5 atoms or below to produce with 1 nm of precision. Already, INTEL renounced the two-year development strategy to drive for a three-year development cycle in 2016.

At these characteristic lengths, influences of physical phenomena on a microscopic scale such as quantum physics become stronger. For instance, tunneling is a big parasitic problem when the scale of IC elements reaches an atomic limit. Devices may malfunction because electrons can move through unwanted paths in the device by tunneling. It also affects the developing cost and time for higher performance of devices. Although various efforts are being made to overcome these limitations, we have to prepare for the end someday.

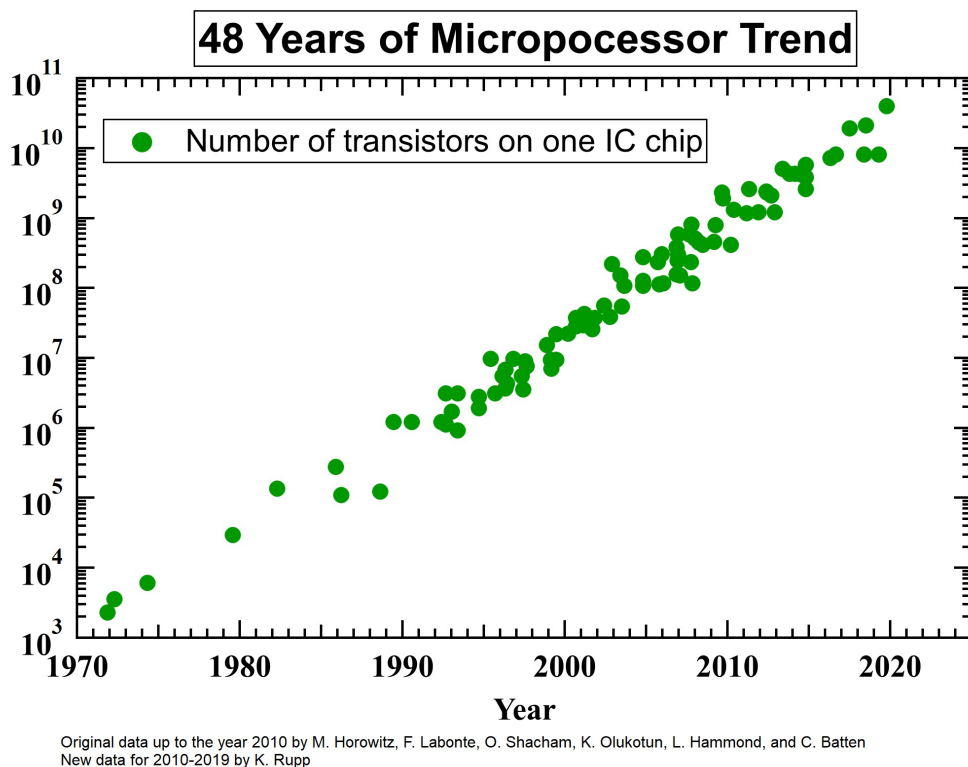


Figure 1.1: Number of transistors on one integrated circuit (IC) chip. [<https://github.com/karlrupp/microprocessor-trend-data>]

Nowadays, a great desire to seek for novel materials and phenomena is ongoing to open the next paradigm. Low-dimensional materials (2D, 1D, 0D) are spotlighted candidates, which exhibit novel phenomena in physics and are not fully understood so far. Among them, two-dimensional materials linked by van der Waals forces have been explosively studied since the discovery of the exfoliation method used for the isolation of graphene using scotch tape in 2004. This method made it possible to conveniently obtain two-dimensional materials from bulk and to study their characteristics. These two-dimensional materials are promising for valleytronics and twistrionics [2]. Fundamental study and understanding of these novel features are valuable in the scientific point of view. One may discover a breakthrough to substitute the current facing limitation of IC paradigm.



nanoribbons (GNR), a quasi-1D system that can be twisted, have been intensively studied. It can be fabricated by lithography techniques, unzipping of carbon nanotubes, and atomic layer deposition [11].  $\text{Bi}_2\text{O}_2\text{Se}$  and  $\text{As}_2\text{S}_3$  have been studied as topological insulators [12, 13, 14, 15, 16, 17] and for their thermoelectric properties [18, 19, 20]. Perovskites in a monolayer limit (ex,  $\text{SrTiO}_3$  in Fig. 1.2) have great potential and have been investigated in the solar cell field due to their competitive optoelectronic and thermodynamic properties [21, 22, 23]. This diversity of 2D materials, which includes as well ferromagnetic ( $\text{CrI}_3$  and  $\text{Fe}_2\text{GeTe}_2$ ) [24, 25, 26, 27] and ferroelectric (ex,  $\text{In}_2\text{Se}_3$ ) [28] materials, promises to open a new era in science and technology.

Importantly, transition metal dichalcogenides (TMD) monolayers can also be found in various bandgap energies with a chemical formula of  $\text{MX}_2$  (M is a transition metal, and X is a chalcogen atom, in Fig. 1.2). TMD monolayers can be insulating, semiconducting, metallic, semimetallic, and superconducting based on the atomic combination and structural phase. Among them, we have studied semiconducting TMD monolayers (M = Mo, W, and X = S, Se, and Te) because of their exciton/valley physics [29]. We will review the basic properties of TMD monolayers in the following section.

## 1.3 Transition metal dichalcogenides (TMDs)

### 1.3.1 Atomic structure

Transition metal dichalcogenides (TMDs) have a hexagonal crystal structure in 2D, and they are formed by weakly coupled monolayers, each one consisting of three stacked X-M-X layers where M is transition metal, and X is chalcogen. As shown in Fig. 1.3a-d, properties of TMDs depend on their structural phases.

The 2H hexagonal phase is displayed in Fig. 1.3a, it is one of the typical stable structural phases. Also, the 1T octahedral phase (Fig. 1.3b) is a natural state for some TMDs and the intermediate/distorted phases (1T', and 1T'' in Fig. 1.3c-d) are possible by phase engineering. TMDs may have different bandgap energy even for the same atomic composition because of their phase difference [30].

Among these possible TMDs configurations, we have studied semiconducting TMD monolayers of the 2H phase with direct bandgap families such as  $\text{MoS}_2$ ,  $\text{MoSe}_2$ ,  $\text{MoTe}_2$ ,  $\text{WS}_2$ , and  $\text{WSe}_2$ . Each layer within the TMD has the same hexagonal structure of graphene, but with two different atoms in an elementary cell. In the monolayer limit, the mixed composition breaks the inversion symmetry, resulting in the opening of a bandgap. Interestingly, due to quantum confinement effects, the bandgap changes from indirect to direct when it is thinned down to a monolayer. This was first confirmed experimentally by photoluminescence spectroscopy of mono and few-layer  $\text{MoS}_2$  in 2010 [33].

Fig. 1.4 shows the electronic band structure of  $\text{MoS}_2$  with different numbers of layers calculated by density functional theory. The red and blue lines indicate the conduction band and valence band, respectively. In bulk TMDs

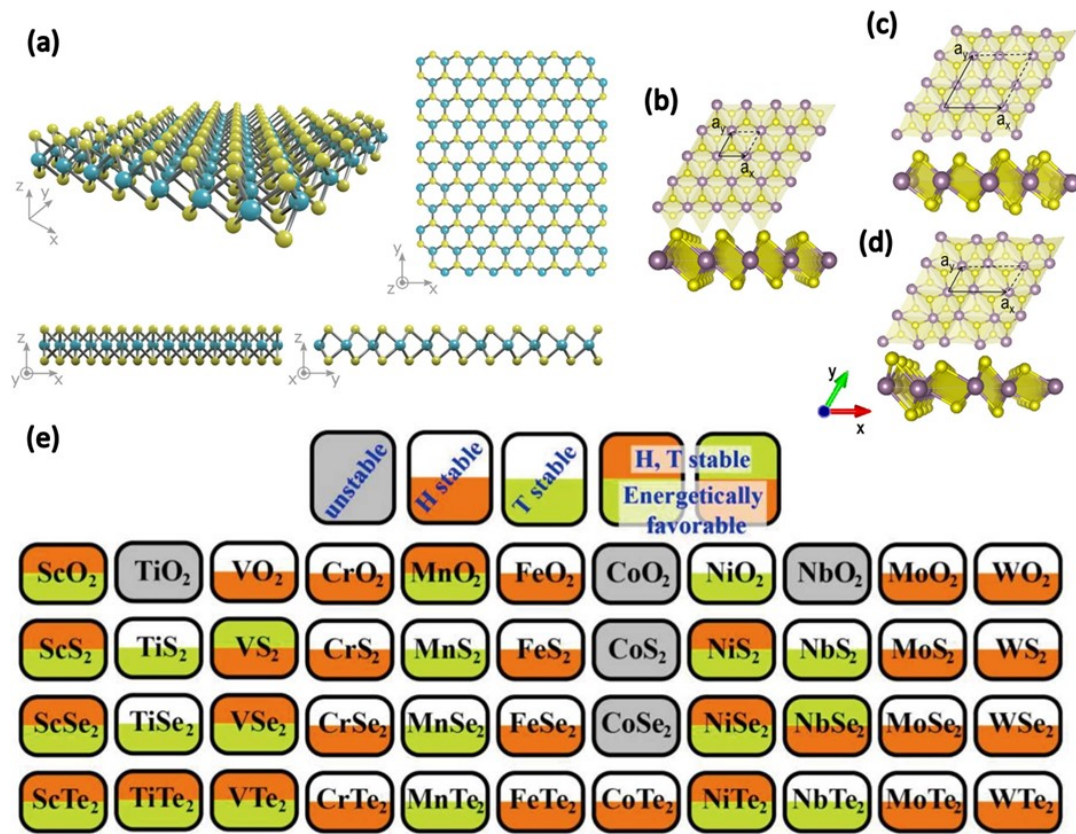


Figure 1.3: (a) atomic structure of a TMD monolayer (2H, hexagonal), where a transition metal is at the center, indicated by the eastern blue color, and chalcogen atoms are on both sides indicated by the yellow color. Atomic configurations of different TMD phases: (b) 1T, (c) 1T', and (d) 1T'' from the reference [31]. (e) a composition table for various TMD monolayers with stable structural phases [32].

down to the bilayer, the valence band maxima (VBM) and the conduction band minima (CBM) are not located at the same position in k-space (VBM is at  $\Gamma$ -point while CBM is between K and  $\Gamma$ ) due to the interlayer interaction of  $p_z$  orbitals between neighboring chalcogen planes. Instead, a monolayer of TMD has a direct bandgap at the K-points, which are the corners of the hexagonal Brillouin zone. Because of inversion symmetry breaking and the strong spin-orbit interaction induced by the heavy transition metal atoms, two non-equivalent and spin-polarized K points (denoted  $K^+$  and  $K^-$ , from now on also referred to as valleys) can be distinguished.

Especially, 2D Semiconducting TMDs (S-TMDs) have been investigated not only for fundamental electronic and optical approaches but also for photonics and optoelectronics applications [35]. We employed photoluminescence spectroscopy to focus on the properties brought by the strong light-matter interaction of 2D S-TMDs in the visible and near-infrared range. The light absorption of TMD monolayers can reach  $2 \sim 10\%$  at resonant energies [36, 37] but it can be enhanced further by engineering the dielectric environment. Indeed, this light absorption efficiency can be enhanced by cavity engineering up to  $90\%$  for WS<sub>2</sub> ML [38],  $\sim 70\%$  for MoS<sub>2</sub> ML, and  $\sim 75\%$  for WSe<sub>2</sub> ML [39]. These numbers are striking in particular if we take into account their thickness (less than 1 nm).

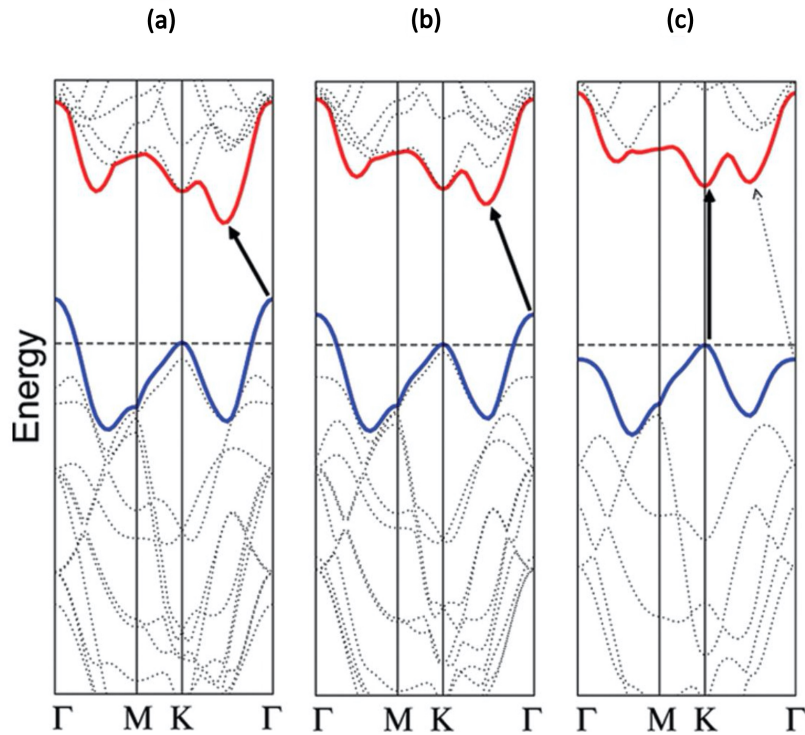


Figure 1.4: Calculated band structures of (a) bulk, (b) bilayer, and (c) monolayer  $\text{MoS}_2$ . The solid arrows indicate the lowest energy transitions. [34]

### 1.3.2 Strongly bound excitons in 2D

An exciton is a quasi-particle state formed by a bounded electron-hole pair which was first proposed as a concept by Yakov Frenkel in 1931 [40]. The exciton has been classified into two types based on the dielectric condition of the surrounding medium: Frenkel excitons are usually found in small dielectric constant, having large binding energies and very small exciton radius. The Wannier-Mott excitons occur in materials with large dielectric constant such as semiconductors [41]. This Wannier-Mott exciton in semiconductors shows a small exciton binding energy and very large radius (compared to the lattice constant) due to the strong dielectric screening of the Coulomb interaction in bulk. For example, GaAs has an exciton binding energy of  $\sim 4$  meV [42]. A GaAs quantum well, a quasi-2D system, shows a slightly increased exciton binding energy of about  $\sim 6$  meV [43]. In any case, the absolute value of the binding energy is small compared to room temperature. Moreover, depending on the quantum well thickness, they can also show a 3D behavior since it is a quasi-2D system [44]. However, this exciton character can be completely different in real two-dimensional semiconductors.

In 3D bulk, excitonic behavior is weakened because of the surrounding dielectric environment. The screening of the Coulomb interaction results in a small exciton binding energy near the bandgap, as shown in Fig. 1.5b. However, the screening of Coulomb interaction is reduced in a monolayer limit because of the surrounding dielectric environment (which includes air or vacuum). A stable exciton can form with considerable binding energy below the bandgap.

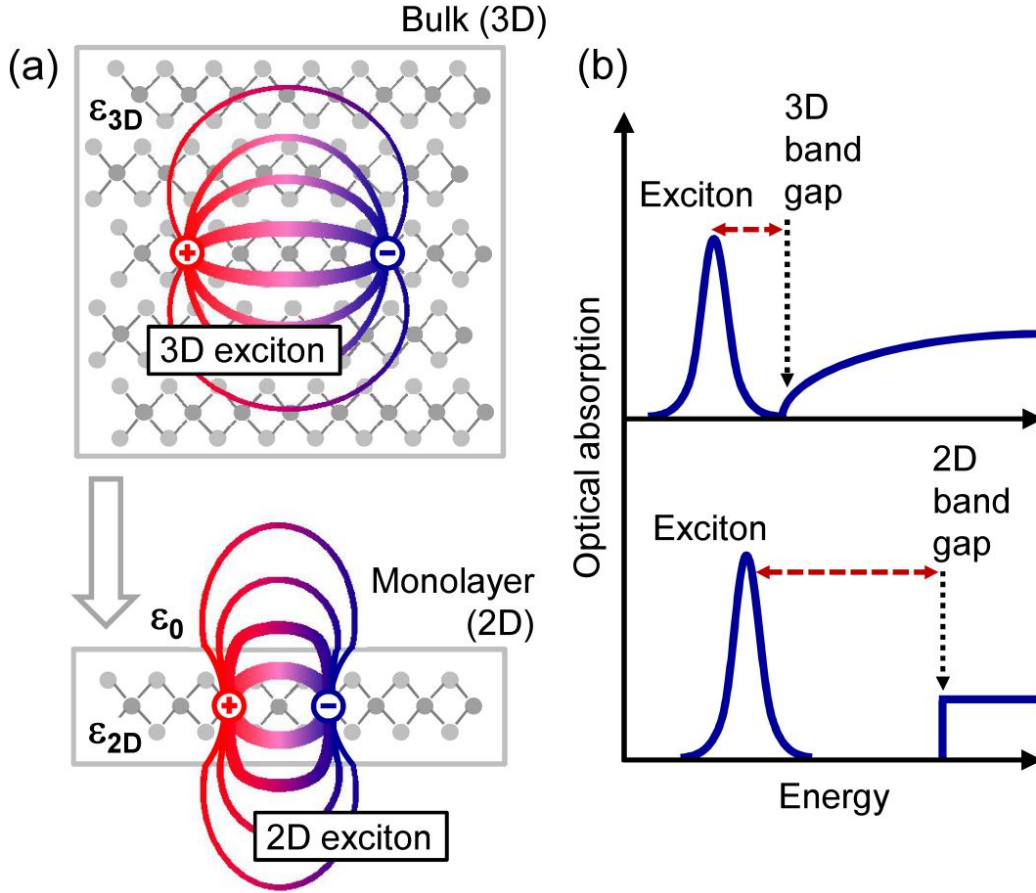


Figure 1.5: (a) Real-space representation of electrons and holes bound into excitons for the three-dimensional bulk and a two-dimensional monolayer. (b) Impact of the dimensionality on the optical absorption. The excited excitonic states and Coulomb corrections for the continuum absorption have been omitted for clarity. [45]

A remarkable feature of TMD MLs is therefore the existence of Wannier-Mott excitons with unusually large binding energies, due to the 2D quantum confinement and weak screening, as shown in Fig. 1.5a. This strong excitonic characteristic with a considerable spin-orbit coupling of the valence band at  $K^+$  ( $K^-$ ) points makes S-TMD MLs follow particular selection rules in optical transitions, which we will discuss in the next section.

The effective in-plane 2D interaction for charges can be modeled by the so-called Keldysh potential [46]:

$$V_{2D}(r) = \frac{\pi e^2}{(\epsilon_1 + \epsilon_2)r_0} \left[ H_0\left(\frac{r}{r_0}\right) - Y_0\left(\frac{r}{r_0}\right) \right] \quad (1.1)$$

Where  $\epsilon_1$  and  $\epsilon_2$  are dielectric constants of the top and bottom of the monolayer, respectively, the screening length  $r_0 = d\epsilon$  (the monolayer thickness  $d$  and isotropic dielectric constant  $\epsilon$ ), and  $H_0$  and  $Y_0$  are the Struve function and the Bessel function of the second kind, respectively. The interaction of the e-h pair strongly depends on the surrounding dielectric environment. The vacuum ( $\epsilon = 1$ ) is characteristic of an ideal environment of the 2D system. Once monolayers are deposited on a substrate, we observe in addition a dielectric disorder which will be discussed in section 1.5.

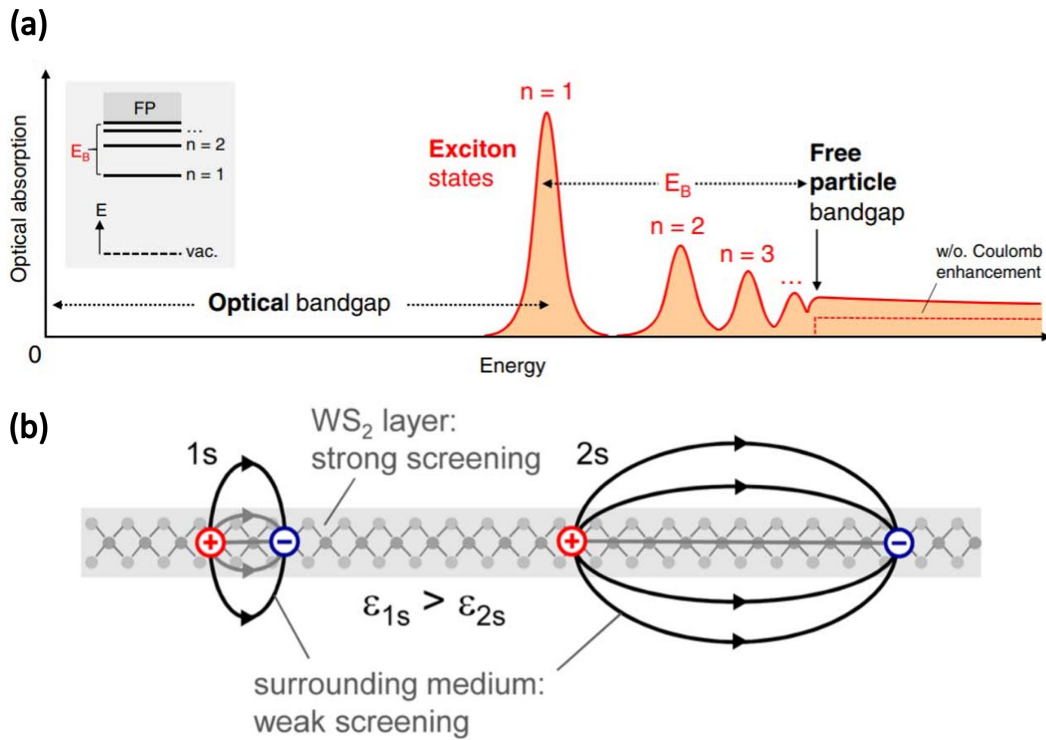


Figure 1.6: Schematic illustration of the optical absorption of an ideal 2D semiconductor, including the series of bright exciton transitions. The inset shows the energy levels of the excited exciton states in analogy with the hydrogen series, the so-called excitonic Rydberg series [47]. (b) Schematic representation of electron-hole pairs forming  $1s$  and  $2s$  excitonic states in a nonuniform dielectric environment [45].

Since the exciton in the 2D semiconductor is tightly bounded by the strong Coulomb interaction, excited states of the exciton, the so-called excitonic Rydberg series, may appear between the ground state of the bright exciton and the free particle bandgap. These Rydberg series are observed in various experiments due to the strong light-matter interaction, such as absorption [45], photoluminescence excitation [48], and magneto-photoluminescence [49] studies. The excited states of the exciton can be calculated and predicted by solving Schrodinger's equation with the potential 1.1. In 2D semiconductors, the effective dielectric constant needs to be treated as a variable depending on the excited states of the exciton because the effective dielectric environment changes with the exciton radius. The dielectric environment is strongly screened in the 2D layer while it is different through the surrounding medium of the 2D layer. The Coulomb interaction of the e-h pair in the exciton is confined more in the 2D layer when the exciton radius is small as shown in Fig. 1.6b. The effective dielectric constant needs to be taken into account to predict the excitonic Rydberg series correctly in 2D.

### 1.3.3 The role of the spin-orbit interaction on the optical selection rules

In Fig. 1.7a, angle-resolved photoemission spectroscopy (ARPES) data of a  $WS_2$  monolayer shows the splitting of the valence band at K points, of 425 meV, due to the dominant contribution of the spin-orbit coupling (SOC) by the

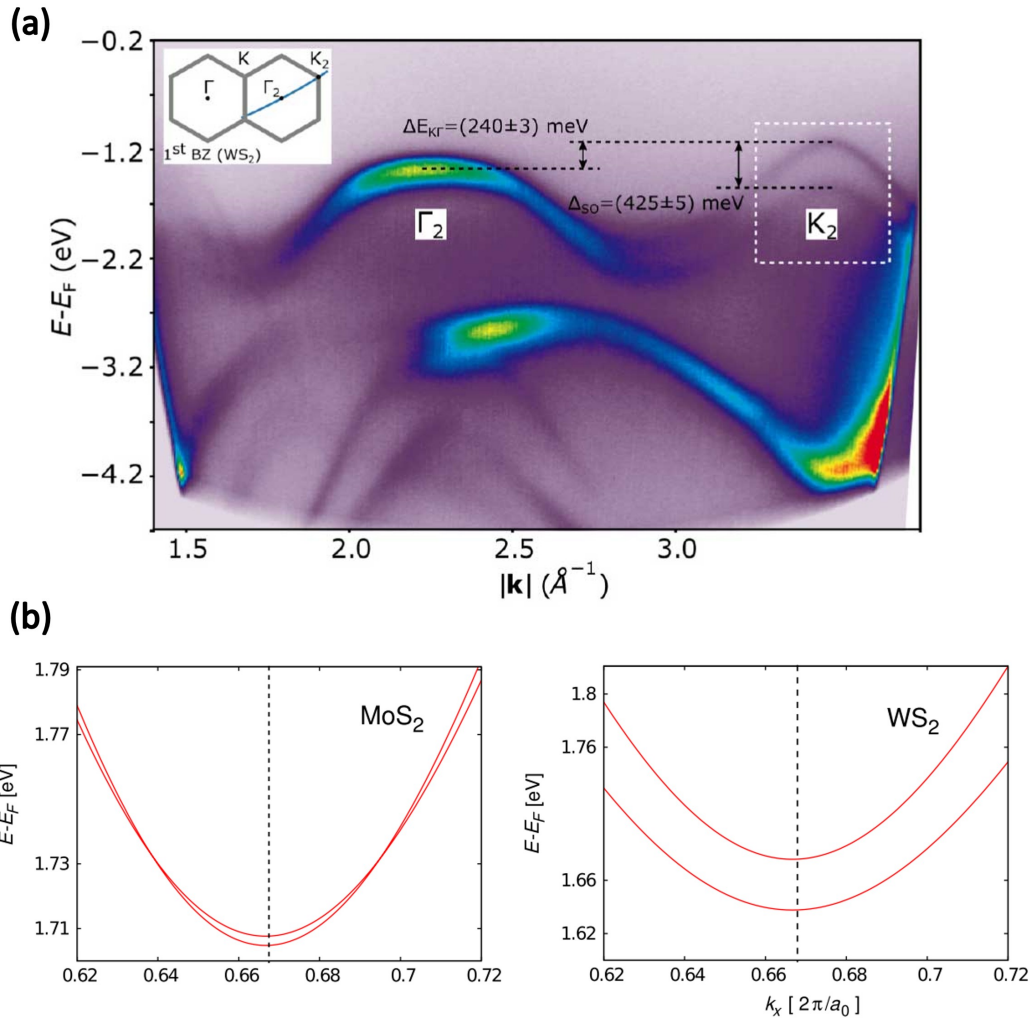


Figure 1.7: (a) ARPES intensity map of WS<sub>2</sub> monolayer [50]. (b) Conduction band structures of MoS<sub>2</sub> and WS<sub>2</sub> monolayer at the vicinity of K point from DFT calculations [51].

$d$ -orbital of the heavy transition metal [50]. SOC of the valence band at K point is usually reported experimentally by ARPES which yields  $\sim 470$  meV for monolayer WSe<sub>2</sub> [52],  $\sim 140$  meV for monolayer MoS<sub>2</sub> [53], and  $\sim 180$  meV for monolayer MoSe<sub>2</sub> [54]. While the conduction band, in Fig. 1.7b, is split by a smaller energy of SOC due to the competition between two contributions from chalcogen atoms and coupling to other bands [55].

For optical transitions, this strong SOC in the valence band maximum makes it possible to discriminate the photoinduced electron and hole generation from the valence subbands by selecting the excitation energy near the bandgap. This discrimination of the split subband structures at K points forces the system to react only to the selective polarization of the light for each  $K^+$  ( $K^-$ ) point.

The particular band structure of TMD monolayers causes interesting optical responses under polarized irradiation, such as chiral optical selection rules. This means circularly polarized light will be absorbed and emitted from the valleys with a valley-dependent helicity. The valleys in the electronic band structure in the vicinity of  $K^+$  and  $K^-$

points are shown in Fig. 1.8a and b for Mo and W-based TMDs, respectively. The conduction and valence band are split by SOC and, importantly, the sign of the spin-orbit splitting in the conduction band depends strongly on the transition metal. Indeed, ab-initio calculations predict a different spin ordering of the bands for Mo-based and W-based monolayers [56]. The splitting of the valence band, of a few hundred meV, is such that we can ignore transitions involving the lowest valence band for light energies close to the optical bandgap. The splitting of the conduction band is predicted to be of a few tens meV at most.

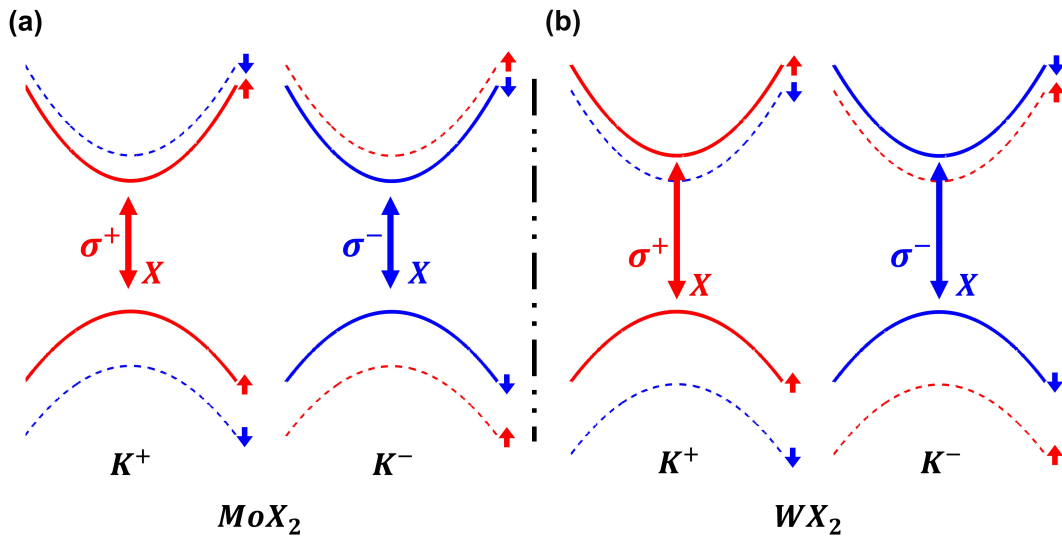


Figure 1.8: Schematic diagrams in a single-particle picture representing the lowest-energy optical transition of single layer (a)  $\text{MoX}_2$  and (b)  $\text{WX}_2$  in the vicinity of the K points. The arrows represent the electron spin along the axis perpendicular to the monolayer.  $\sigma^+$  and  $\sigma^-$  represent the helicity of the circularly polarized photon involved in each vertical transition.

Although  $\text{MoX}_2$  and  $\text{WX}_2$  both belong to the semiconducting TMD group in the monolayer limit, the electronic band structure and in particular the optical properties in the vicinity of the K points are not identical due to the influence of the transition metal on the sign of the spin-orbit splitting of the conduction band. Since optical transitions conserve the electron spin, the most energetically stable exciton in  $\text{WX}_2$  is “optically dark”, whereas in  $\text{MoX}_2$  is “optically bright”. This separation between “bright” and “dark” materials depending on the transition metal was thought to be initially confirmed by looking at the behavior of the photoluminescence intensity as a function of temperature [57]. In reality, the PL yield depends on many other factors and not only on the conduction band ordering. More recently, however, the “dark” and “bright” ordering of the excitons have been confirmed for  $\text{WSe}_2$  and  $\text{MoSe}_2$  monolayers, respectively. [58, 59, 60]. Note that due to the relatively large exciton radius of a few nm, the exciton wavefunction does not spread too far from the K points in the reciprocal space. The chiral optical selection rules are therefore valid also for excitons.

### 1.3.4 Valley polarization and coherence

Generally speaking, the exciton valley (and spin) polarization is defined as  $(n_+ - n_-)/n$ , where  $n_{\pm}$  is the number of excitons in the  $K^{\pm}$  valley and  $n$  is the total number of excitons. PL spectra under circularly polarized light excitation and the degree of circular polarization on a non-encapsulated  $\text{MoS}_2$  ML at  $T = 83$  K from Ref. [61] are shown in Fig. 1.9a. The black curve indicates the degree of circular polarization. The red and blue curves indicate co-circular and counter-circular detections under circularly polarized excitation, respectively. A large degree of valley polarization of excitons under circularly polarized continuous wave excitation has been reported in several TMD MLs [61, 62] at cryogenic temperatures, demonstrating the optical initialization and optical reading of the valley index.

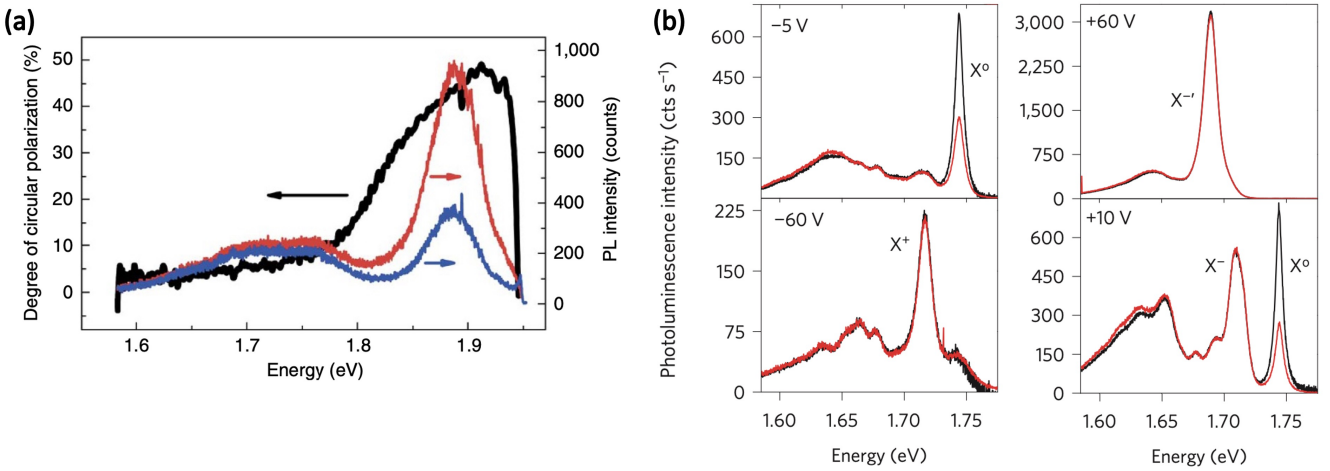


Figure 1.9: (a) Circularly polarized micro-PL of monolayer  $\text{MoS}_2$  at 83 K, along with the degree of circular polarization of the PL. The red and blue curves correspond to the intensities of  $\sigma^+$  and  $\sigma^-$  polarizations, respectively, in the luminescence spectrum. The black curve is the net degree of polarization [61]. (b) Polarization-resolved photoluminescence spectra of  $\text{WSe}_2$  at selected gate voltages for horizontally (H, black curve) and vertically (V, red curve) polarized detection. Incident laser is horizontally polarized [62].

Furthermore, the so-called exciton valley coherence has been observed under linear ( $\pi$ ) excitations [62, 63]. Linear light can be decomposed into a coherent superposition of circularly polarized photons, and the optical transition in a single valley is only possible by absorption of circularly polarized photons. Thus, linear irradiation generates a coherent superposition of excitons in the  $K^+$  and  $K^-$  valley. Due to a very short exciton lifetime at low temperatures (on the order of a few ps) comparable to the valley decoherence time, the excitons recombine while partially preserving their coherent superposition. The PL is thus linearly polarized. The lifetime of this phenomenon is limited by the exciton lifetime and can be shortened by additional dephasing in the system. Thus, we can observe linear polarization of the PL under linear excitation, and the degree of linear polarization is an indication of the ratio between the exciton lifetime and the valley decoherence lifetime.

Fig. 1.9b shows PL spectra of  $\text{WSe}_2$  ML on silicon substrate at  $T = 30$  K under linear laser excitation at different doping regimes [62]. Black curves and red curves indicate co-linear and cross-linear PL detection, respectively.

Note that one can observe negatively charged trions ( $X^-$  and  $X^{-'}$ ) or positively charged trion ( $X^+$ ) for n-type or p-type configuration of resident carriers through changing of the applying gate voltage sign. Here in graphs, the negative gate voltage is p-type so that the  $X^+$  is detected and the positive gate voltage corresponds to n-type and so  $X^-$  and  $X^{-'}$  are detected in PL.

All the other excitonic states ( $X^-$ ,  $X^{-'}$ , and  $X^+$ ) does not exhibit linear polarization. In contrast, the exciton ( $X^0$ ) exhibits a noticeable degree of linear polarization due to the valley coherence.

## 1.4 Fabrication and synthesis

Fabrication and synthesis of 2D TMDs and their heterostructures are a common interest for fundamental research and applications. They are produced by two different strategies. The bottom-up approach is scaling up from atomic size. The top-down method is thinning down the layered materials to a 2D limit by mechanical and chemical exfoliation methods. Developing large-area fabrication and synthesis of 2D materials and heterostructures while ensuring their high-quality atomic structure is one of the main issues. Even though new materials can exhibit excellent properties, many are not adapted to the industry due to limitations of scalable synthesis and control.

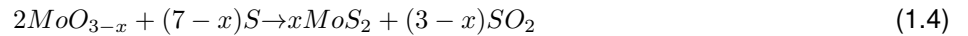
The bottom-up approach has an advantage for the scalable growth of 2D TMDs that can be grown up to wafer-scale depending on the growth conditions and substrate size. However, obtaining high-quality samples and building heterostructures is challenging, and many efforts are currently being made to improve the quality of synthesized 2D TMDs. For 2D heterostructures, the different forming temperatures of 2D materials and lattice constants are the main issues to solve. The top-down method, such as mechanical and chemical exfoliation, is used to obtain high-quality 2D materials from bulk. Any heterostructure can be made by stacking van der Waals layers without being limited from lattice mismatch and growth temperature issues. Note that 2D materials interact with van der Waals force, which can be expected to induce small modification in the layer properties coming from the lattice mismatch. However, It still has to be considered to grow high-quality heterostructures.

This section briefly overviews various fabrication and synthesis methods with the mechanical exfoliation discussed in the last part, which is the method we use for fabrication of our samples.

### 1.4.1 Bottom-up approach: Large-area synthesis

Chemical vapor deposition (CVD) is a widely used technique: chemical reaction produces final solid compounds, different chemical composition starting from the vapor phase source. Since this CVD process contains a wide range of concepts, it can be divided into various techniques depending on the key component used for the syntheses: atmospheric pressure CVD (APCVD), low pressure CVD (LPCVD), plasma enhanced CVD (PECVD), metal-organic CVD (MOCVD), and atomic layer deposition (ALD). Here, we look up a few powerful methods for synthesizing

2D S-TMD starting from CVD, but not all CVD-based methods are adopted for their synthesis. Generally, S-TMD monolayers are synthesized in the CVD reactor by the following reaction (e.g. WSe<sub>2</sub> and two-steps reaction for MoS<sub>2</sub>) [64],



Other 2D S-TMDs (WS<sub>2</sub>, MoSe<sub>2</sub>, and MoTe<sub>2</sub>) can be synthesized by taking different combinations of transition metal trioxide and chalcogen powder [65, 66, 67]. For instance, a schematic of the CVD chamber for synthesizing MoSe<sub>2</sub> monolayers is shown in Fig. 1.10a. First, one installs a SiO<sub>2</sub>/Si or sapphire substrate with transition metal trioxide powder and chalcogen pellets in the CVD furnace. Then, the furnace atmosphere is replaced by Ar/H<sub>2</sub> with low pressure by operating a vacuum pump. MX<sub>2</sub> monolayers are synthesized by elevating the temperature of the furnace. Thus, the synthesis depends on the temperature and its elevating process for the substrate, the pressure of Ar/H<sub>2</sub>, and the substrate. Achieving scalable growth of the monolayers is rather difficult due to their random formation as shown in Fig. 1.10b. Nevertheless, a wafer-scale growth is possible by controlling the parameters as shown in Fig. 1.10d. Also, many efforts have been made to understand the growth mechanism to obtain single crystalline 2D, large-area growth [68], and their heterostructures. Discriminating growth of heterostructures by in-plane and vertical direction is also possible, as shown in Fig. 1.10c. The construction of heterostructure superlattices (Fig. 1.10e) is also reported by MOCVD, introduced by pyrolysis reaction of organic transition metal compounds in the CVD branch.

Various CVD methods have been used for wafer-scale growth. For instance, the two-step CVD technique is commonly employed for a wafer-scale growth of 2D TMDs. First, MO<sub>3</sub> layers are evaporated on the substrate and monolayers are grown through CVD process with chalcogens [72, 73]. This two-step CVD ensures a continuous deposition of the 2D film. Direct deposition on MoO<sub>2</sub> microcrystals is also an efficient method to grow and transfer continuous film [74]. Epitaxial Growth on Au(111) surface can be an adaptable technique for scalable growth [75, 76]. Atomic layer deposition (ALD) is a worthwhile method to think about for area-selective deposition [77]. Pulsed laser deposition (PLD) is useful for building large area heterostructures with different chalcogen compounds [78].

## 1.4.2 Top-down approach: practical methods for vertical heterostructures

Chemical exfoliation and mechanical exfoliation are the two most common examples of the top-down approach. The main advantage of the top-down approach is that it can produce good quality monolayers from highly crystalline bulk TMDs. Moreover, 2D heterostructures are easily made by stacking layers without considering their lattice mismatch,

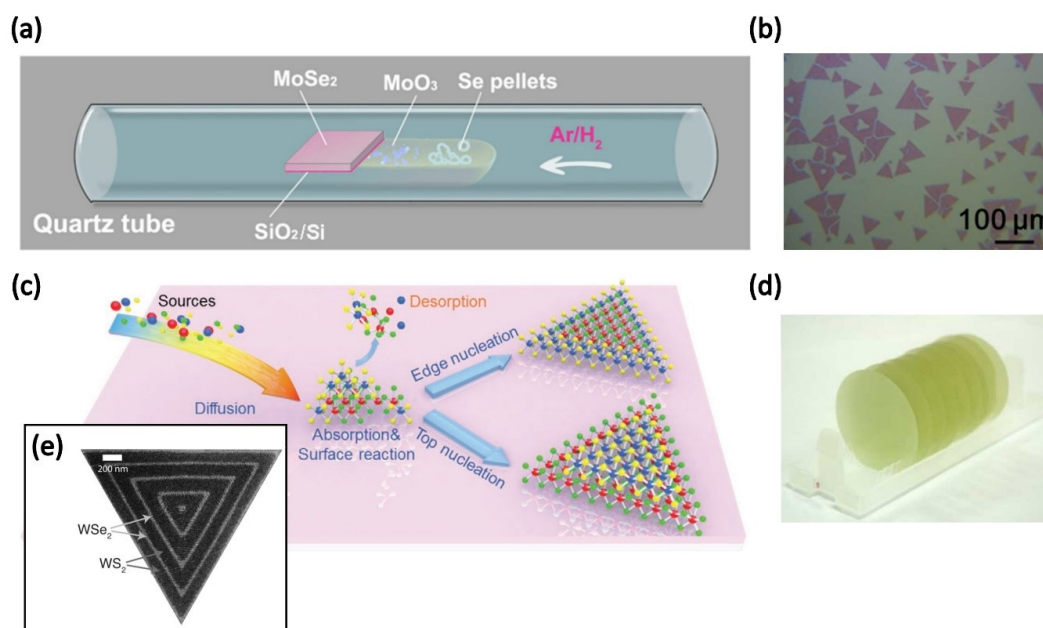


Figure 1.10: (a) a schematic of the CVD chamber to synthesize  $\text{MoSe}_2$  monolayer. (b) an optical image of monolayer triangles. (c) a schematic of the general CVD process in 2D TMDs. (d) an optical image of  $\text{MoS}_2$  monolayers on 2-inches sapphire substrates by CVD. (e) a SEM image of monolayer  $\text{WS}_2/\text{WSe}_2$  superlattices by MOCVD. Images were taken from (a)-(b) [66], (c) [69], (d) [70], and (e) [71]

growth & decomposition temperature difference, and twisted angle, which are the general issues of the bottom-up method.

General concepts of the chemical exfoliation are represented in Fig. 1.11. For instance, ion interaction can be a key to separate TMD layers by chemical interaction. It can be declined in various types depending on the interaction between molecules or ions by non-covalent bonding with solvent [79]. Ion exchange is another concept adapted to thin down in chemical way for layered materials with exchangeable interlayer of cationic counterions structures such as metal oxides [80]. Especially, sonication-assisted exfoliation has widely been adapted for TMDs [81, 82], and graphene because pressure fluctuations in the solvent by ultrasonication efficiently separate Van der Waals layers [83]. The kinetic energy supply of ultrasound initiates the exfoliation, making the roles of solvents less critical as a trigger. However, a proper selection of solvents and sonication can improve the qualities of exfoliated monolayers by considering the interactions between the layered materials and the solvents, which requires well-understood chemistry knowledge in solvents [84].

Mechanical exfoliation is a physical approach to separate stacks of 2D layers by breaking the weak attraction force between van der Waals layers. Since the exfoliation of graphene by scotch tapes in 2004, this method has become well known and is commonly used for graphene and other layered materials (e.g., TMDs) for fundamental studies, device applications, and for building heterostructures [85]. This technique has the following advantages: 1) Operators can produce 2D materials from highly crystalline bulk without profound knowledge of growing techniques (top-down approach) or chemistry (chemical exfoliation) as introduced previously. 2) The main equipment

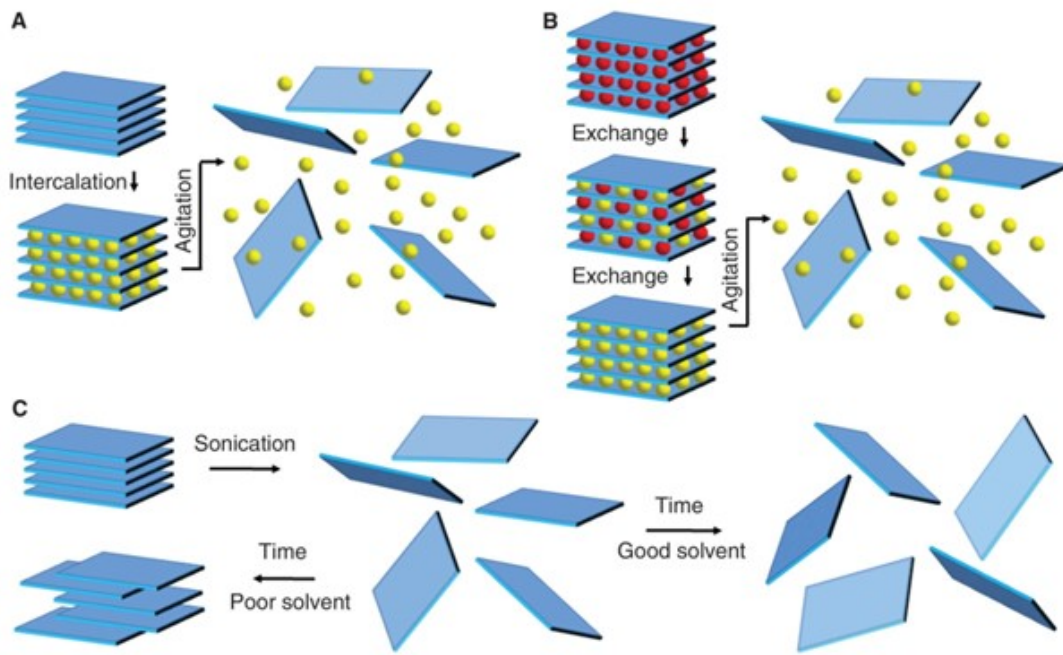


Figure 1.11: Schematic description of the main liquid exfoliation mechanisms (a) ion intercalation. (b) ion exchange (c) sonication assisted exfoliation. [80]

of mechanical exfoliation is a combined system for an optical microscope and a stamping stage, as shown in Fig. 1.12a. Monolayers can be oriented and manipulated deterministically on the substrate, which is allowed by adopting viscoelastic polymers such as polydimethylsiloxane (PDMS) [86]. 2D flakes can be transferred deterministically by balancing the attraction force between the substrate and 2D flakes with the adhesive force. This viscoelasticity makes it possible to transfer (or pick up) by peeling off the PDMS slowly (or quickly), as shown in Fig. 1.12b. Thermal heating may assist this process. The details of mechanical exfoliation will be discussed in chapter 2.

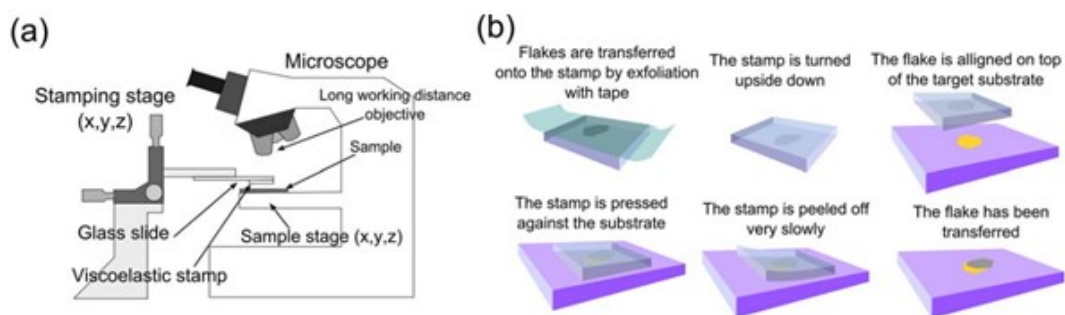


Figure 1.12: Deterministic transfer setup and process. (a) schematic diagram of the experimental setup. (b) diagram of the steps for the viscoelastic stamp and the deterministic transfer. [86]

However, this exfoliation method has the disadvantage of getting 2D flakes of relatively small size. In general, graphene can be exfoliated into flakes of hundreds of micrometers of lateral size, whereas this size is only a few ten micrometers for TMDs. This limitation requires  $\mu\text{m}$  scale resolution of the setup to perform experiments on 2D samples fabricated by mechanical exfoliation. Many efforts have been made to obtain large monolayers by

improving the exfoliation method, such as gold-assisted exfoliation [87, 88]. These reports have demonstrated that TMD monolayers of mm scale can be obtained by exploiting the strong affinity between Au and sulfur on atomically flat Au substrate. However, a special etchant, which do not melt monolayers but only gold, is required to transfer exfoliated monolayers from the gold substrate due to the strong adhesion.

Mechanical exfoliation is also powerful to fabricate vertical heterostructures and superlattices (e.g., Moiré) by staking 2D layers vertically and with different atomic orientations [89, 90, 91].

## 1.5 Suppression of dielectric disorder by hBN encapsulation

There are many imperfection factors that degrade the optical quality of monolayers. A good quality is important to study spin/valley physics. As shown in Fig. 1.13a, intrinsic disorder may occur due to different kind of defects: Vacancy is an absence of an atom in the lattice. An anti-site is a replacement of atoms by the pair atomic element of the material. Substitution is an exchange of atoms by a different group in the periodic table that induces doping on the system, whether positive or negative. Discontinuity of 2D material's edges also may induce disorder. Poor crystallinity and grain boundaries contribute to disorder. Extrinsic disorder can arise when monolayers lie on a rough substrate such as silicon, for example strain may be produced due to the van der Waals interaction between layers but also due to the roughness of the substrate. A tensile strain induces a redshift of the exciton PL emission, and a compressive strain introduces a blueshift of the exciton spectrum [92]. Also, as shown in Fig. 1.13b, the monolayer

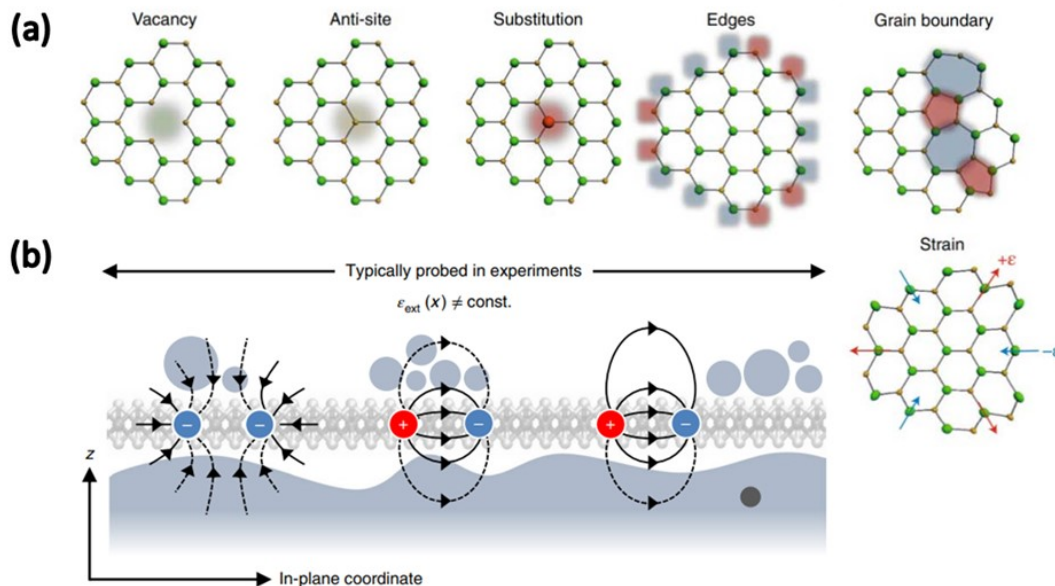


Figure 1.13: Typical disorder. (a) vacancy, anti-site, substitution, edges termination, grain boundary, and strain [93]. (b) Schematic illustration of the electron-electron and electron-hole interaction affected by environmental screening fluctuations due to the substrate roughness, impurities, and adsorbates [94].

is in an inhomogeneous dielectric environment due to contamination when it is deposited on the substrate. All these

factors degrade the optical and electronic properties of the materials. Moreover, photoinduced doping may appear in optical experiments [95]. This increase of the dielectric disorder leads to increased energy fluctuations of excitonic states and causes an important inhomogeneous broadening of the transitions [94].

As shown in Fig. 1.14a, hexagonal Boron Nitride (hBN, 2D insulator) encapsulation provides an atomically flat surface contact with 2D S-TMDs since both are van der Waals layered materials. It strongly suppresses dielectric disorders by the surrounding environment, especially from the substrate. Thus, the substrate becomes irrelevant to the hBN encapsulated monolayer. In the PL experiment of Fig. 1.14b, one can resolve excitonic complexes with a narrow linewidth close to the homogeneous limit by isolating the monolayers from the substrate at low temperatures. Also, STM topography and charge density maps of graphene proved that the hBN layer ensures more homogeneous conditions, which cannot be obtained on SiO<sub>2</sub>/Si substrates [93].

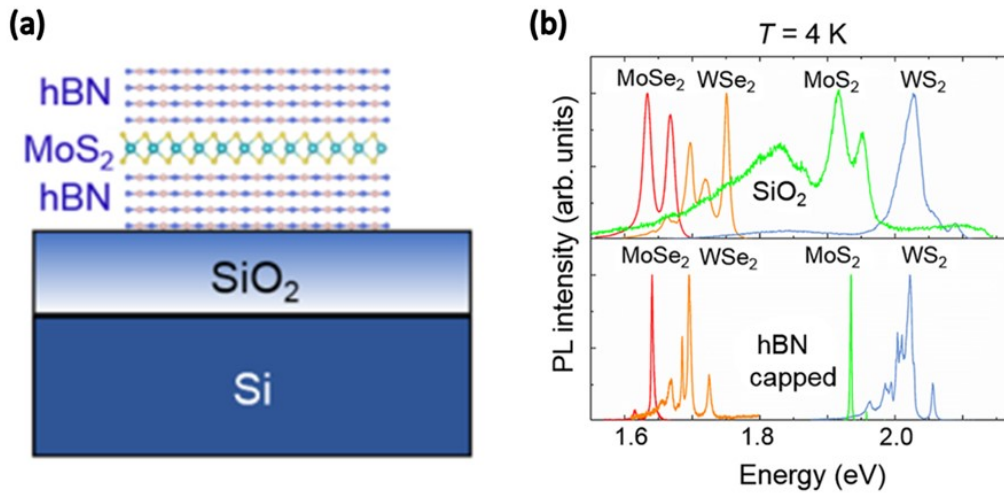


Figure 1.14: (a) a schematic of hBN encapsulated MoS<sub>2</sub> monolayer. (b) photoluminescence spectra of S-TMD monolayers (top) on SiO<sub>2</sub>/Si substrate (bottom) encapsulated by hBN at T= 4 K. [96]

However, there might be still non-negligible substrate effects on monolayers even after hBN encapsulation. Y. Zhou et al. [97] have reported that the homogeneity of PL spectra is higher for suspended hBN encapsulated MoSe<sub>2</sub> monolayer. They have obtained PL spectra in the suspended area which give a narrow linewidth of  $\sim 1.5$  meV and very small energy fluctuations across this region. These results show how more work is still necessary to reduce disorder and approach ideal conditions, but also how external screening engineering can be an extremely sensitive tool for a fine control of 2D materials properties.

## 1.6 Conclusions

We briefly went through the overview of various 2D materials that have been studied recently such as graphene (a zero-gap material), 2D perovskites, 2D ferromagnetic materials, topological insulators, and TMDs. Especially, TMDs

can be insulating, semiconducting (S-TMD), metallic, semi-metallic, and superconducting. Among them, S-TMDs (e.g., MoS<sub>2</sub>, MoSe<sub>2</sub>, MoTe<sub>2</sub>, WS<sub>2</sub>, WSe<sub>2</sub>) are attractive due to their indirect-direct bandgap transition in the atomic layer limit. In the monolayer limit, semiconducting TMDs show extraordinary features close to the bandgap in the so-called K valleys. The conduction band minima (CBM) and the valence band maxima (VBM) occur at the K<sup>+</sup> and K<sup>-</sup> corners of the Brillouin zone. Strong light-matter interaction with excitonic formation (with a binding energy of ~ hundreds of meV) arises at the valleys due to the weakening of dielectric screening, heavy electron/hole effective mass ( $m^* \sim 0.5m_e$ , where  $m_e$  is the free electron mass), and 2D quantum confinements. These new physics brought by the spin-polarized valleys has been intensively studied for valleytronics and spintronics fields. These exciton/valley physics is still under heavy investigation.

We employed an optical method to study fundamental exciton/valley physics in 2D S-TMDs. Before discussing our experimental results, the following chapter (chapter 2) will introduce the experimental methods to prepare and characterize 2D samples and the main optical setup based on polarization-resolved photoluminescence microscopy.

## Chapter 2

# Sample preparation & experimental methods

In the previous chapter, we explored the basic background of 2D S-TMDs from their properties to fabrication and synthesis methods. Importantly, we discussed that the chiral optical selection rules are valid for transitions at the bandgap energy. We employed polarization-resolved micro-photoluminescence spectroscopy developed by our group to study 2D S-TMDs, which exploits the optical valley selection rules.

This chapter will introduce the main experimental methods used in this work. First, the mechanical exfoliation setup to fabricate TMD monolayers and devices. This method permits to obtain high-quality 2D samples with compatible lateral size with our photoluminescence microscope. After fabrication of 2D samples with the mechanical exfoliation, we also have performed room temperature PL, Raman, and we use atomic force microscopy (AFM) to characterize our samples before the main experiment at cryogenic temperature. Secondly, the polarization-resolved micro-photoluminescence spectroscopy to investigate their optical properties at low temperatures. The details of the experimental setup and analyzing techniques will be introduced in the last part of this chapter.

### 2.1 Mechanical exfoliation

We employed mechanical exfoliation, also known as the scotch tape method, to fabricate 2D TMDs and their devices. Since van der Waals forces link TMD layers, we can efficiently thin them down with scotch tape because the adhesive strength between layers is weaker than the stickiness of the tape. This method yields TMD monolayers of typically tens of  $\mu\text{m}$  of lateral size, which are large enough for  $\mu\text{PL}$  experiments whose resolution is given by the sub- $\mu\text{m}$  size of the laser spot. The scotch tape method has several advantages: we can obtain high-quality monolayer samples with a much simpler method compared to the bottom-up approach. Indeed, mechanical exfoliation requires

relatively simple equipment: a standard optical microscope, a transfer stage, bulk materials to thin down, and tapes. In contrast, synthesizing 2D materials by chemical methods requires many efforts to optimize the experimental parameters of the growth [98]. Hence, one can fabricate any heterostructure or device with different layered materials by simply stacking them together. The same result would be difficult to achieve by direct growth due to the different growing conditions. For example, growing high-quality vertical heterostructures may have difficulties due to lattice mismatch. Growing temperature is also an important factor since the temperature of the second layer must be lower than the melting temperature of the first layer. Also, a proper substrate for growing must be selected. Moreover, we can efficiently obtain hBN encapsulation which improves the optical response of TMD monolayers obtained with mechanical exfoliation. Therefore, mechanical exfoliation is widely used for many studies due to its flexibility, simplicity, and the resulting high optical quality of the samples [99, 100, 101, 102, 103]. Thus, we have successfully prepared samples for the thesis with this method. The process of mechanical exfoliation done in our lab will be introduced below.

### 2.1.1 Process

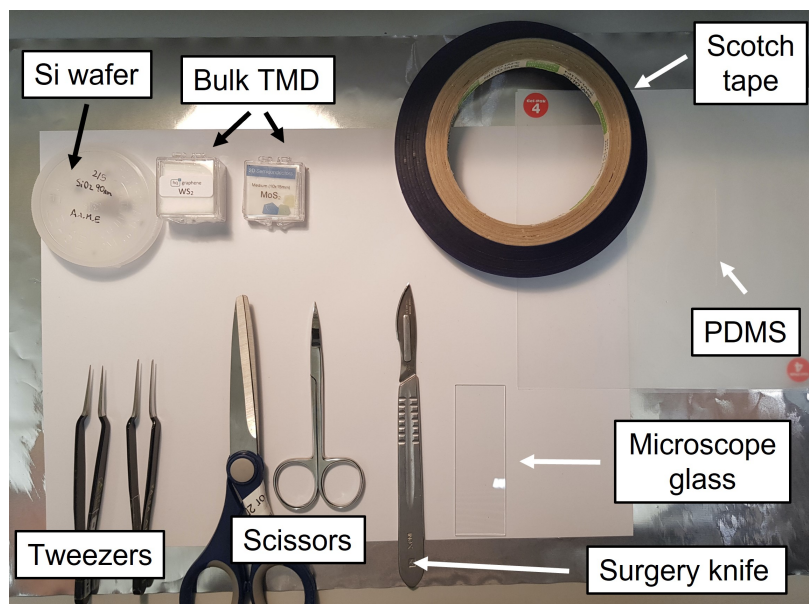


Figure 2.1: Required equipment for mechanical exfoliation. (Image was especially taken from outside of the glovebox for demonstration)

Fig. 2.1 shows the materials and tools required to exfoliate layered materials: SiO<sub>2</sub> (90 nm)/Si wafer (previously cleaved), with pre-patterned metal contacts in the case of contacted devices, bulk TMD (from commercial sources such as 2D semiconductors or HQgraphene), blue scotch tape (Nito, Rubans de Normandie), polydimethylsiloxane (PDMS, Gelpack 4), tweezers (round tip, sharp tip), scissors (standard, surgery), a knife (surgery), a microscope glass.

## Step 1. Exfoliation with the scotch tape

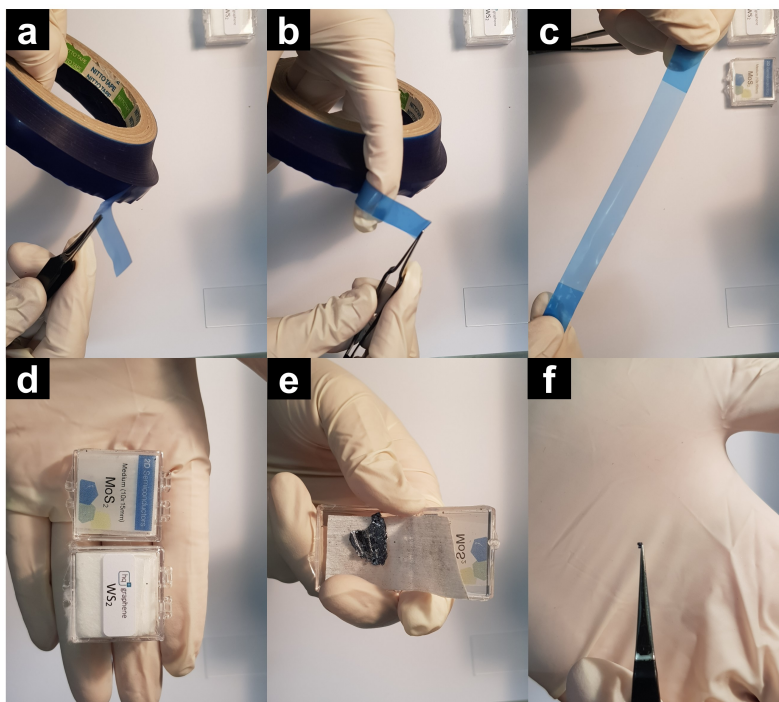


Figure 2.2: Steps to prepare the scotch tape (a-c) and a small flake of TMD (e-f) for the exfoliation. (Images were especially taken from outside of the glovebox for demonstration)

First, we prepare a scotch tape for thinning down TMDs. As shown in Fig. 2.2a-c, we fold both edges of the scotch tape to grab and handle the scotch tape for manipulation. We take a small flake (a lateral size of  $\sim 1$  mm) of TMD to put on the scotch tape as shown in Fig. 2.2d-f. Note that a tiny flake is sufficient for the exfoliation because it is thinned down and spreads out on the scotch tape. We use two tweezers to take off the flake with one tweezer while grabbing the bigger piece of TMD with the other.

Then, as shown in Fig. 2.3a, we put the TMD flake on the center of the scotch tape. We fold and unfold it many times at different angles, as shown in Fig. 2.3b-e, to separate layers through the adhesive force of the scotch tape. Like this, we detach layers from bulk by placing flakes onto an empty area of the scotch tape.

Now, we put a small PDMS piece onto the microscope slide's edge, as shown in Fig. 2.4a. One may unintentionally create bubbles between the PDMS piece and the microscope glass, as shown in Fig. 2.4b. To correct this, we pick up one edge of the PDMS piece while keeping the other edge attached. Then, we release it slowly, with the round-tip tweezer to avoid possible scratches, to eliminate the interlayer bubbles through the process in Fig. 2.4c-d. This technique removes bubbles, as shown in Fig. 2.4e. Dust may interfere during the whole process in an unclean environment because the demonstration happened in a dust-rich condition. One can observe small dust on the surface of the microscope glass in Fig. 2.4a-e. They cannot be efficiently removed once they are produced because one may produce scratches on the PDMS piece to remove them. As with bubbles and dust, these scratches reduce

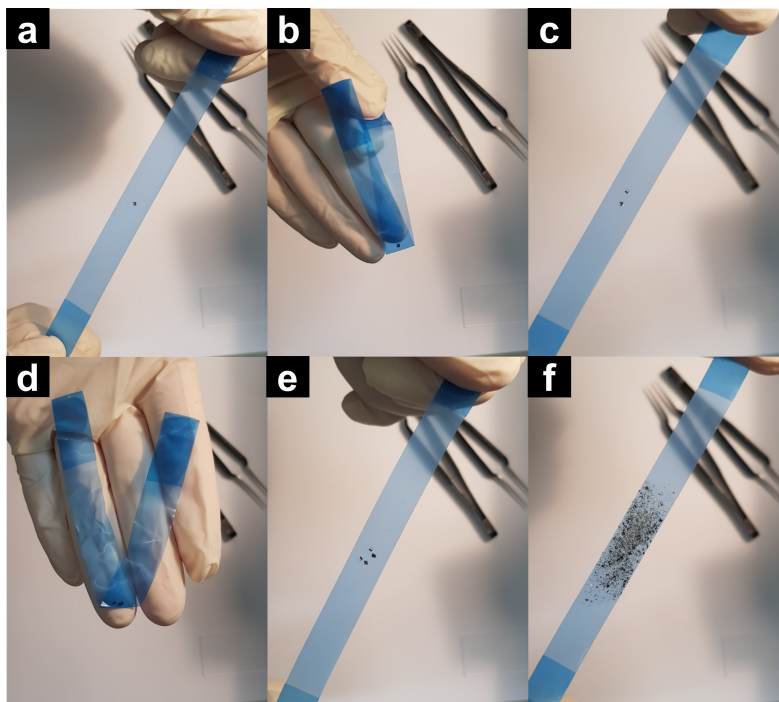


Figure 2.3: Process to thin down layers with the scotch tape (a-f). repeat (b-e) by taking different folding angles to get thinned flakes (f). (Images were especially taken from outside of the glovebox for demonstration)

the active area of the PDMS piece for the transferring of monolayers. Dust and scratches physically interrupt the optical microscopy to visualize TMD flakes through the PDMS piece. Bubbles will make the transfer of monolayers difficult because they introduce displacement of TMD flakes during the stamping process if they are on the location of the bubbles. The stamping introduces a pressing force between the substrate and the microscope glass which moves the bubbles. Considering our typical size of TMD monolayers ( $\mu\text{m}$  scale), this movement is a critical factor in fabricating the device. Additionally, in this step, we may have two choices: either having small (A) or big (B) PDMS pieces (see Fig. 2.4f). While it may seem efficient to choose (B) to increase the chance of finding monolayers, this is not always the case. We will discuss the details later in Step 3. transfer and stamping part.

As shown in Fig. 2.5a, we attach the adhesive side of the tape onto the PDMS piece and rub it lightly to produce good contact between them. (Fig. 2.5b) Then, we remove the tape quickly to leave thinned flakes onto the PDMS that stay favorably on the PDMS piece due to its viscoelastic property [86]. After this step, one can start looking for monolayers and transfer them into the substrate using the optical microscope/transfer stage.

## Step 2. Finding monolayers

We use an optical microscope to find monolayers on PDMS and transfer them to desired positions on the substrate. We can distinguish mono, bi, and few layers of TMDs by the difference of transparency, brightness, and chroma under an optical microscope with a white light source. The contrast between layers of different thicknesses can

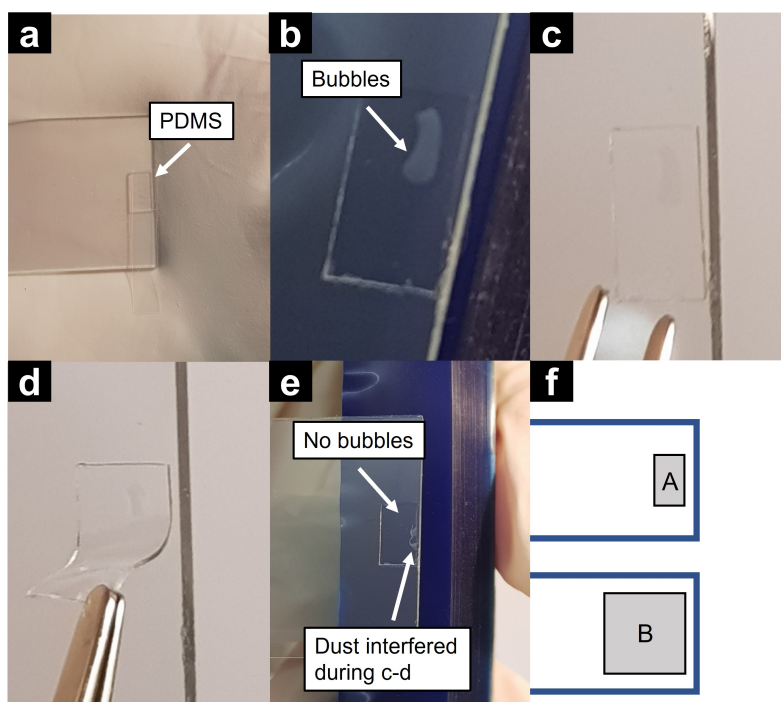


Figure 2.4: (a) A small piece of PDMS is cut and placed onto the edge of the microscope glass. (b) Sometimes bubbles and dust can be trapped between the glass and the polymer stamp. (c-d) Procedure to remove the bubbles. (e) The goal is to achieve a clean interface between the PDMS and the glass. Here, we see dust that was not there before due to the unclean condition for the demonstration. (f) two possible choices for the PDMS size. (Images were especially taken from outside of the glovebox for demonstration)

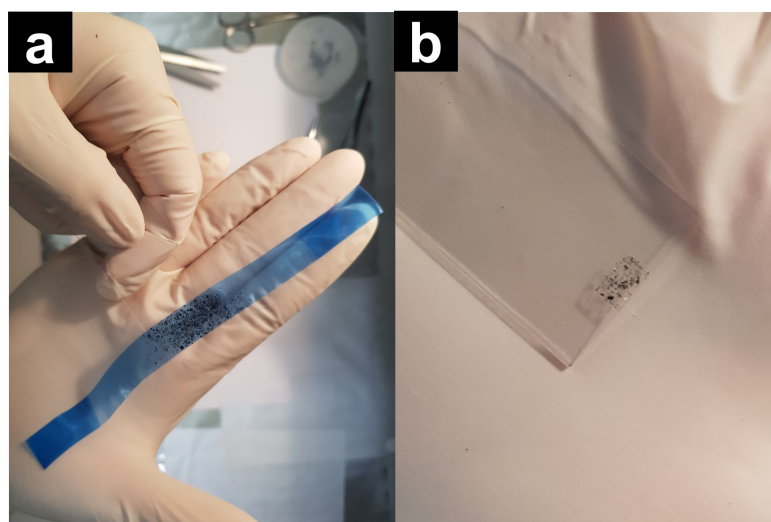


Figure 2.5: (a) The sticky side of the scotch tape is put on the PDMS piece. (b) TMD flakes stay preferentially on the PDMS piece. (Images were especially taken from outside of the glovebox for demonstration)

be enhanced if TMD layers lie on a  $\text{SiO}_2/\text{Si}$  substrate with a  $\text{SiO}_2$  thickness of 90 or 270 nm due to interference effects [104, 105]. However, we do not expect this effect when the flakes lie on PDMS. So, we use PL and Raman spectroscopy to verify that it has the desired thickness before stamping.

The stamping microscope stage consists of a standard optical microscope and transfer stages (one rotation and two xyz-translations) parts as shown in Fig. 2.6a-b. The microscope part is fixed on an optical table and isolated from

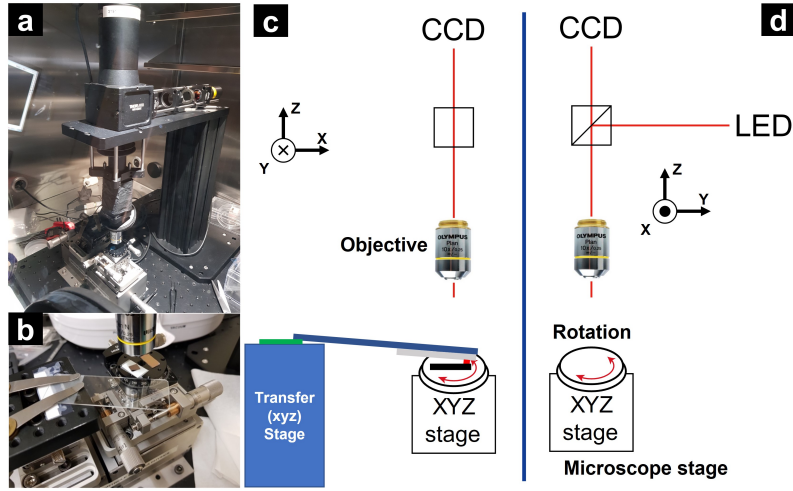


Figure 2.6: (a-b) optical images of the stamping microscope setup inside a glovebox (c-d) schematics of the setup with difference side views indicated by the Cartesian coordinates.

the transfer stage. We use either a x10 objective (Olympus, Plan N,  $NA = 0.25$ ) to stamp flakes or a x20 (Olympus, LD Epiplan,  $NA = 0.4$ ) to find monolayers by their contrast difference. The x10 is preferred for the stamping due to the large depth of field ( $\pm 3 \mu\text{m} \sim 5 \mu\text{m}$  for visible range  $400 \text{ nm} \sim 700 \text{ nm}$ ), which permits to see the substrate and flakes on the glass/PDMS at the same time when the flakes approach the substrate. It is essential to see both for stacking many layers in the same place, especially for the fabrication of contacted devices. The following equation estimates the depth of field.

$$\text{Depth of field} = \pm \frac{\lambda \sqrt{n^2 - NA^2}}{2NA^2} \quad (2.1)$$

where  $NA$ : numerical aperture,  $\lambda$ : wavelength of light and  $n$ : refractive index. The x20 objective has a small field of depth value ( $\pm 1 \mu\text{m} \sim 2 \mu\text{m}$  for visible range  $400 \text{ nm} \sim 700 \text{ nm}$ ), so it is not ideal for stamping. However, it has the advantage of providing a larger magnification, which is useful to examine small flakes carefully.

The transfer stage (xyz translation) is placed on the side of the microscope stage independently. The translation below the objective holds the substrate with a rotational and xyz-translation for effective positioning. The substrate is fixed on the stage by the blue scotch tape which is glued to the stage through double sided tapes. We mount the microscope glass on the second stage with clips, where papers underneath the glass introduce a slight inclination. This slope is essential to avoid complete contact between the substrate and the surface of the PDMS when stamping. In that case, the substrate sticks to the PDMS entirely due to the large surface contact. Therefore, it will be removed together with the PDMS from its stage when the PDMS is picked up. Thus, the slight slope of the microscope glass is needed to touch only a particular area on the substrate. Once we find the flake to transfer, for instance, a TMD

monolayer, it can be verified by the optical contrast under white light illumination or by characterization in PL, Raman, and AFM.

### Step 3. Transfer

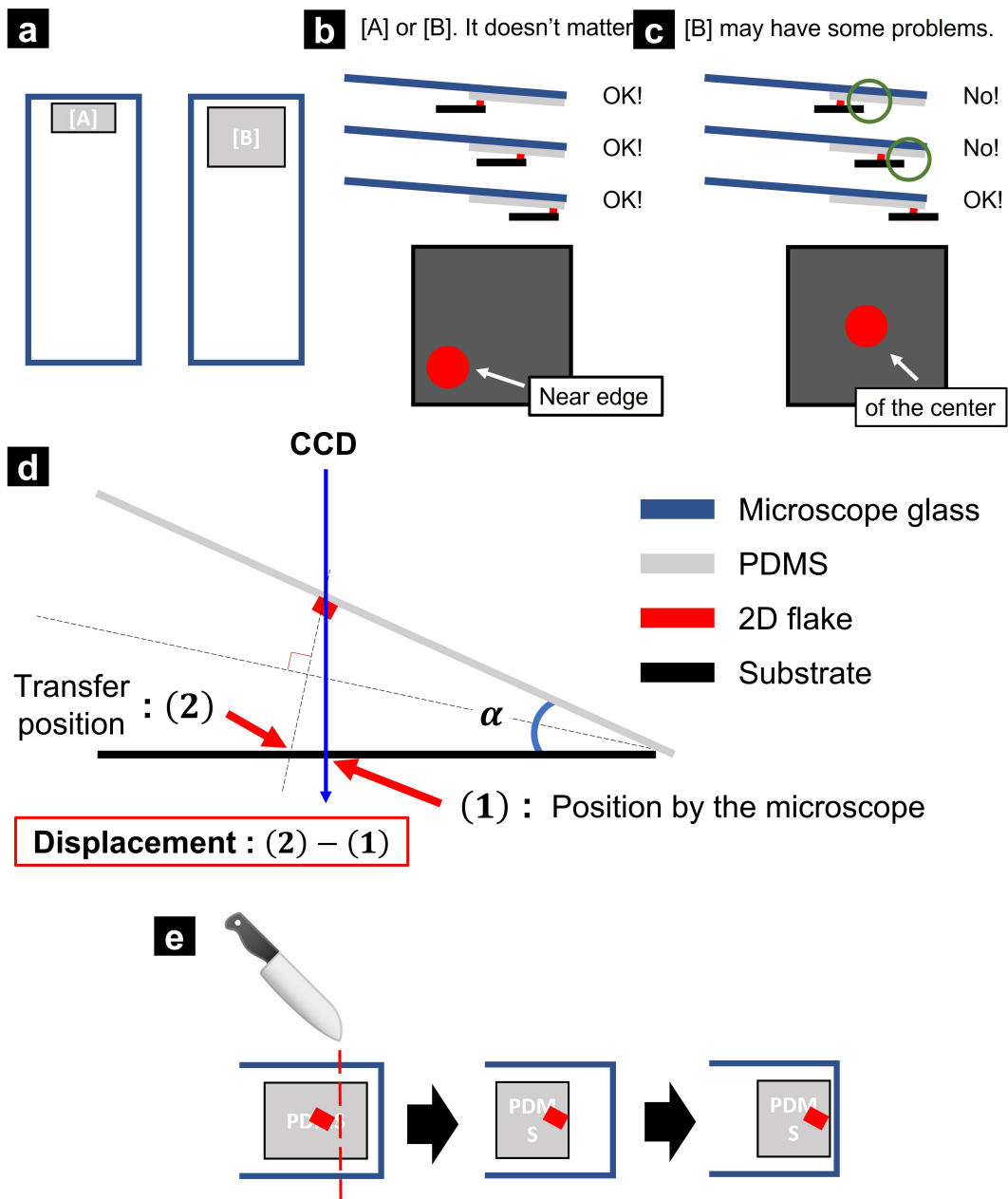


Figure 2.7: Issues of difference sizes of PDMS on microscope glass. (a) the two possible configurations for taking different size of PDMS. **[A]**: using a small size of PDMS and **[B]**: using a relatively large size of PDMS. (b) Possible situations to transfer flakes to the edge of the substrate for **[A]** and **[A]** cases. (c) Possible situations to transfer flakes to the center of the substrate. The **[B]** case may have an issue since the edge of the substrate and PDMS may touch first so that a displacement may appear from the top view as shown in schematic (d). (e) A possible solution is that the flake to transfer on PDMS can be moved by cutting the PDMS and repositioning it.

We can think of two typical cases when fabricating heterostructures, where the flakes are located either on an edge or at the center of the substrate, as represented in Fig. 2.7b-c. One must choose a suitable size of PDMS such as **[A]** (a small size) and **[B]** (a big size) accordingly. Using a considerable size of PDMS increases the chances of finding good flakes, but it has a drawback due to the size. Generally, we fabricate monolayers with hBN encapsulation on the edge of the substrate because it is easy to find the substrate's corners. Moreover, we can avoid the main problems of the exfoliation process which are due to the interaction between the PDMS and the substrate. For example, as shown in Fig. 2.7b, we are free from any conflict if one locates the flake to the edge of the substrate.

On the other hand, as shown in Fig. 2.7c one may have an issue if we wish to fabricate samples at the center of the substrate (as is the case of our patterned substrate for devices). Suppose we lower the transfer stage to touch the flake and the substrate. In that case, the outer corner of the substrate and the PDMS will touch first. The contact area will be large when the flake is located at the center of the PDMS or the inner side of the microscope glass. The PDMS may be detached from the microscope glass and stick on the substrate when we bring it upwards due to the large contact area. Plus, we created an angle of the microscope glass for the stamping. It produces more considerable displacement if we have a large distance between the flake and the first contact plane. This situation happens because we locate the position based on a projection view of the optical microscope before the transfer. The distance from the center to the edge is 5 mm in our patterned substrates. Considering we created about  $1 \sim 2$  degree slope, we end up with about  $0.7 \sim 3 \mu\text{m}$  displacement. One may re-position the PDMS with the surgery knife and tweezers, but it brings a risk of losing the flake. This side effect is critical for fabricating devices because we have a limited area to stack layers and need delicate handling of the transfer for graphite electrodes on TMD monolayers [106]. So, choosing the **[A]** kind of PDMS stamp is more suitable to fabricate heterostructures at the center of the substrate.

A stamping procedure will be introduced to fabricate a heterostructure. In this example, we fabricated an encapsulated TMD monolayer of top-hBN/WS<sub>2</sub> monolayer/bottom-hBN studied in Chapter 3.

Transferring the bottom-hBN is the first step for fabricating an encapsulated TMD monolayer. Images in Fig. 2.8 show how the PDMS is brought into contact with the substrate to transfer the bottom hBN, which is the pink flake at the center of the image. We see the lighter region in the image of Fig. 2.8a where PDMS and the substrate are in physical contact. We also see a different area on the left where the PDMS and substrate are not touching. Now, we slowly move the microscope glass up to bring the PDMS to remove it from the substrate leaving the hBN behind the substrate, as shown in Fig. 2.8b-c. The hBN will remain on the substrate due to the viscoelastic properties of the polymer.

The second step is to stack a monolayer TMD, as the monolayer WS<sub>2</sub> shown in the yellow circle of the image Fig. 2.9a, on top of the hBN. We must align both positions, the WS<sub>2</sub> monolayer/PDMS and the bottom-hBN/substrate, by changing the focal plane from the PDMS to the substrate as shown in Fig. 2.9a-b. We bring the microscope glass

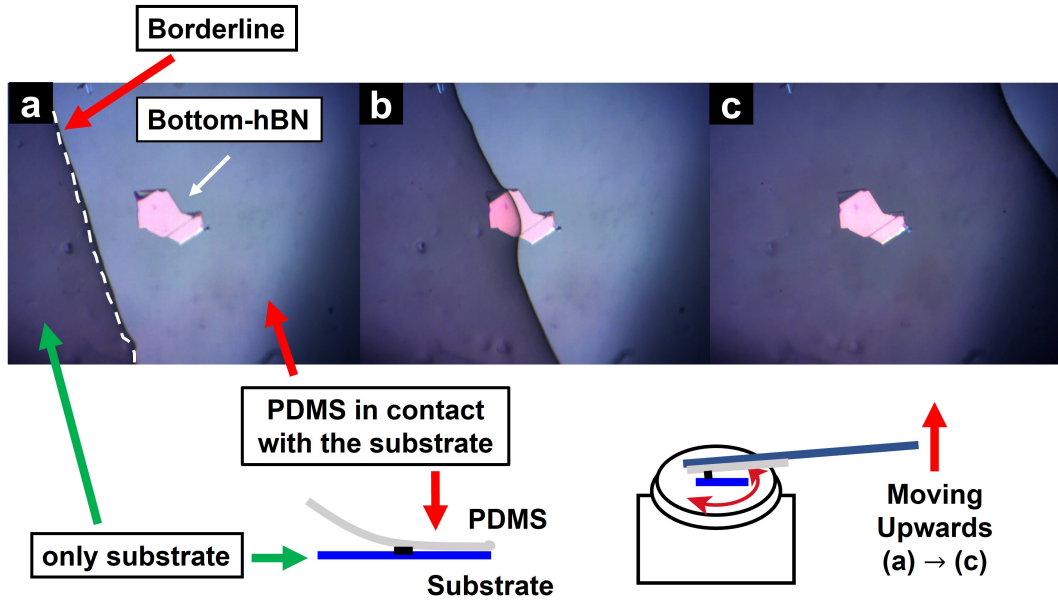


Figure 2.8: Optical microscope images of stamping process for the bottom-hBN taken with the x10 objective.

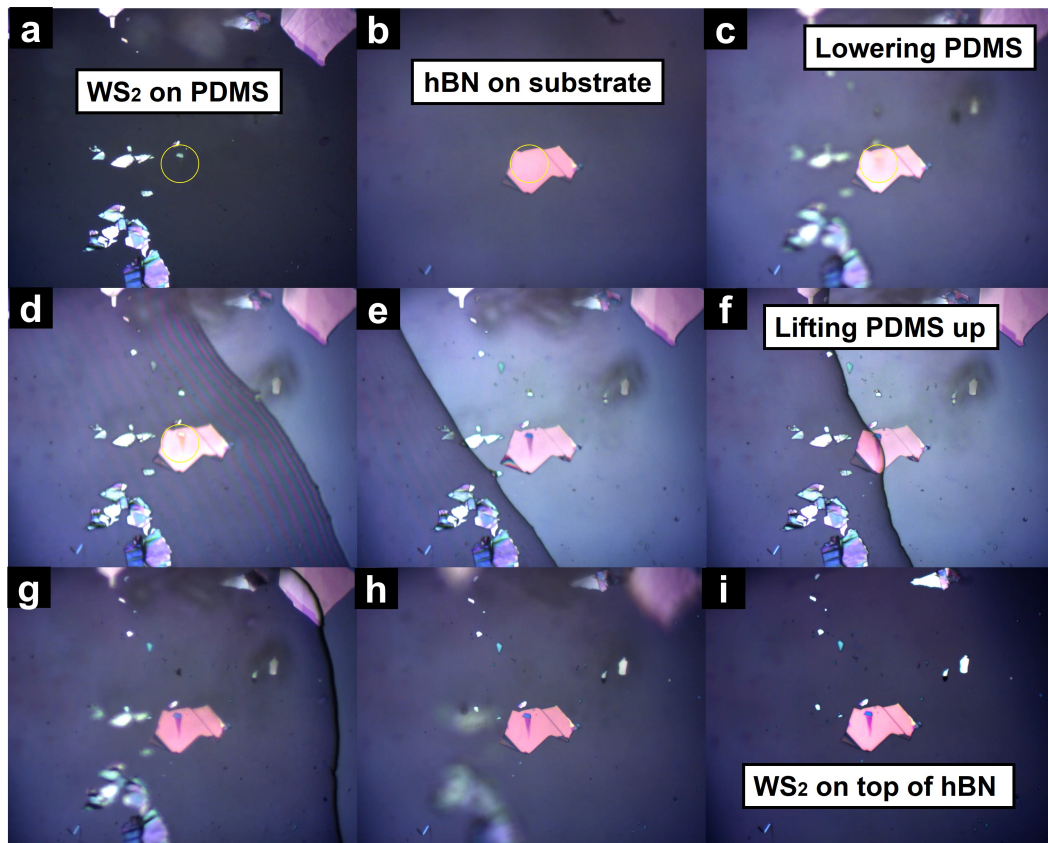


Figure 2.9: Optical microscope images of the stamping process for the TMD monolayer taken with the x10 objective.

down to stamp it, as shown in Fig. 2.9c-e. Then, we slowly move the microscope glass up once the monolayer and the hBN are in physical contact, as shown in Fig. 2.9e-i. We observe that the flakes on the polymer disappeared

except for the  $\text{WS}_2$  which stayed on the bottom hBN. The monolayer  $\text{WS}_2$  was transferred to the desired position.

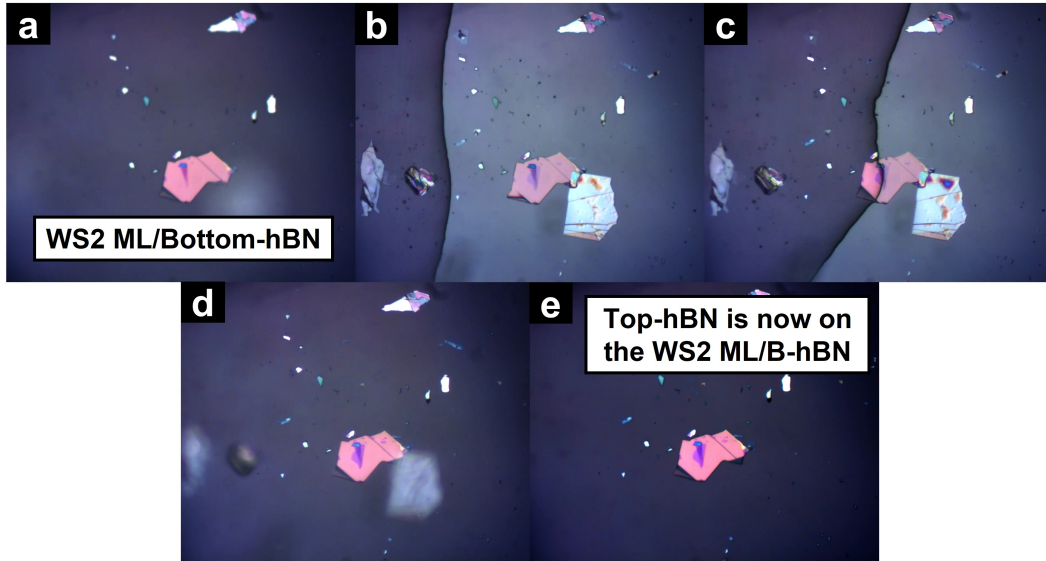


Figure 2.10: Optical microscope images of stamping process for the top-hBN taken with the x10 objective.

Fig. 2.10 shows the final step to cap the monolayer with a top-hBN. We approach the polymer after locating a thin top-hBN on the monolayer, as shown in Fig. 2.10a-b, and bring it up slowly, followed by the step in Fig. 2.10b-d. The thin hBN lies on the monolayer for the top-encapsulation layer, as shown in Fig. 2.10e.

In this way, we have fabricated the TMD heterostructures, as well as the contacted device studied in this thesis. The following subsection will introduce the characterization methods used after fabricating the encapsulated TMD monolayers.

## 2.1.2 Characterization of TMD monolayers

After the fabrication, we perform quick characterizations based on PL & Raman spectroscopy (HORIBA, LabRAM HR Evolution) at room temperature as well as AFM (tapping mode, Agilent (AFM, KPFM)/Scientec (Resiscope), PicoScan 3000). This process provides us quantitative information about the quality of the monolayer, morphology, and homogeneity. Here, the detailed information of the  $\text{WS}_2$  monolayer fabricated in the previous subsection will be used as an example.

Fig. 2.11a shows an optical image of an hBN encapsulated  $\text{WS}_2$  on a  $\text{SiO}_2$  (90 nm)/Si substrate. The black dashed lines highlight the edges of the different layers, which can be distinguished by optical contrast. The thin top hBN covers almost all the area of the  $\text{WS}_2$  except for a small part of the monolayer. A nice aspect of this sample is that one can find partially encapsulated ML (black), fully encapsulated ML (red), 2L (blue), and 3L (green)  $\text{WS}_2$  all at once. As shown in Fig. 2.11c, 2 or more layers shows a broad and nonintense indirect bandgap PL.

In contrast, monolayer  $\text{WS}_2$  shows a single intense PL at room temperature, as shown in Fig. 2.11c, due to

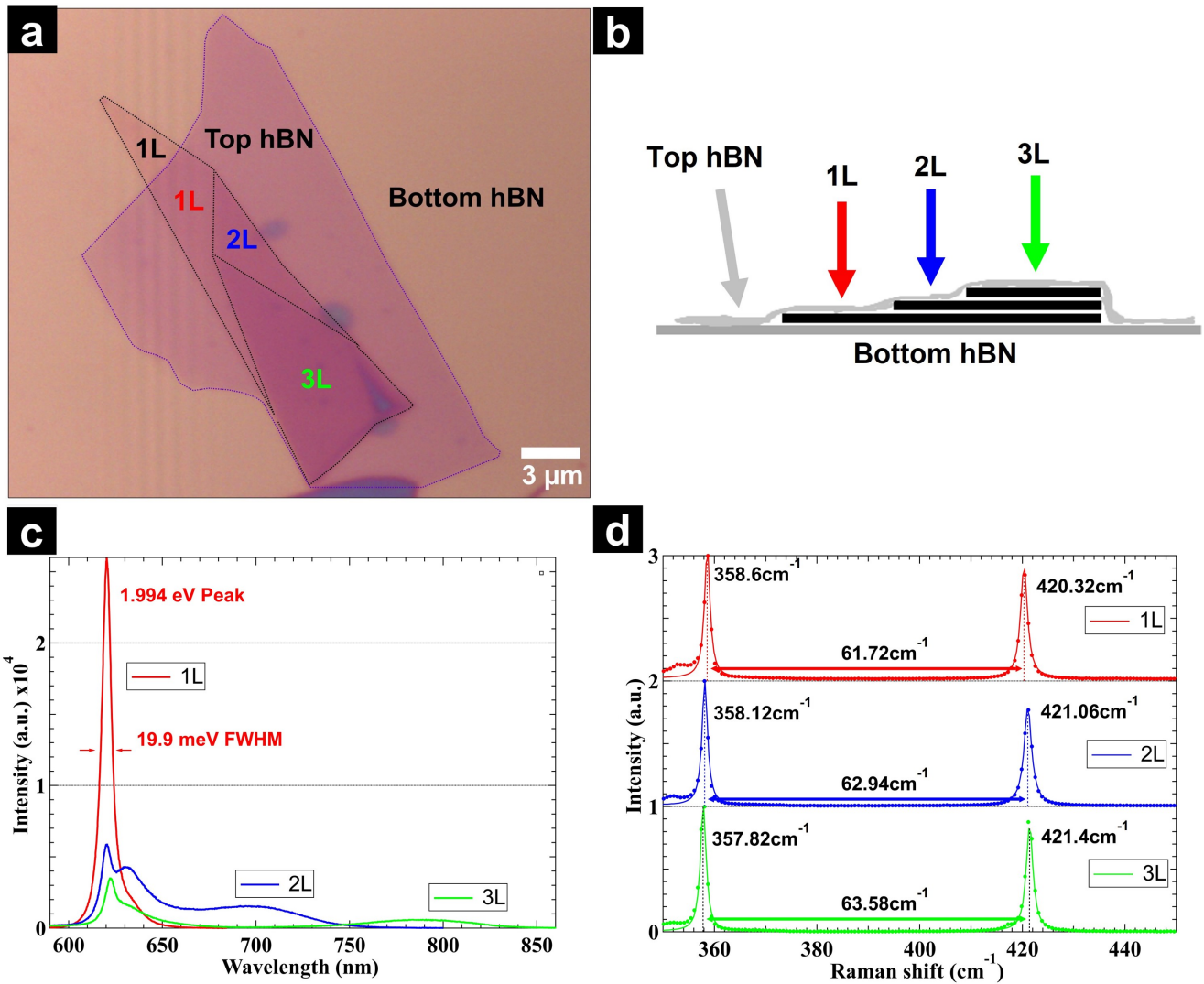


Figure 2.11: (a) An optical image and (b) a side view schematic of the encapsulated WS<sub>2</sub> monolayer. (c) PL spectra and (d) Raman shifts of different layers from 1L to 3L at room temperature. The colors of the letter on the image correspond to the colors of Raman and PL spectra.

strong excitonic emission related to a direct bandgap. This optical band gap (1.994 eV) is much smaller than the single-particle band gap due to the strong exciton binding energies of the order of hundreds of meV [107, 108, 109]. A linewidth of only 19.9 meV was observed on the encapsulated 1L part thanks to the hBN encapsulation, which suppresses dielectric disorder and reduces inhomogeneous broadening [96].

Raman shifts at different positions on the flake are shown in Fig. 2.11d. Two peaks at  $\sim 358 \text{ cm}^{-1}$  and  $\sim 420 \text{ cm}^{-1}$  correspond to the  $E_{2g}^1$  (in-plane vibration) and  $A_{1g}$  (out-of-plane vibration) modes, respectively. The spacing between the two modes increases from  $61.72 \text{ cm}^{-1}$  to  $63.58 \text{ cm}^{-1}$  when increasing the number of layers, since  $E_{2g}^1$  redshifts and  $A_{1g}$  blueshifts by the interlayer interaction [110, 111].

Mapping PL (or Raman) can also be used to check the uniformity of the sample. Fig. 2.12a-b (c-d) shows histograms of the exciton ( $X^0$ ) energy and FWHM in the black (red) lined region of the optical image (c). The WS<sub>2</sub>

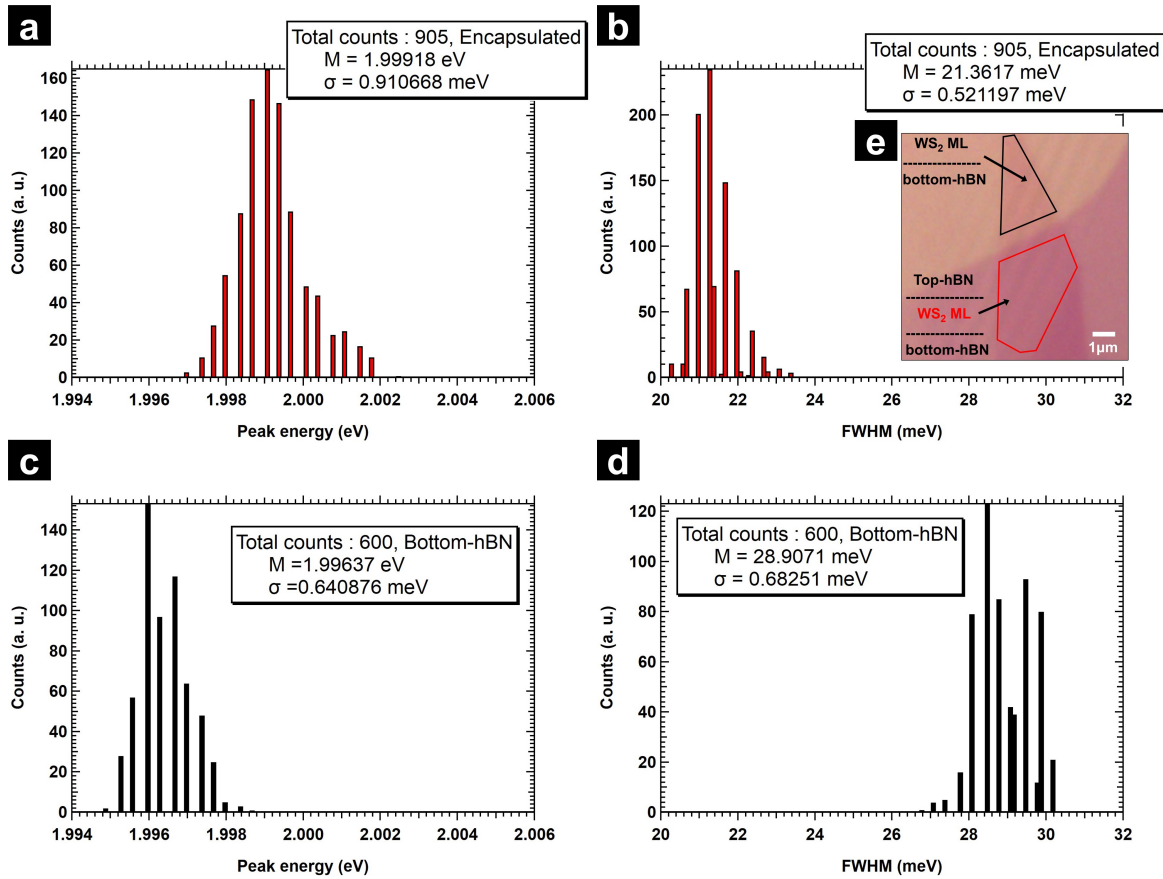


Figure 2.12: Histogram of the (a) exciton emission energy and (b) FWHM in the encapsulated (black), (c) the exciton emission energy, and (d) FWHM in half encapsulated (red) regions in the optical microscope image (e).

monolayer in the black region has only the bottom-hBN, and the red region is fully encapsulated by hBN. In the black region, disorder from dielectric interactions with the substrate is significantly suppressed by the bottom-hBN, the average FWHM is 28.9 meV with a standard deviation of  $\sigma = 0.68$  meV. This number is a significantly reduced value compared with exfoliated WS<sub>2</sub> monolayers on SiO<sub>2</sub>/Si substrate. As shown in Fig. 2.12b, the fully encapsulated WS<sub>2</sub> monolayer gives typical values of the average FWHM (21.3 meV) with a standard deviation of  $\sigma = 0.52$  meV. We obtained a reduction in linewidth of 7.5 meV (with  $\Delta\sigma = 0.16$  meV) by isolating it from the air and molecules on the surface. In contrast, the average X<sup>0</sup> emission energy increased to 1.999 eV by 2.81 meV (with  $\Delta\sigma = 0.27$  meV).

Interestingly, we observed a blueshift for the fully encapsulated WS<sub>2</sub> compared with the half encapsulated part, which is strange. Generally, the higher dielectric constant of hBN will lower the bandgap and the binding energy, both effects almost compensate each other but normally the exciton (X<sup>0</sup>) emission energy should redshift. We have no clear explanation for this blueshift but strain may play a role since tensile strain induces redshift and compressive strain induces blueshift [92]. This blueshift may be related with strain by the partially encapsulated geometry of WS<sub>2</sub>. Importantly, the hBN encapsulation ensures high-quality TMD monolayers in the optical experiment by suppressing inhomogeneity from the surrounding environment.

AFM is a direct measurement technique to identify layer thickness, as shown in Fig. 2.13a which scanned (tapping mode) the bottom left side of Fig. 2.11a. The thicknesses of the layers are distinguished from the line profile in Fig. 2.13b. The height of the 1L region is higher  $\sim 0.8$  nm than the hBN layer without WS<sub>2</sub>, and the 3L area is higher  $\sim 1.6$  nm than 1L with the borders indicated by red and orange arrows, respectively. These values are similar to reported data [112, 113, 114]. This result is consistent with PL, Raman, and optical microscope data. These AFM results also show us the high-resolution morphology compared with the optical microscope image. An-

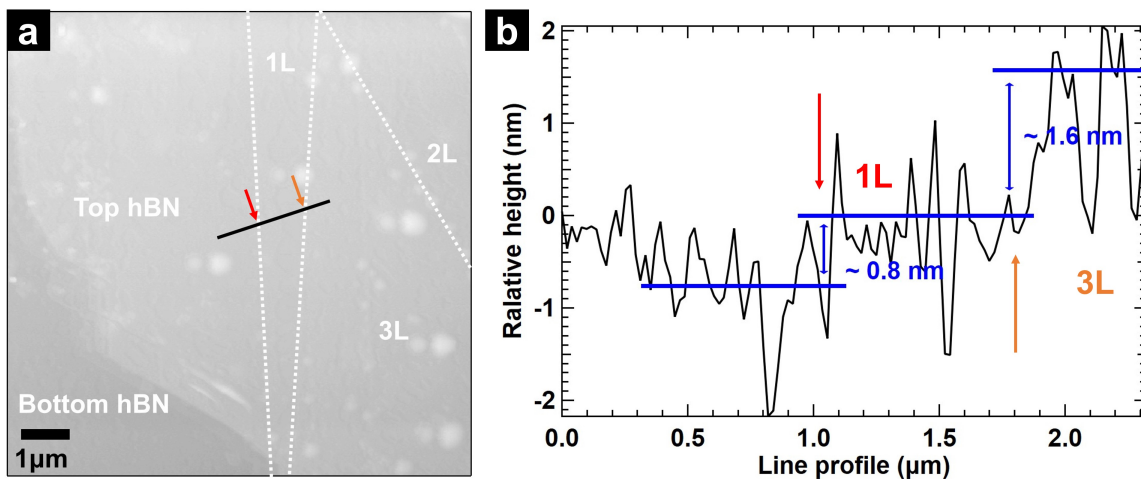


Figure 2.13: (a) an AFM image of the encapsulated WS<sub>2</sub> monolayer where is zoomed in bottom-left side of Fig. 2.11a. (b) line profile of the black line in the image (a). Transition points of layers are indicated as red and orange arrows.

other key feature of this technique is that the layers can be identified through the top hBN even after encapsulation (here, the thickness of the top hBN is about 10 nm). However, the AFM measurement may also give a non correct thickness value of TMD layers due to charging, defects and contaminants [115]. This method, therefore, cannot be a conclusive proof by itself. The characterization must combine AFM with other methods such as PL to show consistency.

We obtained detailed information on our samples before studying them with the main micro-PL experiment at cryogenic temperature. These are the first characterization steps to conduct all experiments of the thesis.

### 2.1.3 Vacuum annealing

In various fields, annealing in a vacuum is a widely used method for recrystallization, degassing, and removing hydrocarbon materials to achieve clean surfaces [116, 117, 118, 119, 120].

This annealing process in a vacuum accelerates the self-cleansing process of TMD monolayers [121, 122]. It efficiently removes residues of the surface polymer by the high vacuum and high temperature conditions. Cleaning the surface of a layer is an important step before adding a layer on the top. If residues exist between van der Waals

layers, either they are pushed away from the interface, which is ideal, or aggregate in the interface and form bubbles that cannot be easily removed once they have appeared. These bubbles change the local environment of the system. It increases inhomogeneous broadening by dielectric disorder or local doping, impacting the optical properties of TMD monolayers. Thus, we cleaned residues on the surface after each stacking to reduce the probability of the interlayer bubbles. In that way, we have successfully fabricated a heterostructure and device for the thesis.

We built an annealing chamber to remove residues of our samples induced by the exfoliation and stamping process. The annealing chamber, shown in Fig. 2.14, is equipped with a vacuum gauge (Agilent, Pirani inverted magnetron), thermocouple (TC) PT100, heater, a turbomolecular pump (Agilent, twistorr 74 fs), and primary pump (Agilent, IDP-3 dry scroll pump). We measure the temperature of the heating plate, which gives the exact temperature of the sample tested by an extra heat sensor on the substrate. We apply current and voltage to give manual feedback based on the resistance readout of the TC. The temperature/resistance table can be found in appendix A.4.

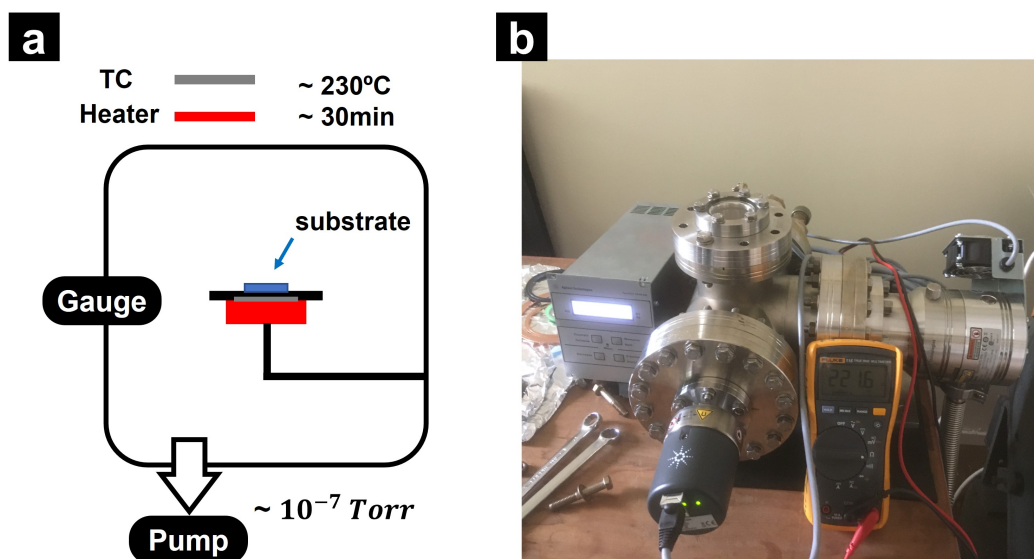


Figure 2.14: (a) A schematic of the annealing chamber and (b) the optical image

The annealing was done after stacking each layer of the sample. We pump the chamber to keep the pressure below  $10^{-7}$  Torr and increase the temperature at a rate of  $10^\circ\text{C}/\text{min}$  speed up to  $\sim 230^\circ\text{C}$ . The sample is annealed by keeping this temperature for 30 minutes and cool down naturally by turning the heater off. We set the annealing temperature  $\sim 230^\circ\text{C}$  based on several references [123, 124, 125]. This temperature value is high enough to remove the residues introduced by the transfer process and low enough to prevent monolayers damage induced by higher temperatures annealing processes.

## 2.1.4 Fabrication of contacted devices

Depositing TMDs on top of Au electrodes (or evaporating them after transfer) is the first approach to apply electrical contacts to 2D materials. However, the electrical contact between TMDs and evaporated metals is not ideal [126, 127]. It can lead to hybridization and/or ultrafast charge transfer, quenching the PL yield dramatically [128]. Thus, we have employed thin layers of graphite for the electrical contacts which partially covers the TMD monolayer to fabricate the device. Graphene and thin layers of graphite (or a few layers of graphene) have been widely used in many applications because of their excellent electrical properties [129, 130, 131].

This layered electrode offers several advantages: 1) We fabricate this contact in the glovebox and perform the mechanical exfoliation for the electrodes in the same setup. 2) We can select any device geometry by searching its proper shape. 3) Graphite provides an atomically flat contact to other layered materials (hBN, TMD monolayers). It ensures homogeneous electric conditions to the monolayers compared with Au electrodes deposited on the substrate.

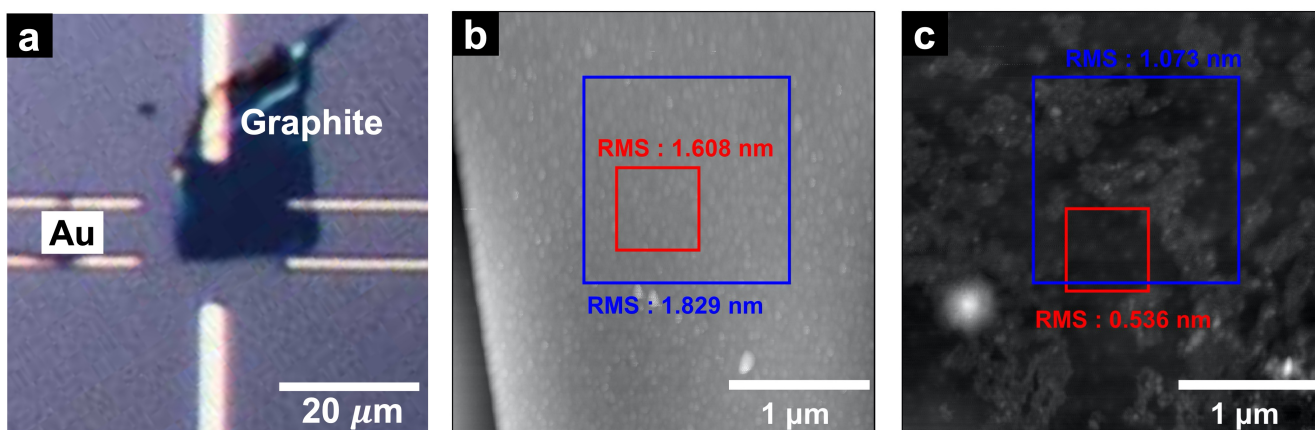


Figure 2.15: (a) An optical image of the patterned  $\text{SiO}_2/\text{Si}$  substrate. AFM images on (b) Au electrode and (c) graphite.

Fig. 2.15a shows an optical microscope image of graphite transferred by exfoliation onto the Au (100 nm)/Ti (5 nm) patterned  $\text{SiO}_2$  (90 nm)/Si substrate by lithographic techniques and physical vapor deposition (PVD). The surface roughness of a gold electrode and graphite are shown in Fig. 2.15b and c, respectively. The surface roughness ( $R_{MS}$ ) of the selected region is shown in the image with the corresponding color (red and blue). The  $R_{MS}$  of the Au electrode is = 1.608 nm for the red area and 1.829 nm for the blue square. In contrast, the  $R_{MS}$  of graphite exhibits a smaller value, which is 0.536 nm for the red and 1.073 nm for the blue area, than Au electrodes. On the graphite surface, one can find atomically flat regions, for example, the red square in Fig. 2.15c. Note that single-layer graphene is about 0.35 nm thick. We can also see some layered grains/or flakes on the surface since it was exfoliated from natural graphite, not highly oriented pyrolytic graphite (HOPG). It still allows us to obtain near atomically flat surface contact, which is not the case with Au electrodes. Note that the round residue on the left side of the red square of

(c) can be removed after annealing once we stack another 2D layer on the top [121, 122].

We selected the bottom gate structure for our device, as shown in Fig. 2.15a. For the bottom gate, the thickness of the bottom hBN is enough to avoid significant leakage currents. However, it needs a higher voltage for the electric field than the top gate configuration due to the hBN thickness. This bottom gate geometry is also suitable for the optical experiment because we do not add any layer on the top, which may induce optical losses. Compared with the bottom gate, the top gate structure may lose optical efficiency by adding one absorbing layer on the top. This effect can be minimized by taking a thin top layer of graphite, but still the top hBN should be thin. This has limitations related to leakage currents.

In that way, we have fabricated a charge tunable device for the optical pumping experiment by changing the doping state of the TMD monolayer by an electrical method (see the MoS<sub>2</sub> device in Chapter 5)

## 2.2 Polarization-resolved $\mu$ -photoluminescence spectroscopy

Polarization-resolved micro-photoluminescence ( $\mu$ -PL) spectroscopy is our main experimental technique used to explore exciton/valley physics in 2D S-TMDs at cryogenic temperature. As we discussed previously in the sample fabrication and pre-characterization section, PL spectra of TMD monolayers always show exciton dominant emissions and other excitonic complexes do not appear or cannot be easily observed at 300 K. For example, a room temperature PL spectrum of hBN encapsulated WS<sub>2</sub> monolayer shows the intense exciton emission at 1.994 eV while a small peak can be found at around  $\sim$  1.96 eV which is the trion emission. This trion state, which has an energy about 30 meV below the exciton, is almost unstable at room temperature due to the thermal fluctuation ( $T = 300 \text{ K} \sim 25 \text{ meV}$ ). In WS<sub>2</sub> monolayers, other excitonic states can be found at energies of tens of meV below the exciton energy such as bi-exciton, charged bi-exciton, dark exciton, and two separated trions. These states are non-detectable at room temperature. However, these excitonic complexes become visible at cryogenic temperature and we can also significantly narrow the linewidth of excitonic emissions thanks to the hBN encapsulation.

Therefore, we can study spin/valley dynamics of 2D S-TMDs by the optical pumping method with well-resolved spectra by the combination of low temperature conditions and hBN encapsulation. We will discuss first about our polarization-resolved  $\mu$ -PL setup such as polarization-resolved optics, laser sources, spectrometer, and cryostat. Then, we will go through the alignment procedures and the analyzing methods of polarization-resolved spectroscopy. Finally, the PL imaging technique which is another key feature of our setup will be introduced.

### 2.2.1 Setup

A schematic of our microscope setup is shown in Fig. 2.16. Two tunable lasers are installed in the bottom optical table. They cover all the TMD monolayers' optical bandgaps from the visible (Dye) to the near-infrared (Ti: sapphire)

range, including MoTe<sub>2</sub> monolayer ( ~ 1.1 eV). A Ti: sapphire laser and a InGaAs CCD are required for this case. The photon beams are transferred to the other optical table where the cryostat is installed, one finds the main op-

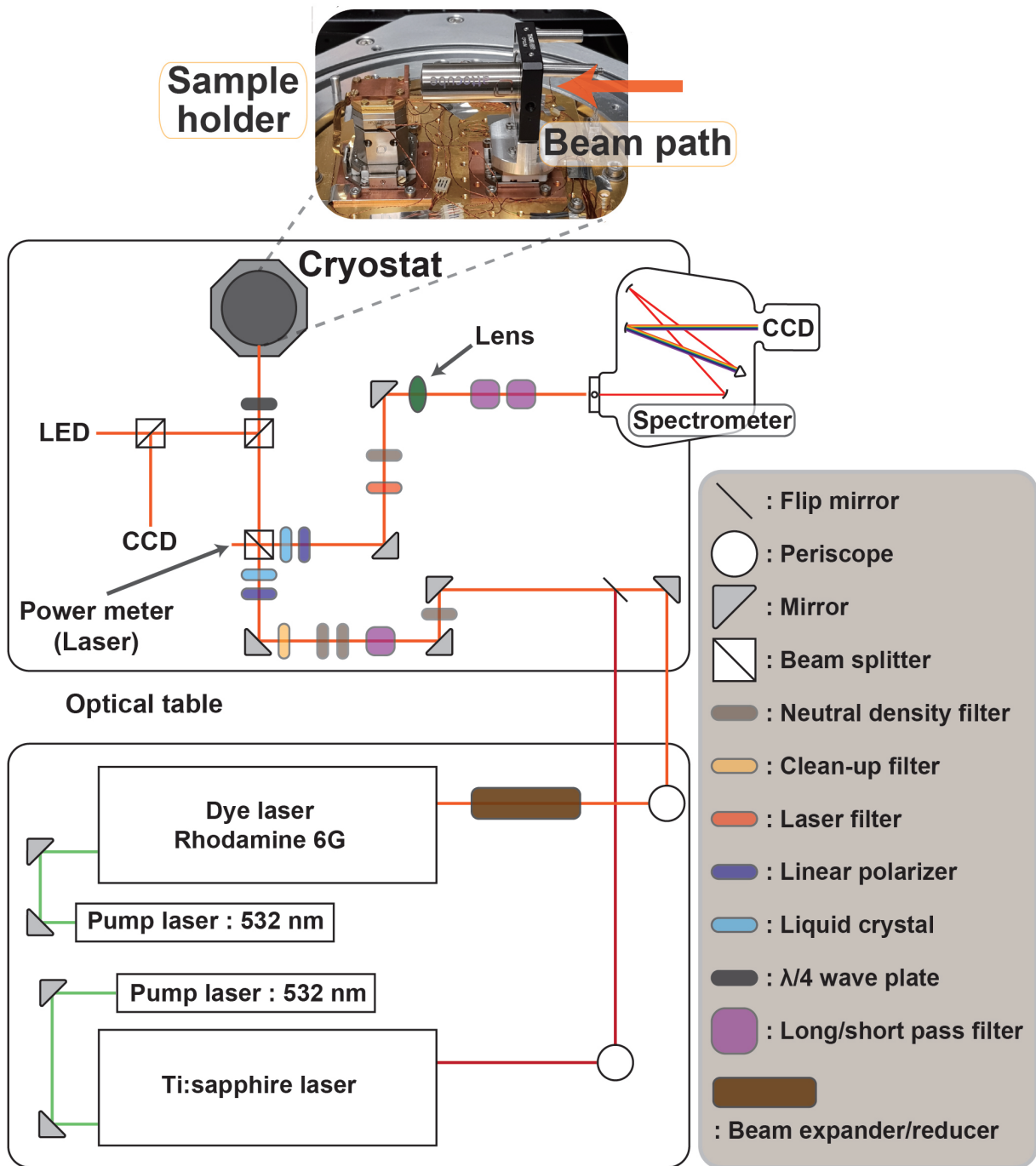


Figure 2.16: A schematic of the polarization resolved micro-PL setup.

tical components to resolve polarization of PL, a spectrometer equipped with a CCD, a closed-cycle cryostat. The samples and the objective are mounted on piezo positioners for scanning samples and focusing beams in the cryostat. The objective and the piezo positioners are vacuum and cryogenic compatible. A second optical microscope is installed on the left of the optical table for the imaging of the sample's surface. Note that we mount the samples

vertically and the objective horizontally. As such, all the beams remain on the same horizontal plane 212 mm above the optical table.

We have particular features on the setup: 1) We can quickly switch from from one laser to the other thanks to a flip mirror, where the laser first arrives on the upper optical table. 2) The power meter on the left side of the 50:50 beam splitter detects the excitation laser power in real time. 3) The beam splitter for the extra optical microscope can be dismantled to avoid optical losses and interferences during the PL experiment. 4) The closed-cycle He cryostat offers a stable environment mechanically decoupled from the vibration coming from the compressor and the pumps. 5) A heater for the sample is installed inside the cryostat for temperature-dependent experiments. 6) The objective (vacuum and cryogenic compatible) is mounted inside the cryostat. This choice allowed us to avoid optical aberrations that occur when a window is placed between the sample and the objective. 7) Linear polarizers and liquid crystals retarders are mounted to control and resolve the polarization of the laser and the PL, respectively. We can switch from a circular to a linear basis for the polarization analysis by controlling the orientation of the  $\lambda/4$  wave plate placed just before the objective. 8) The  $\lambda/4$  wave plate is positioned in front of the cryostat to always keep the light linearly polarized in the microscope optics, regardless of the polarization basis (circular or linear) chosen. 9) The light is always vertically polarized until the liquid crystal of the laser part and after the linear polarizer of the spectrometer part. It prevents issues from the different reflectance of mirrors with vertically/horizontally polarized light.

## Laser sources

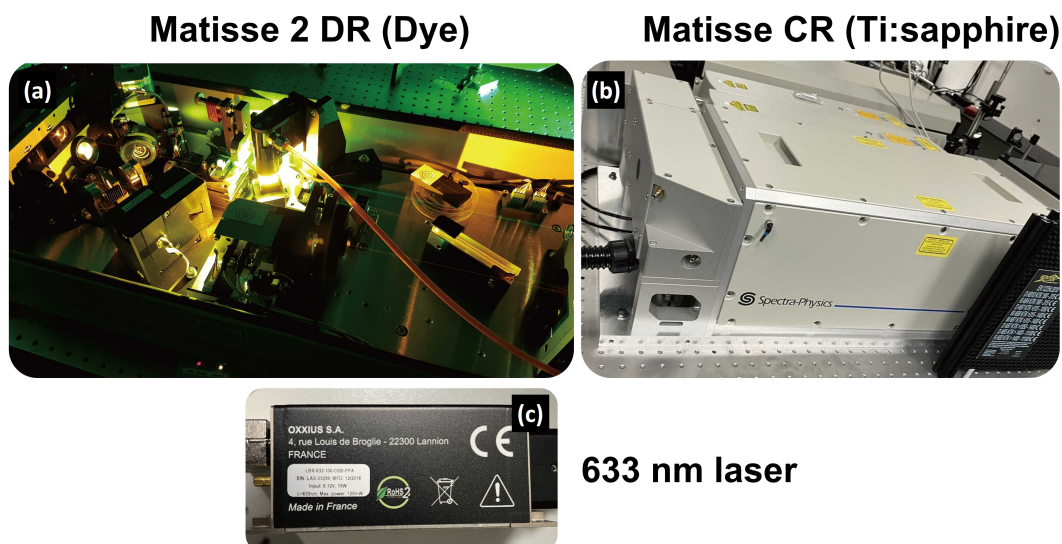


Figure 2.17: Optical images of (a) Rhodamine 6G Dye laser (Spectra-physics & Sirah) (b) Ti:Sapphire laser (Spectra-physics & Sirah) (c) 633 nm semiconductor laser (Oxxius).

As shown in Fig. 2.17, three laser sources were used for our low temperature experiments: 1) Ti:Sapphire

tunable laser (Matisse CR, Spectra-physics & Sirah) was used for MoSe<sub>2</sub> in Chapter 4. 2) Dye (Rhodamine 6G) tunable laser (Matisse 2 DR, Spectra-physics & Sirah) was used for the experiments for WS<sub>2</sub> and MoS<sub>2</sub> Chapter 3 and 5, respectively. 3) 633 nm semiconductor laser (Max power = 120 mW, Oxxius France) was used for MoSe<sub>2</sub> and MoS<sub>2</sub> experiments in Chapter 4 and 5, respectively.

Table. 2.1 shows the specifications of two tunable laser sources which were activated from 532 nm pump laser source ( $P_{MAX} = 20$  W, Millennia Pump Laser, Spectra-physics & Sirah). The pump laser and output lasers from the cavity are horizontally polarized.

Model	Matisse 2 DR	Matisse CR
Company	Spectra-physics & Sirah	
Gain Medium	Rhodamine 6G (Dye)	Ti:Sa
Wavelength range	550 - 660 nm	662 - 1050 nm
Mode	Continuous wave (CW)	
Linewidth	<20 MHz rms	<1 MHz rms (100 msec)
Beam Diameter	1.4 mm (typical)	0.8-1.0 mm (typical)
Beam Divergence	<1 mrad	<1.2 mrad
Amplitude Noise	<0.5% rms	<0.1% rms
Scan Range	>60 GHz (at 575 nm)	>50 GHz (at 780 nm)

Table 2.1: Specifics of two tunable lasers from spectra-physics ([www.spectra-physics.com](http://www.spectra-physics.com)) and sirah ([www.sirah.com](http://www.sirah.com)) websites.

## CCD & Spectrometer

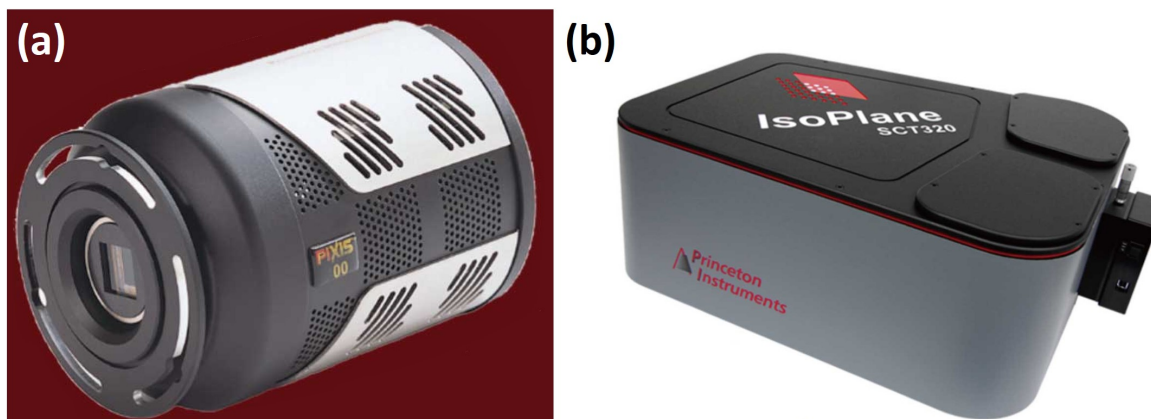


Figure 2.18: Optical images of (a) PIXIS: 400 BR eXcelon and (b) IsoPlane SCT320. (<https://www.princetoninstruments.com/>)

PIXIS: 400 BR eXcelon (Princeton Instruments) CCD and IsoPlane 320 (Princeton Instruments) spectrometer were used for polarization-resolved  $\mu$ -PL experiments. The main characteristics of the CCD is that it has a  $1340 \times 400$  imaging array with  $20 \times 20 \mu\text{m}$  pixels. It is also compatible for visible wavelengths (400 nm  $\sim$  900 nm). The spectrometer has three gratings which are 300 g/mm (blaze wavelength: 750nm), 600 g/mm (blaze wavelength: 750nm), and 1800 g/mm (holographic: Visible). The details of the CCD and spectrometer can be found in the

<https://www.princetoninstruments.com> website.

## Cryostat

We recently installed a closed-cycle He cryostat on the polarization-resolved micro-PL setup from [Absolute systems], as shown in Fig. 2.19. A compressor on the rooftop (left of the image) supplies a cold helium flow to the central rotary tank (right in the image). It circulates the flow to sustain  $T = 20$  K for the cold plate of the sample in the chamber. Also, we installed the heater for the sample inside the chamber to have the temperature variation from 20 K to 300 K.



Figure 2.19: Optical images of (left) the helium compressor and (right) the cryostat.

To operate the cryostat, we first pump the chamber with the primary/turbo pump (Agilent, IDP-3 dry scroll pump / twistorr 84 fs) up to the middle  $10^{-4}$  Torr range. Then, we launch the compressor to cool the chamber down to the cryogenic temperature. Finally, we get 20 K for the cold plate and the sample under  $10^{-7}$  Torr after  $\sim 12$  hours. The cold plate in the chamber also acts as a cold trap to keep the high vacuum. The turbo pump operation do not modify the quality of the PL experiment. A long term experiment can be performed over 30 days in stable cryogenic conditions of 20 K and  $10^{-7}$  Torr.

## Piezo stage & Optical components

Fig. 2.20 shows the inside of the vacuum chamber where the samples and objective are located. The vacuum & cryogenic compatible objective (LT-APO/VIS/0.82, Attocube, Numerical Aperture NA = 0.82) is mounted in the vacuum chamber. This configuration is important to avoid the optical aberrations by placing the objective in the cryostat so that there is no window between the objective and the sample. There are three piezo translations (vacuum & cryogenic compatible) to move the sample and change the focal plane. On the sample mount part, ANPz102 (Attocube) vertical piezo translation and ANPx311 lateral piezo translation are mounted to scan the sample surface.

On the objective part, ANPx311 piezo translation is mounted to focus and collect light. These three piezo stages are connected to the piezo motion & readout controller (ANC 350, Attocube) through the wires on the cold plate. The list of optical components can be found in appendix A.3.

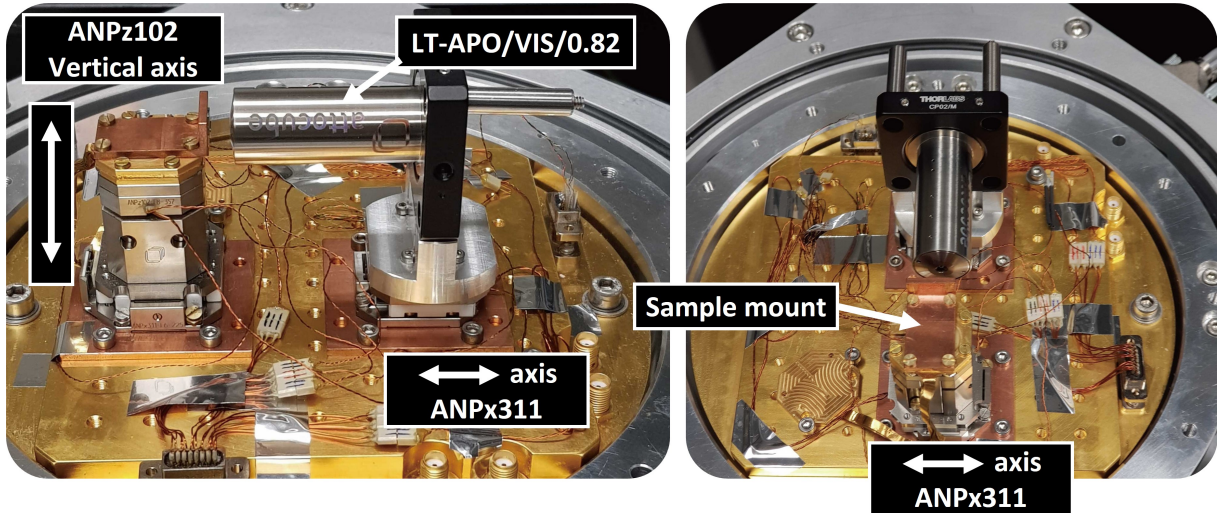


Figure 2.20: Optical images of the inside of the vacuum chamber. The sample holder with xy piezo translations and the objective with z piezo translation are mounted on the cold plate. The objective and piezo translations are vacuum & low temperature compatible bought from Attocube.

## 2.2.2 Alignment

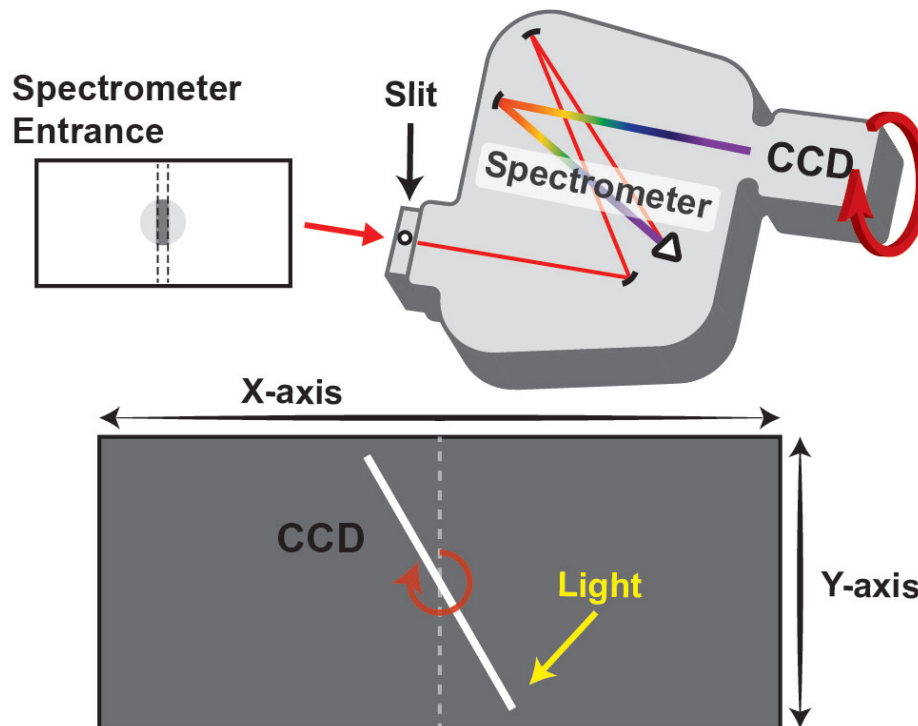
We can mention four main steps to align the setup: 1) We align the CCD and the spectrometer to resolve PL correctly. We do not repeat this procedure once it is done unless we replace the Si-CCD with the InGaAs-CCD or vice versa. 2) Then, we align the general optics with a laser source for the micro-PL spectroscopy. 3) The alignment for the polarization-resolved setup can be done afterwards because we operate this by additional polarizing components on the micro-PL setup. 4) Finally, we fine-tune the optics with a mounted sample in the cryostat.

### Tunable lasers

We followed the alignment procedure of the two cavity lasers (Dye, Ti:sapphire) based on the manual from the website: Spectra-physics/Sirah (<https://www.spectra-physics.com>, **Matisse User's Guide**).

### CCD & Spectrometer

Aligning CCD and spectrometer is an essential part of the experiment. Here, we have two small steps for the alignment: 1) We align the short axis of the CCD vertically to the optical table, so that the long axis of the CCD is parallel to the entrance slit of the spectrometer. 2) We calibrate the wavelength with a known source.



- One pixel line (of detected light) appears due to the slit.
- It may have an angle, If the CCD is not aligned.
- We rotate the CCD to make the line vertical.

Figure 2.21: A schematic for aligning CCD and spectrometer

First, we must be aware of the geometry of the spectrometer to set the CCD orientation correctly. The long axis of the CCD must be orthogonal to the orientation of the slit of the spectrometer which is the x-axis of the spectrometer to resolve wavelength, as shown in Fig. 2.21. We send light to the spectrometer entrance with the narrowest slit width to see the only one pixel width line on the CCD. It must show the vertical line of the light along the y-axis as the orientation of the spectrometer entrance. Usually, we see a tilted line of the detected light on the CCD before orienting it. So, we rotate the CCD for the proper orientation for the y-axis.

Second, we calibrate wavelength for all three gratings with a mercury spectral lamp. Identifying peaks is done by the reference of the software (LightField by Princeton Instruments).

### General optics

We used 30 mm cage system of Thorlabs.

### Polarization (linear & circular)

We operate the micro-PL setup on a linear basis for the light except for the objective-sample part after the  $\lambda/4$  wave plate. It can work on a linear or circular basis for excitation and detection. For example, by using circular light, one

can obtain two different components  $\sigma^{++}$ ,  $\sigma^{+-}$  of PL from the setup.  $\sigma^{+\pm}$  refers to  $\sigma^{\pm}$  polarized PL under the  $\sigma^{+}$  excitation. The combination  $\sigma^{++}$ , for instance, allows detecting the  $\sigma^{+}$  component of PL under  $\sigma^{+}$  laser excitation. Polarization of light (excitation laser and PL) is controlled by a  $\lambda/4$  wave plate and two liquid crystals combined with two linear polarizers. The first liquid crystal on the laser part transforms the polarization of the excitation laser light between two linearly polarized states, vertical or horizontal, by applying a voltage on the liquid crystal. To obtain  $\sigma^{\pm}$  excitation, the linearly polarized laser light is then converted to circularly polarized one passing through the  $\lambda/4$  wave plate placed just before the microscope objective. The two circularly polarized components of PL,  $\sigma^{\pm}$ , are transformed to two orthogonal linearly polarized states by the  $\lambda/4$  wave plate and only one component is selected at a time by the second liquid crystal and the polarizer before entering the spectrometer. In other words, the second polarizer is fixed vertically and the second liquid crystal determines the polarization of the light by adjusting the retardation. The vertically polarized light will pass if no retardation is applied, whereas only the horizontal part will pass if the latter is transformed into vertical by a retardation of the liquid crystal retarder. In this way, the four different combinations of the two liquid crystals and polarizers allow us to acquire selectively polarized excitation and PL.

Thus, we align on a linear basis and add  $\lambda/4$  wave plate for a circular basis later for the experiment. One can separate the alignment procedure for two polarization parts of 1) laser 2) PL. We start from the polarization alignment of the laser part.

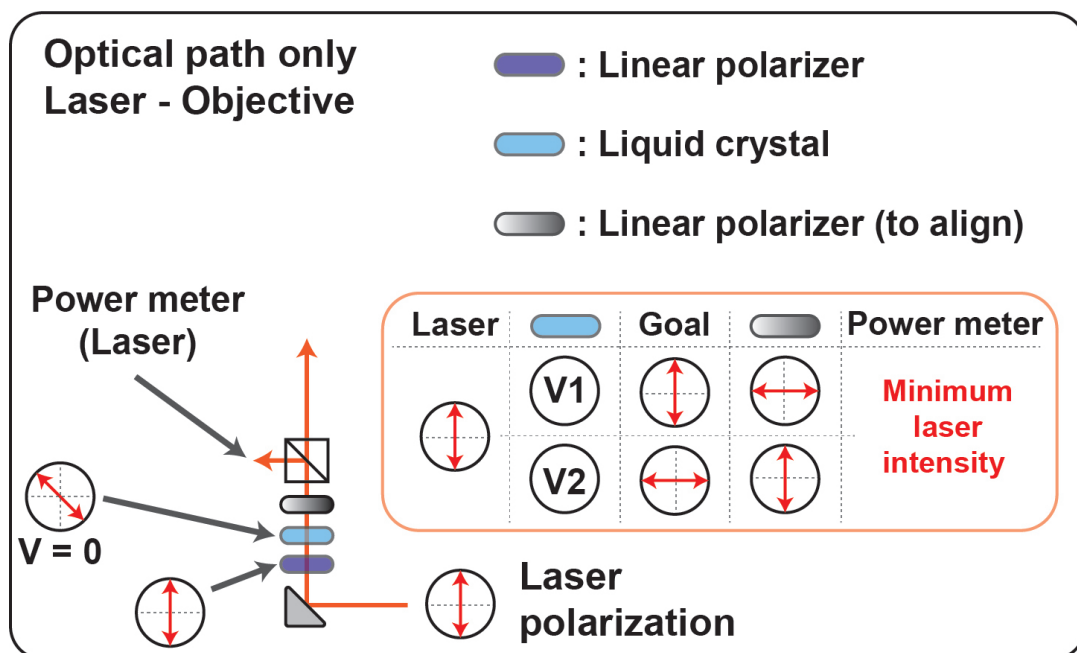


Figure 2.22: A schematic for an alignment of the laser polarization.

Vertically polarized lasers arrive on the optical table, where all the optics are. We focus on the polarizing elements to control the laser polarization, as shown in Fig. 2.22. The laser first undergoes a linear polarizer, aligned vertically. Then, the beam passes a liquid crystal, to convert it horizontally polarized/ or keep it vertically polarized. We place

the neutral axis of the liquid crystal 45 degrees from the vertical axis. We apply two voltage states, V1/V2, to make the beam vertically/horizontally polarized by changing the retardation rate of the liquid crystal from the beam axis. Thus, we add an extra linear polarizer with a cross-polarization to kill the beam (goal of our polarization) after the liquid crystal. Then, we calibrate the voltage of V1/V2 to measure a minimum laser intensity on the power meter, as shown in Fig. 2.22. We remove the extra linear polarizer to generate a vertical/horizontal polarization for V1/V2 on a linear basis.

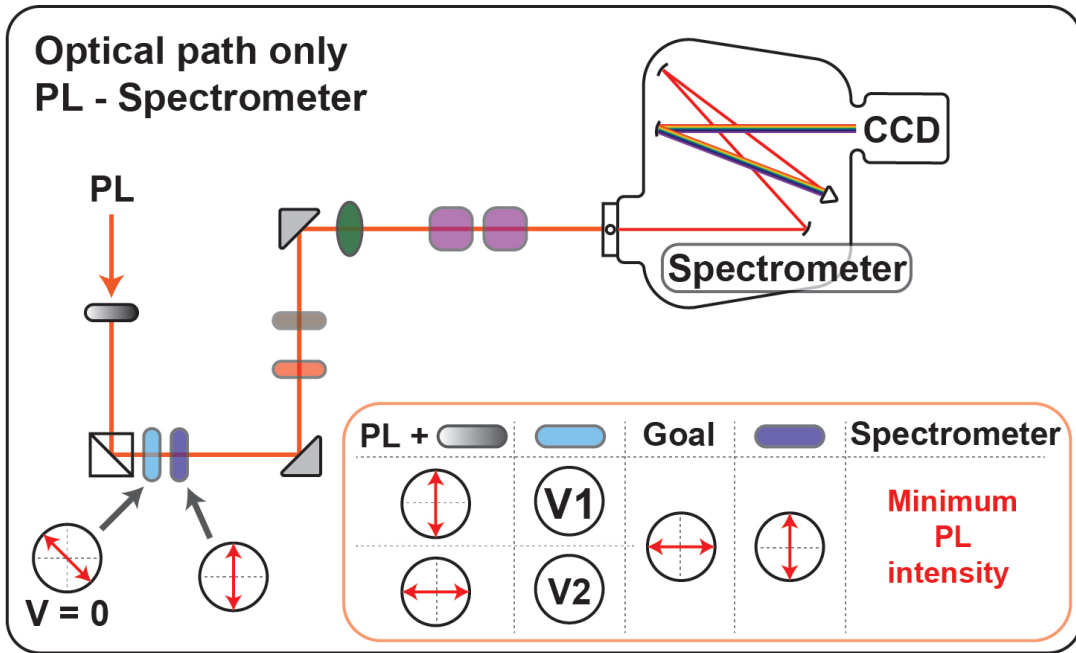


Figure 2.23: A schematic for an alignment of the PL polarization.

We place the extra linear polarizer on the PL path to generate linearly polarized light. Note that we use vertical/horizontal polarization of the laser to obtain vertical/horizontal polarization of PL since the extra polarizer is on the crossing path of the laser and PL. V1/V2 analyzes horizontal/vertical polarization, and the other polarization is killed by combining the linear polarizer and liquid crystal. So, we again use the strategy to find a minimum PL intensity by the crossing polarization. The extra polarizer produces a vertical/horizontal PL for V1/V2. We set the voltage of V1/V2 to get a minimum PL intensity on the spectrometer.

### 2.2.3 Polarization resolved spectroscopy

The polarization-resolved setup is a key component for our optical experiment since chiral optical selection rules are valid in TMD monolayers [132]. Here, we assume symmetrical optics for the polarization dependent experiment in which the beam splitter has an equal reflectance for the vertical/horizontal linear polarization  $\pi^{Y/X}$  resulting  $\pi^Y = \pi^X$  under  $\pi^{Y/X}$  excitation also the equal reflectance for circular polarization  $\sigma$ , and TMD monolayers are a symmetric system in optical valley selection rules. Thus, we consider only  $\sigma^+(\pi^Y)$  laser excitations to simplify in the

following polarization dependent analysis.

Note that, generally, using four combinations ( $\sigma^{++}, \sigma^{+-}, \sigma^{--}, \sigma^{-+}$ ) has the advantage of suppressing any spurious effect due to the optics' eventual birefringence or polarization-dependent properties. However, since we work on a linear polarization basis at all parts (except between the  $\lambda/4$  and the sample), these effects were found to be negligible. As shown in Fig. 2.24, the two polarization plots calculated from 2 components (blue line) and 4 components (blue dashed line) superpose without a significant difference through the full energy range for PL of  $\text{WS}_2$  monolayer.

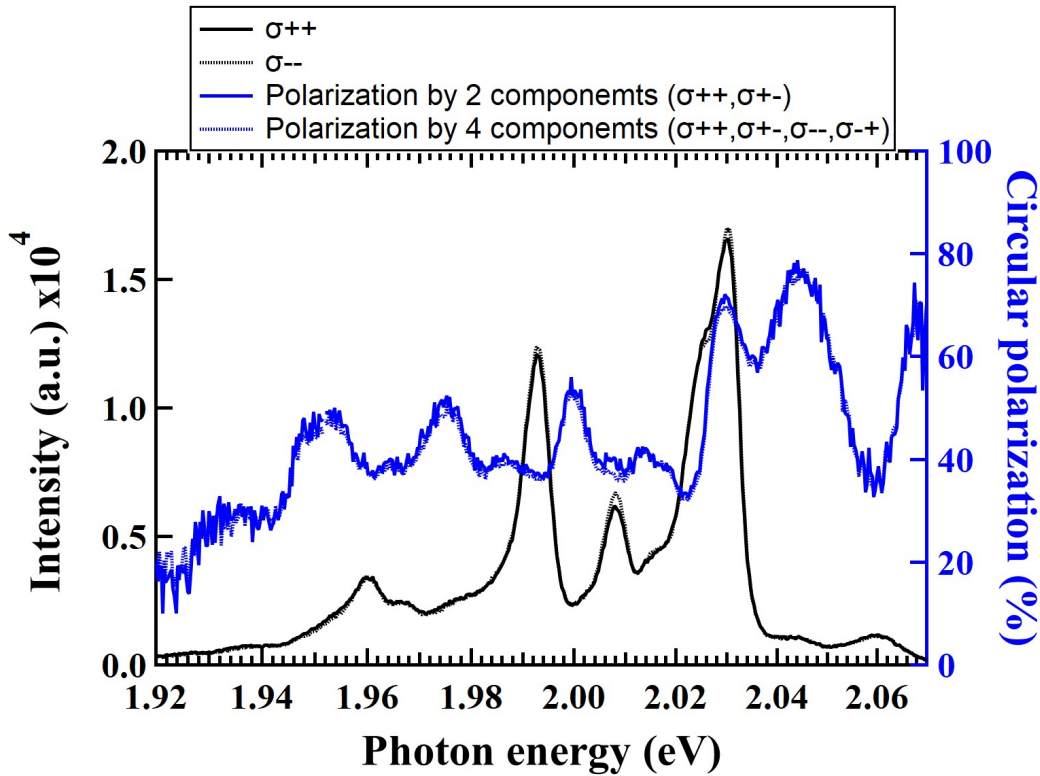


Figure 2.24: PL spectra and circular polarization of  $\text{WS}_2$  monolayer at 20 K.  $\sigma^{++}$  (or  $\sigma^{--}$ ) corresponds to co-circular component of  $\sigma^+$  laser excitation &  $\sigma^+$  PL detection (or  $\sigma^-$  laser excitation &  $\sigma^-$  PL detection). The blue line exhibits circular polarization taken out from 2 components on  $\sigma^-$  excitation basis. The dashed blue lines correspond to circular polarization by 4 components to take into account spurious effects of the optics.

### Circular basis

We measure, under the circular basis  $\sigma$ , a sum  $I_+^\sigma$  and a difference  $I_-^\sigma$  PL intensities and those two PL intensities are obtained by combining two polarization measurements given by the following equations,

$$I_+^\sigma = \sigma^{++} + \sigma^{+-} \quad (2.2)$$

$$I_-^\sigma = \sigma^{++} - \sigma^{+-} \quad (2.3)$$

where the circular polarization is defined as  $I_-^\sigma/I_+^\sigma$ . This ratio gives us a measurement of the spin/valley polarization in TMD monolayers due to the optical selection rules.

### Linear basis

The analysis can be done under the linear basis,  $\pi$ , by removing the quarter wave plate. We define a sum  $I_+^\pi$  and a difference  $I_-^\pi$  as,

$$I_+^\pi = \pi^{YY} + \pi^{YX} \quad (2.4)$$

$$I_-^\pi = \pi^{YY} - \pi^{YX} \quad (2.5)$$

where the linear polarization is defined as  $I_-^\pi/I_+^\pi$ .

### $\sigma/\pi$ ratio

We define R as the PL intensity ratio obtained after  $\sigma$  and  $\pi$  excitations under the same excitation power represented in the following equation.

$$R = \frac{I_+^\sigma}{I_+^\pi} \quad (2.6)$$

Generally, systems show the same value in total PL intensity regardless of the laser polarization, which means no polarization asymmetry in the absorption-recombination process. However, exceptions exist such as spin-dependent recombination in GaAsN [133]. Thus, If one discovers a difference in PL intensity, It may give us an insight into a recombination/formation process depending on light polarization in our experiments in TMDs (see chapter 3).

## 2.2.4 Imaging

Imaging PL, another essential feature of our experimental setup, guarantees hyperspectral imaging with a submicron spatial resolution. It allows us to study phenomena arising due to the spatial gradients. This technique has two configurations. A two-dimensional spatial imaging, so-called 0th order, requires the CCD and filters. A spectrum-space resolved imaging, so-called first order, is operated by the combination of CCD and spectrometer. Also, we can resolve the polarization by applying the method discussed in 2.2.3. Particularly, these imaging methods were applied for the study of MoSe2 monolayer in chapter 4.

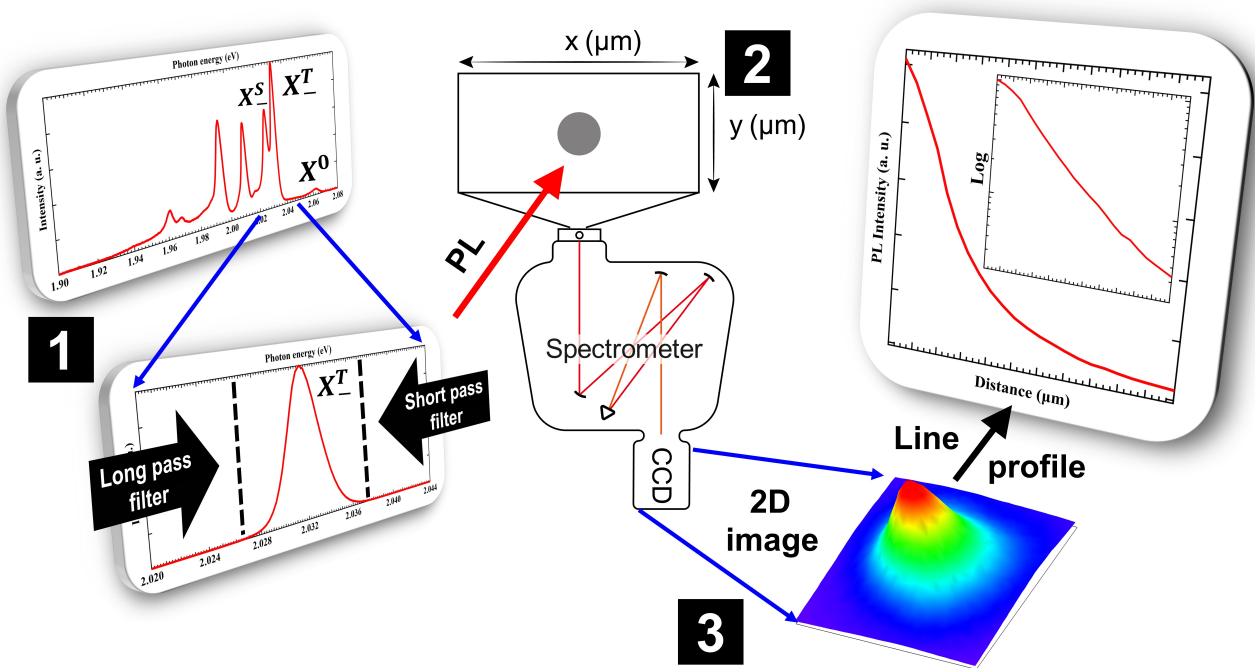


Figure 2.25: Demonstration for obtaining and analyzing 0th order PL image of  $\text{WS}_2$  monolayer at  $T = 20$  K.

### $0^{\text{th}}$ order imaging

The experimental process for the  $0^{\text{th}}$  imaging is shown in Fig. 2.25. Here, the grating of the spectrometer functions as a mirror for two-dimensional imaging, and long/short pass filters differentiate a selective PL emission from a multi-peak spectrum. For instance, we focus on the trion triplet ( $X^T$ ) emission of the  $\text{WS}_2$  monolayer at  $T = 20$  K, and separate the trion triplet emission from others, as shown in Fig. 2.25(1). We confirm that the filters have successfully suppressed the exciton ( $X^0$ ) emission by the short pass and, especially, the trion singlet ( $X^S$ ) by the long pass filter, which differs only  $\sim 6$  meV from the  $X^T$ . We remove the slit and position the grating such that the  $0^{\text{th}}$  order diffraction pattern (i.e. the specular reflection) of the PL is centered on the CCD. Then, the discriminated  $X^T$  emission enters on the spectrometer and arrives at the CCD keeping its 2D shape of the PL as shown in Fig. 2.25(2). Finally, the CCD counts intensity per pixel position as shown in Fig. 2.25(3). One can extract one dimensional profile by choosing several lines crossing the center of PL,  $r = 0$ , at the position of the excitation laser in order to average possible asymmetries of the image.

### $1^{\text{st}}$ order imaging

In the first-order configuration, the spectrometer resolves the PL spectra in the x-axis while keeping the y-axis for the distance unit. Here, we keep the original shape of PL until the spectrometer entrance, as shown in Fig. 2.26(1). We put the slit at the spectrometer entrance to obtain one vertical pixel line on the CCD, as shown in Fig. 2.26(2). The

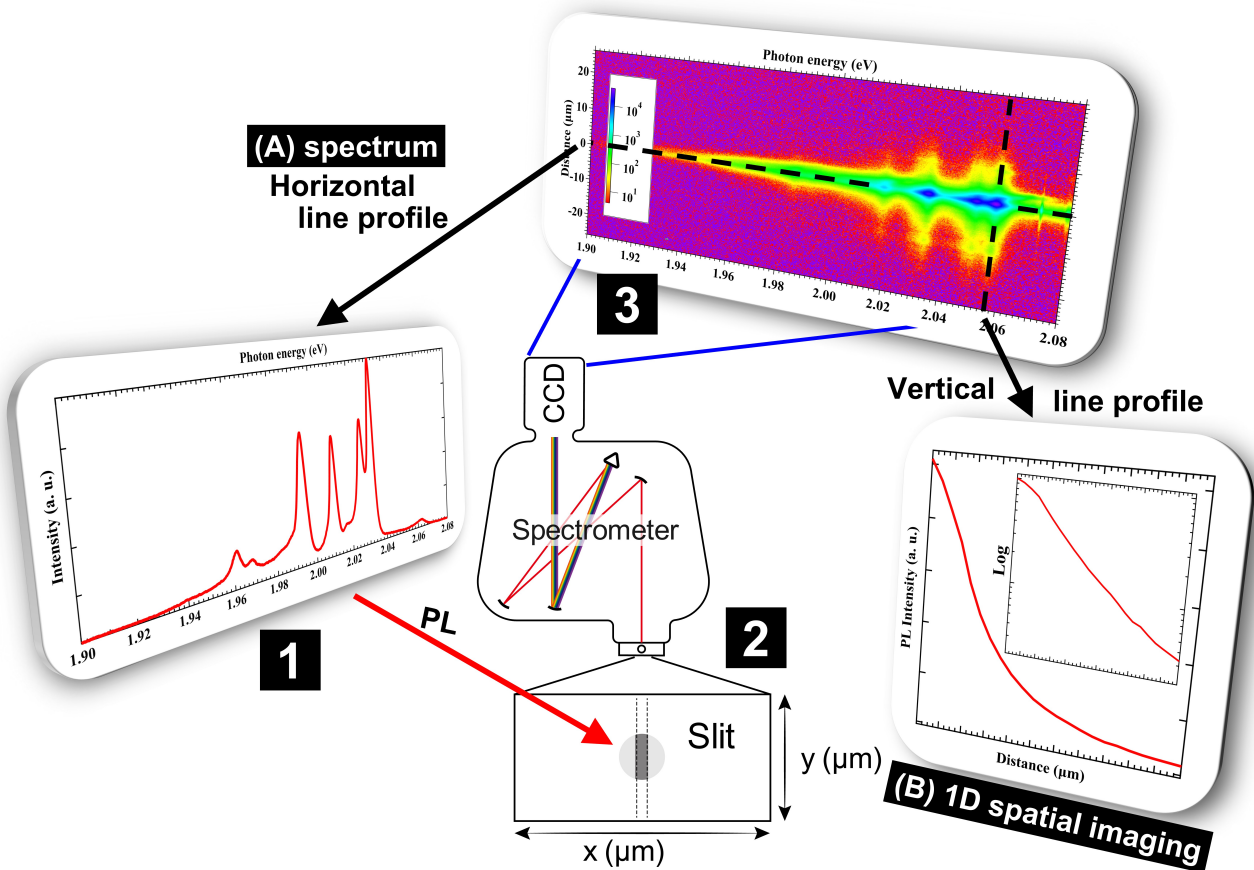


Figure 2.26: Demonstration for obtaining and analyzing first-order PL image of WS<sub>2</sub> monolayer at T = 20 K.

center of the PL image and the slit must be aligned to capture the vertical slice. This procedure offers well-resolved spectra and removes the dimension of the x-axis (distance) because the x-axis will be assigned for the wavelength unit by the grating of the spectrometer. Then, we get the following first-order image: x-axis for the wavelength, y-axis for the distance, and pixel count for the intensity of the PL, as shown in Fig. 2.26(3). The spatial distribution of PL on its emission energy (wavelength) can be obtained by slicing the first-order image vertically. Also, the spectra on different positions from the laser spot,  $r = 0$ , can be analyzed by the horizontal slice. Compared with the 0th order image, the advantages of this method are analyzing the spatial distribution for a specific PL emission energy and position dependent spectra. Of course, it has the drawback that we only have the vertical slice of the PL due to the geometry of the spectrometer and CCD, losing orders of magnitude on the detected intensity. We may have a reliability issue compared with the 0th order method if the PL has a spatial inhomogeneity of its shape. Nevertheless, the first-order method is a powerful technique for hyperspectral imaging.

## 2.3 Conclusions

We discussed the fabrication method based on mechanical exfoliation and the optical and AFM characterizations of hBN encapsulated TMD monolayers and devices. Mechanical exfoliation is a powerful technique to obtain high-quality monolayers with a lateral size of tens of  $\mu\text{m}$  from bulk. This lateral size is enough for our polarization-resolved  $\mu\text{-PL}$  experiments considering the focused laser in the sub- $\mu\text{m}$  range. This exfoliation is also efficient for building vertical heterostructures and contacted devices. Also, we demonstrated the characterization of fabricated samples at room temperature by PL, Raman, and AFM.

For polarization-resolved  $\mu\text{PL}$ , we discussed the details of the experimental setup and its key features. We also demonstrated that spin/valley polarization dynamics of TMD monolayers can be studied by exploiting the chiral optical selection rules in our polarization-resolved microscope under a circular and linear polarization basis. We would like to emphasize that hyperspectral imaging makes it possible to study the excitonic transport of TMDs which can also be polarization-resolved.

In the following chapter, we will discuss experimental results of spin/valley pumping on WS<sub>2</sub> monolayer which was done by polarization-resolved  $\mu\text{PL}$  setup. This sample was introduced in this chapter for the demonstration of mechanical exfoliation and characterizations at room temperature.



## Chapter 3

# Demonstration of spin/valley pumping of resident electrons in WS<sub>2</sub> monolayers

In the previous chapter, we have shown the main experimental technique and demonstrated and explained the fabrication of hBN encapsulated WS<sub>2</sub> monolayer through mechanical exfoliation. We also have characterized the sample at room temperature. At  $T = 300$  K, the exciton emission is dominant in PL (see Fig. 2.11.) so that other excitonic complexes are not visible. Other excitonic emissions are unstable due to the thermal energy at room temperature, which is higher than their binding energies. However, the dominant exciton emission evolves at low temperatures, where other excitonic states become distinguishable.

This chapter introduces experiments performed on a WS<sub>2</sub> monolayer encapsulated by hBN at low temperatures, which in PL exhibits various excitonic states below the neutral exciton due to the sign of spin-orbit splitting of the conduction band. We performed all experiments at cryogenic temperature to successfully resolve the different excitonic species, which are narrow in PL thanks to the hBN encapsulation.

At  $T = 20$  K, we identified excitonic states and in particular we resolved the fine structure of the negatively charged trion. We also studied the power dependency under two different excitation polarizations (circular and linear), each time resolving the polarization state of the photoluminescence.

We have observed a very high circular polarization of  $\sim 80$  % for the trion triplet ( $T_1$ ) under circular excitation and that its total PL intensity is higher under a circular excitation than under a linear excitation of the same power. Complementary time-resolved photoluminescence (TRPL) experiments performed by collaborators at the LPCNO showed that this phenomenon does not come from a spin-dependent recombination mechanism. Instead, we propose a spin-dependent formation of negatively charged trions. The mechanism relies on the fact that a continuous input of photoexcited electron-hole pairs in one valley under circular excitation induces an imbalance of resident electrons in the sub-conduction valleys, in other words, there is a dynamical spin-valley polarization of the resident

electrons. We also observed that this dynamical polarization can be enhanced under resonant excitation.

The experimental results and data are partially used in the paper (Nature communications 12, article number: 5455, 2021) [100], which has been done in collaboration with the LPCNO-INSA Toulouse group.

## 3.1 Observed excitonic complexes at $T = 20$ K

### 3.1.1 PL spectra at $T = 20$ K

The normalized low-temperature spectra of the encapsulated  $\text{WS}_2$  monolayer at  $9 \mu\text{W}$  and  $1.6 \text{ mW}$  excitation powers (radius of the laser spot  $0.4 \mu\text{m}$ ) are shown in Fig. 3.1a and b, respectively. In Fig. 3.1a, the neutral exciton ( $X^0$ ) peak is positioned at  $2.062 \text{ eV}$ , and other excitonic states are easily identified by the relative energy difference from the neutral exciton peak [134, 135, 136, 137, 138, 99].

The observation of negatively-charged complexes is a consequence of unintentional electron doping (n-type) of the monolayer. The binding energies of the two negatively charged trion peaks ( $T_1$  and  $T_2$ ) are  $\Delta E = 30.3 \text{ meV}$  and  $\Delta E = 36.3 \text{ meV}$ , with a  $\sim 6 \text{ meV}$  difference between the two due to the exchange interaction. Note that  $T_1$  and  $T_2$  are well resolved with narrow linewidth ( $5 \text{ meV}$ , FWHM), which is not the case in non-encapsulated samples [134, 139].

The negatively charged trion  $T_1$  ( $T_2$ ) corresponds to the triplet (singlet) state, bounded quasi-particle formation of exciton in one valley with an electron of the same spin for the other valley (opposite spin in the same valley). The quasi-particle formations of the  $T_1$  and  $T_2$  are shown in the inset of Fig. 3.1a.

Generally, this trion triplet  $T_1$  is not observed in semiconductors because the Pauli repulsion makes the state unbounded. Here, in tungsten-based TMD monolayers, the two trion states are visibly stable in PL emission due to the combination of valley configuration and a positive sign of spin-orbit splitting in the conduction band, which results in a weakening of the Pauli repulsion to form the trion triplet. The exchange interaction, which influences only the trion triplet between the exciton (e-h pair) and the inter-valley electron, lowers their binding energy by  $\sim 6 \text{ meV}$  in  $\text{WS}_2$  monolayer, similar to the splitting observed in the negatively charged trion's fine structure in  $\text{WSe}_2$  [140].

A small bump corresponding to the dark exciton ( $X^D$ ) peak is distinguished at  $\Delta E = 46.1 \text{ meV}$  from the  $X^0$ . This exciton is only visible thanks to a high numerical aperture, which collects a significant fraction of the light with a non-zero in-plane wavevector. The negatively charged bi-exciton ( $XX^-$ ) peak appears at  $\Delta E = 52.3 \text{ meV}$  from  $X^0$ . In the inset of Fig. 3.1b (blue curve), the dark trion emission was observed below  $5.5 \text{ meV}$  from the  $XX^-$  emission energy under  $2.047 \text{ eV}$  laser excitation at  $10 \mu\text{W}$ , which is slightly lower energy than the exciton resonance ( $\sim 2.056 \text{ eV}$ ). This  $T^D$  usually can be seen in the experiments with the help of an in-plane magnetic field [141]. Unidentified peaks  $L_1$ ,  $L_2$ , and  $L_3$  are observed at the low-energy side of the spectrum, and some of them are possibly related to localized excitons. They were recently reported as semidark trions ( $L_1$ ) and phonon replicas of the dark trion ( $L_2$  and  $L_3$ ) [142]. In this thesis, we have not focused on the proper identification of these peaks.

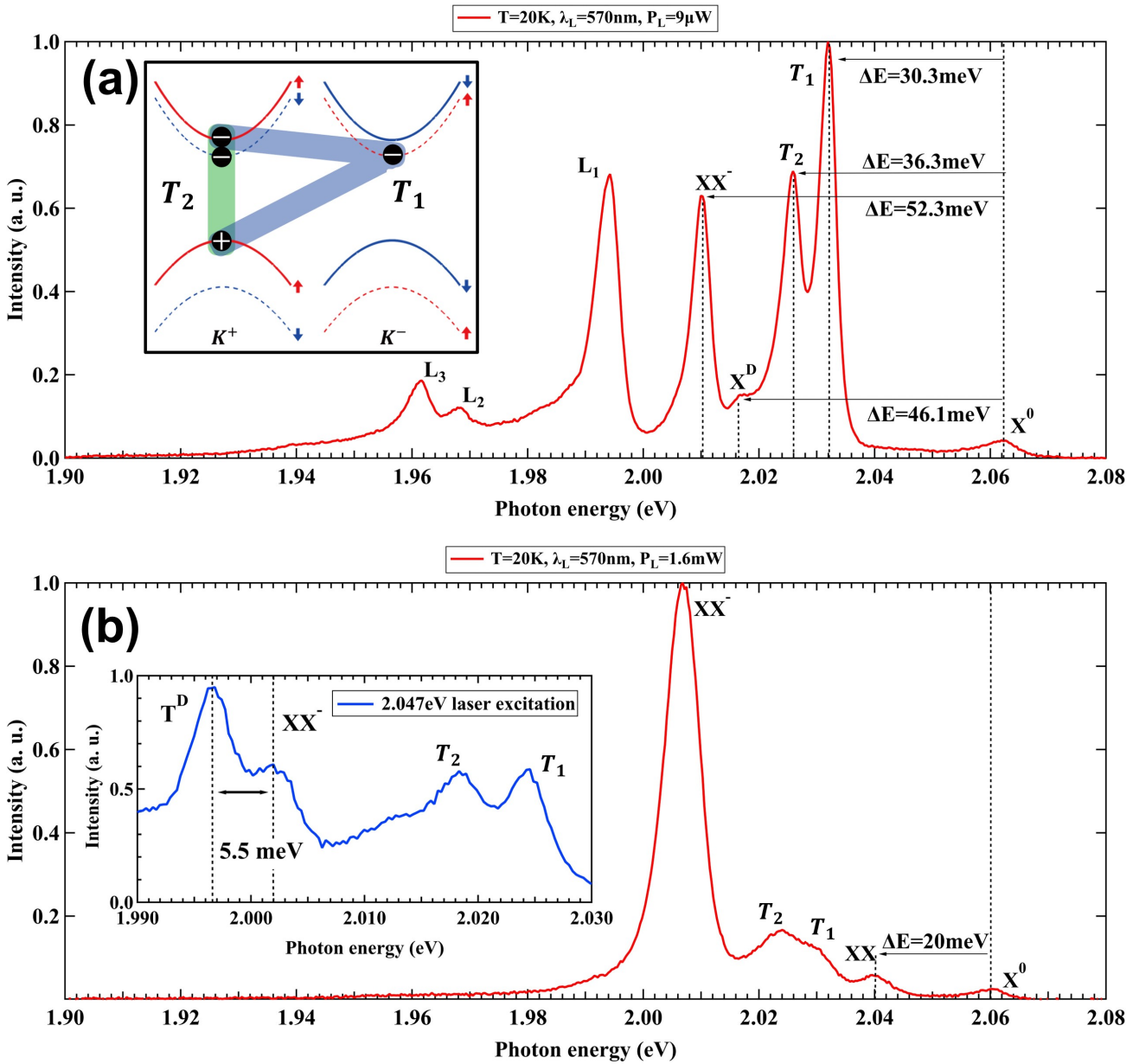


Figure 3.1: Photoluminescence spectrum (PL) under an excitation power of (a)  $9\ \mu\text{W}$  and (b)  $1.6\ \text{mW}$  at  $T = 20\ \text{K}$  of an hBN encapsulated  $\text{WS}_2$  monolayer. The excitation wavelength of the laser was  $570\ \text{nm}$  ( $2.1754\ \text{eV}$ ). Several excitonic peaks are identified in the spectrum ( $X^0$ ,  $T_1$ ,  $T_2$ ,  $X^D$ ,  $XX$ , and  $XX^-$ ). The dark exciton ( $X^D$ ) and localized (or phonon-related) states ( $L_1$ ,  $L_2$ , and  $L_3$ ) are observable at (a) low excitation power. In contrast, bi-exciton ( $XX$  and  $XX^-$ ) peaks dominate the emission at (b) high excitation power. The inset schematic of (a) describes  $T_1$  and  $T_2$  formations, which are the inter-valley trion singlet and intra-valley trion triplet, respectively. The red/blue colors indicate the spin (up/down) states of sub-valleys. The blue inset curve of (b) shows the PL spectrum at  $10\ \mu\text{W}$  under the excitation energy  $2.047\ \text{eV}$ , below the  $X^0$  energy. A PL peak appears at the energy below  $5.5\ \text{meV}$  from the  $XX^-$  emission. This energy emission corresponds to the dark trion.

At high excitation power (Fig. 3.1b), the neutral bi-exciton peak is also identified at  $\Delta E = 20\ \text{meV}$  from the  $X^0$ . The  $X^0$  peak shows a redshift from  $2.062\ \text{V}$  to  $2.060\ \text{V}$  with increasing power, but the relative energy difference between excitonic peaks changes by less than  $1\ \text{meV}$ . Also, a broadening of linewidth is observed for the two trions

and negatively charged bi-exciton, which implies heating of the system induced by the high power laser.

### 3.1.2 Power dependence

We performed power-dependent PL experiments by scanning the excitation power from 100 nW up to 5 mW at an excitation wavelength of 570 nm (2.1754 eV) laser. PL spectra and peak intensity as a function of the excitation power plot are shown in Fig. 3.2a and b, respectively. The inset of Fig. 3.2b shows relative peak positions as a function of the excitation power, where  $\Delta E$  is the peak position shift compared to the peak positions of the low powers spectrum. Each color of dots in Fig. 3.2b and the inset correspond to excitonic states indicated in the legend on the right bottom side. The power dependence trends of excitonic species are guided with dashed lines the slope of which is indicated by the numbers.

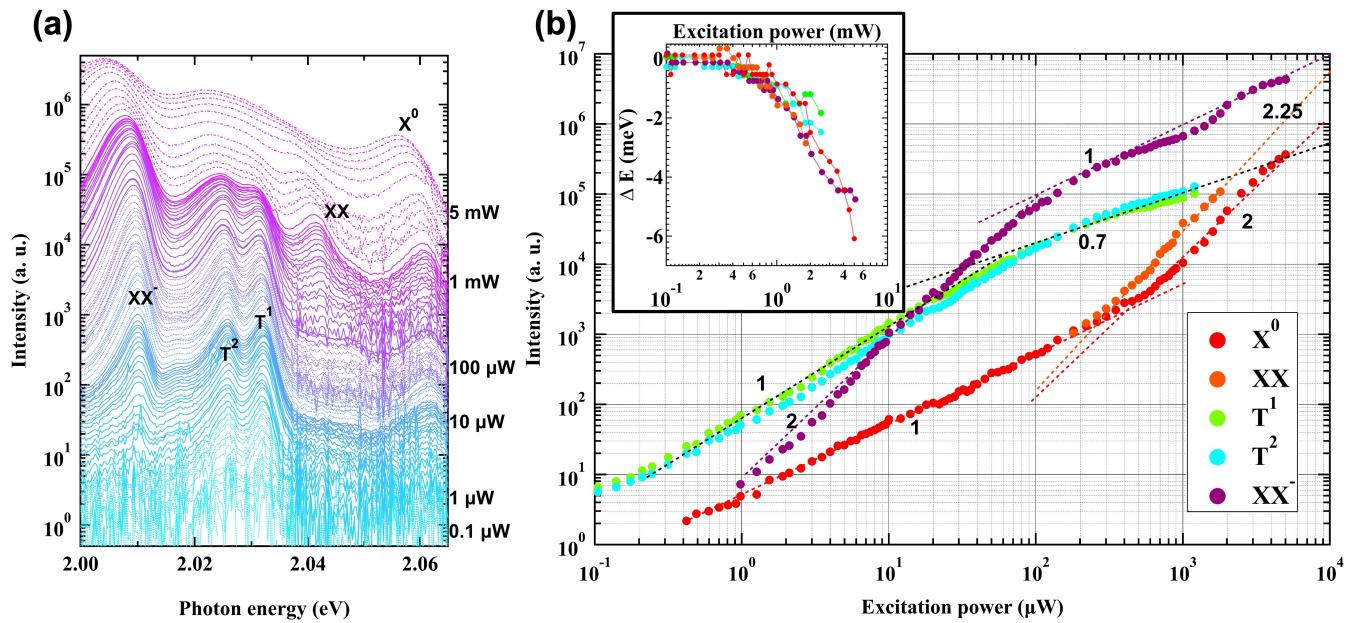


Figure 3.2: Power dependent (a) spectra and (b) peak intensity of power-dependent spectra (excitation power from 100 nW to 5 mW at 20 K).

At high excitation powers above  $\sim 1$  mW, bi-exciton emission is visible in the spectrum. Moreover, we see that peaks redshift (inset of Fig. 3.2b) with a broadening of linewidth (in Fig. 3.2a), which results from the system's heating by the laser. Further increase of the laser power makes the power dependence more challenging to interpret without a proper deconvolution.

At low excitation power below  $\sim 1$  μW, two trions ( $T_1$ ,  $T_2$ ) and the exciton ( $X^0$ ) are visible with the intensity of the trions being much higher than that of the  $X^0$ , implying that the sample has unintentional electron doping with a sufficiently large density.

The negatively charged bi-exciton ( $XX^-$ ) starts to be visible from  $\sim 1$  μW because the rich photo-excited exciton population increases the probability of bi-exciton formations. The trions show a linear dependence below  $\sim 100$

$\mu\text{W}$  while a non-linear behavior is observed above that excitation power. At these excitation densities, trions cannot be formed as efficiently as before because too few resident electrons are available compared to the photoexcited exciton density. The main limiting factor for trion formation in this regime is the finite density of the resident electrons in the system, originating from unintentional doping. The negatively charged bi-exciton ( $XX^-$ ) shows a non-linear behavior around  $\sim 100 \mu\text{W}$  as well. Spectra evolve as the power increases, bi-exciton ( $XX$ ) appears with a slope of 2 when the charged bi-exciton ( $XX^-$ ) starts to be non-linear.

So, the bi-exciton appears in the spectra with a slope of 2 when it cannot be transformed to the  $XX^-$ . Interestingly, a linear relation is observed for the exciton ( $X^0$ ) below  $\sim 500 \mu\text{W}$  while showing a quadratic behavior at higher excitation power, which is in contrast with the sub-linearity of the charged species ( $T_1$ ,  $T_2$ , and  $XX^-$ ) and the appearance of the bi-exciton ( $XX$ ). This brighter neutral exciton intensity is also an indication of the laser-induced heating effects. Indeed, the exciton emission becomes brighter when the temperature is increased in  $W$ -based monolayers. This explanation is consistent with the broadening of linewidth and redshift of PL at high excitation powers. Note that an Auger-like process (exciton-exciton annihilation), which induces the saturation at a high-density regime, may appear from tens of mW in our experiment [143].

Note that a similar situation as in Ref. [144] may explain the mono to the bi-molecular transition of the exciton. At a low excitation regime, photogenerated excitons preferentially form charged excitonic states due to the binding with resident electrons in the system. The exciton transition becomes bimolecular when the photogenerated exciton density is considerable, charged excitonic states ( $XX^-$ ,  $T_1$ , and  $T_2$ ) undergo saturation due to the finite resident electron density.

## 3.2 Demonstration of optical spin/valley pumping

We now discuss the polarization behavior of the PL under circular and linear excitation and pay particular attention to the behavior of the trion triplet ( $T_1$ ) which, as will be discussed later, allows us to conclude that the sea of resident electrons become highly spin/valley polarized under circular photoexcitation.

Fig. 3.3 shows  $\sigma_+$  (black, co-circular) and  $\sigma_-$  (red, cross-circular) PL spectra under  $\sigma_+$  excitation at  $10 \mu\text{W}$  for a laser excitation at  $569.8 \text{ nm}$ . The blue and golden dots indicate the degree of circular and linear polarization, respectively. The inset shows the degree of circular polarization of the  $T_1$  and  $T_2$  as a function of the excitation power.

The degree of linear polarization is close to zero for all excitonic species except the neutral exciton which exhibits  $\sim 30\%$  of linear polarization. This linear polarization is observed because the exciton lifetime (ps range) is very short and comparable to the valley decoherence time, a phenomenon widely observed in TMD MLs, as we discussed in chapter 1 (1.3.3).

In contrast, one can observe a circular polarization of  $\sim 40\%$  in average. The  $T_1$  (inter-valley trion triplet) exhibits

$\sim 75\%$  circular polarization and the  $T_2$  (intra-valley trion singlet) exhibits  $\sim 20\%$  circular polarization. The  $T_1$  has higher circular polarization than the average value ( $\sim 40\%$ ), meanwhile the  $T_2$  has a lower value than the average.

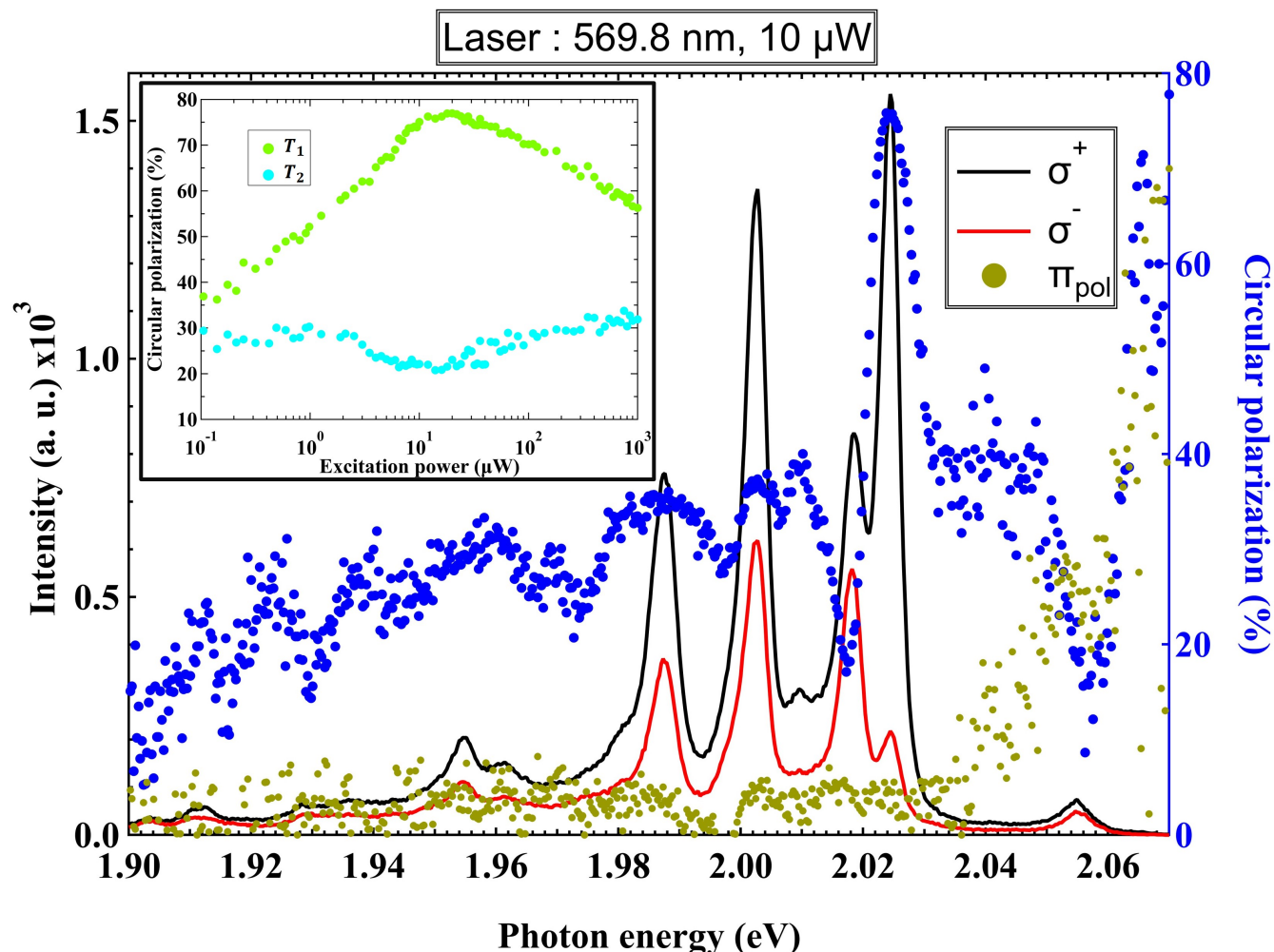


Figure 3.3: Photoluminescence (PL) spectra and degree of circular/linear polarization (blue/gold circles) for a circularly/linearly-polarized excitation laser of wavelength 569.8 nm at  $10\ \mu\text{W}$ . The black (red) line corresponds to  $\sigma_+$  ( $\sigma_-$ ) detection under circularly polarized excitation. The inset shows the degree of circular polarization for the  $T_1$  and  $T_2$  as a function of the excitation power. The degree of circular polarization is calculated by  $\frac{I^{\sigma_+} - I^{\sigma_-}}{I^{\sigma_+} + I^{\sigma_-}} \times 100$  (%), as well as the degree of linear polarization on a linear basis.

Most research on polarization-resolved PL in  $\text{WS}_2$  monolayers has reported a circular polarization of  $\sim 30\%$  at  $T = 4\ \text{K}$  for non-encapsulated samples, in which excitonic species were not resolved [145, 134] as well as Lin et al. [146] who demonstrated a circular polarization of  $\sim 90\%$  on CVD growth  $\text{WS}_2$  monolayer at  $T = 80\ \text{K}$  by explaining that exciton-defect collision produces non-radiative recombination. For hBN encapsulated  $\text{WS}_2$ , Vaclavkova et al. [138] reported a maximum circular polarization of  $\sim 50\%$  for trion triplet and  $\sim 28\%$  for trion singlet while showing smaller values that we observed.

As shown in the inset of Fig. 3.3, we performed a power-dependence experiment to look for further details of the degree of circular polarization for the  $T_1$  and  $T_2$ . The degree of circular polarization for the  $T_1$  first increases with

the excitation power, it reaches a maximum of  $\sim 78\%$  when the excitation power is  $\sim 18\ \mu\text{W}$ , and then it decreases with excitation powers above  $\sim 18\ \mu\text{W}$ . In contrast, the  $T_2$  exhibits  $\sim 30\%$  circular polarization except for a small decrease at excitation powers around  $\sim 18\%$  precisely where the  $T_1$  exhibits a maximum circular polarization. Note that the maximum polarization is achieved while still in the linear excitation regime of Fig. 3.2b. The sub-linearity of PL intensity appears at around  $100\ \mu\text{W}$  for the two trions. Indeed, these evolutions occur in the regime where the resident electron density is enough to efficiently form trions with photogenerated electron-hole pairs.

We now focus on the evolution of the  $T_1$  and  $T_2$  under two different excitation states (circular/linear) to discuss more in details the polarization dependence.

### 3.3 Demonstration of a dynamical spin/valley polarization of the resident electrons

#### 3.3.1 Trion ( $T_1$ and $T_2$ ) emission intensity under circular and linear excitation

Comparing the PL intensity under different circular and linear excitation may give us valuable information to understand an eventual spin-dependent formation and/or recombination of photogenerated carriers. In Fig. 3.4, the total PL spectrum,  $I^\sigma$  ( $I^\pi$ ), is represented as the black (red) curve, and the purple circles exhibit the ratio between the PL intensity under circular and linear excitation ( $R = I^\sigma/I^\pi$ ). An excitation power of  $18\ \mu\text{W}$  and excitation laser of wavelength  $569.8\ \text{nm}$  were selected. The inset of Fig. 3.4 shows the  $R$  for the  $T_1$  and  $T_2$  as a function of the excitation power.

All the excitonic emissions except for the two trions show the same intensity regardless of the laser polarization. In contrast, the trion triplet ( $T_1$ ) shows a peak intensity  $\sim \times 1.9$  higher under circular excitation compared with linear one. The trion singlet ( $T_2$ ) shows a very small difference ( $\sim \times 1.1$  higher for circular than linear) between the two excitation configurations.

As shown in the inset of Fig. 3.4, the  $R$  of trion triplet ( $T_1$ ) is close to 1 when the excitation power is low and increases with the excitation power until tens of  $\mu\text{W}$  while the trion singlet ( $T_2$ ) does not show significant variation as a function of excitation power, exhibiting a slight increase of the ratio to  $\sim 1.1$  in the regime where the  $T_1$  reaches a maximum. A strong spin-dependent intensity ratio ( $R$ ) of the trion triplet ( $T_1$ ) appears between  $10 \sim 50\ \mu\text{W}$  excitation, and the asymmetry decreases when the excitation power further increases. Notably, these trends are coherent with the circular polarization of the  $T_1$  as a function of the excitation power (the inset of Fig. 3.). For the  $T_1$ , the circular polarization and the asymmetry show a maximum for an excitation power of  $\sim 18\ \mu\text{W}$ . For the  $T_2$ , one can notice that a slight decrease in the degree of circular polarization is observed when the asymmetry gets higher for the excitation power at around  $\sim 18\ \mu\text{W}$ .

So, we can summarize the following observations: 1) The  $R$  ratio reaches a maximum at the excitation power of

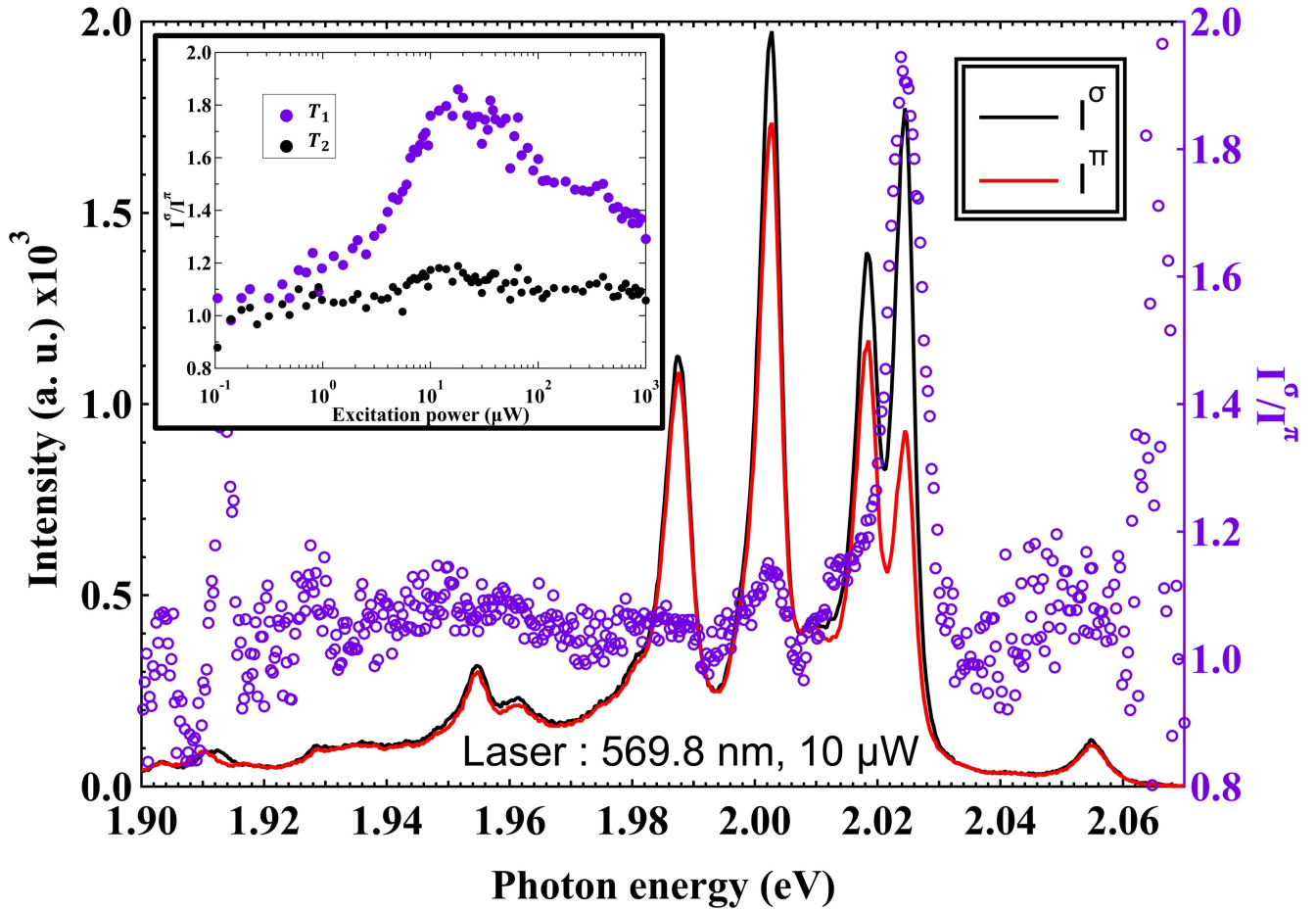


Figure 3.4: Total PL spectra and intensity ratio under circular/linear bases for an excitation laser of wavelength 569.8 nm at 10  $\mu\text{W}$ . The black (red) line corresponds to PL spectrum under  $\sigma$  ( $\pi$ ) excitation. Purple circles correspond to the PL intensity ratio ( $I^\sigma/I^\pi$ ). The inset presents the  $I^\sigma/I^\pi$  ratio for the  $T_1$  and  $T_2$  as a function of the excitation power.

$\sim 18 \mu\text{W}$ . 2) When the R increases, the degree of circular polarization for the  $T_1$  ( $T_2$ ) increases (decreases). Note that these excitation powers are in a linear (I vs P) regime. 3) For a maximum R regime, one could say that the PL component  $\sigma+$  for the  $T_1$  ( $\sigma-$  for the  $T_2$ ) increases. This observation implies that we are modifying the processes of formation and/or recombination of trions by pumping the system with circularly polarized light.

### 3.3.2 TRPL: investigation of build-up and recombination under circular/linear excitation

We have performed time-resolved photoluminescence (TRPL) experiments in order to understand the contribution of the formation and/or recombination process under circular/linear excitation. The TRPL measurements of the  $T_1$  at  $T = 5.1 \text{ K}$  are shown in Fig. 3.5. The red and black curves correspond to total PL intensity under circular and linear excitations at 1  $\mu\text{W}$ , respectively. Note that we used a ps-pulsed optical parametric oscillator (OPO) at 570 nm for  $\text{WS}_2$ . The signal is detected by a Hamamatsu streak camera with a time resolution of  $\sim 2\text{-}3 \text{ ps}$  [100]. Note that this excitation power ( $\sim 1 \mu\text{W}$ ) of the pulsed-laser (tens of Mhz repetition frequency, ps range pulse) corresponds to an

excitation power of  $\sim 10$  mW for continuous wave excitation.

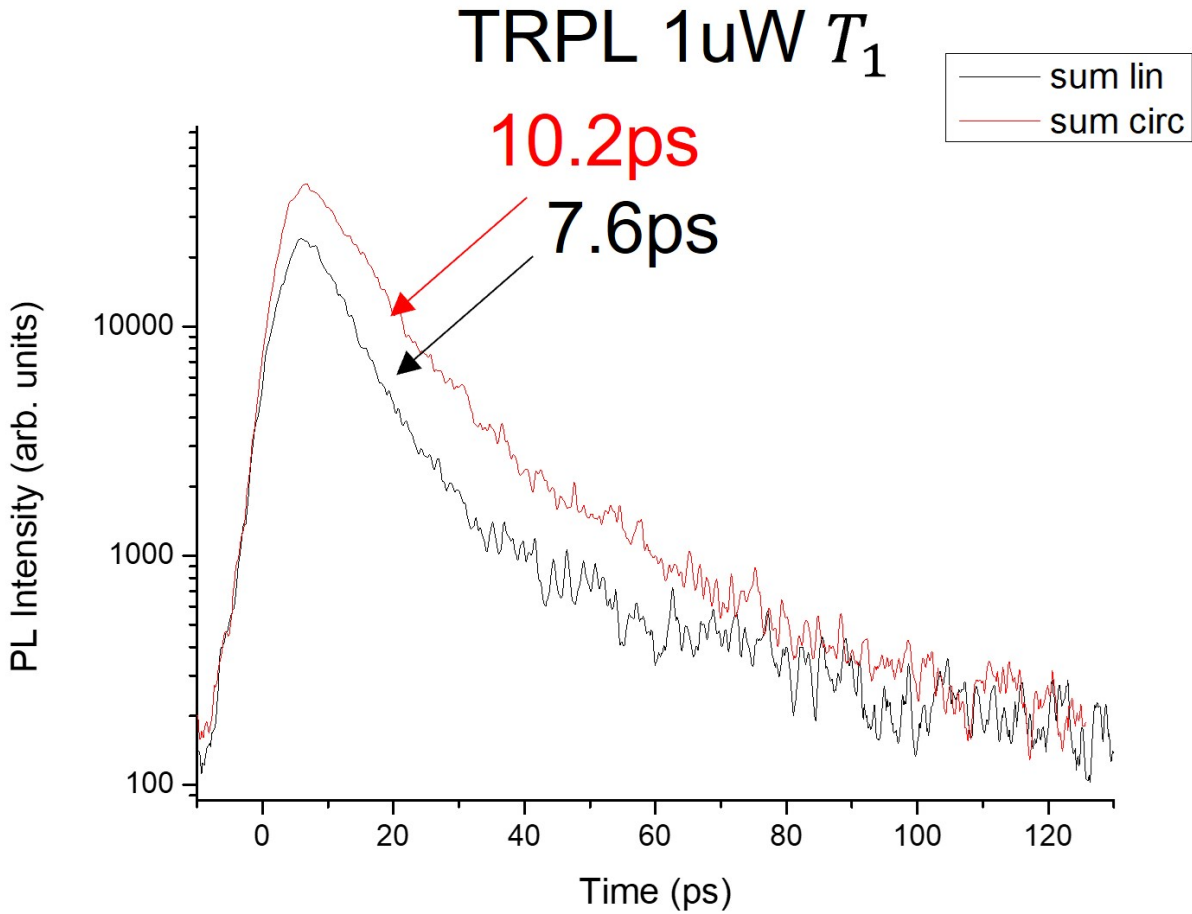


Figure 3.5: Time-resolved photoluminescence (TRPL) of the trion triplet ( $T_1$ ) under circular (red) and linear excitations (black) at  $T = 5.1$  K under the excitation laser power of  $1 \mu\text{W}$ . The experiment was performed by the collaboration group in Toulouse (LPCNO).

We can extract two different pieces of information for (1) recombination and (2) build-up of the  $T_1$  under circular and linear excitations. First, the  $T_1$  exhibits a slightly different recombination lifetime under the two excitation polarizations, which are 10.2 ps for circular and 7.6 ps for linear. The lifetime of the  $T_1$  is therefore 34 % longer under circular excitation than linear one. Second, the initial build-up population is different. Note that the total PL intensity (y-axis) is shown in a log scale. The total PL intensity of the  $T_1$  at short times is 78 % higher under circular excitation than linear excitation, which implies that the initial build-up of the  $T_1$  is the most dominant contribution for the spin-dependent intensity of the  $T_1$ . Note that we obtained a maximum PL intensity ratio of  $\sim 1.9$  for the  $T_1$  under circular and linear excitations, which represent a  $\sim 90$  % higher total PL intensity for circular excitation than linear excitation.

From these observations, we attribute the asymmetric behavior under  $\sigma/\pi$  excitation to the difference in the build-up of the  $T_1$  formations. In other words, the initial formation of the  $T_1$  under  $\sigma/\pi$  excitation is different, resulting in

the asymmetric behavior in PL, whereas the recombination lifetime can be considered, as a first approximation, as constant.

### 3.3.3 Qualitative explanation for the dynamical polarization of resident electrons

We built a model to explain the observations from the PL intensity difference under circular/linear excitation and TRPL experiments.

This difference in intensity of the  $T_1$  and  $T_2$  under circular and linear excitation can be explained by the following mechanism [100]. Under  $\sigma_+$  excitation, the continuous supply of photogenerated excitons in the  $K^+$  valley creates an imbalance of resident electrons in the lowest sub-conduction bands in  $K^+$  and  $K^-$  valleys, which is called the dynamical polarization of resident electrons. The different resident electron density in the  $K^+$  and  $K^-$  valleys results in a difference on the probability of formation of  $T_1$  and  $T_2$ .

Fig. 3.6 shows a schematic which explains the mechanism of dynamical polarization of resident electrons. We first assume that the TMD ML is n-doped, which is the case in our  $WS_2$  monolayer. 1) At  $t = 0$  without laser excitation, the resident electrons are equally distributed in the  $K^+$  and  $K^-$  sub-valleys. 2) We photoexcite the system with  $\sigma_+$  excitation. The photogenerated electron-hole pairs are created in the  $K^+$  valley due to the chiral optical selection rules. 3) Then, the photoexcited electrons undergo relaxations in the valley with spin-flip (intra-valley relaxation) or into the opposite valley by conserving their spin (inter-valley relaxation). If the inter-valley relaxation is faster than the intra-valley relaxation,  $\tau_{inter} < \tau_{intra}$  [147]. Thus, the number of resident electrons in the  $K^-$  valley becomes higher than the resident electrons in the  $K^+$  valley.

Due to the imbalance of resident electrons in the sub-conduction bands between the  $K^+$  and  $K^-$  valleys, the resident electrons scatter into the opposite valley through inter-valley spin-relaxation with the characteristic time  $\tau_{sv}$ . Under continuous  $\sigma_+$  excitation, a competition of these two processes determines the polarization of resident electrons. We obtain a certain amount of polarization of resident electrons if the inter-valley spin-relaxation is slower than the dynamical polarization process by polarized optical pumping. 4) We attribute this dynamical polarization buildup of resident electrons to a high degree of circular polarization in the  $T_1$  and weaker circular polarization for the  $T_2$ . Since the negatively charged trion formation is strongly influenced by the resident electron density, formation is more (less) favorable for the  $T_1$  ( $T_2$ ) under  $\sigma_+$  excitation. Consequently, the degree of circular polarization becomes higher (lower) than the average value.

We can explain the main observations through a simple bi-molecular model of trion formation [100]. The trion population is proportional to the number of photoexcited excitons times the number of resident electrons in the sub-conduction valleys. For example, the population of  $T_1$  in the  $K^+$  valley ( $N_{T_1}^{K^+}$ ) is proportional to the number of photoexcited excitons in the  $K^+$  valley ( $N_{X_0}^{K^+}$ ) and to the population of resident electrons in the  $K^-$  valley ( $N_e^{K^-}$ ).

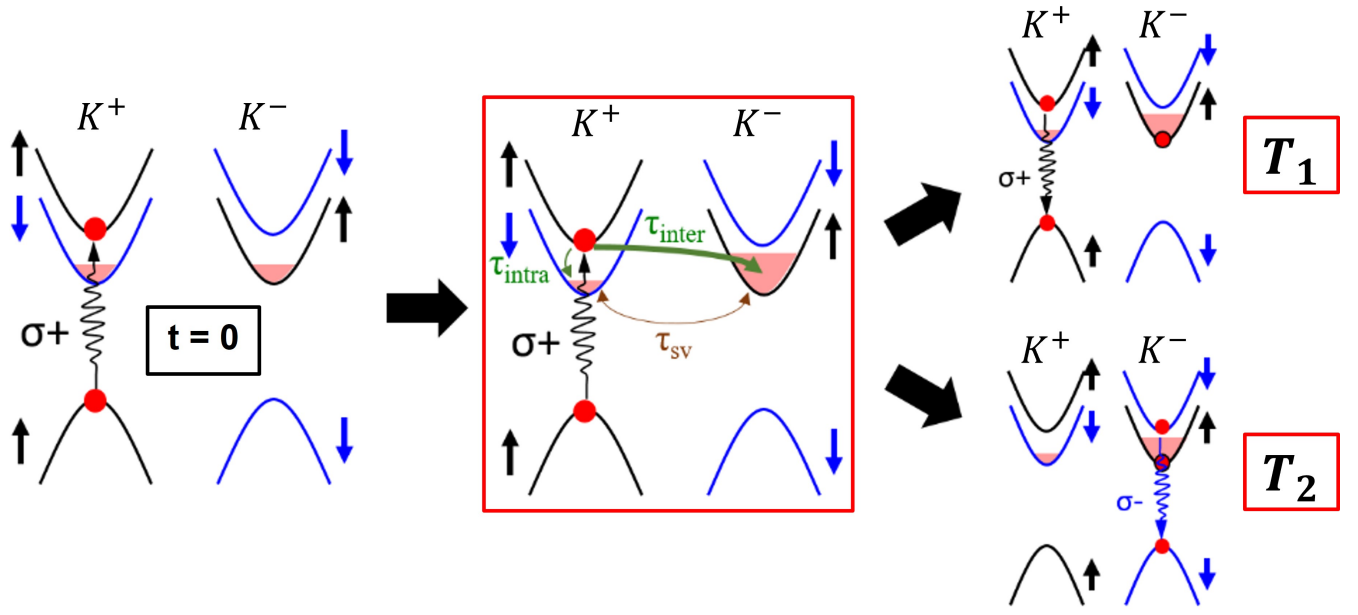


Figure 3.6: Sketch of the dynamic polarization of resident electrons for trions with  $\sigma+$  excitation.  $\tau_{inter}$  ( $\tau_{intra}$ ) represents the inter-valley spin-conserving (intra-valley spin-flip) relaxation times of topmost electrons while  $\tau_{sv}$  corresponds to the spin/valley relaxation time of resident electrons [100].

The degree of circular polarization for the  $T_1$  ( $P_{T_1}$ ) and  $T_2$  ( $P_{T_2}$ ) is expressed as,

$$P_{T_1} \propto \frac{N_{X_0}^{K^+} N_e^{K^-} - N_{X_0}^{K^-} N_e^{K^+}}{N_{X_0}^{K^+} N_e^{K^-} + N_{X_0}^{K^-} N_e^{K^+}} \quad (3.1)$$

$$P_{T_2} \propto \frac{N_{X_0}^{K^+} N_e^{K^+} - N_{X_0}^{K^-} N_e^{K^-}}{N_{X_0}^{K^+} N_e^{K^+} + N_{X_0}^{K^-} N_e^{K^-}} \quad (3.2)$$

Also, the degree of photoexcited exciton polarization is  $P_{X_0} = \frac{N_{X_0}^{K^+} - N_{X_0}^{K^-}}{N_{X_0}^{K^+} + N_{X_0}^{K^-}} \times 100$  (%) and the degree of resident exciton polarization is  $P_e = \frac{N_e^{K^+} - N_e^{K^-}}{N_e^{K^+} + N_e^{K^-}} \times 100$  (%), which can be rewritten as the following,

$$\frac{1 - P_{X_0}}{1 + P_{X_0}} = \frac{N_{X_0}^{K^-}}{N_{X_0}^{K^+}} \quad (3.3)$$

$$\frac{1 + P_e}{1 - P_e} = \frac{N_e^{K^+}}{N_e^{K^-}} \quad (3.4)$$

Finally, we can rewrite Eq. 3.1 and 3.2 by using Eq. 3.3 and 3.4,

$$P_{T_1} = \frac{P_{X_0} - P_e}{1 - P_{X_0} P_e} \quad (3.5)$$

$$P_{T_2} = \frac{P_{X_0} + P_e}{1 + P_{X_0} P_e} \quad (3.6)$$

From these equations, we can estimate the degree of photoexcited exciton and resident electron polarization for  $P_{T_1}$

= 78 % and  $P_{T_2} = 18$  %. Then, we get  $P_{X_0} = 48.2$  % and  $P_e = -40.7$  %. Therefore, we observe a higher degree of circular polarization for the  $T_1$  than the average since the  $T_1$  formation in the  $K^+$  valley is much more favorable than the  $T_2$  when the density of resident electrons is higher at the  $K^-$  valley, and so the  $T_2$  shows a lower degree of circular polarization than the average.

At low excitation powers, this dynamical polarization of resident electrons is negligible with respect to the thermal distribution of resident electrons so that the dynamical polarization of resident electrons is not observable. As the excitation power increases, the polarization in the sub-conduction valleys becomes high enough so one can observe the imbalance of the total PL intensity under circular and linear excitations.

This mechanism also can explain the intensity difference of the  $T_1$  and  $T_2$  under circular and linear excitation. Under  $\sigma+$  excitation, the  $T_1$  formation in the  $K^+$  valley is more favorable since the resident electrons in the  $K^-$  valley are accumulated due to the dynamical polarization of resident electrons, resulting in the total PL intensity increase under circular excitation compared with the case under linear excitation. These can be explained by the same bi-molecular description. We can express the total PL intensity under circular/linear excitation as [100],

$$I_{T_1}^\sigma \propto N_{X_0}^{K^+} N_e^{K^-} + N_{X_0}^{K^-} N_e^{K^+} \quad (3.7)$$

$$I_{T_2}^\sigma \propto N_{X_0}^{K^+} N_e^{K^+} + N_{X_0}^{K^-} N_e^{K^-} \quad (3.8)$$

$$I_{T_1}^\pi = I_{T_2}^\pi \propto \frac{1}{2} (N_{X_0}^{K^+} + N_{X_0}^{K^-}) (N_e^{K^+} + N_e^{K^-}) \quad (3.9)$$

Then, the PL intensity ratio  $R$  for the  $T_1$  and  $T_2$  is given by,

$$R_{T_1} = \frac{I_{T_1}^\sigma}{I_{T_1}^\pi} = 1 - P_{X_0} P_e \quad (3.10)$$

$$R_{T_2} = \frac{I_{T_2}^\sigma}{I_{T_2}^\pi} = 1 + P_{X_0} P_e \quad (3.11)$$

We obtain  $R_{T_1} \approx 1.2$  and  $R_{T_2} \approx 0.8$  for  $P_{X_0} = 48.2$  % and  $P_e = -40.7$  %. Note that our experimental  $R_{T_1}^{exp} = 1.9$  is higher and that  $R_{T_2}^{exp} \approx 1.1$ . This model has a limitation since we assumed the simplest case taking into account only the bi-molecular process. The model can be improved by taking into account other formation process of excitonic species and non-resonant photoexcitation of electron-hole pairs. Nevertheless, this simple version of the model gives us the physical insight for the understanding of the observed phenomena.

### 3.3.4 Dynamic valley polarization under resonance excitation of the excited excitonic states

We performed photoluminescence excitation (PLE) spectroscopy thanks to the rhodamine 6G dye laser. Fig. 3.7 shows the asymmetry ( $R$ ) ratio map where we increase the excitation wavelength from 565 nm (2.19469 eV) to

603.6 nm (2.05434 eV), maintaining the excitation power at  $10 \mu\text{W}$ . Note that we do not see any ratio for the exciton emission for excitation energies below  $\sim 2.115$  eV due to the long pass filter for the laser. The inset shows the total PL intensity of the  $X^0$  as a function of the excitation energy under  $\sigma+$  excitation.

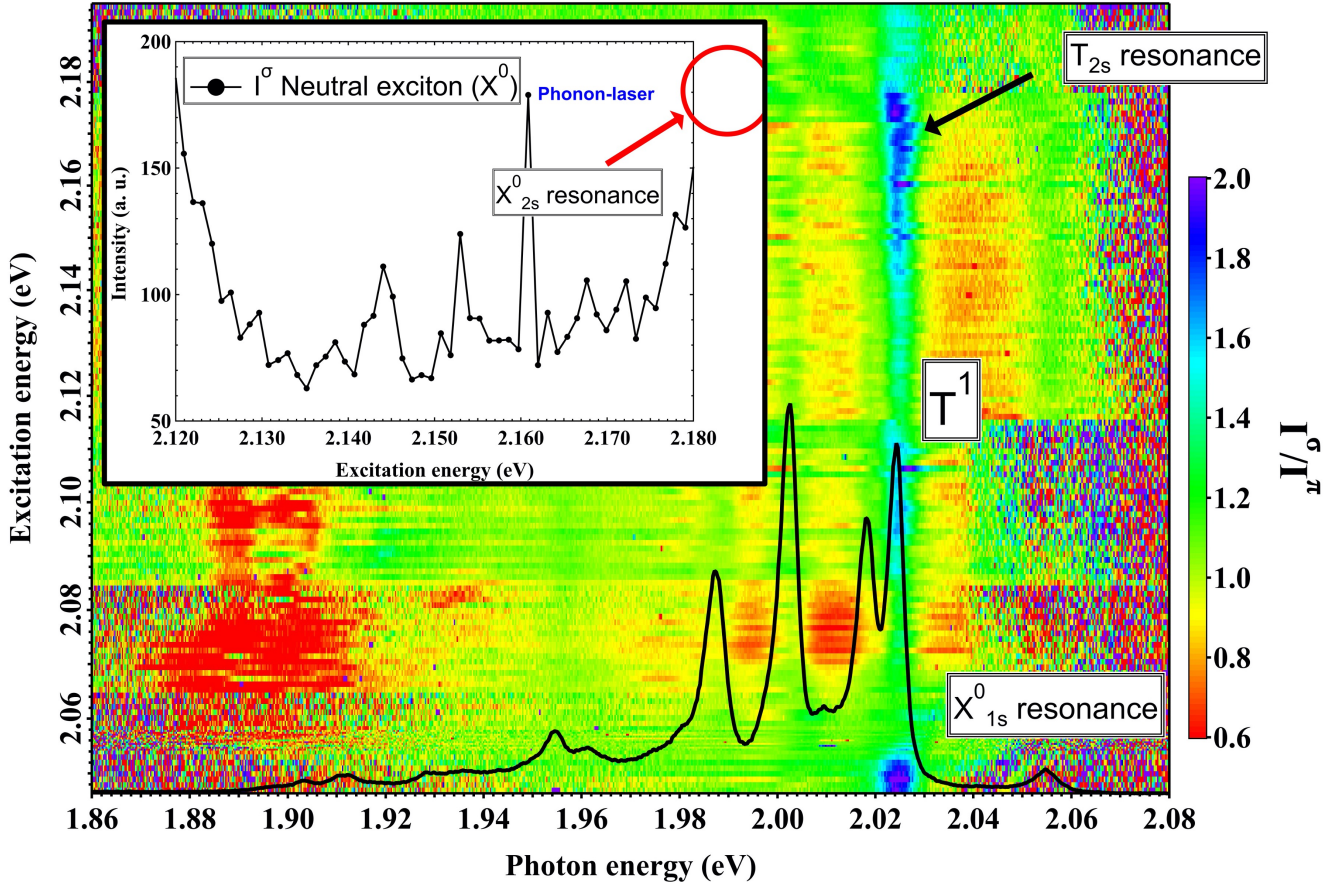


Figure 3.7: Photoluminescence excitation spectroscopy (PLE) of  $I^\sigma/I^\pi$  ratio for an excitation laser of wavelength 565 nm  $\sim$  605.8 nm at  $10 \mu\text{W}$ . The black curve indicates a normalized PL spectrum. The inset shows the neutral exciton ( $X^0$ ) intensity as a function of the excitation energy at a fixed excitation power of  $10 \mu\text{W}$ . One can observe that the  $I^\sigma/I^\pi$  ratio increases for the two exciton resonances (neutral exciton ground state and first excited state of the trion). Note that we do not see the first excited state of the exciton resonance in PLE due to the maximum photon energy available with our laser source. (the red circle of the inset).

The R ratio of the  $T_1$  locally increases at the excitation energy of  $\sim 2.175$  eV and  $\sim 2.056$  eV. These energies correspond to the excitonic resonance states, which are the first excited state of the T ( $\sim 2.175$  eV) and the ground state of the  $X^0$  ( $\sim 2.056$  eV) at  $T = 20$  K [148]. These results are coherent with our model and previous observations of power-dependent experiments since it can be expected that the dynamical valley polarization of resident electrons is enhanced due to the efficient optical pumping under the resonance excitation.

Interestingly, we can clearly identify the first excited state of the trion ( $T_{2s}$ ) in the R ratio map, which shows very weak oscillator strength at  $T = 20$  K so that it is not easy to identify in the absorption spectrum because of the strong  $X^0_{2s}$  resonance [148]. Note that the first excited state of the neutral exciton ( $X^0_{2s}$ ) should be observed at

around 2.196 eV. We see an increase of the total PL intensity of the  $X^0$  when the excitation energy goes to the upper limit of our scanning range (indicated by the red circle of the inset of Fig. 3.7.). It may imply that the dynamical valley polarization is much more sensitive than the absorption process for excited states of trion. It can also be a useful method to identify excitonic Rydberg states for those who show PL intensity difference by the dynamical valley polarization.

### 3.4 Conclusions

In conclusion, we have identified excitonic complexes in  $WS_2$  monolayer at cryogenic temperatures, which were not visible at room temperature, as discussed in chapter 2. We have obtained PL spectra of a narrow linewidth thanks to the hBN encapsulation. We distinguished the fine structure of negatively charged trions ( $\sim 6$  meV) with linewidths (5 meV, FWHM) for the  $T_1$  and  $T_2$ .

We have demonstrated the spin/valley polarization through the polarization-resolved  $\mu$ -PL setup. Under linear excitation, we observed a degree of linear polarization of  $\sim 30\%$  for the neutral exciton  $X^0$ , implying that the valley coherence is experimentally observable. Under  $\sigma$  basis, the PL exhibits a circular polarization of  $\sim 40\%$  (average), while the  $T_1$  ( $T_2$ ) exhibits a maximum (minimum) circular polarization of  $\sim 80\%$  ( $\sim 18\%$ ) at  $\sim 18 \mu W$ . At this range of excitation powers, we observed a significant intensity difference for the  $T_1$  under  $\sigma/\pi$  excitations. We revealed that this asymmetric behavior (a maximum R ratio of  $\sim 1.9$ ) under the two excitation bases originates from a different build-up mechanism under  $\sigma/\pi$  excitations. This idea is supported by TRPL measurements for the  $T_1$  which shows that the build-up PL intensity under  $\sigma$  excitation is 78% higher than the one under  $\pi$  excitation, while the lifetime under  $\sigma$  excitation is only 34% higher than the other one.

In our model (for n-type TMD MLs), a continuous input of photoexcited electron-hole pairs in one valley under circular excitation induces an imbalance of resident electrons in the sub-conduction valleys, a dynamical spin-valley polarization of the resident electrons. In return, one can observe a big difference in the degree of circular polarization of negatively charged trions (higher for the inter-valley trion triplet  $\sim 80\%$  and lower for the intra-valley trion singlet  $\sim 18\%$  than the average degree of circular polarization  $\sim 40\%$ ) due to the distribution change of resident electrons in the  $K^+$  and  $K^-$  valleys. We have built a simple bi-molecular model to explain these experimental observations based on the fact that the trion population is proportional to the population of photoexcited excitons times the population of resident electrons. We estimated the resident electron polarization of -40.7% and the photoexcited exciton polarization of 48.2%. Also, this dynamical polarization of resident electron results in higher PL intensity ( $R_{T_1}^{exp} = 1.9$ ,  $R_{T_1}^{model} = 1.2$ ) under circular excitation than under linear excitation for the inter-valley trion triplet ( $T_1$ ). These observations are coherent with our model since the  $T_1$  formation in the  $K^+$  valley is more favorable under  $\sigma+$  excitation than  $\pi$  excitation. Although we found a difference between the  $R^{exp}$  and  $R^{model}$ , this model provides an insight to understand the hidden mechanism behind the observed behavior of trions under polarized excitation.

We also showed that this dynamical polarization can be enhanced under resonant excitation. In the first excited T resonance, this response of dynamical valley polarization is much more sensitive than the exciton PL intensity variation as a function of the excitation energy.



## Chapter 4

# Exciton physics under high excitation fluences in MoSe<sub>2</sub> monolayers

In the previous chapter, we have demonstrated spin/valley polarization of the hBN encapsulated WS<sub>2</sub> monolayer through polarization-resolved  $\mu$ PL spectroscopy. Especially, we have shown that optically induced dynamical valley polarization of resident electrons can be established in W-based TMD MLs, implying that a strong spin-dependent PL intensity is observed under circular/linear excitation polarizations. However, all the results presented up to now were obtained in regimes where the PL peak intensities grow linearly with the laser intensity. In this chapter, I will present excitonic behaviors in higher excitation regimes.

For the WS<sub>2</sub> monolayer, many excitonic species and localized states appeared in the PL spectrum with a linewidth of ( $< 4$  meV) as well as small energy differences ( $< 10$  meV) compared to other excitonic complexes in the material. A proper deconvolution of the PL spectrum is required to investigate more details of excitonic species. At high excitation powers, analyzing the spectrum is much more complicated due to the broadening of linewidths. They become comparable to the energy differences between excitonic states. Especially, a well-filtered configuration is required to image PL in 2D space for our imaging technique (0<sup>th</sup> order imaging). Also, the intense charged-bi exciton emission gives us difficulties to appreciate the details appearing at high excitation powers.

For these reasons, we have chosen an encapsulated MoSe<sub>2</sub> monolayer that exhibits a relatively simpler PL spectrum. Only two excitonic states can be found in the PL spectrum of the MoSe<sub>2</sub> monolayer at low temperatures due to the different conduction band splitting configurations. Also, the PL emissions of excitonic species are positioned with a larger energy difference ( $> 25$  meV). This configuration will make it convenient to investigate details of excitonic behavior at high excitation laser fluences, including the imaging methods.

In this chapter, we studied excitonic transport in MoSe<sub>2</sub> monolayer (in Fig. 4.1) by the hyperspatial imaging technique of our micro-PL setup. In our lab, this technique has been used as a powerful method to investigate not

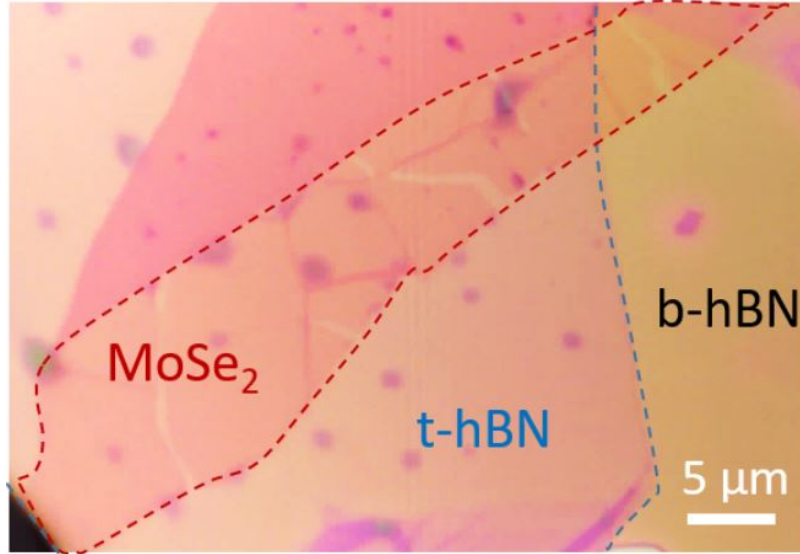


Figure 4.1: An optical image of the hBN encapsulated MoSe<sub>2</sub> monolayer. [149]

only the charge and spin transports of doped GaAs [150, 151] but also TMD monolayers [152, 153]. For the MoSe<sub>2</sub> monolayer, we observed a negligible circular polarization for the trion and exciton peak which will be discussed in the first part of the chapter. Then, we will discuss the spatial imaging part, in which we observed an unusual shape of the spatial PL distribution at high excitation powers. We will discuss the origin of the halo shape PL and propose numerical modeling to describe the halo phenomena. The results are published in 2D Materials (2D Mater. 8 045014, 2021) [149].

## 4.1 Peak identification & polarization-resolved spectra

### 4.1.1 Experimental results

The low-temperature PL spectrum of the hBN encapsulated MoSe<sub>2</sub> monolayer under a 633 nm laser excitation is shown in Fig. 4.2. The black and the red lines correspond to  $\sigma^+$  and  $\sigma^-$  PL detections under the  $\sigma^+$  excitation, respectively. We identified the exciton ( $X^0$ ) emission at 1.647 eV, and a strong emission of a charged exciton (trion, T) is identified at 1.621 eV. Also, a negligible circular polarization is observed for both  $X^0$  and T, where the black and the red curves exhibit almost the same PL intensity.

Fig. 4.3 shows photoluminescence excitation (PLE) scan by decreasing the excitation energy from 1.8102 eV (685 nm) to 1.6456 eV (753.5 nm) with 0.5 nm wavelength step at a fixed excitation power of 5  $\mu$ W. The black and red dots correspond to the integrated PL intensity for the exciton and trion, respectively. The black and red lines (with cross marks) correspond to the degree of circular polarization for the exciton and the trion, respectively. The integrated PL intensity increases when the excitation energy changes close to  $\sim 1.65$  eV (the A-exciton energy) and increases over 1.80 eV (close to the B-exciton energy). The degree of circular polarization for the exciton and trion

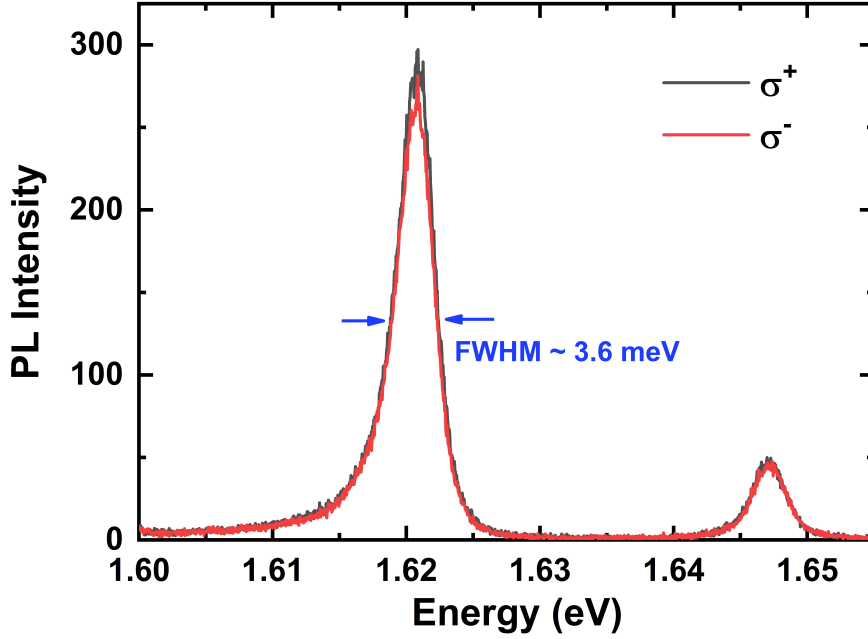


Figure 4.2: PL spectra of the hBN encapsulated MoSe<sub>2</sub> monolayer under  $\sigma^+$  laser excitation at  $T = 20$  K ( $P = 9 \mu\text{W}$ ,  $\lambda_{laser} = 633$  nm).

is observed as  $\sim 2\%$  and  $\sim 5\%$ , respectively. However, the circular polarization of the exciton increases slowly when the excitation energy decreases close to the exciton resonance. The periodic increase of the exciton circular polarization might originate from the artificial effect of the optics, but more investigations are required.

Here, we can point out: 1) The sign of the trion's charge is not clarified yet whether it is negative or positive. 2) A negligible circular polarization of both for the trion and the exciton in contrast to the results from the WS<sub>2</sub> monolayer in Chapter 3. We will focus on the two findings in this subsection.

#### 4.1.2 Identification of the trion type

The trions can be formed into two types: the negatively charged exciton (an exciton with an extra electron) and a positively charged exciton (an exciton with an extra hole). In TMD MLs, the type of trion strongly depends on the type of resident carriers originating from unintentional doping of the sample. In the MoSe<sub>2</sub> monolayer, identifying the charge sign of this trion is less direct when compared to the WS<sub>2</sub> monolayer in chapter 3. In WX<sub>2</sub> (conduction band  $\Delta\text{SOC} > 0$ ), it is clear that the negatively charged trion (an exciton with an electron) displays two distinct emission peaks due to the inter and intra valley trions at low temperature. In contrast, the positively charged trion (an exciton with a hole) exhibits only one PL emission peak.

In MoSe<sub>2</sub> ML, the  $\Delta\text{SOC}$  of the conduction band at K+(K-) points is negative so that both positively and negatively charged trions exhibit a single PL peak. The sign of the charge could be easily verified by applying an electric field

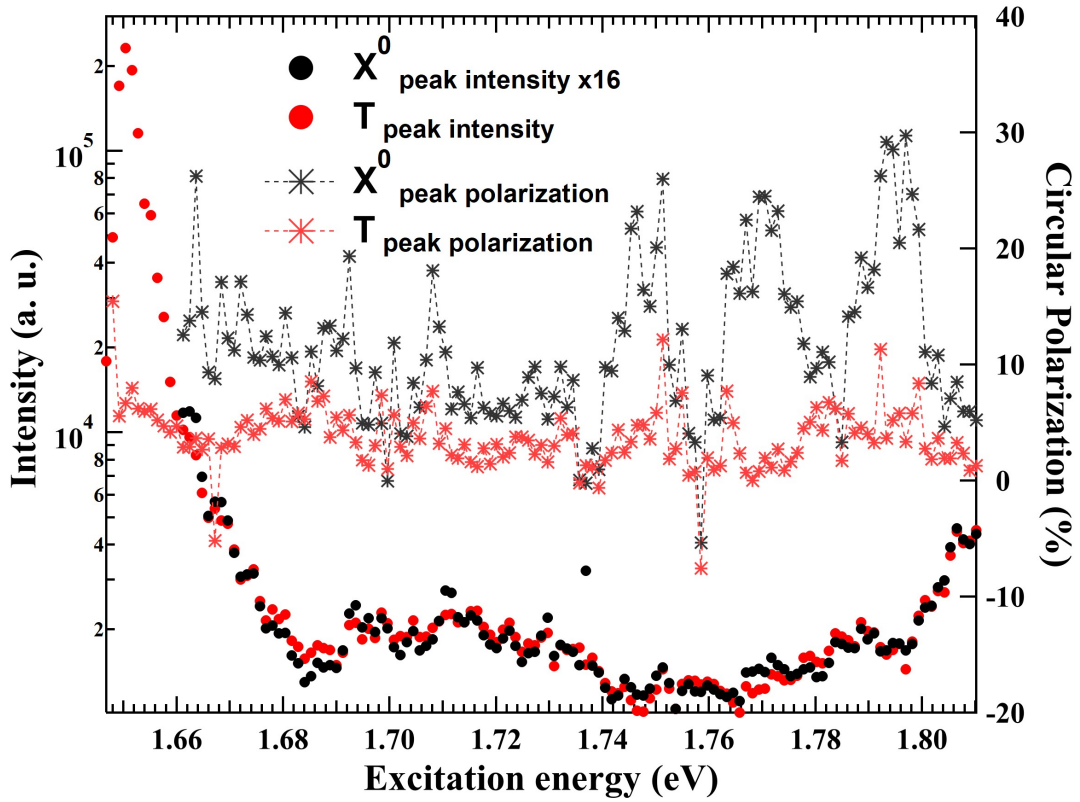


Figure 4.3: Peak intensities (left axis) and circular polarization (right axis) of the exciton (black) and the trion (red) in photoluminescence excitation (PLE) experiments performed at  $T = 20$  K with a laser power  $P_{laser} = 5 \mu\text{W}$ . The laser wavelength increased from 685 nm (1.8102 eV) to 753.5 nm (1.6456 eV) by 0.5 nm step. The emission intensity and circular polarization of the exciton from 1.661 eV to higher excitation were excluded from the graph due to the laser leak of the tunable longpass filter. Unfiltered laser light prevents us from acquiring precise spectra at the exciton emission energy when the laser energy goes close to the exciton resonance. The regular rise and decrease of the exciton circular polarization from 1.74 eV to 1.81 eV might originate from a parasitic issue due to the multiple filters and mirrors.

to the monolayer to obtain p- or n- like doping states of the monolayer electrically, but this is not the case for our encapsulated sample. Moreover, the negatively charged trion and positively charged trion are located at 26.1 eV and 24.3 eV below the exciton peak, respectively [154]. The authors explained that the energy splitting of two trions could vary by the doping density, as shown in Fig. 4.4. The splitting energies of the two trions shift to higher energy in a few meV range when the resident carrier density in  $\text{MoSe}_2$  ML changes up to  $10^{12} \text{ cm}^{-2}$ , but this trion energy shows no strong shift in energy when the resident carrier density is  $< 10^{12} \text{ cm}^{-2}$ .

In our case, the trion emission (Fig. 4.2) appears 26 meV below the exciton emission. Hence we can attribute it to the negatively charged trion, but the resident carrier density needs to be verified to estimate the correct energy splitting of the trions. We can estimate the resident carrier density from the power-dependent experiment in the trion's intensity saturation discussed in 4.2. Our sample's doping level is estimated to be  $\sim 2 \times 10^{10} \text{ cm}^{-2}$ , which is 2 orders of magnitude smaller than the carrier density value in Fig. 4.4. Thus, we believe that our  $\text{MoSe}_2$  monolayer is n-type.

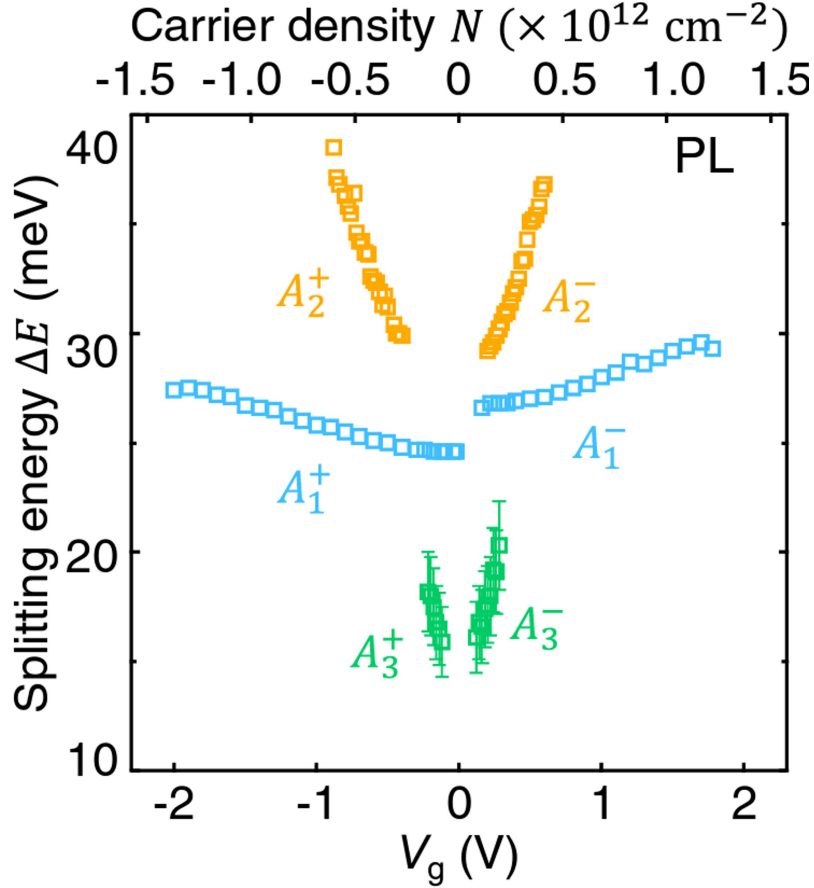


Figure 4.4: Gate-dependent PL splitting energy between  $A_1^\pm$ ,  $A_2^\pm$ ,  $A_3^\pm$  and  $A_{1s}$ ,  $A_{2s}$ ,  $A_{3s}$ , respectively (denoted by cyan, orange, and green squares, respectively). 1s, 2s, and 3s are the Rydberg states. The  $A^+$  and  $A^-$  represent the negatively and positively charged trions, respectively. [154]

Note that unintentional doping is often n-type in TMDs which may happen for several reasons: vacancy or oxidization of the monolayer, irradiation of the laser [155], and contaminations [156].

### 4.1.3 A negligible circular polarization for both trion and exciton

Unlike other TMD monolayers, the  $\text{MoSe}_2$  monolayer exhibits a negligible circular polarization for both the exciton and the trion. The degree of circular polarization in PL can be comprehended in terms of initial carrier formation, valley relaxation, and the lifetime of carriers.

The general process to emit PL from the photoexcitation is the following: 1) Photoexcited hot electrons are created in the  $\text{MoSe}_2$  ML by the circularly polarized excitation light source. The hot electrons relax to form excitons and trions at  $K^+$ ( $K^-$ ) valleys within the ps scale. The initial degree of valley polarization is defined during this process. Note that the exciton formation time in TMDs is estimated to be in the sub-ps range and for trions have a typical characteristic time of  $\sim 2$  ps [157, 158]. Studying ultrafast dynamics below 1ps was difficult due to the resolution limit of the experimental setup [159]. Recently, a high-resolution pump-probe setup made it possible to resolve the

ultrafast formation time of exciton in the sub-ps range in TMDs [160, 161].

2) Photogenerated excitons and trions undergo radiative recombination, nonradiative recombinations, and scattering process that destroy the degree of valley polarization such as the transition from an exciton in  $K^+$  valley to  $K^-$  valley by flipping its pseudospin. Thus, the degree of valley polarization in PL at a steady state is related to the initial formation of valley polarization and the ratio between the lifetime of carriers ( $\tau_{eff}$ ) and the valley polarization lifetime ( $\tau_{valley}$ ). For instance, the initial valley polarization will be completely lost if the valley relaxation rate is much faster than the carrier recombination process.

In steady-state PL, the circular polarization can be expressed by the simple model,

$$P = \frac{P_0}{1 + \frac{\tau_{eff}}{\tau_{valley}}} \quad (4.1)$$

where  $P_0$  is the circular polarization at  $t = 0$  from the initial carrier's formation [162].

The almost zero circular polarization observed in experiments may be due to a fast valley relaxation decay. The fast enough valley relaxation of excitons and trions results in negligible circular polarization for both regardless of their lifetimes. Note that the reported recombination lifetime of the exciton is a few ps, and the trion is  $\sim 100$  ps in  $MoSe_2$  monolayers [163].

We can also point out that the ground state of the B-exciton is located  $\sim 220$  meV above the A-exciton energy in the  $MoSe_2$  monolayer [164]. Note that A-exciton is an exciton transition between the highest valence sub-valley and conduction valley. B-exciton is an exciton transition between the second-highest valence sub-valley and conduction valley. We may excite not only A-exciton in  $K^+$  valleys but also B-exciton in the same valley in Fig. 4.2. Note that we have excited the monolayer with a 633 nm laser, about 300 meV higher than the exciton emission while the energy range of the PLE (Fig. 4.3) can generate only A-excitons.

A similar trend in other reports shows that the degree of circular polarization is only significant when the  $MoSe_2$  monolayer is photoexcited resonantly [162, 165]. Indeed, the circular polarization decreases when increasing the excitation energy of light. The polarization degree reaches almost zero when the excitation energy is higher than 100 meV from the exciton resonance in contrast with  $MoS_2$ ,  $WS_2$ , and  $WSe_2$ .

Few papers have reported this strong valley relaxation of circular polarization in the  $MoSe_2$  monolayer. For example, F. Mahmood et al. [166] have studied the exciton valley relaxation of the  $MoSe_2$  monolayer by time-resolved PL. They reported that the relaxation rate increases at higher pump fluence due to exciton-exciton collisions, but this model fails to explain our observations at low excitation fluence.

A possible argument is that the valley relaxation is enhanced for hot excitons excited by high excess energy in  $MoSe_2$  monolayer due to the Rashba type mixing of the bright and dark exciton (with an energy difference  $\Delta E_{bright-dark} = 1.5$  meV for a zero center-of-mass momentum) [167]. In  $MoSe_2$  monolayers, the conduction band exhibits a negative spin-orbit coupling ( $\Delta E_{SOC} < 0$ ) at the K points. For instance, the split conduction band minimum

and valence band maximum are at the same spin state (spin up,  $+1/2$ ) at  $K^+$  valleys. The lowest conduction band has a lighter effective mass than the upper one meaning that the two conduction subbands cross at the vicinity of the  $K^+$  ( $K^-$ ) valley. This conduction band crossing appears closer to the  $K$  points when spin-orbit splitting in the conduction band is smaller. In other words, the band cross happens for  $\Delta E_{\text{bright-dark}} > 0$ , and it appears close to  $K$  points if  $\Delta E_{\text{bright-dark}}$  is close to zero. Photoexcited hot excitons quickly relax their valley index due to the band crossing when excitons are excited above the crossing point in the conduction band. This fast valley depolarization process can explain our situation of negligible circular polarization in the  $\text{MoSe}_2$  monolayer.

## 4.2 Power dependent excitation: sublinear behavior of PL at high excitation powers

A low temperature ( $T = 19$  K) power-dependent spectra taken under a 570 nm laser excitation are shown in Fig. 4.5a with a log scale for PL intensity. We increased the excitation power from 15 nW to 23 mW. The different spectra are indicated by different colors from purple to red in the legend. At high excitation powers, the peak positions of exciton and trion shift towards low energy. A saturation of PL intensity with a broadening of linewidth is also observed for exciton and trion. First, we plot the integrated PL intensity as a function of excitation power for exciton and trion in Fig. 4.5b. The lines (black, red) correspond to a slope  $R = 1$ , a linear relationship between excitation power and PL intensity. Both trion and exciton show a linear behavior of PL intensity at excitation powers below  $\sim 100 \mu\text{W}$  for trion and  $\sim 3$  mW for exciton. At higher excitation powers, the trion PL intensity increases sublinearly above  $\sim 100 \mu\text{W}$  and saturates from  $\sim 800 \mu\text{W}$ . While for the exciton, the sublinearity appears at excitation powers above 1 mW and no saturation is detected up to 23 mW. Note that we have increased the excitation power from low to high and repeated the PL measurement from high to low excitation power. No significant change in the PL spectra was observed during the cycle, meaning that the laser-induced photodoping effect can be excluded in these experiments. The laser-induced photodoping effect appeared before this experiment (see Fig. A.1 in appendix A).

Fig. 4.6 shows the excitation power dependence of (a) peak position and (b) linewidth for trion and exciton peaks ( $T = 19$  K,  $\lambda_{\text{laser}} = 570\text{nm}$ ). The exciton and trion peaks redshift by 2 meV and 1 meV, respectively, at 23 mW compared with low excitation powers below  $100 \mu\text{W}$ . Also, a broadening of linewidth is presented at high excitation powers. Those two features are typical signatures of the local lattice heating induced by the optical excitation.

In this part, we will discuss mainly two features: 1) One can estimate the unintentional doping density from the sublinear-saturation excitation powers of trions. It is because the trion formation rate is strongly related to the remaining electron density in the system. 2) At high excitation powers, local heating of the laser induces modification of the spectrum. However, the sublinear feature of PL intensity appears at different excitation powers and by different reasons for trions and excitons. For example, the trion saturation originates from the finite numbers of resident

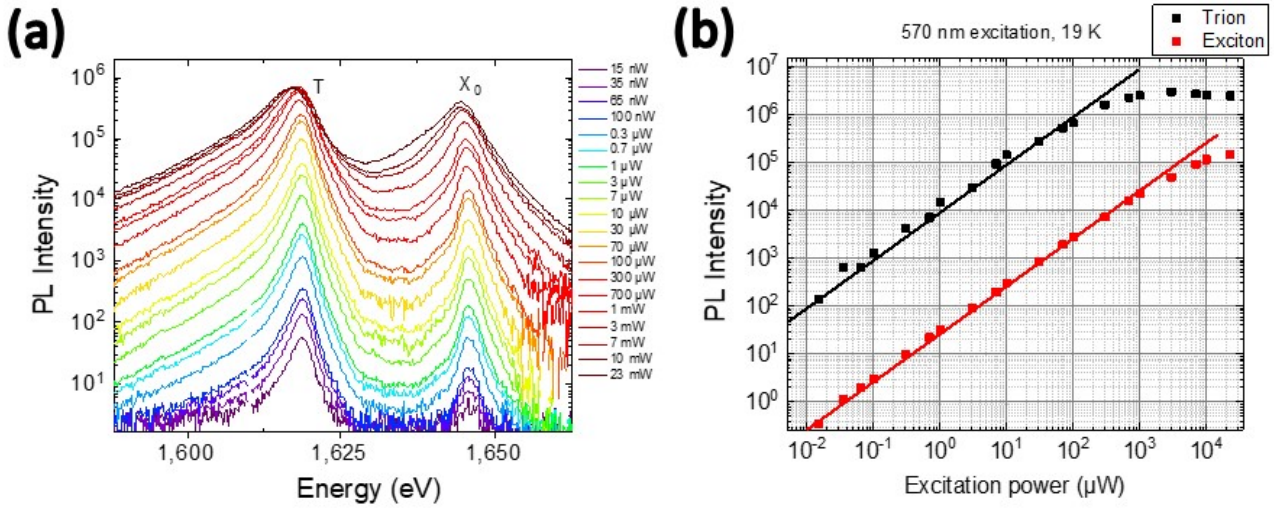


Figure 4.5: (a) Power dependent PL spectra (b) Integrated PL intensity of exciton and trion at  $T = 19\text{ K}$  ( $\lambda_{laser} = 570\text{ nm}$ ). [149]

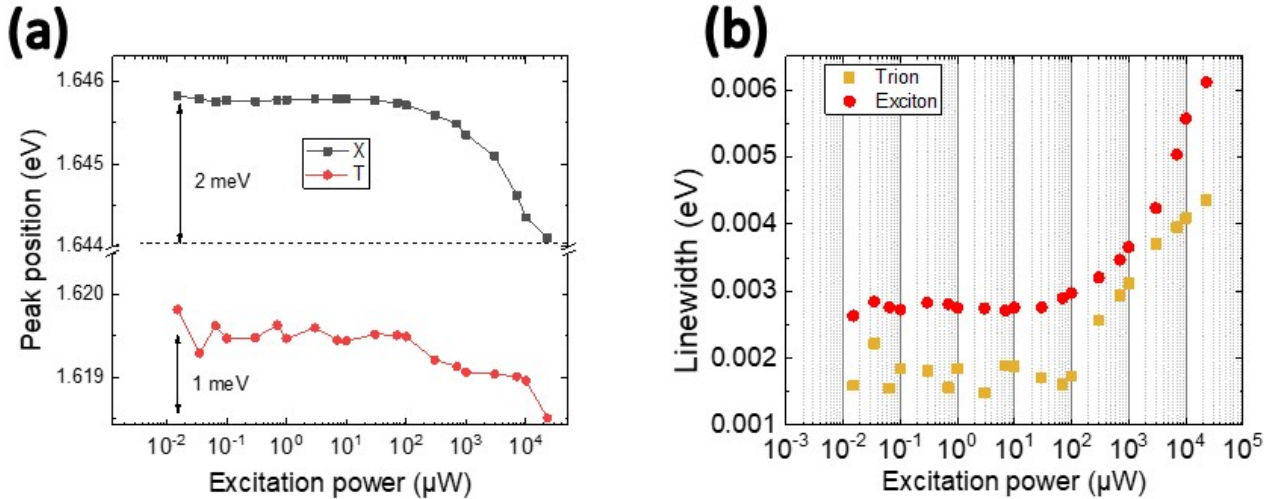


Figure 4.6: Power dependent (a) peak position and (b) linewidth of the hBN encapsulated MoSe<sub>2</sub> monolayer at  $T = 19\text{ K}$  ( $\lambda_{laser} = 570\text{ nm}$ ). [149]

electrons in the MoSe<sub>2</sub> monolayer. For exciton ( $X^0$ ), the Auger-like exciton-exciton annihilation is involved above 1 mW to make the PL intensity sublinear.

#### 4.2.1 The estimation of the doping level

We start from the following arguments to estimate the resident carriers' density,

1. Sublinear behavior for excitons and trions start at different excitation power for different reasons.
2. The sublinear behavior of the exciton will be observed at higher excitation power above 23 mW, probably due to the Auger-like process (exciton-exciton annihilation) [168, 143]. The Auger-like process is visible at a carrier

density of  $\sim 10^{12} \text{ cm}^{-2}$  in hBN encapsulated monolayers [169].

3. The main contribution of trion creation is the binding of photoexcited excitons with resident carriers in the MoSe<sub>2</sub> monolayer, which are present at a finite density.
4. The saturation of trion PL intensity, which starts from  $\sim 100 \mu\text{W}$  and reaches a plateau from  $\sim 800 \mu\text{W}$ , is due to the fact that more excitons than resident carriers are photogenerated.

The resident carrier density can be estimated from the saturation of trion PL intensity. We assume that one photon absorbed generates one electron-hole pair. The 570 nm excitation laser with a power of  $\sim 400 \mu\text{W}$  creates an exciton density equal to the resident carrier density inducing the appearance of the saturation. The number of photons arriving on a unit surface of the sample can be expressed by,

$$P \frac{\lambda}{hc} \times \frac{1}{\pi\sigma^2} = \#_{\text{photon}} \times \text{cm}^{-2} \quad (4.2)$$

Where  $P = 400 \mu\text{W}$  is the excitation power,  $h$  is the Planck constant,  $c$  is the speed of light,  $\lambda = 570 \text{ nm}$  is the wavelength of the excitation laser, and  $\sigma = 0.5 \mu\text{m}$  is the Gaussian excitation spot size measured experimentally from our setup. Finally, we can formulate the average creation density of electron-hole pairs in a unit 2D volume by adapting the absorption coefficient approximately  $A = 0.15 \%$  to Eq. 4.2. The absorption coefficient  $A$  is chosen because: 1) the absorption coefficient at the neutral exciton resonance is about  $5 \%$  [170]. 2) We observed a factor of 25 higher for the PL intensity of trion at the exciton resonance than off-resonance (570 nm) excitation for a given power. Thus, we obtain the generation rate of electron-hole pairs  $G \approx 2.16 \times 10^{20} \text{ cm}^{-2}$  for  $P = 400 \mu\text{W}$  with  $\lambda = 570 \text{ nm}$  excitation. The trion density can be estimated by the following relation,

$$G \approx \frac{\Delta n_{tr}}{\tau_{tr}} \quad (4.3)$$

$$\Delta n_{tr} \approx \Delta n_{resi} \quad (4.4)$$

where  $\tau_{tr} = 140 \text{ ps}$  is the trion lifetime [163] and  $\Delta n_{tr}$  is the trion density, which is equal to the resident carrier density ( $\Delta n_{resi}$ ).

We get the resident carrier density about  $\sim 2 \times 10^{10} \text{ cm}^{-2}$ . As we previously discussed, our MoSe<sub>2</sub> monolayer is expected to be n-type considering the estimated doping level with the trion energy splitting  $\Delta E = 26.1 \text{ meV}$  from the following reference [154].

## 4.2.2 Effective temperature of the trion and exciton

We can estimate the effective temperature of exciton and trion by fitting their spectrum. However, exciton and trion have different mechanisms for PL emission (see Fig. 4.2). Schematics to explain the general mechanism of the

exciton radiative decay are shown in Fig. 4.7a. Excitons radiative decay occur within the light cone by emitting photons only when their center of mass momentum  $p$  is smaller (in magnitude) than a critical value  $p_c$  ( $-p_c < p < p_c$ ). This radiative decay of the occupied population creates the exciton PL emission of Lorentzian distribution. However, more details are required to understand exciton emission for the encapsulated MoSe<sub>2</sub> monolayer. For instance, a high energy tail in the exciton PL emission appears for higher lattice temperature ( $T > 25$  K) for hBN encapsulated MoSe<sub>2</sub> monolayer originated by the fact that the exciton-phonon interaction makes radiative decay possible outside the light cone [171].

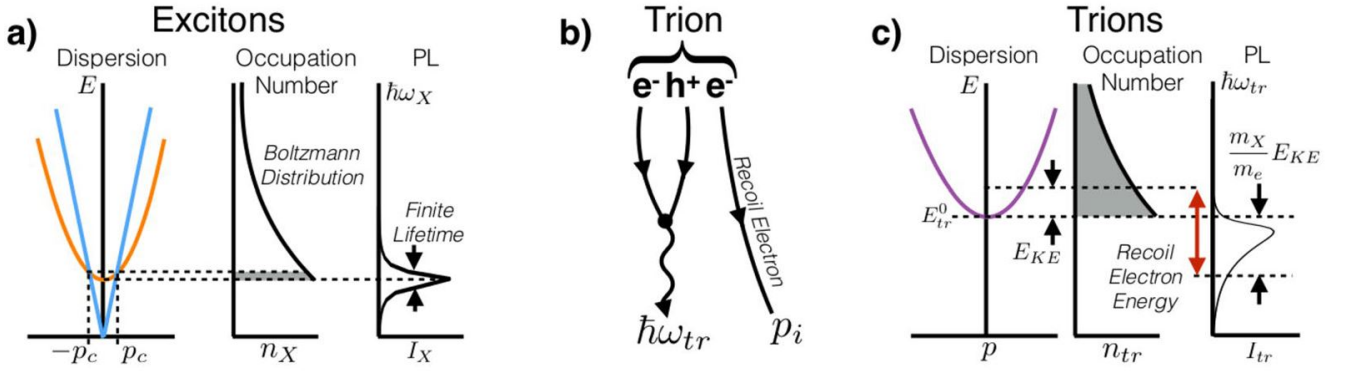


Figure 4.7: (a) The exciton dispersion is shown in orange and photon dispersion in blue with exaggerated momentum,  $\sim \times 200$ , to make the light cone visible. Only excitons within the light cone,  $|p| < p_c$ , can radiative decay. This population is highlighted in the narrow, delta function like region in the occupation number plot, which results in a Lorentzian shaped PL. (b) The Feynman diagram for trion radiative decay. One of the electrons recombines with the hole to emit a photon while the other electron is kicked out to conserve energy and momentum. (c) The trion dispersion is shown in purple with the zero-momentum and kinetic energies of a trion denoted. All trion states can radiatively decay, so all states in the occupation plot are allowed optical transitions. To convert from the occupation distribution to the PL, we must account for the energy of the recoil electron resulting in the long low-energy tail. [172]

In contrast, the process of trion radiative decay is different from that of the exciton, as shown in Fig. 4.7b. When trion decays radiatively, an electron-hole pair of the trion recombines to emit a photon and the remaining electron recoils away with a non-zero momentum. This non-zero contribution of the recoil electron increases as temperature increases resulting in an enhancement of the asymmetric PL emission of trions with a tail spectrum at the low energy side, as shown in Fig. 4.7c. Thus, we can estimate the effective trion temperature by fitting the low-energy trion tail, which holds information about the thermal distribution of trions. The trion PL intensity can be expressed by the convolution of Boltzmann distribution of trion kinetic energies and Lorentzian distribution, taking into account the trion's center-of-mass momentum dependence of the transition energy [172, 173],

$$I(h\nu) \propto e^{-(E_0 - h\nu)/\epsilon} \Theta(E_0 - h\nu) * g(h\nu) \quad (4.5)$$

where  $h$  is the emitted photon's energy,  $E_0$  is the emission energy of a trion with zero center-of-mass momentum,  $g$  is a Lorentzian representing the non-zero linewidth of the transition,  $\Theta$  is the Heaviside function, and  $\epsilon \approx 2k_B T$  where  $k_B$  is Boltzmann's constant. The latter approximation is valid since the trion's radius is of the order of nanometers

and the electron and hole effective masses are comparable.

We can extract the trion temperature from the PL spectrum tail of the low energy side based on the Eq. 4.5. The effective temperature of the trion and exciton gas is shown in Fig. 4.8. Both temperatures significantly increase above 1 mW, starting from 10 K for the trion and 20 K for the exciton. At low excitation powers, the exciton temperature matches with the sample's temperature 20 K. In contrast, the trion temperature ( $\sim 10$  K) shows an offset compared to the lattice temperature. It implies that a systematic error is present in the Eq. 4.5 model, which can be investigated for future work. Note that the spectrum was acquired by the spatially averaging method. The effective temperatures were underestimated because this situation originated from the local effect induced by the tightly focused excitation laser (Gaussian excitation laser spot  $\sigma = 0.5 \mu\text{m}$ ).

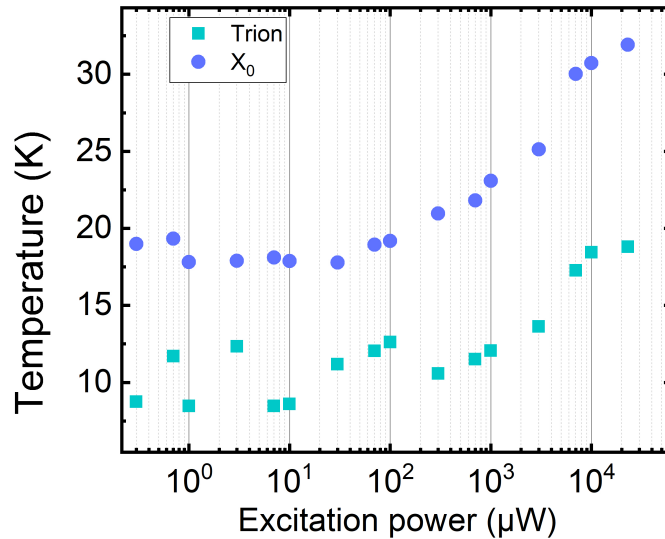


Figure 4.8: The effective temperature of the trion and exciton gas extracted from power-dependent spectra of Fig. 4.5a.

## 4.3 Imaging of the Halo: Laser-induced local heating of trions and excitons

### 4.3.1 Experimental results

We performed spatially resolved PL imaging to study the local heating effect on trion and exciton transport under a tightly focused laser of  $r = 0.5 \mu\text{m}$  Gaussian radius. 2D spatial images of trion and exciton for different excitation powers are shown in Fig. 4.9a. Exciton and trion luminescence are properly filtered by an interferential tunable filter. The Exciton (trion) PL images were obtained using a shortpass (longpass) to correctly suppress the other

peaks. Both exciton and trion present a similar spatial distribution at low excitation powers, while exciton and trion behave differently at high excitation powers. The spatial distribution of trion PL shows a halo shape at high excitation powers (e.g. 10 mW and 22 mW for trion), meaning that the center of the excitation spot ( $r = 0$ ) does not correspond anymore to the maximum PL intensity position. We extracted 1D line profiles of trion and exciton to study details of the power-dependent behavior by averaging multiple linear lines that cross the center of the PL spot (see black lines of the trion image at 22 mW in Fig. 4.9a) since the 2D PL images are not completely symmetrical. Fig. 4.9b shows 1D line profiles of trion and exciton at different excitation powers indicated in the legend. The black dots and lines correspond to the excitation laser profile. PL intensity is normalized to 1 for  $r = 0$  to better identify the halo evolution when varying the excitation power. An intensity raise of the trion profile is observed around  $r = 1 \mu\text{m}$  at 1 mW excitation. This relative increase of trion intensity with respect to the center of the laser spot grows continuously and shifts further away from the center as the excitation power increases. While a slight increase of the exciton profile for  $r = 1 \mu\text{m}$  is observed at the excitation power above 10 mW, the halo shape, which is observed for the trion profile at high excitation power, is not detected for the exciton profiles up to 22 mW.

The PL profiles for excitons (blue) and trions (red) at 1  $\mu\text{W}$  and 22 mW are shown in Fig. 4.10a and b, respectively. The black squared lines represent the laser profile, where it can be seen that the exciton and trion luminescence comes from a spatial region which extends significantly beyond the excitation spot. As shown in Fig. 4.10b, the purple dashed lines correspond to the profiles at 1  $\mu\text{W}$  excitation. The green dots represent the temperature profile of the trion taken out from the spectra at different positions in the 1st order imaging method. Note that the exciton and trion exhibit almost the same profiles at 1  $\mu\text{W}$  excitation in a linear scale plot. The normalized PL intensity is a logarithmic scale in Fig. 4.10a while it is a linear scale in Fig. 4.10b.

At 1  $\mu\text{W}$  excitation, similar effective diffusion lengths of  $1.49 \pm 0.05 \mu\text{m}$  and  $1.27 \pm 0.05 \mu\text{m}$  were obtained for  $X^0$  and T, respectively. The effective diffusion length ( $L$ ) is acquired from the PL fit with the analytical solution of the following 2D steady-state diffusion equation [152]:

$$n(r) \propto \int_{-\infty}^{\infty} K_0(r/L_X) e^{-(r-r')^2/w^2} dr' \quad (4.6)$$

Where  $K_0$  is the modified Bessel function of the second kind and  $L = \sqrt{D\tau}$ ,  $D$  and  $\tau$  are lifetime and diffusion coefficient (of excitons or trions). At 22 mW excitation, the trion profile exhibits the halo behavior and the exciton profile is also broadened as compared with the profile at 1  $\mu\text{W}$  (purple dashed lines). The trion temperature profile (green) behaves similar to the exciton and the trion profiles at 1  $\mu\text{W}$ .

### 4.3.2 A role of the hot exciton formation in the exciton and trion profiles

At 1 mW, we obtained the effective diffusion lengths of  $1.49 \pm 0.05 \mu\text{m}$  and  $1.27 \pm 0.05 \mu\text{m}$  for the  $X^0$  and T, presenting about  $\sim 15\%$  difference. This result is already surprising given that the lifetime of both species differs by

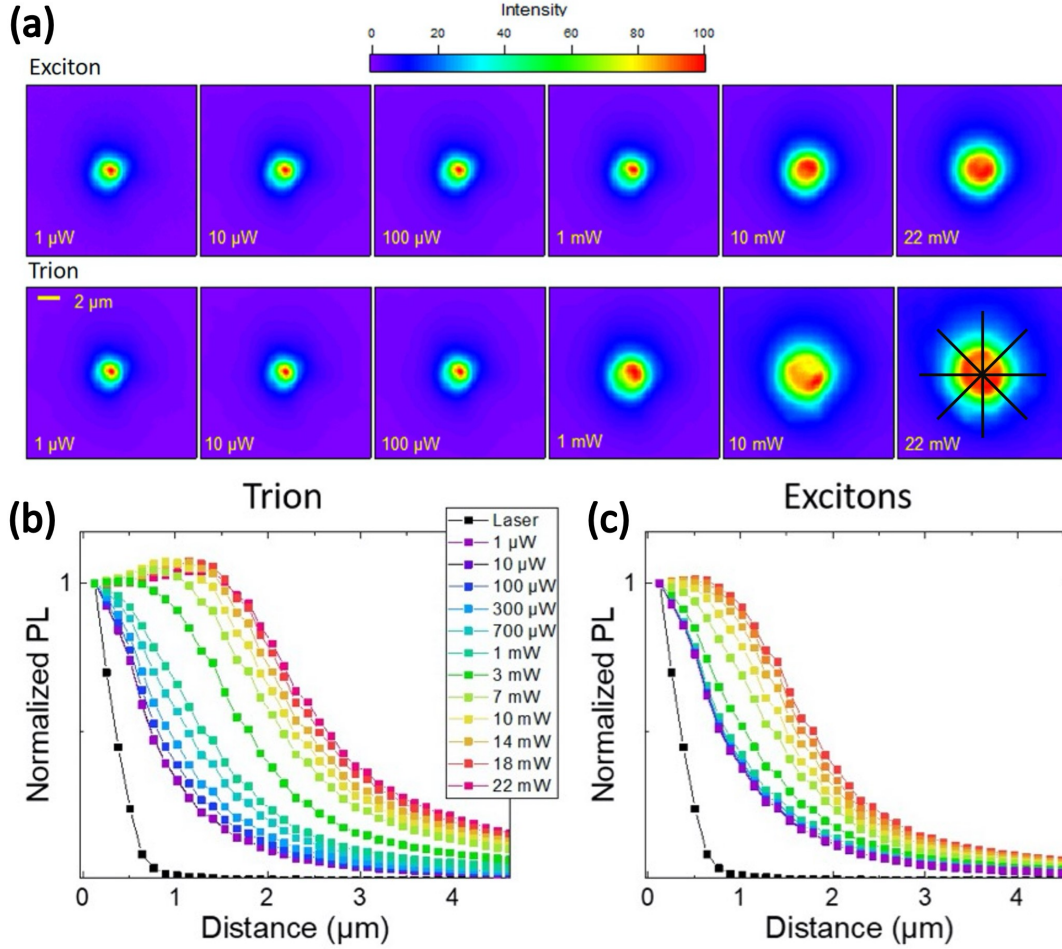


Figure 4.9: (a) PL's spatial distribution of excitons and trions for selected excitation powers. The images have a lateral size of 14  $\mu\text{m}$ . Measured PL's radial profile for trions (b) and excitons (c) for selected excitation powers. PL intensity is normalized by 1 at  $r = 0$  where is the center of the excitation spot. Black is the laser profile and each color corresponds to the written excitation powers in the legend. [149]

more than one order of magnitude considering  $L = \sqrt{D\tau}$  relation. We interpret these low-excitation profiles as the result of the diffusion of hot excitons.

Here, we consider the following process in the presence of the spatial profiles at low excitation powers since no external electric field is present in the  $\text{MoSe}_2$  monolayer: 1) The laser irradiation photo-generates e-h pairs in higher energy than the ground state of the A-exciton. 2) The photogenerated e-h pairs, so-called hot excitons, relax into bright excitons and trions in their characteristic times. The hot excitons can diffuse during this process [174]. 3) The excitons and trions diffuse until recombination takes place through PL emission.

We put a parameter of the excitation laser profile to fit the analytical solution of the 2D steady-state diffusion equation (Eq. 4.6). In the assumption of the solution, we attributed the formation of both excitonic species to the laser profile. The laser irradiation creates the excitons and trions exactly at the place. However, the diffusion of hot excitons is involved in making our assumption complicated, combined with their comparable relaxation times and short diffusion lengths. The relaxation of hot excitons into bright excitons and trions is reported on a timescale of the

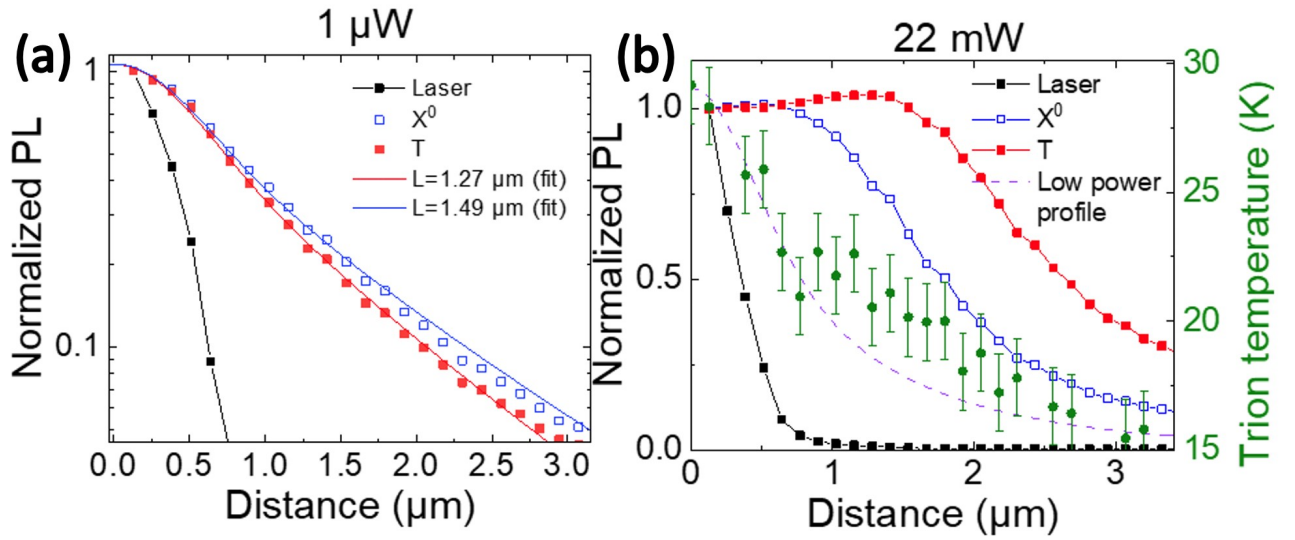


Figure 4.10: (a) Normalized radial profile for excitons and trions at low excitation power in a logarithmic scale. Also shown is the laser profile and fits of the 2D diffusion equation. (b) Radial profiles at the highest excitation power, normalized to one at the center in a linear scale. Also shown is the trion temperature was extracted from the 1st order image which is the method described in chapter 2. [149]

order of 18 ps [163] which is a comparable number with the exciton ( $< 5$  ps) and trion ( $\sim 140$  ps) relaxation time in MoSe<sub>2</sub> monolayers.

If the subsequent diffusion of excitons and trions is slow enough, then we would indeed expect to see the same profile for both species. Note that momentum-indirect dark excitons can also constitute a reservoir of excitons at the steady-state and possibly contribute to the low excitation profile [175]. Therefore, the spatial profiles of the exciton and trions could be more influenced by the diffusion of hot excitons than the subsequent diffusion of bright excitons and trions.

Note that the exciton diffusion lengths in TMD MLs were reported within 1 μm and the experiments mainly were done at room temperature [176]. Also, the exciton lifetime in TMD MLs is expected to be smaller at low temperature ( $\sim$  ps) than at room temperature ( $\sim$  ns) [177].

### 4.3.3 The origin of the halo at high excitation powers

The PL profiles of excitons and trions are deformed at high excitation powers. The formation of a hollow at the center of the profile is pronounced for the trions. This halo behavior for trions starts to appear at around 1 mW. This behavior correlates with the saturation of the PL intensity of trions, as we discussed in 4.2 previously.

Also, A spatial gradient of the temperature profile was observed for the trions (from 30 K at the center to 15 K at 3 μm in Fig. 4.10b). This temperature profile of the trion follows the profiles (excitons and trions) at low excitation powers, which can be understood as a consequence of the phonon emission of the hot exciton relaxation. A high

density of hot carriers creation induces an increase in the number of hot phonon emissions and the dense hot phonon emission results in an increase of the trion and exciton temperatures. Moreover, a strong temperature gradient may induce a thermal drift that could contribute to the halo formation.

This halo type spatial distribution of excitonic emission in TMD monolayers was previously observed on WS<sub>2</sub> monolayers, but under different experimental conditions such as pulsed laser excitation and at T = 300 K [178, 179]. The authors proposed a model to explain their halo based on Auger recombination and the creation of a temperature gradient by hot phonon emission. In their study, auger-like processes were considered as the main source of this phenomenon due to their excitation and sample condition. In time-resolved PL, the pulsed laser excites the system with a high photon density (10<sup>12</sup> cm<sup>-2</sup>) which donates an efficient condition for Auger like scattering. Moreover, the WS<sub>2</sub> monolayer of the experiment in ref [178, 179] was deposited on a SiO<sub>2</sub>/Si substrate while our results were obtained on a hBN encapsulated monolayer. The Auger like process can be effectively suppressed by hBN encapsulation [180]. Indeed, if the temperature gradient was created by Auger-like non radiative recombination, we would expect the steady-state spatial dependence of the temperature to be non-monotonic and to exhibit a halo as well.

#### 4.3.4 Seebeck drift: Modeling for the halo based on the thermal gradient

Therefore, we built a model to interpret our halo based on the fact that the temperature gradient plays a major role and the Auger-like process is relatively irrelevant to our case. Note that all the details of the calculation can be found in our publication Ref. [149]. Also, we made assumptions to simplify our model to describe the halo effect. Consequently, there are arising open questions that can be considered in the future as a further investigation.

We applied the Seebeck effect in the 2D steady-state drift-diffusion equation. Here, the Seebeck coefficient S of our model is a universal constant independent of doping and temperature.

In general, the idea of Seebeck effect is based on the fact that carriers at higher temperatures have higher average kinetic energy than carriers at low temperatures. The carriers in the higher temperature part drift/diffuse by the gradient into the lower temperature side to be in equilibrium condition. This phenomenon creates the current flow.

We started from Boltzmann's equation for a condition electron gas by a thermal distribution. We defined the Seebeck coefficient to describe the thermal drift of trions and excitons by limiting the situations for a classical gas. Then, we obtain the Seebeck coefficient [149],

$$S = \left(\frac{d}{2} + r + 1\right) \frac{k_B}{e} \quad (4.7)$$

Where d is the dimension, k<sub>B</sub> is the Boltzmann constant, and e is the charge of an electron. Here, we supposed that the momentum relaxation time  $\tau$  depends on the kinetic energy  $\epsilon$  as  $\tau(\epsilon) \propto (\epsilon - E_c)^r$  in the classical limit. The

Parameter	Trion	Exciton	Ref
Mobility, $\mu$ (cm <sup>2</sup> /Vs)	100	150	
Seebeck coefficient, $S$ ( $\mu$ V/K)	300	400	
Lifetime, $\tau$ (ps)	140	5	[163]

Table 4.1: Parameters for the numerical calculation of trions and excitons profiles.

Seebeck coefficient for trions and excitons can differ from each other. We start from the recombination rate  $R$  based on the drift-diffusion of charged particles in semiconductors [149]:

$$R = R_{spont} + R_{SRH} + R_{Auger} \quad (4.8)$$

Where  $R_{spont}$  is spontaneous radiative recombination across the bandgap,  $R_{SRH}$  is Shockley-Read-Hall (SRH) recombination, and  $R_{Auger}$  is the Auger process. We assume that the transport of trions and excitons is unipolar to impose this to trions and excitons. It is because they diffuse/drift independently from other excitonic quasi-particles. We also suppose that there is no coupling between the trion and exciton populations, which is in agreement with previous time-resolved measurements where totally independent dynamics has been observed for both complexes.

The Seebeck effect can be added into the current density term considering that the hole current density induced by the Seebeck effect is zero or negligibly small. Finally, we obtained the following 2D steady-state drift-diffusion equation:

$$G - \frac{n}{\tau} - \gamma n^2 = \vec{\nabla} \cdot (-D \vec{\nabla} n - \sigma S \vec{\nabla} T) \quad (4.9)$$

Where  $n$  is the concentration of either  $X^0$  and T,  $G$  is the generation rate, here representing the spatial distribution of hot carriers (low excitation profiles in Fig. 4.10a),  $\tau$  is the lifetime,  $\gamma$  is the Auger coefficient,  $D = (k_B T/q)\mu$  with  $\mu$  the mobility,  $q$  the elementary charge, and  $\sigma = q\mu n$  is the conductivity. We demonstrated the halo by solving the Eq. 4.9 numerically.

Fig. 4.11 shows numerically calculated 1D profiles of Eq. 4.9 for trions and excitons under various excitation powers from 1  $\mu$ W to 22 mW, which is the same steps of excitation powers with the experiment (in Fig. 4.9b-c). The legend indicates the excitation powers for each color curve. The black curves correspond to the laser profile for the Gaussian excitation spot  $\sigma = 0.5 \mu$ m. The parameters, which were used for the calculations, are shown in Table. 4.1. The exciton lifetime is estimated to be  $\tau = 5$  ps, considering an intrinsic radiative lifetime (in vacuum) of 2.7 ps and cavity effects. The mobility of trions ( $\mu_{tr} = 100$  cm<sup>2</sup>/Vs) was selected based on our first assumption: The diffusion is slow enough so that the hot electron diffusion dominates the spatial distribution of PL. Also, the mobility of excitons ( $\mu_{ex} = 150$  cm<sup>2</sup>/Vs) was chosen by the effective mass difference from the trion. We clearly reproduced the halo for trions and slow changes for excitons, which were experimentally observed. Moreover, the halo of trions at high excitation powers can be explained without the need of considering Auger processes.

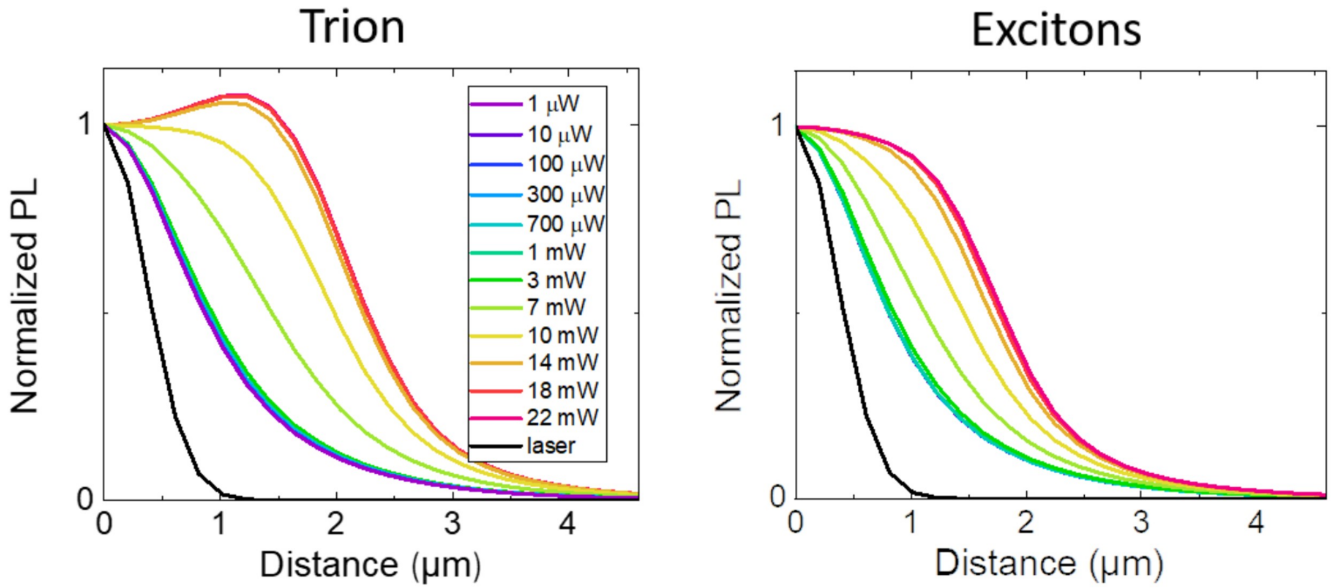


Figure 4.11: Calculated profiles of trion and exciton obtained with a numerical solution of Eq.4.9 [149]

However, further investigation must be followed to discuss more details of the Seebeck coefficient because we made a few assumptions to simplify the model. For instance, the trion temperature taken from the tail fit requires more details to justify the accuracy. We inferred the unknown mobility  $\mu$  based on our experimental observation.

### 4.3.5 Exciton ( $X^0$ ) resonant excitation

We have performed the hyperspectral 1st order diffraction imaging at the exciton ( $X^0$ ) resonance excitation with  $\sim 5\%$  absorption estimated by considering optical cavity effects in the heterostructure. As shown in Fig. 4.12a, the trion 1<sup>st</sup> order diffraction image at 20 mW excitation exhibits a much more pronounced crater at the center than the off-resonance excitation. The maximum intensity spatial distribution expanded to  $\sim 2.5 \mu\text{m}$  (at resonance in Fig. 4.12b) from  $\sim 1.2 \mu\text{m}$  (at off-resonance in Fig. 4.10b) at 22 mW. We can also extract a spatial profile of the trion temperature, as shown in Fig. 4.12c. The temperature gradient increases as the excitation power increase up to 10 mW. However, as shown in the inset of Fig. 4.12b, the temperature gradient undergoes saturation above 10 mW excitation. It even decreases at 20 mW excitation. This temperature saturation of a hot exciton gas at high densities has been previously reported in encapsulated  $\text{WSe}_2$  MLs and attributed to the balancing between Auger heating and phonon cooling [174]. The trion temperature at the center of the excitation spot exhibits 45 K at 10 mW excitation with  $\sim 17$  K at a distance of  $3 \mu\text{m}$ . This temperature difference  $\Delta T_{\text{center}-3\mu\text{m}} \sim 28$  K is about 3 times higher than the maximum  $\Delta T_{\text{center}-3\mu\text{m}}$  from the off-resonance excitation at 22 mW, which are  $T_{\text{center}}^{\text{trion}} = 25$  K and  $T_{3\mu\text{m}}^{\text{trion}} = 15$  K.

Here, we assume that the resonant excitation does not create hot excitons since the optical pumping energy corresponds to the ground state of “bright” exciton transition energy. However, the halo behavior is enhanced under the exciton resonant excitation. It can be explained by the fact that resonant exciton-exciton Auger scattering involves

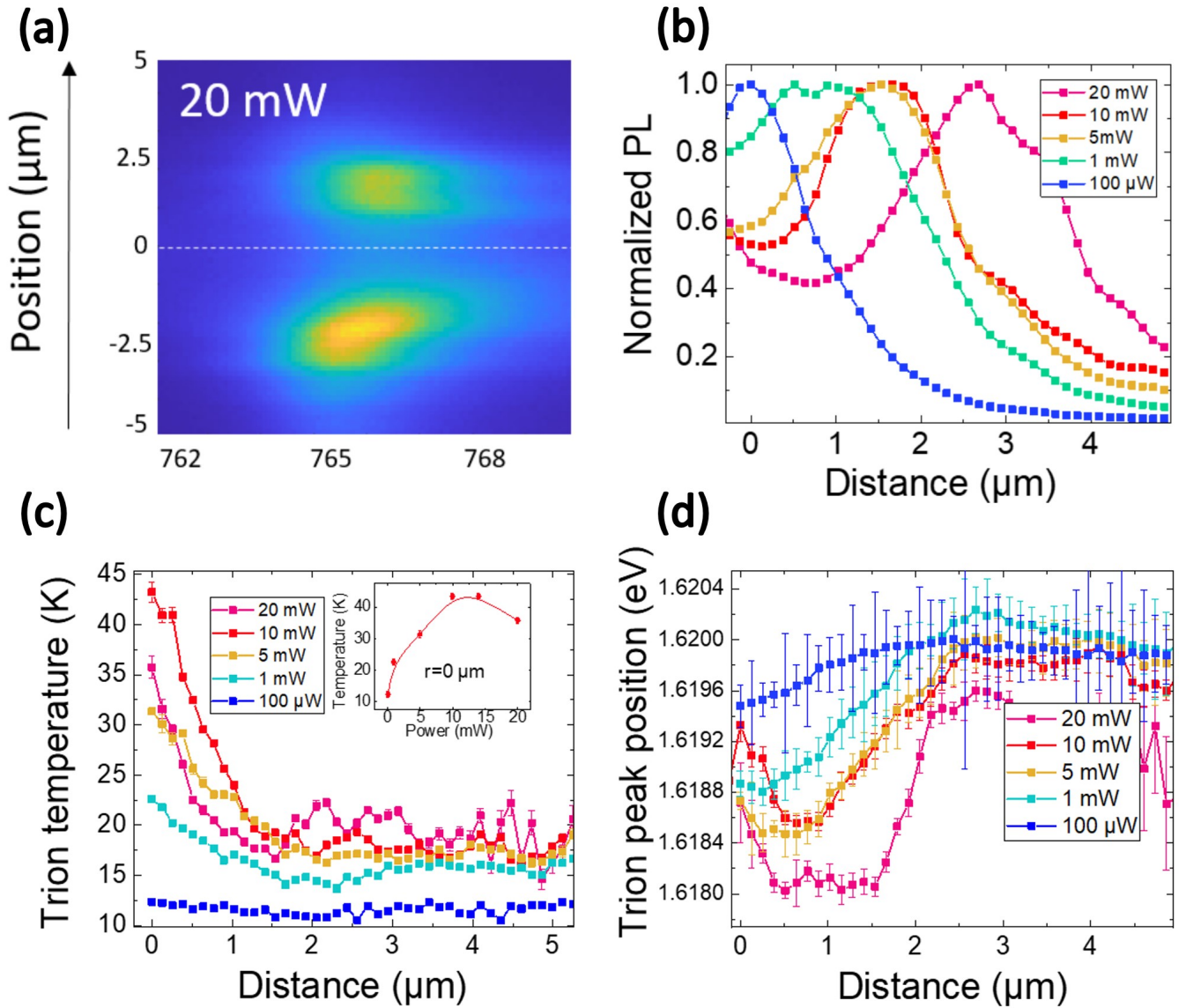


Figure 4.12: (a) Spatial dependence of the trion's luminescence spectrum at 20 mW when exciting resonantly the neutral exciton (b) Normalized trion profiles obtained from the figures in (a) by integrating the trion's spectrum at different distances from the excitation spot. (c) Trion's temperature as a function of position. The inset shows the measured temperature at the excitation spot, the continuous curve is a guide to the eye. (d) Trion's peak energy as a function of position. [149].

an excited conduction band, which was recently proposed to explain the very efficient PL upconversion observed in  $\text{MoTe}_2$  and  $\text{MoSe}_2$  MLs under resonant excitation of the neutral exciton [181].

Fig. 4.12d shows trion peak positions as a function of distance from the excitation spot. The trion peak position exhibits redshift where the temperature gradient exists as increasing the excitation powers. It may result in a lower absorption coefficient, counterbalancing the effect of a higher excitation on the photocreated density. At high excitation powers, where the temperature saturation happens (in Fig. 4.12c), blueshift-redshift crossover appears near the center, exhibiting a similar shape with the laser profile for the Gaussian excitation spot  $\sigma = 0.5 \mu\text{m}$ .

Note that such a crossover of the exciton absorption energy on ML  $\text{WS}_2$  at 300 K has been reported and

attributed to the onset of a repulsive exciton-exciton interaction at the Mott density  $2 \times 10^{12} \text{ cm}^{-2}$  [182]. Here, the crossover can be equally attributed to a repulsive interaction between hot excitons, which, near the center, are then converted into trions by binding to an extra charge carrier.

## 4.4 Conclusions

In conclusion, we have investigated the behavior of trions and excitons in the MoSe<sub>2</sub> monolayer at cryogenic temperatures as a function of excitation power from their spectrum and imaging of the spatial distribution of trions and excitons. Also, we focused on the characteristic observations at high excitation powers.

First, we have observed the negligible valley polarization of trions and excitons. The degree of valley polarization remained near zero for trions and excitons in the overall PLE experiment except that the exciton circular polarization increased slightly near the resonance. This negligible degree of circular polarization behavior is different from other TMD monolayers (e.g., WS<sub>2</sub> in chapter 3 and MoS<sub>2</sub> in chapter 5). We have discussed that it can be understood by a fast valley depolarization process due to the conduction subband crossing by the small and positive energy difference of  $\Delta E_{\text{bright-dark}}$ .

Second, we have estimated the unintentional doping density of the MoSe<sub>2</sub> monolayer based on the following idea: The main contribution of the trion formation comes from the resident carrier density, which is finite. One can estimate the resident carrier density from the optical pumping density of electron-hole pairs by the excitation laser. Also, the unintentional doping type can be verified from the binding energy of trions. Thus, we find the resident carrier density of  $\sim 2 \times 10^{10} \text{ cm}^{-2}$ . We identified that the MoSe<sub>2</sub> monolayer is n-type from the trion binding energy of 26 meV, which corresponds to the binding energy of negatively charged trion ( $\sim 26.1 \text{ meV}$ ) at a doping level of  $\sim 2 \times 10^{10} \text{ cm}^{-2}$ .

Third, we have observed a halo shape of spatial PL distribution. It was especially dramatic for the trion. This halo spatial distribution was observed under pulsed laser at room temperature in WS<sub>2</sub> monolayers. However, for our experiment, we obtained a well-separated trion and exciton spectrum at cryogenic temperature in the hBN encapsulated MoSe<sub>2</sub> monolayer. This configuration allowed us to perform 2D/hyperspectral imaging for trions and excitons separately. To do so, we confirmed that the excitons and trions behave differently in the halo formation. We could exclude a contribution of the Auger-like process in the trion's halo. We also confirmed from hyperspectral imaging that a strong temperature gradient appears for trions at high excitation powers. The photoexcited trions are pushed away from the excitation center, which leads to the appearance of a halo.

The following description can explain the appearance of a halo for trions: 1) The laser excitation creates electron-hole pairs with much higher energy than the gap, generating hot excitons out of the light cone. 2) these hot excitons diffuse out of the excitation spot with a characteristic distance while relaxing into trions and excitons. 3) The hot excitons emit phonons during the process of (2). This hot phonon emission process generates a thermal gradient.

4) At high excitation powers, the process of (3) is strengthened so that a strong thermal gradient generates the Seebeck drift, which dominates over diffusion. In contrast, the halo feature for the exciton is much less pronounced, which is a consistent result based on the fact that the exciton lifetime is much shorter than the trion's one.

We built a model to interpret the halo formation by including the Seebeck drift by a thermal gradient into a 2D steady-state drift-diffusion equation. We successfully reproduced the halo for trions by solving the equation numerically.

Finally, in the exciton ( $X^0$ ) resonance excitation, we have revealed that the halo feature can be enhanced even though we generated the electron-hole pairs with resonant energy. We expect that resonant exciton-exciton interactions create hot excitons, thus mimicking the effect of an off-resonance excitation.

So far, we have used the hBN encapsulated MoSe<sub>2</sub> monolayer, which is an unintentionally n-doped sample. We have discussed optical responses of excitonic complexes based on the observations at high excitation fluences. However, there is plenty of space to improve this study for further detailed investigation since complex phenomena get involved in making our investigation difficult at the high-density regime.

Nevertheless, we firmly believe this work is a step towards a more detailed understanding of the different physical phenomena that can govern excitonic transport at high excitation fluences.

## Chapter 5

# Visualizing positively & negatively charged excitonic species and the dynamical valley polarization of resident carriers in MoS<sub>2</sub> monolayers

In the previous two chapters, we have investigated the spin/valley polarization and exciton physics from low to high excitation regimes for WS<sub>2</sub> and MoSe<sub>2</sub> monolayers. Since both samples are unintentionally doped n-type, we could see mainly negatively charged exciton species, but we could not observe positively charged ones. This motivated us to build devices where the application of gate voltages can be used to tune the resident carrier density.

By fabricating a charge tunable device with TMD MLs we can change the doping level of the sample to obtain n-, p-, and neutral regimes. Excitonic complexes for both negatively/positively charged exciton species in one sample can be visualized.

In this chapter, we present the fabrication of a charge tunable device composed by a MoS<sub>2</sub> monolayer with hBN encapsulation and graphite contacts. We selected MoS<sub>2</sub> because it has been much less studied than WSe<sub>2</sub> and MoSe<sub>2</sub> by optically pumped PL experiments, even though the first PL observation in TMD monolayers was demonstrated in MoS<sub>2</sub> [34]. The main reason is that unencapsulated MoS<sub>2</sub> monolayers suffer significant inhomogeneous broadening and strong photoinduced irreversible changes in the PL emission after laser exposure [183, 184]. As a result, the PL spectrum of MoS<sub>2</sub> at low temperatures was systematically dominated by negatively charged excitons. The electrostatic doping in the hole regime was never achieved. Only very recently, electrostatic p-doping was achieved in MoS<sub>2</sub> monolayers encapsulated with h-BN [185]. For that reason, we fabricated the charge tunable

device with hBN encapsulated MoSe<sub>2</sub> of high optical quality in order to achieve the p-type regime and investigate the valley polarization and coherence.

We performed PLE and power-dependent PL experiments with polarized light to investigate excitonic complexes in different doping regimes. We also imaged the spatial distribution of PL by applying an in-plane electric field, but we did not see noticeable changes in PL images.

We will now discuss our device characteristics and excitonic species in n-, p-, and neutral regimes together with their valley polarization. In the last part, we show that the resident carrier valley polarization can be tuned in MoS<sub>2</sub> monolayers and is detected through changes in the trion intensity in both n and p-type regimes. Note that the results are published in Communications Physics (5, article number: 73, 2022) [106].

## 5.1 Fabrication and characterization of the MoS<sub>2</sub> charge tunable device

The gated MoS<sub>2</sub> monolayer device we fabricated is presented in Fig. 5.1. A schematic side view and an optical microscope image of the device are shown in Fig. 5.1a and b, respectively. The device was fabricated by mechanical exfoliation in the center of a SiO<sub>2</sub> (90 nm)/Si substrate, where 100 nm (Au)/5 nm (Ti) lines were pre-patterned. All fabrication procedures were performed inside a glove box where O<sub>2</sub> and H<sub>2</sub>O levels were kept below 1 ppm. The sample was annealed in a vacuum chamber at 220-230 °C for 30 min after the transfer of each layer. The temperature was increased at a rate of 10 °C/min and cooled down naturally after turning off the heater while keeping the pressure at 10<sup>-7</sup> Torr. Graphite was used to provide electrical contact between gold and the MoS<sub>2</sub> monolayer. The back gate graphite ensures a uniform electric field for the monolayer through the bottom hBN.

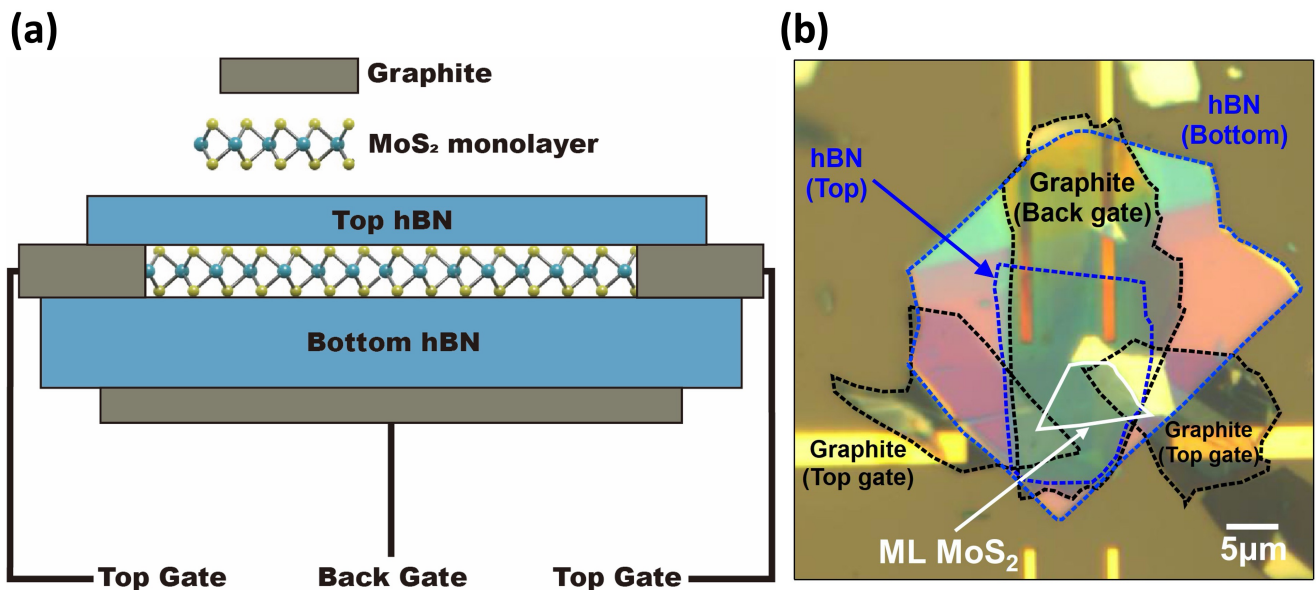


Figure 5.1: The MoS<sub>2</sub> charge tunable device. (a) schematic side view (the SiO<sub>2</sub>/Si substrate is not indicated here). (b) an optical microscope image [106].

Since the device has two separated electrodes for the top gate contact, we can apply the gate voltages in two different configurations: 1) We apply a voltage between the top ( $V_{top}$ ) and back ( $V_{back}$ ) gates while keeping the same potential for the two top gates. In this way, we can vary doping of the MoS<sub>2</sub> monolayer by applying a gate bias  $V_g$ , where  $V_g = V_{top} - V_{back}$ . For  $V_g = 0$ , we will see negatively/positively charged excitonic emissions in the PL spectrum depending on the unintentional doping. We can obtain an intrinsic regime by tuning the voltage to  $V_g = V_{neutral}$  to cancel out the resident charge. For  $V_g > V_{neutral}$ , we accumulate a positive charge in the monolayer so that we can observe positively charged excitonic emissions in the PL spectrum from the electrically p-doped monolayer. For  $V_g < V_{neutral}$ , we accumulate a negative charge in the monolayer, negatively charged exciton species appear. 2) An in-plane electric field can be applied by applying a potential difference between the two top electrodes. This second configuration of the two top electrodes was tried expecting to observe the drift of charged excitons with the in-plane electric field.

We performed a pre-experiment to check the optical quality of the sample before going to the main experiment at cryogenic temperature. A room temperature spatial PL map (at  $V_g = 0$ ) was performed under 473 nm laser excitation at 10  $\mu$ W with a scanning step size of 0.1  $\mu$ m (the Gaussian laser spot size was  $\sigma = 0.1 \mu$ m). Fig. 5.2a shows PL spectra of the MoS<sub>2</sub> ML at two different positions where the trion intensity is strong (the red curves) or weak (the green curves). The circles (red and green) and the lines indicate the experimental data and their fits, respectively. The fit was done with two Voigt functions which are indicated as the dashed lines. Each spectrum was taken out from positions **A** and **B**, which are indicated on the map in Fig. 5.2d. The room temperature spectrum of the MoS<sub>2</sub> monolayer shows a mixture of the exciton and trion emissions. The trion contribution of the spectrum strongly depends on the unintentional doping level which is therefore not spatially homogeneous.

Fig. 5.2b shows the peak energy map in which the white-lined area indicates where the MoS<sub>2</sub> monolayer and graphite/MoS<sub>2</sub> contacted regions are located. The histogram of the peak energy taken out from the MoS<sub>2</sub> ML region without graphite/MoS<sub>2</sub> area is shown in Fig. 5.2c. The average peak energy is 1.8776 eV with a standard deviation of  $\sigma = 4.10$  meV. Fig. 5.2d and 5.2e show FWHM map and histogram, respectively. The histogram counted values in the monolayer region except the graphite/MoS<sub>2</sub> area. The average FWHM energy is 51.3 meV with a standard deviation of  $\sigma = 4.23$  meV. The red points in Fig. 5.2d correspond to the region where the unintentional doping rate is high. Note that we extracted FWHM of the spectrum from the map without the deconvolution process, meaning that the trion contribution has a dominant role in the FWHM broadening ( $> \sim 58$  meV).

The following low-temperature experiments were performed near position **B** (in Fig. 5.2d) because this region in the MoS<sub>2</sub> monolayer shows a strong exciton emission and a relatively homogeneous environment with a lower doping rate.

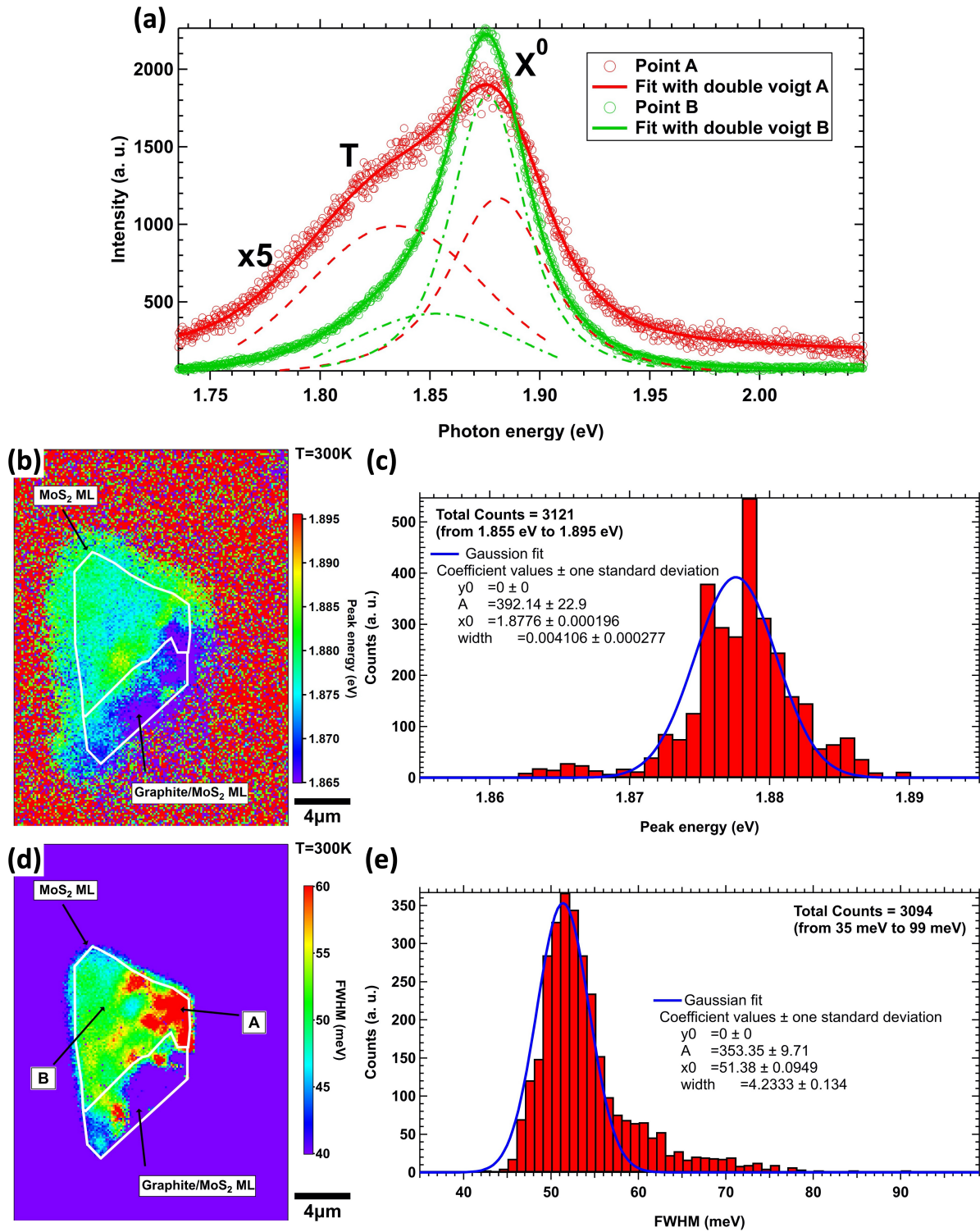


Figure 5.2: PL spectra of the MoS<sub>2</sub> device under a 473 nm (10  $\mu\text{W}$ ) laser excitation at  $T = 300\text{K}$ . (a) PL spectra were taken from points A and B in Fig. 2d. The fitting was done by two Voigt functions. (b) A spatial map and (c) An histogram of the neutral exciton ( $X^0$ ) emission energy. (d) A spatial map and (e) An histogram of the FWHM of the experimental spectrum. The white lines in panels (b) and (d) indicate the MoS<sub>2</sub> monolayer with and without graphite contact on the monolayer.

## 5.2 Observing excitonic Rydberg states

Experimental photoluminescence excitation (PLE) results are shown in Fig. 5.3. Here, we fixed the laser power at  $100 \mu\text{W}$  and measured spectra at  $T = 20 \text{ K}$  by changing the wavelength of the excitation laser (dye laser). We decreased the laser wavelength from  $598 \text{ nm}$  ( $2.0735 \text{ eV}$ ) to  $580 \text{ nm}$  ( $2.1379 \text{ eV}$ ). We selected a step of  $0.1 \text{ nm}$  for  $595 \text{ nm} \sim 586 \text{ nm}$  ( $0.3 \text{ nm}$  for  $> 595 \text{ nm}$  and  $< 586.7 \text{ nm}$ ).

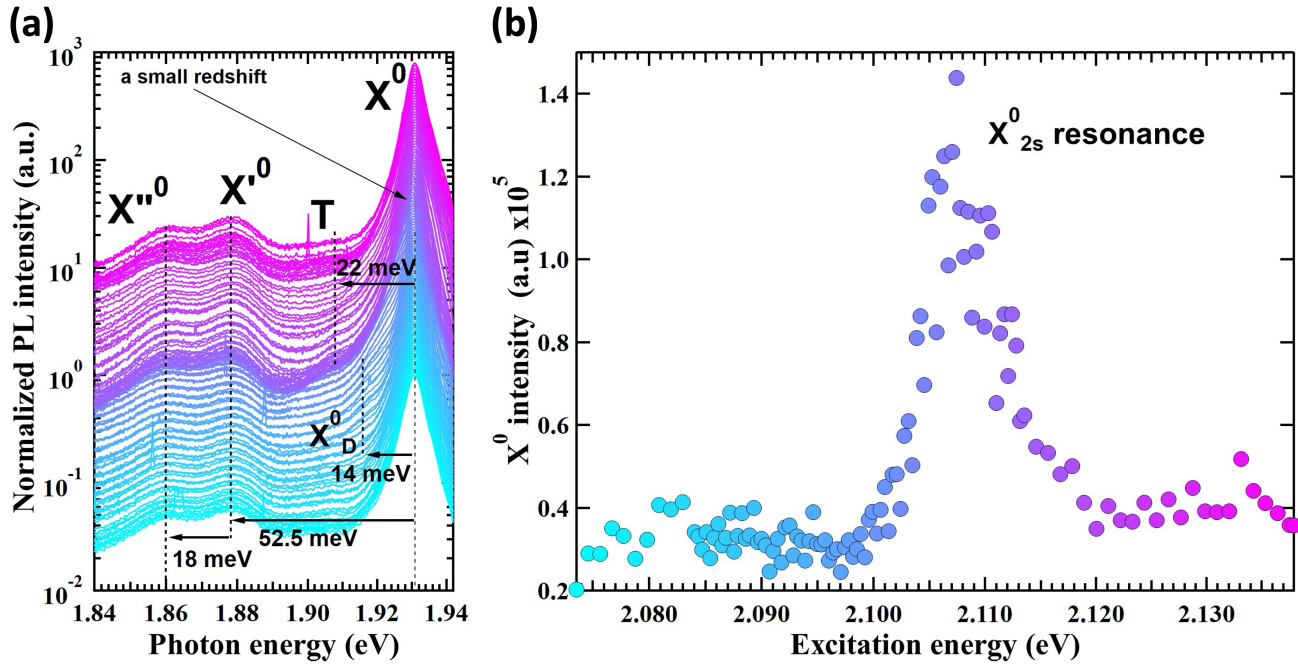


Figure 5.3: Photoluminescence excitation (PLE) experiment at  $100 \mu\text{W}$ ,  $T = 20 \text{ K}$  and  $V_g = 1.5 \text{ V}$  (neutral regime). (a) PL spectra (log scale). The spectra were normalized to 1 and multiplied arbitrary numbers to introduce vertical shift of the even distance in the log scale. (b) The exciton PL intensity. The spectrum color of (a) corresponds to the circle of (b), indicating the excitation laser energy.

As shown in Fig. 5.3a, the neutral exciton emission can be identified at around  $1.93 \text{ eV}$ . When increasing the excitation energy, a small emission is observed  $\sim 14 \text{ meV}$  below the exciton emission energy. This energy emission coincides to the energy recently reported for the dark exciton [186]. The  $X^0$  emission intensity reaches a maximum for an excitation energy of  $\sim 2.107 \text{ eV}$ , as shown in Fig. 5.3b. This energy is in resonance with the first excited  $X^0$  state [170, 187].

The B-exciton resonance can be found at the energy around  $\sim 2.075 \text{ eV}$ , which is very close to the  $X_{2s}^0$  resonance. This B-exciton resonance is much more efficient and stronger than the excited states of the A-exciton resonance. The  $X_{2s}^0$  resonance may not be observed clearly for poor optical quality samples that have a strongly disordered dielectric environment, which can be found for example in second harmonic generation (SHG) spectroscopy [188, 189, 190]. In our device, we only see clear resonance of the  $X_{2s}^0$  thanks to the homogeneous dielectric environment protected by hBN. This is another indication that we have fabricated a good quality sample since one cannot

distinguish the 2s state from the B-exciton resonance due to the broadening in non-encapsulated MoS<sub>2</sub> monolayers.

At the X<sub>2s</sub><sup>0</sup> resonance, the X<sup>0</sup> emission redshifts slightly due to the attractive exciton-exciton interaction from the higher photo-excited exciton density than off-resonance excitation [182]. Also, a small emission below ~ 19 meV is observed near the resonance. This could be a trion according to the binding energy of ~ 19 meV. We also found two emission states, denoted as X'<sup>0</sup> and X''<sup>0</sup>, with binding energies of ~ 52.5 meV and ~ 70.5 meV, respectively. The PL intensities of the two states vary together with the X<sup>0</sup> in the overall scanning range. We will discuss it later again with the polarization experiments 5.4.2.

## 5.3 Visualization of excitonic complexes while electrically controlling the doping state

### 5.3.1 Experimental results

PL map as a function of the applied gate voltage ( $V_g$ ) is shown in Fig. 5.4a. PL spectra with the differential reflectivity spectrum at selected gate voltages are shown in Fig. 5.4b. The differential reflectivity is defined as  $(R_{ML} - R_0)/R_0$ , where  $R_{ML}$  is the reflected spectrum obtained when illuminating the monolayer with a white light source and  $R_0$  is the reflected spectrum when illuminating all the layers except for the MoS<sub>2</sub>. Various peaks appear depending on the  $V_g$  applied.

At  $V_g = 0$  V, a strong neutral exciton emission is observed with a small contribution of negatively charged trion emission. The neutral exciton peak exhibits a maximum PL intensity at  $V_g = V_{neutral} = 2$  V (in Fig. 5.4b) with no trions emission. This implies that our MoS<sub>2</sub> monolayer is slightly unintentionally n doped. The linewidth of the X<sup>0</sup> emission is 4.3 meV (T = 20 K). This linewidth corresponds to ~ 3.2 meV at T = 4 K [96] by considering the acoustic phonon broadening of linewidth. This value of linewidth ensures that our sample has a high optical quality comparable to the state-of-the-art values [191].

The negatively charged trion emissions dominate the PL spectrum for  $V_g < V_{neutral}$ . For instance, the exciton emission is no longer visible, and two emission peaks (T<sub>1</sub> and T<sub>2</sub>) from the X<sup>-</sup> can be seen at  $V_g = -20$  V (they are shown in Fig. 5.4b). The recombination energies of the T<sub>1</sub> and T<sub>2</sub> are 22.4 meV and 33.3 meV below the exciton. These two trion states cannot be found in other Mo-based TMDs, keeping in mind their valley configurations (see Fig. 1.8 in chapter 1).

The charge density in the MoS<sub>2</sub> ML changes into p-type at a positive bias  $V_g > 7$  V. The intensity of the positively charged trion, with a binding energy of 25.5 meV, increases when increasing  $V_g$ . Moreover, an emission at ~ 1.8 eV, denoted as X'<sup>+</sup>, is detected, and the exciton emission can be seen even at the highest  $V_g$  applied.

Importantly, no significant hysteresis is observed in the behavior of the PL when varying the gate voltage. The neutrality point, defined as the value of  $V_g = V_{neutral}$  for which the X<sup>0</sup> intensity is maximized always occurs at

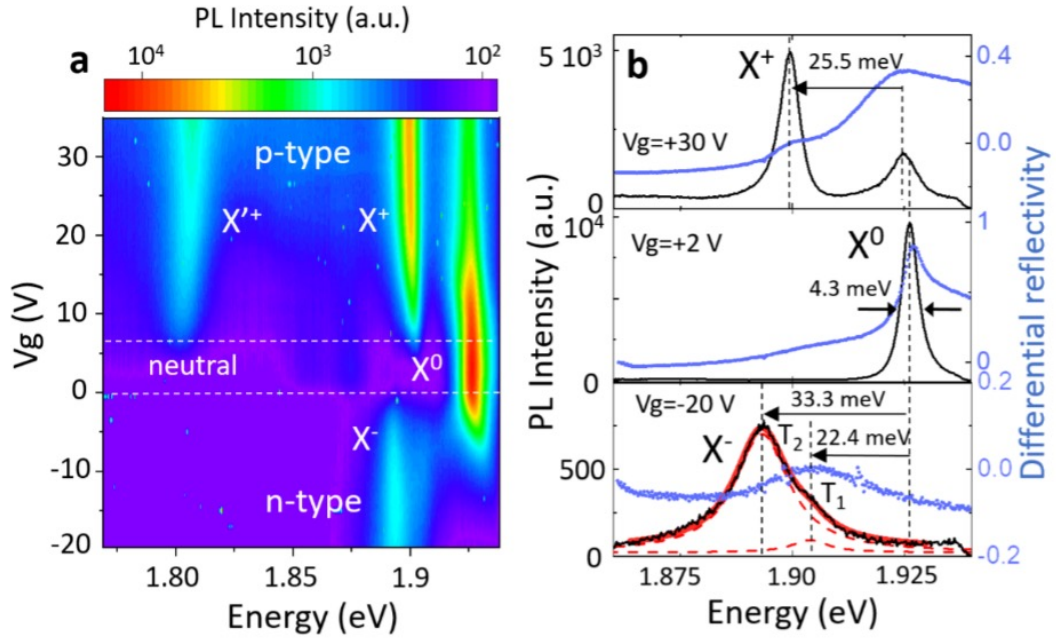


Figure 5.4: (a) PL intensity on a logarithmic scale under cw laser excitation at  $10 \mu\text{W}$  as a function of photon emission energy and gate bias (b) PL spectra at selected gate voltages corresponding to the p-type (top), neutral (middle) and n-type doping regime (bottom). [106]

voltages between 2 and 3 V. No change in the PL spectrum is observed after laser exposure, excluding the presence of laser-induced photodoping effects [183].

### 5.3.2 The fine structure of the negatively charged trion ( $T_1$ and $T_2$ )

Two states from the negatively charged trion were observed (see Fig. 5.4b), which is generally not the case in the  $\text{MoX}_2$  family considering their valley configurations. The conduction valleys at the K points are split by  $\Delta E > 0$ , as the other Mo-based TMDs (e.g.,  $\text{MoSe}_2$  and  $\text{MoTe}_2$ ) as shown in Fig. 5.5a. The ground state of exciton formation is optically "bright" so that only one type of negatively charged trion can be formed under light excitation. The formation of  $X^-$  will be obtained by the combination of an exciton in one valley (the optically "bright" ground state) and an electron from the lowest sub-conduction band in the opposite valley.

However, in  $\text{MoS}_2$  monolayers the local and nonlocal exchange interactions modify the bright character of the exciton [192]. It flips the sign of conduction subbands at K points in the excitonic picture. Thus, the conduction valley configurations become a "WX<sub>2</sub>-like", as shown in Fig. 5.5b. Consequently, a fine structure for the negatively charged trion arises so that two singlets and one triplet can be theoretically possible, as shown in Fig. 5.5c. Now we draw the valley schematics (in Fig. 5.5c.) from the exciton's perspective. Then, the intra valley trion singlet ( $T_S^{\text{intra}}$ ) and inter valley trion triplet ( $T_S^{\text{inter}}$ ) are possible, which are the typical formations of negatively charged trions in the  $\text{WS}_2$  family. Since excitons and free electrons see the valleys differently, the inter valley trion singlet ( $T_S^{\text{inter}}$ ) will be a more stable than  $T_S^{\text{intra}}$  because the electron of the  $T_S^{\text{inter}}$  lies on the ground state the conduction sub-band. This

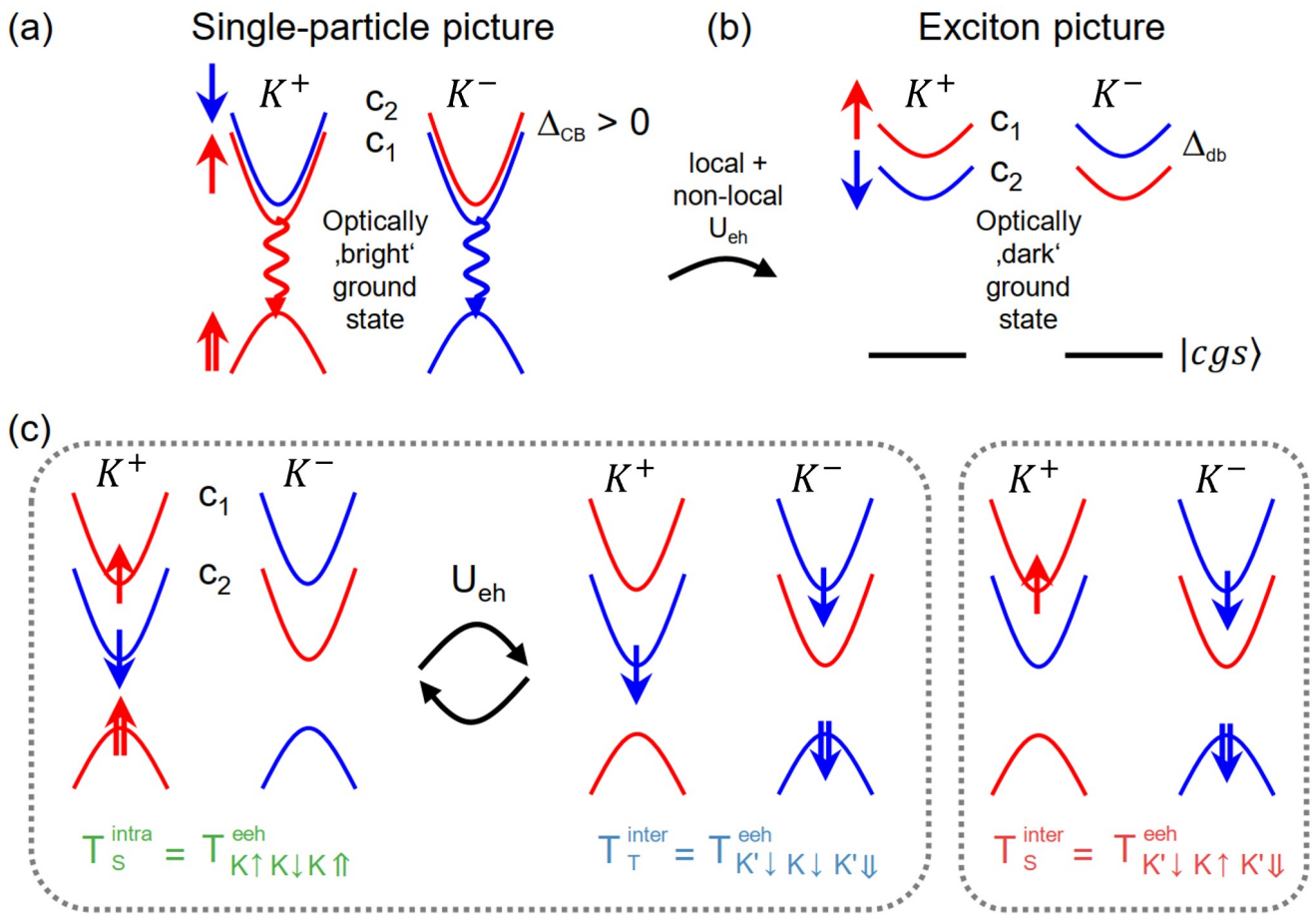


Figure 5.5: (a) Monolayer MoS<sub>2</sub> is optically bright in a single-particle picture with  $\Delta_{CB} > 0$ . (b) Local and non-local exchange interaction  $U_{eh}$  reorders exciton spin configurations resulting in the lowest excitonic transition to be optically dark. This is schematically depicted as a flip of the conduction bands. (c) Trion fine structure in monolayer MoS<sub>2</sub>. [192]

can explain what we observed in Fig. 5.4b. The two negatively charged trions are expected to be the  $T_S^{inter}$  and  $T_S^{intra}$  states.

### 5.3.3 PL asymmetry in the $V_g$ response and $X'^+$ emission

Sulfur vacancies are the most common intrinsic defects in MoS<sub>2</sub> monolayers, which likely contribute to the difficulties in obtaining a high-quality MoS<sub>2</sub> compared with WSe<sub>2</sub> and MoSe<sub>2</sub>. These defects may also play a role in the asymmetric  $V_g$  response of the PL spectrum.

Fig. 5.6 shows the calculated density of states (DOS) of the perfect (a), sulfur adatoms (b), and sulfur vacancies (c) MoS<sub>2</sub> monolayers. The calculations of Ref. [193] say that sulfur adatoms introduce hole trap states and narrow the bandgap by 0.069 eV compared with the perfect case. The sulfur vacancies create a deep electron trap at 0.54 eV below the conduction band edge and a shallow hole trap, shrinking the bandgap by 0.030 eV. The hole trap states have been observed by scanning tunneling spectroscopy and transport measurements, to be inside the bandgap

for MoS<sub>2</sub> monolayers [194, 195].

One could expect that the trap states create a bypass for a fast non-radiative decay process in the n-doped regime. This could explain the decrease of PL yields of negatively charged trion compared with the positively charged one. On the contrary, the trap states are neutralized by capturing holes in the p-doped regime. This can also explain the emission observed at  $\sim 1.8$  eV and denoted as  $X'^+$ , which probably stems from positive trions in which the recombining hole is bound to one of these traps. Finally, this hole trapping can also explain why, in the p-type regime, the neutral exciton emission never disappears completely, even at the largest voltages applied. Trapping holes can indeed limit the maximum density of positive trions that we can achieve in our device.

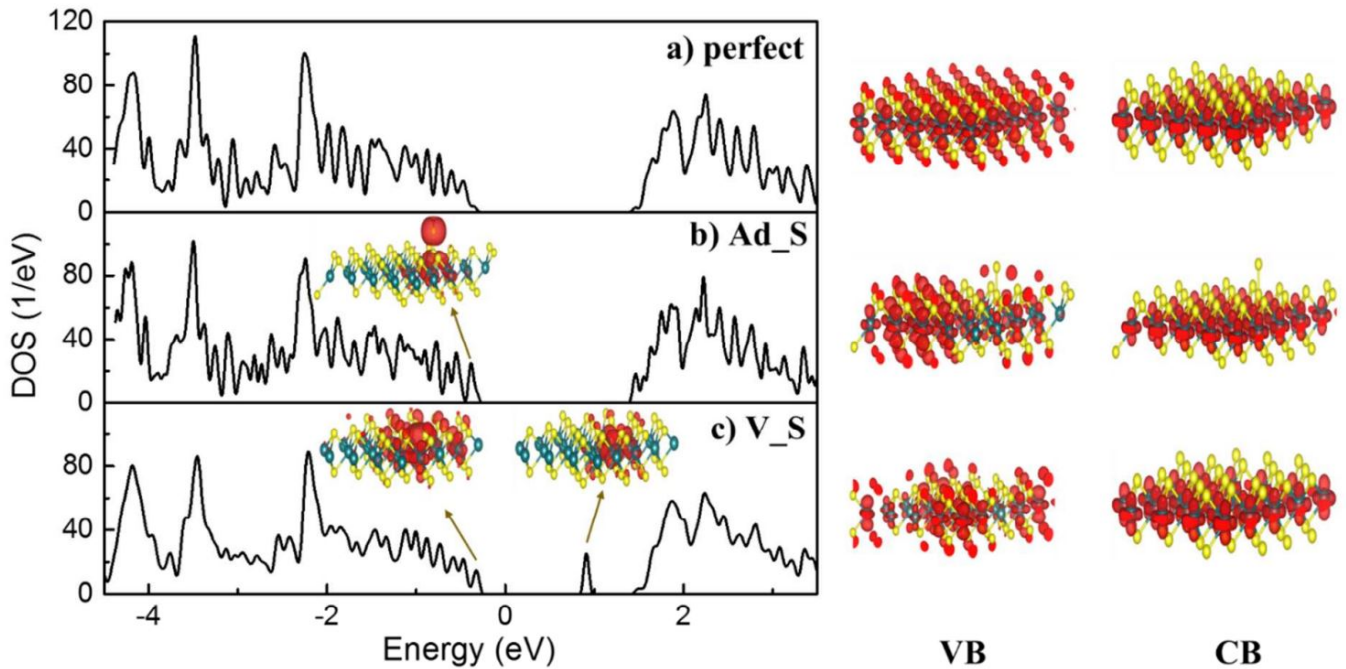


Figure 5.6: Density of states (left panel) and charge densities (right panel and inserts) of (a) perfect MoS<sub>2</sub> monolayer and monolayers with (b) Ad\_S (sulfur adatoms) and (c) V\_S (sulfur vacancies). Inserts show charge densities of the defect states. The right panel shows charge densities of band edge states. Ad\_S has a shallow localized hole trap state next to the VB edge. V\_S has two trap states: a shallow hole trap close to the VB edge and a deep localized electron trap 0.6 eV below the CB edge. The charge densities of the VB edge states are strongly perturbed by defects, while CB edge states remain unchanged. [193]

Note that the absence of the LA(M) mode in the Raman spectrum (see Fig. A.2 in appendix) allows us to exclude a density of vacancies larger than  $10^{12}$  cm<sup>-2</sup> [196], which is the typical density of vacancies found in pristine monolayers exfoliated from natural MoS<sub>2</sub>.

### 5.3.4 Estimation of doping level at $V_g = +30$ V and $V_g = -20$ V

#### p-type regime: $V_g = +30$ V

We can start from the relationship between the trion energy and fermi level to estimate the doping density at  $V_g = +30$  V. The negative trion absorption energy increases linearly with the fermi level energy when the fermi level energy is positioned in the conduction band (for  $E_C = 0$ ) [197, 198], as shown in Fig. 5.7a. The  $\omega_A$  and  $\omega_{A^-}$  indicate the absorption energy of exciton and trion, respectively.

One can understand this phenomenon by the dissociation energy of the extra electron from a trion. As shown in the inset of Fig. 5.7a, the authors [197] explained that the shift of the energy difference between trion and exciton corresponds to the energy that excites electron from the bottom of the conduction band to the fermi level when the fermi level is positioned in the conduction band. Here, we refer to the PL emission energy difference between trion and exciton as "trion apparent binding energy". This energy implies that the trion energy can be lowered by the amount of energy involving the extra electron into the excitation. When the fermi level is placed in the conduction band, the trion apparent binding energy shift at higher energy by the difference of  $E_F - E_C$ . That is why this energy variation  $\omega_A - \omega_{A^-}$  can be observed when the fermi level is placed in the band.

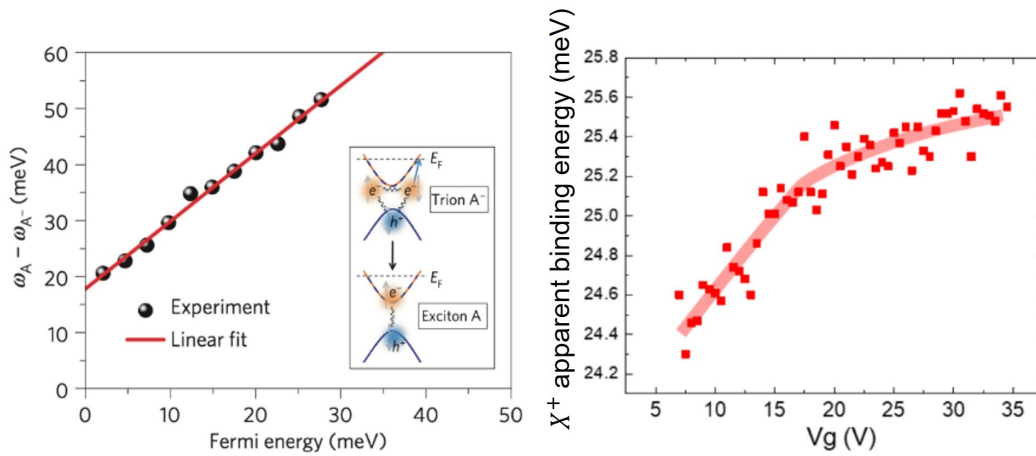


Figure 5.7: (a) The difference in the exciton and trion energies,  $\omega_A - \omega_{A^-}$  (symbols), as a function of Fermi energy  $E_F$ . The red line is a linear fit to the  $E_F$  dependence with a slope of 1.2 and an intercept of 18 meV. The latter determines the trion binding energy. Inset: representation of the dissociation of a trion into an exciton and an electron at the Fermi level [197]. (b) Evolution of the  $X^+$  apparent binding energy measured in PL as a function of the applied gate bias. The continuous line is a guide to the eye [106].

We can adapt this model for the positive trion to our case in order to estimate the hole doping rate at  $V_g = +30$  V. As shown in Fig. 5.7b, the positive trion  $X^+$  binding energy increases with the  $V_g$ . The continuous line shows a linear behavior with two separate regimes for below/above +20 V. Photocurrent and hole trapping effects may lead to the decrease of slope observed above  $V_g = +20$  V, which limits the injecting hole density of our experiment at a high  $V_g$ . The positive trion  $X^+$  binding energy increases about  $\sim 1$  meV overall. In other words, the fermi level ( $E_F$ )

is located (roughly) 1 meV below the top of the valence band ( $E_V$ ) when  $V_g = +30$  V.

Then, the hole doping density can be calculated with following equation:

$$p = N_V \ln \left[ 1 + \exp \left\{ \frac{-(E_F - E_V)}{k_B T} \right\} \right] \quad (5.1)$$

Where  $N_V$  is the effective density of states. For a 2D system  $N_V$  is given by

$$N_V^{2D} = \frac{m^*}{2\pi\hbar^2} k_B T \quad (5.2)$$

Where  $m^*$  is the effective hole mass of  $m^* = 0.5 m_0$  ( $m_0$  is the free electron mass), and  $T = 20$  K is the sample's temperature. Finally, we can estimate a hole density of  $p \sim 3.6 \times 10^{11} \text{ cm}^{-2}$  from Eq 5.1.

### **n-type regime: $V_g = -20$ V**

For  $V_g = -20$  V, estimating the doping density from the binding energy shift is unsuitable since we cannot precisely identify and deconvolute the exciton emission peak from the PL spectrum at  $V_g = -20$  V and the negatively charged trions exhibit broad linewidth emissions (see Fig. 5.4b). Instead, we have performed gate-dependent Raman spectroscopy on the MoS<sub>2</sub> device based on the idea that the electron-phonon interaction induces renormalization of the two modes  $A_{1g}$  and  $E_{2g}^1$  [199]. Fig. 5.8a and b show the experimental results and DFT calculation data as a function of the electron concentration, respectively. The  $E_{2g}^1$  mode exhibits a negligible redshift while the  $A_{1g}$  mode exhibits a more pronounced redshift because the electron-phonon coupling of the  $A_{1g}$  mode is much stronger than the  $E_{2g}^1$  mode, as shown in Fig. 5.8c. We can estimate the electron doping density from the redshift of the  $A_{1g}$  mode. Fig. 5.8d shows the Raman modes ( $E_{2g}^1 = 383.5 \text{ cm}^{-1}$  and  $A_{1g} = 403.8 \text{ cm}^{-1}$ ) of our MoS<sub>2</sub> monolayer at  $V_g = 1.5$  V (neutral regime). The peak position of the  $A_{1g}$  mode redshifts as the  $V_g$  changes towards  $-20$  V (n-type regime). The shift of the  $A_{1g}$  mode at  $V_g = -20$  V is  $0.5 \text{ cm}^{-1}$  compared to the peak position at the neutral regime, as shown in Fig. 5.8e. This redshift corresponds to a maximum areal electron density of  $n \sim 1.5 \times 10^{12} \text{ cm}^{-2}$  according to the theoretical prediction of Fig. 5.8b. This value is consistent with the absence in our spectra of the low energy feature observed in [192], which only appears above a density of  $4 \times 10^{12} \text{ cm}^{-2}$ . Note that the  $A'_{1g}$  peak shifts with a much reduced slope in the p-doped regime, due to a strong electron-hole asymmetry in the softening of the out-of-plane vibrational modes [200].

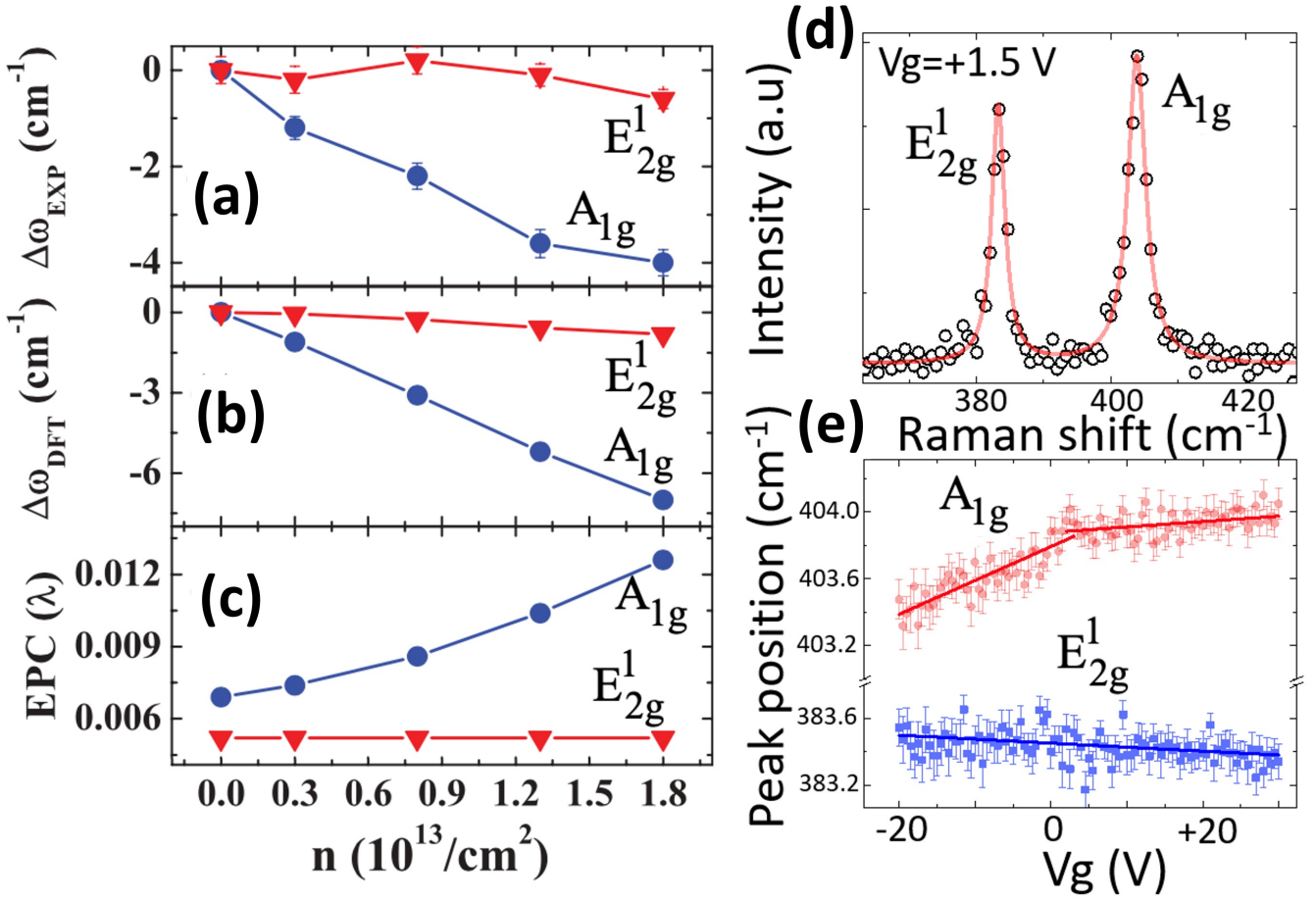


Figure 5.8: Change in zone center phonons  $\Delta\omega$  of (a) from experiment and (b) from DFT calculations as a function of electron concentration  $n$ . (c) Electron-phonon coupling of  $A_{1g}$  and  $E_{2g}^1$  modes as a function of  $n$ . (d) Raman spectrum in the neutral regime, exhibiting the well-known  $E'$  and  $A'1$  vibrational modes. (e) Peak position for both modes of the panel (d) as a function of gate bias. (a-c) Ref. [199]. (d-e) Data were taken from our charge tunable  $\text{MoS}_2$  monolayer [106].

## 5.4 Circular & linear polarization in the different doping regimes

### 5.4.1 Experimental results

Fig. 5.9 shows the polarization-resolved PL spectra under a circular and linear excitation at  $10 \mu\text{W}$  in the different doping type regimes. The neutral exciton ( $X^0$ ) exhibits a linear polarization of  $\sim 50\%$  due to the valley coherence [153]. The other excitonic states ( $X^-$ ,  $X^+$ ,  $X'^+$ ,  $X'^0$ , and  $X'^0$ ) show negligible degree of linear polarization. The degree of circular polarization of  $\sim 50\%$  is observed for  $X^0$ ,  $X^+$ , and  $X'^+$ . In contrast, the  $X^-$  exhibits a particularly high circular polarization of  $\sim 70\%$ .

Fig. 5.10 shows (a) the integrated PL intensity and (b) the degree of circular/linear polarization for  $X^0$ ,  $X^+$ , and  $X^-$  as a function of excitation power from  $0.1 \mu\text{W}$  to  $100 \mu\text{W}$ . We ensured that the excitation power up to  $100 \mu\text{W}$  is within a linear excitation regime. In this power range, the degree of circular polarization exhibits a small variation for

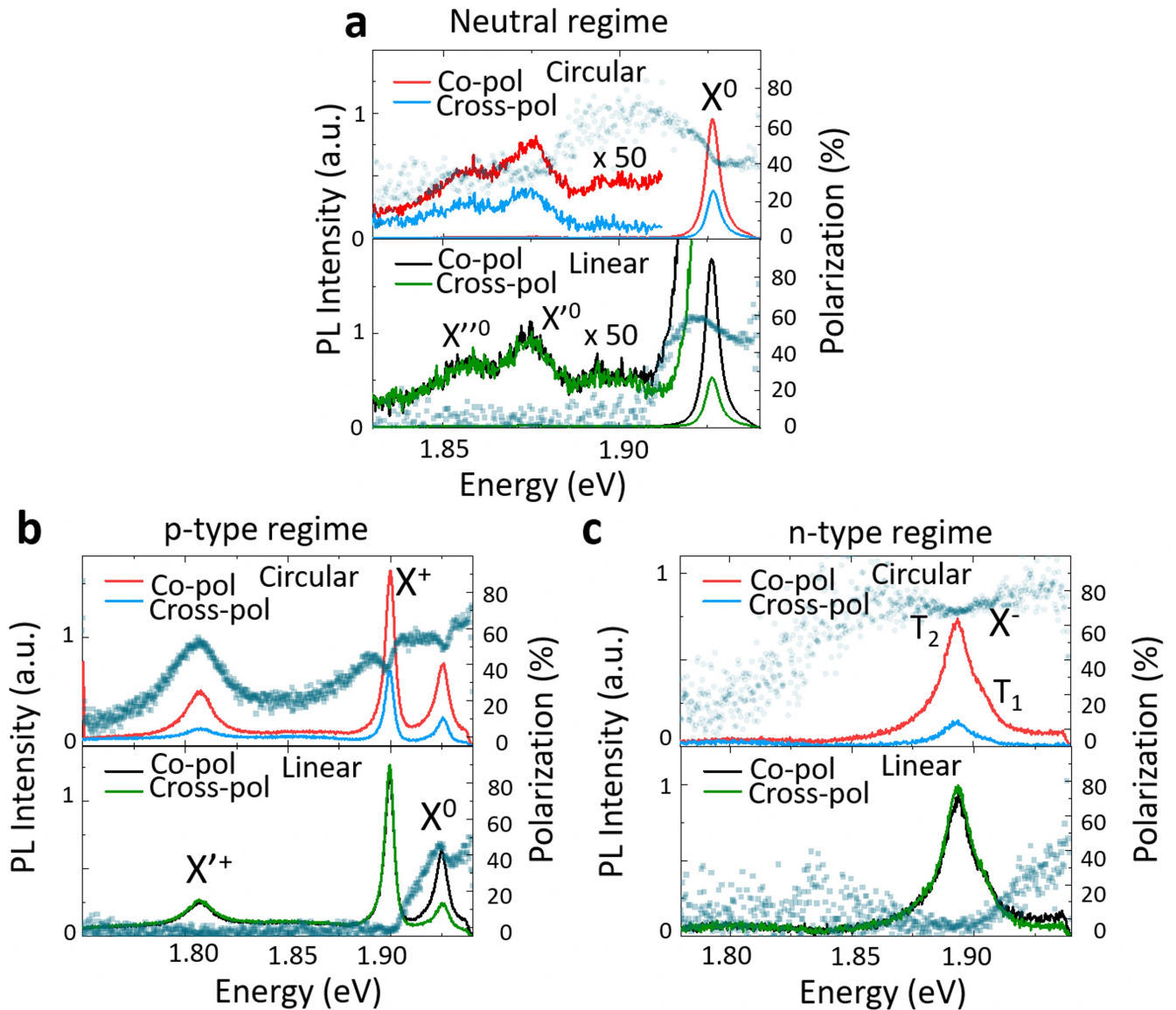


Figure 5.9: Polarization-resolved photoluminescence (PL) emission under circularly polarized excitation and linearly polarized excitation for different gate voltages, +3V (a), +30 V (b) and -20 V (c). Also shown is the energy-resolved degree of PL polarization (blue dots). [106]

all excitonic complexes while the linear polarization of the  $X^0$  decreases above a few tens of  $\mu\text{W}$ .

#### 5.4.2 $X'^0$ and $X''^0$ emission states

In the neutral regime, we observed  $X'^0$  and  $X''^0$  emission states with binding energies of  $\sim 52.5$  meV and  $\sim 70.5$  meV, respectively. PL intensities of these states vary together as a function of  $V_g$ , excitation power and energy. The two states exhibit zero degree of linear polarization, so one can exclude the possibility of them being phonon replicas of the  $X^0$ . A certain amount of linear polarization should be detected if they were simply phonon replicas of the  $X^0$ . The  $X'^0$  and  $X''^0$  emissions exhibit a circular polarization of  $\sim 30\%$ , which is a slightly lower value than the

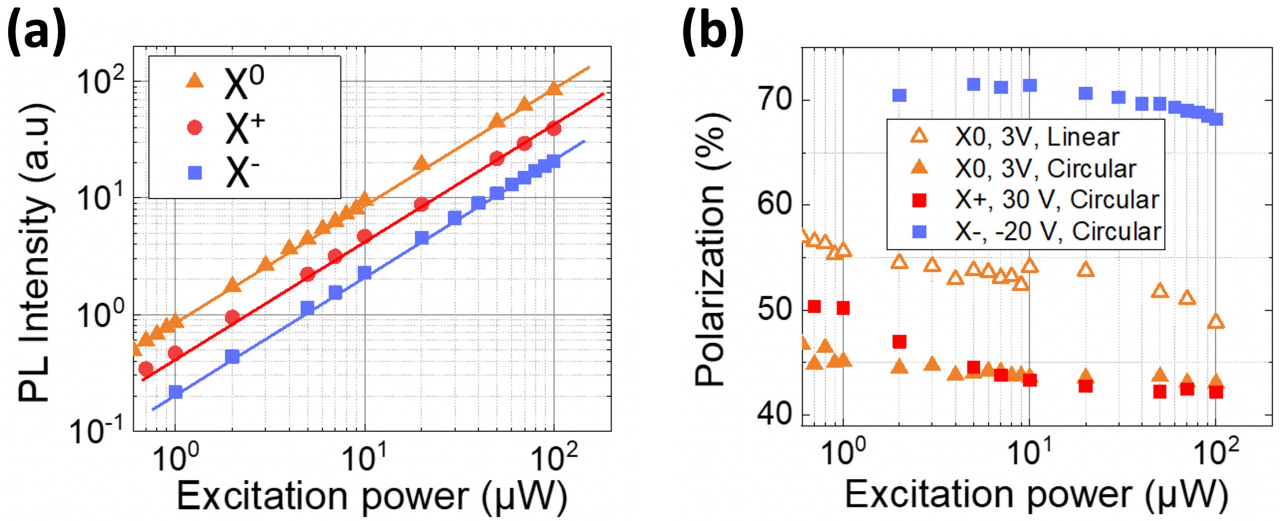


Figure 5.10: (a) Integrated intensity as a function of excitation power. (b) Degree of polarization as a function of excitation power. [106]

$X^0$  circular polarization of  $\sim 40\%$ , as shown in Fig. 5.9a.

Therefore, we denoted these states as  $X^0$  and  $X'^0$  because we tentatively ascribe them to phonon-assisted recombination of indirect excitons, although more experiments will be required to determine the exact nature of these transitions.

### 5.4.3 Negatively charged trions ( $T_1$ and $T_2$ ): very large valley polarization

The two negatively charged trions exhibit a circular polarization of  $\sim 70\%$ , which is significantly higher than the degree of circular polarization of  $\sim 50\%$  for other excitonic species ( $X^0$ ,  $X^+$ , and  $X'^+$ ). This higher polarization of the negatively charged trions can be understood with the following valley schematics, as shown in Fig. 5.11. In the n-type regime, photo-excited excitons are combined with resident electrons to form negatively charged trions. One can expect that resident electrons are filled from the lowest conduction subband. Therefore, we assume two possible formations: (a) inter-valley singlet and (c) intra-valley singlet. The continuous (dashed) lines indicate the “exciton (single-particle) point of view” for the valley configurations.

First, we denoted the intra- and inter-valley trion singlets as  $T_1$  and  $T_2$ , respectively. Under  $\sigma_+$  excitation, the probability of (a) formation is expected to be higher than the probability of (c) formation because most resident electrons occupy in the lowest conduction subband. The inter-valley singlet (a) would exhibit a higher emission than the intra-valley singlet state in the PL spectrum. Thus, we have denoted the higher intensity of the negatively charged trion emission (in Fig. 5.9c) as the  $T_2$  inter-valley singlet.

Such high circular polarization  $\sim 70\%$  of  $T_1$  and  $T_2$  can be explained in terms of the inter-valley scattering process that would imply a simultaneous spin (and momentum) flip of the extra electron. Fig. 5.11b shows the

inter-valley scattering of  $T_2$  that would result in  $\sigma^-$  PL. This process is forbidden by the Pauli principle. For  $T_1$ , the configuration becomes different after the inter-valley transfer process, as shown in Fig. 5.11d. This formation is likely unbound [201] since the extra electron in the opposite valley lies on the upper conduction subband. Moreover, it would recombine at a different energy than that of  $T_1$  and  $T_2$ , even if this formation emits PL. For those reasons, the inter-valley transfer path is inactive for the  $T_1$  and  $T_2$  to emit  $\sigma^-$  PL under  $\sigma^+$  excitation. This picture can qualitatively explain the high circular polarization of  $\sim 70\%$  for the negatively charged trions.

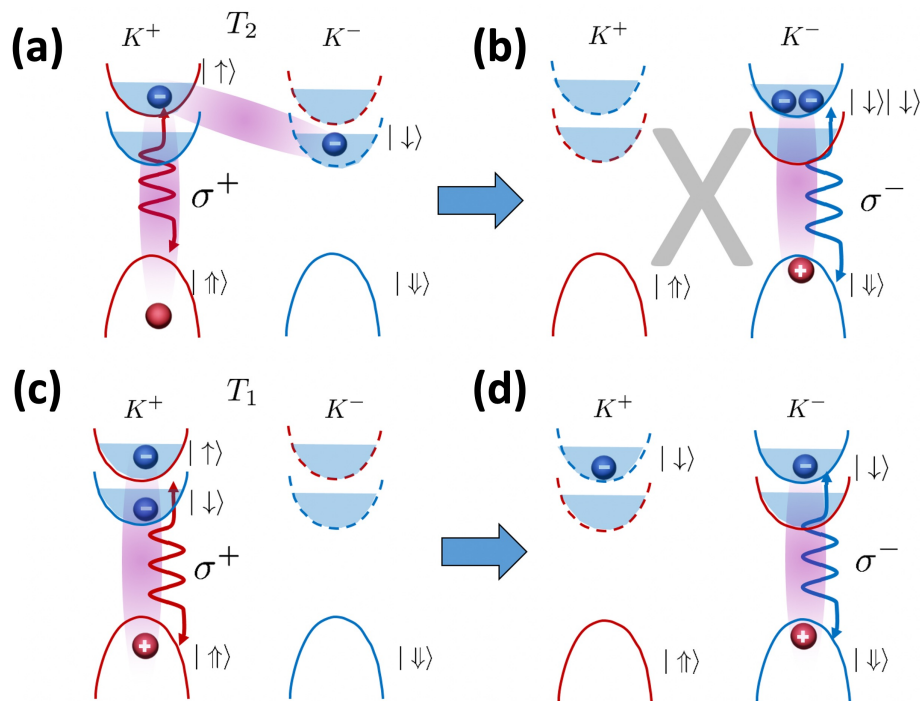


Figure 5.11: The continuous (dashed) lines represent the ordering of the conduction bands in the excitonic (single-particle) picture. (a) Schematics of a negatively charged trion in the  $K^+$  valley corresponding to a spin-singlet state in which both electrons reside at opposite valleys. (b) State obtained after moving the exciton from the  $K^+$  to the  $K^-$  valley for the trion depicted in (a). This state is forbidden by the Pauli principle. (c) Negatively charged trion in the  $K^+$  valley corresponding to a spin-singlet state in which both electrons reside in the same valley  $K^+$ . (d) State obtained after moving the exciton from the  $K^+$  to the  $K^-$  valley for the trion depicted in (c). [106]

More detailed experiments with time-resolution and tunable excitation energy could give more insights into the role of excess energy and whether any significant valley relaxation occurs during the trion lifetime.

## 5.5 Demonstration of optically induced dynamical valley polarization of resident carriers (n- and p- types)

### 5.5.1 Experimental results

Fig. 5.12a-c shows total PL intensity under circular and linear excitation for (a) n-type at  $90 \mu\text{W}$  (top) and  $2 \mu\text{W}$  (bottom), (b) p-type at  $100 \mu\text{W}$  (top) and  $2 \mu\text{W}$  (bottom). The black and red lines correspond to circular and linear excitations, respectively. The blue dots indicate the difference between the black and red curves. Notably, the PL intensity exhibits asymmetric behavior under circular/linear excitations at high excitation powers, unlike at low excitation powers. Fig. 5.12b shows polarization-resolved PL under circular excitation in the p-type regime at  $100 \mu\text{W}$ . The solid lines correspond to a fit with a double, asymmetrical peak which takes into account the hole recoil effect [172, 173, 202]. The  $X^+$  and  $X^0$  show a small splitting between the co-circular and cross-circular PL emissions. To fit the  $\sigma_+$  and  $\sigma_-$  components of the PL, we have kept all the parameters fixed except for the amplitudes and energy positions of each peak. We extract a splitting of the  $X^+$  of  $\Delta E = \Delta E_{\sigma_+} - \Delta E_{\sigma_-} = 350 \pm 50 \mu\text{eV}$ .

### 5.5.2 Model : dynamical valence valley polarization

We have observed the asymmetrical PL responses for  $X^-$ ,  $X^0$ ,  $X^+$ , and  $X^{'+}$  between circular and linear excitations at high excitation powers, as shown in Fig. 5.12. This feature is an evidence of dynamical valley polarization of resident carriers, which was observed in  $\text{WS}_2$  and  $\text{WSe}_2$  monolayers for resident electrons in chapter 3. The  $X^-$ ,  $X^0$ , and  $X^{'+}$  exhibit a higher PL intensity under circular excitation than under linear excitation. In contrast, the  $X^+$  exhibits the opposite behavior under the two excitation conditions that the PL intensity under linear excitation is higher than one under circular excitation.

We can explain these behaviors by considering the following scenario schematically shown in Fig. 5.13. We first assume that the sample is in the p-type regime to consider resident hole valley polarization: In steady-state, the  $\sigma_+$  excitation continuously generates excitons in the  $K^+$  valley, as shown in Fig. 5.13a. The  $X^+$  can be populated in the  $K^+$  valleys since the trion generation rate increases with resident hole density. The  $X^+$  can scatter into the opposite  $K^-$  valleys by the valley relaxation process, as shown in Fig. 5.13b. The scattered  $X^+$  relaxes by recombination of electron and hole in the  $K^-$  valley. In this way, we can create an imbalance of the hole valley population between the  $K^+$  and  $K^-$  valleys if the hole valley relaxation is faster than the scattering process. Note that the hole valley relaxation can be a very low process due to the significant spin-orbit splitting of the valence bands. The  $K^+$  valleys have continuous input of holes by optical pumping. In contrast, the  $K^-$  valleys consume resident holes by recombination and they have slow input by the hole scattering process. Finally, the hole population in the  $K^+$  valleys will be higher than the hole population in the  $K^-$  valleys.

These descriptions are coherent with the asymmetric responses of PL under circular/linear excitations which

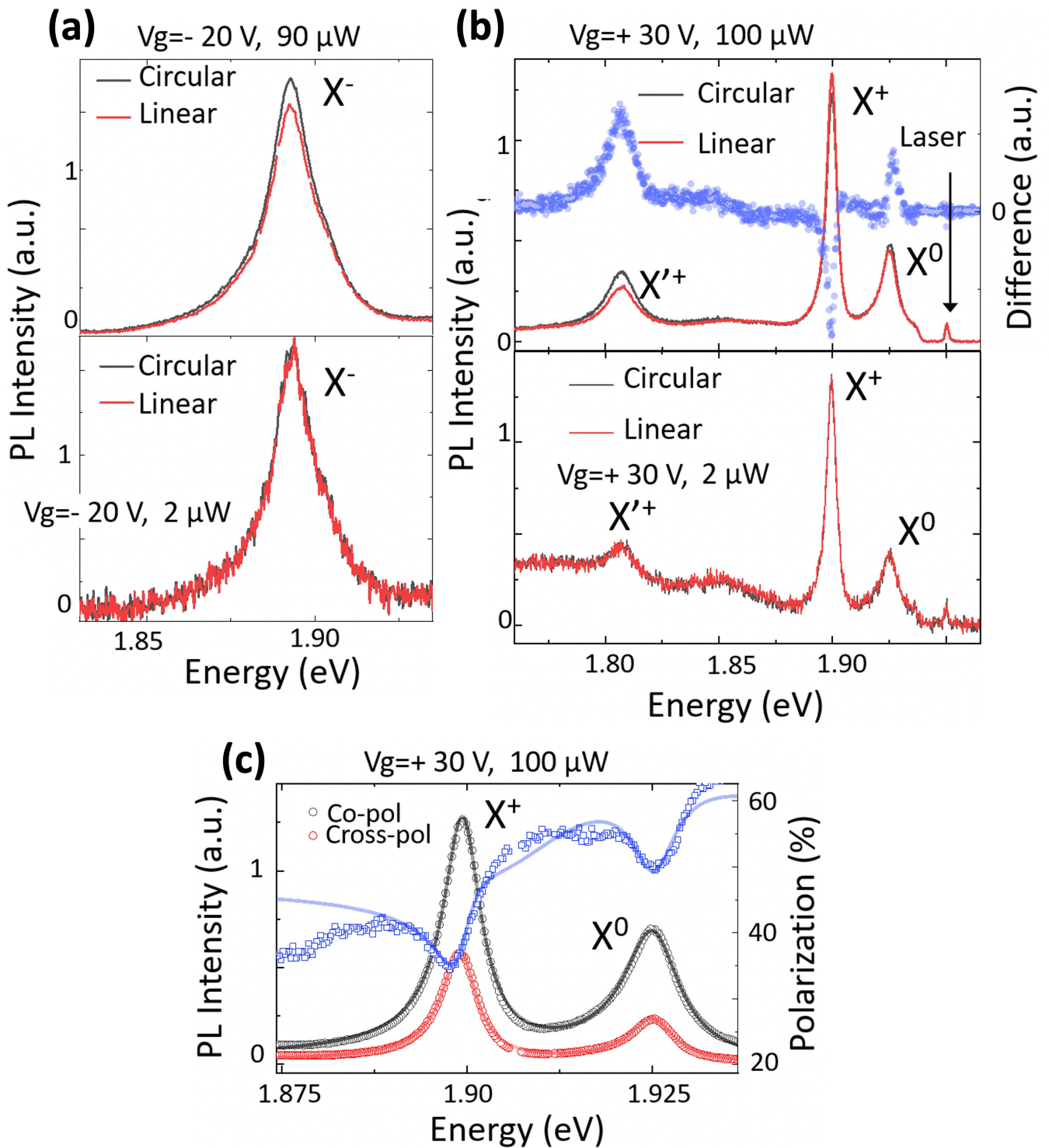


Figure 5.12: (a) Total PL intensity under circular (black) and linear (red) excitation in the n-type regime for an excitation power of  $90 \mu\text{W}$  (top) and  $2 \mu\text{W}$  (bottom). (b) Total photoluminescence (PL) intensity under circular (black) and linear (red) excitation in the p-type regime at an excitation power of  $100 \mu\text{W}$  (top) and  $2 \mu\text{W}$  (bottom). Blue dots are the difference between these two curves. (c) Polarized PL emission under circular excitation and degree of circular polarization (blue dots) in the p-type regime at an excitation power of  $100 \mu\text{W}$ . [106]

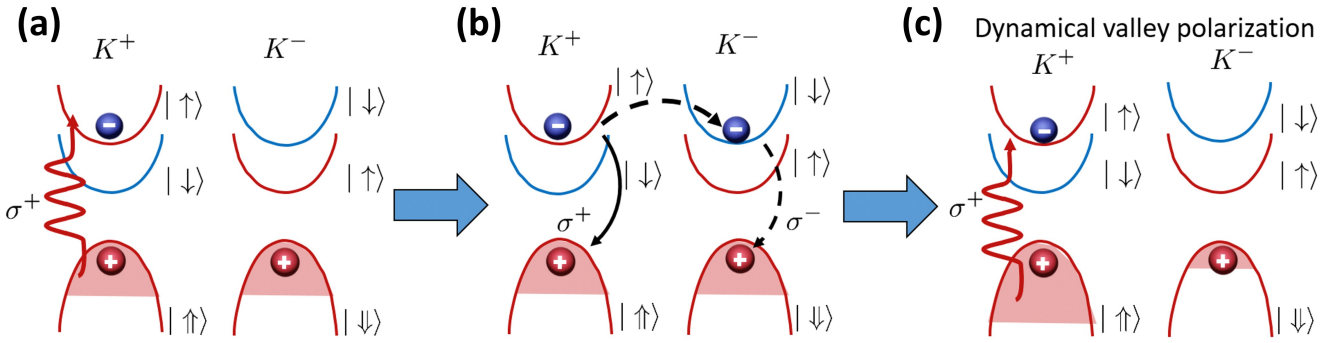


Figure 5.13: (a) Formation of a positively-charged trion in the  $K^+$  valley following right-handed circular polarization. (b) A trion in the  $K^+$  can either recombine radiatively or scatter to the opposite valley before recombination. (c) In a steady-state, the process (a) and (b) will lead to a spin and valley-polarization of the valence band. [106]

we observed for the excitonic species. The  $X^+$  PL intensity decreases under circular excitation compared to linear excitation due to the imbalance of the valley hole population. The  $X^+$  formation rate is related to the resident hole density in the opposite valleys since the photogenerated electron-hole pairs combine with holes in the opposite valleys to form the  $X^+$ . One decreases the hole density in the opposite valley due to the imbalance between the possible process of Fig. 5.13. The  $X^+$  formation rate can thus be suppressed, resulting in the decrease of PL intensity under  $\sigma$  excitation. Also, the  $X^0$  population will increase because excitons are less likely to form charged trions, which cannot be formed to positively charged trions due to the hole valley polarization. The fact that  $X^+$  intensity is larger under circular excitation is consistent with its assignment to a trion in which the additional hole is trapped by an in-gap state.

Finally, we can estimate the degree of hole valley polarization from the splitting of the peaks  $\Delta E = \Delta E_{\sigma^+} - \Delta E_{\sigma^-} = 350 \pm 50 \mu\text{eV}$ , as shown in Fig. 5.12c. We can calculate the valence band hole density for the  $K^+$  and  $K^-$  valleys from the equation 5.1 with their energy levels of  $1 \pm 0.175 \text{ meV}$ . We obtain a hole valley polarization of  $\sim 6.3 \%$ , which is significantly smaller than the resident carrier valley polarization of 80 % achieved in n-doped  $\text{WSe}_2$  monolayers and of around 40 % for our  $\text{WS}_2$  (In chapter 3).

This is consistent with the much smaller variations of PL intensity under circular and linear excitation observed here in monolayer  $\text{MoS}_2$ . The smaller spin-orbit splitting of the valence band in Mo-based TMDs may be at the origin of this smaller steady-state hole valley polarization.

## 5.6 Conclusions

In conclusion, we have fabricated a charge tunable  $\text{MoS}_2$  device and successfully observed different doping states (n-type, neutral, and p-type) when changing the gate bias. Our  $\text{MoS}_2$  sample showed high optical quality, exhibiting a linewidth of  $\sim 4.3 \text{ meV}$  at  $T = 20 \text{ K}$  for the exciton ( $X^0$ ) emission in the neutral regime. This value corresponds to a linewidth of  $\sim 3.2 \text{ meV}$  at  $T = 4 \text{ K}$  [96], which is close to the current state of the art value  $\sim 1.3 \text{ meV}$  [191].

We performed polarization-resolved PL experiments in the different doping regimes. By controlling the doping level, we observed neutral and negatively charged excitonic species but also positively charged ones. This method allows us to investigate details of the excitonic valley dynamics.

We revealed that the electrical doping is asymmetrical between hole and electron injections at a given (positive or negative)  $V_g$  from the neutral regime. The trap states related to sulfur vacancies in  $\text{MoS}_2$  monolayers may play a role in the asymmetrical carrier injection behavior.

We estimated the hole doping level of  $p \sim 3.6 \times 10^{11} \text{ cm}^{-2}$  at  $V_g = + 30 \text{ V}$  (p-type) from the  $X^+$  binding energy shift. Also, the electron doping level is estimated to be  $n \sim 1.5 \times 10^{12} \text{ cm}^{-2}$  ( $V_g = - 20 \text{ V}$ ), which is calculated from the  $A_{1g}$  Raman mode shift.

We observed two negatively charged trions in the n-type regime, which is unusual for the  $\text{MoX}_2$  family. This observation is consistent with recent studies, which propose that local and nonlocal exchange interactions lead to the modification of the conduction band in the excitonic picture [192]. From the exciton perspective, the valley configurations become “ $\text{WX}_2$ -like” for excitons so that more than one type of negatively charged trion can exist.

In the neutral regime, we found small emissions with binding energies of  $\sim 52.5 \text{ meV}$  and  $\sim 70.5 \text{ meV}$  denoted as  $X^0$  and  $X'^0$ , respectively. We tentatively ascribe these emissions to be phonon-assisted recombination of indirect excitons, considering the degree of circular/linear polarization analysis. However, a further investigation is required for their proper identification. In the p-type regime, we visualized the positively charged trion  $X^+$ . We also found the emission at  $\sim 1.8 \text{ eV}$  and denoted as  $X'^+$ , which probably originated from positive trions bound to hole trap states from sulfur vacancies in  $\text{MoS}_2$  monolayers.

Finally, we observed a circular polarization  $\sim 70 \%$  for the negatively charged trions and discussed its possible valley relaxation mechanisms that explains the high degree of circular polarization observed. We have also demonstrated that optically induced valley polarization of resident carriers is also possible in  $\text{MoS}_2$  monolayers and we estimate a hole valley polarization of  $p \sim 6.3 \%$  in steady state. These results demonstrate that the dynamical valley polarization and spin-dependent PL emission are not restricted to tungsten-based TMD monolayers.

We believe that this work can contribute to the continuous progress to extend our understanding of TMD monolayers which is of crucial importance for future valleytronic based devices.



## Chapter 6

# Conclusions and perspectives

This thesis work aimed to extend our understanding of excitonic spin/valley physics in TMD MLs. TMD MLs were fabricated by mechanical exfoliation, which enabled us to fabricate encapsulated monolayers of high optical quality. In this way, we could isolate TMD MLs from dielectric disorder induced by the substrate, resulting in the suppression of inhomogeneous broadening of the linewidth in the PL spectra.

We have employed a polarization-resolved  $\mu$ -PL technique to selectively excite the  $K^+$  and  $K^-$  valleys and detect valley polarization in PL due to the chiral optical selection rules in TMD MLs. Also, our hyperspectral imaging technique enables one to investigate the diffusion-drift transport of excitonic species. With those methods, we have investigated various TMD MLs such as  $WS_2$  (in chapter 3),  $MoSe_2$  (in chapter 4), and  $MoS_2$  (in chapter 5).

For  $WS_2$  monolayer, we have fabricated a high-optical quality sample and observed the fine structures of negatively charged trions ( $\sim 6$  meV) with narrow linewidths (5 meV, FWHM) for the  $T_1$  and  $T_2$  thanks to the hBN encapsulation. We have demonstrated an efficient optically-induced spin/valley polarization through the polarization-resolved  $\mu$ -PL setup. Under  $\sigma$  excitation, we observed that the  $T_1$  ( $T_2$ ) exhibits a maximum (minimum) circular polarization of  $\sim 80\%$  ( $\sim 18\%$ ), where the average PL exhibits a circular polarization of  $\sim 40\%$ . Notably, we revealed that a big difference in PL intensity under circular/linear excitation polarizations for the  $T_1$  (a maximum ratio of  $I^\sigma/I^\pi \sim 1.9$ ) originates from a different  $T_1$  formation rate under  $\sigma/\pi$  excitations. This mechanism assumes that a continuous input of photoexcited electron-hole pairs in one valley under circular excitation induces an imbalance of resident electrons in the sub-conduction valleys, called dynamical spin-valley polarization of the resident electrons. We demonstrated that this dynamical valley polarization is very sensitive to resonant excitations. We have proposed a simple bi-molecular model for trions and interpreted the polarization behavior of the  $T_1$  and  $T_2$  with an estimated maximum resident electron polarization of  $\sim 40.7\%$ .

For  $MoSe_2$  monolayer, we studied excitonic transport at high excitation fluences by the hyperspectral imaging technique of our micro-PL setup. We revealed an appearance of a halo in the spatial distribution of PL at high excitation fluences and interpreted the origin of the halo in our experiment by modeling the steady-state drift-diffusion

equation, including the Seebeck drift induced by a thermal gradient. The following description can explain the appearance of a halo for trions: 1) The laser excitation creates electron-hole pairs with much higher energy than the gap, generating hot excitons out of the light cone. 2) these hot excitons diffuse out of the excitation spot over a characteristic distance while relaxing into trions and excitons. 3) The hot excitons emit phonons during the process of (2). This hot phonon emission process generates a thermal gradient. 4) At high excitation powers, the process of (3) is strengthened so that a strong thermal gradient generates the Seebeck drift, which dominates over diffusion. In contrast, the halo feature for the exciton is much less pronounced, which is a consistent result based on the fact that the exciton lifetime is much shorter than the trion's one. We successfully reproduced the halo for trions by solving the steady-state drift-diffusion equation of the model numerically.

For the MoS<sub>2</sub> monolayer device, we performed polarization-resolved PL experiments in the different doping regimes. By controlling the doping level, we visualized neutral and negatively charged excitonic species but also positively charged ones. This method allows us to investigate details of the excitonic valley dynamics. Importantly, we observed a circular polarization  $\sim 70\%$  for the negatively charged trions and discussed its possible valley relaxation mechanisms that explain the high degree of circular polarization observed. We have also demonstrated that optically induced valley polarization of resident carriers is also possible in MoS<sub>2</sub> monolayers, and we estimate a hole valley polarization of  $p \sim 6.3\%$  under continuous excitation. These results demonstrate that the dynamical valley polarization and spin-dependent PL emission are not restricted to tungsten-based TMD monolayers.

From those investigations, we suggested new concepts/insights to explain the novel findings. However, it is also true that we have limitations in our understanding of some features since we have performed a wide range of studies in various S-TMD MLs. For example, analysis of the results obtained in chapter 3 were limited to the regime of low excitation. PL spectrum at high excitation powers requires a proper deconvolution of excitonic species, while the spectrum analysis of excitonic complexes is not fully understood yet. (In chapter 4) we have demonstrated the appearance of a halo by modeling and solving drift-diffusion equation numerically. It is still a qualitative model since some parameters such as the mobility are not measured experimentally and the Seebeck drift term depends on the temperature gradient. We extracted the effective temperature by fitting the spectrum, but the fitting model is far from perfect. (In chapter 5) There are unidentified emissions that we tentatively ascribed the X<sup>'0</sup> and X<sup>'0</sup> to phonon-assisted recombination of indirect excitons.

Recently, we submitted a project to Soleil for ANTARES ARPES beamline (beam size of 1  $\mu\text{m}$ ). We are working on preparing a gated TMD device with a very thin top hBN (or no top hBN). We expect to observe a direct correlation between excitonic properties and electronic structure in TMD monolayers.

In the short term, we are currently working on improving our experimental station: 1) A heating stage for temperature-dependent experiments, which is available but requires some minor modification. 2) We are planning to mount a high-resolution scanning stage for 2D mapping of the spectrum. This will give us statistical information at low temperatures, which will improve our research quality. 3) We are currently working on scanning electrolumines-

cence (EL) experiments with STM setup for 2D S-TMDs, which provide atomic resolution information. Moreover, the two experiments with different resolutions ( $\mu\text{m}$ , atomic-scale) could give us an unrevealed correlation for spin/valley physics in 2D materials.

Further experiments on  $\mu\text{-PL}$  by applying a magnetic field would be an interesting improvement for the study of dynamical polarization of resident carriers. Also, time-resolved or spin-resolved ARPES [203, 204] with 2D S-TMD devices would be promising for future experiments. Since the experimental method of  $\mu\text{-PL}$  is an indirect way of investigating spin/valley physics (mostly related to excitonic species), the ARPES technique provides a direct observation of the occupied states of the single particle band structure. This combination of indirect/direct observation methods may give us more clear insight into the mechanism of the dynamical valley polarization of resident carriers.

Lastly, the research topic slowly moves to vertical/horizontal heterostructures investigations, for example, inter-layer exciton and moiré superlattices. We should develop our mechanical exfoliation setup to stack heterostructures by controlling the lattice angle of each monolayer.

Notwithstanding these are remaining open questions for future investigation, we would like to emphasize that these studies provide a further understanding of the rich exciton and spin/valley physics in these 2D semiconductors, a crucial step for future optoelectronic and valleytronic applications.



## Appendix A

# Appendix

### A.1 Before/after laser irradiation in MoSe<sub>2</sub> monolayer

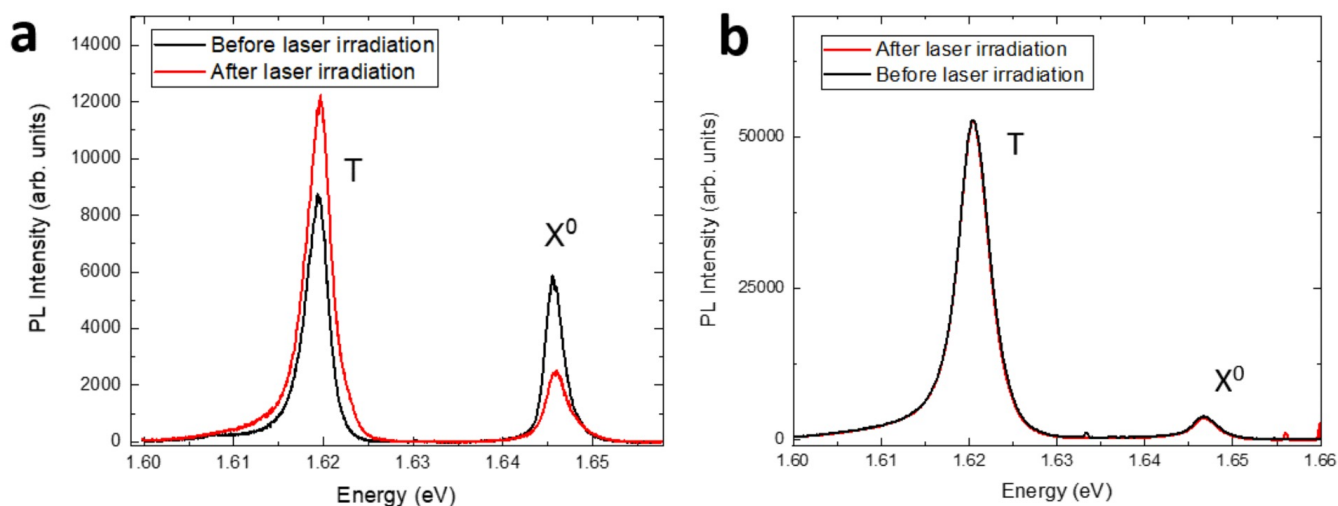


Figure A.1: PL spectrum (MoSe<sub>2</sub> monolayer) under a continuous excitation before (black) and after (red) excitation with the same laser. (a) The first cycle for laser irradiation. A He-Ne laser (632.8 nm) of 40 μW is used at T = 15 K. (b) The same sample was exposed by the laser irradiation and cooling cycles from the RT to cryogenic. An excitation power of 9 mW under a wavelength of 751 nm is used at T = 20K. [149]

### A.2 Before/after laser irradiation in MoSe<sub>2</sub> monolayer

### A.3 Optical components (for μ-PL)

**λ/4 wave plate** AQWP05M-600, thorlabs

**Liquid crystals** full-wave plate, thorlabs

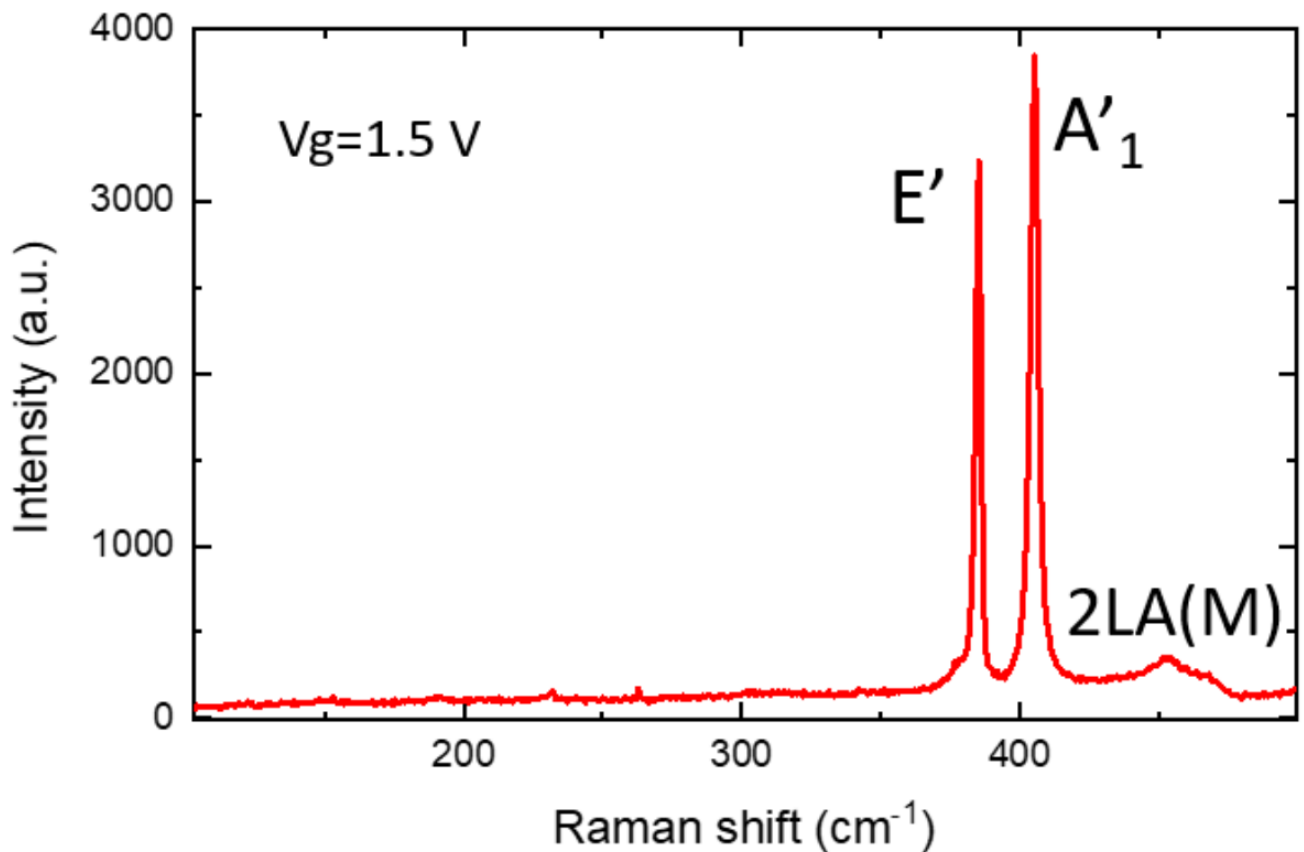


Figure A.2: Raman spectrum of the MoS<sub>2</sub> monolayer upon excitation with a cw laser at 473 nm [106].

**Linear polarizers** LPNIR100, thorlabs

**Beamsplitter (laser/PL)** BS013 (50:50 for 400 ~ 700 nm), thorlabs

**Beam expander/reducer** BE052-A/B, thorlabs

**Lens for the spectrometer part** AC254-500-B, thorlabs

**Photodiode power sensors (laser power meter)** USB type, thorlabs

**The extra CCD part** DCC1545M (CMOS Camera, thorlabs), AC254-200-B/LA4306/AC254-300-A (Lens, thorlabs),  
red LED/convex lens

**neutral density filters**

We used [thorlabs.com](http://thorlabs.com) neutral density filters for lasers and PL.

- NE05B, 10B, 20B, 30B, 40B, 50B, 60B, 502A, 501A
- NDC-50C-2M (continuously variable ND filter)

## **Mirrors**

- PF10-03-P01(Silver Mirror, thorlabs)
- BB1-E03 (Broadband Dielectric Mirror, 750 ~ 1100 nm, thorlabs)

## **Short/long pass and laser filters**

We used short/long pass filters from [thorlabs.com](http://thorlabs.com) and [semrock.com](http://semrock.com).

**Thorlabs** FEL0600, FES0600

**Semrock** TSP01-628, TLP01-628, TSP01-704, TSP01-790, LL01-633-25 (laser filter)

## A.4 PT100 temperature table (annealing chamber)

# RTD Temperature vs. Resistance Table

For American Curve, Alpha = .00392

1° Celsius Increments

°C	Ohms	°C	Ohms	°C	Ohms	°C	Ohms	°C	Ohms	°C	Ohms	°C	Ohms	°C	Ohms	°C	Ohms
-100	59.57	-38	84.80	24	109.51	86	133.75	148	157.53	210	180.86	272	203.74	334	226.17	396	248.16
-99	59.98	-37	85.20	25	109.90	87	134.14	149	157.91	211	181.23	273	204.11	335	226.53	397	248.51
-98	60.39	-36	85.60	26	110.30	88	134.52	150	158.29	212	181.61	274	204.47	336	226.89	398	248.86
-97	60.80	-35	86.01	27	110.69	89	134.91	151	158.67	213	181.98	275	204.84	337	227.25	399	249.21
-96	61.21	-34	86.41	28	111.09	90	135.30	152	159.05	214	182.35	276	205.20	338	227.61	400	249.56
-95	61.63	-33	86.81	29	111.48	91	135.68	153	159.43	215	182.72	277	205.57	339	227.96	401	249.91
-94	62.04	-32	87.21	30	111.88	92	136.07	154	159.81	216	183.09	278	205.93	340	228.32	402	250.26
-93	62.45	-31	87.61	31	112.27	93	136.46	155	160.19	217	183.47	279	206.30	341	228.68	403	250.61
-92	62.86	-30	88.01	32	112.66	94	136.84	156	160.57	218	183.84	280	206.66	342	229.04	404	250.96
-91	63.27	-29	88.42	33	113.06	95	137.23	157	160.95	219	184.21	281	207.02	343	229.39	405	251.31
-90	63.68	-28	88.82	34	113.45	96	137.62	158	161.33	220	184.58	282	207.39	344	229.75	406	251.66
-89	64.09	-27	89.22	35	113.84	97	138.00	159	161.70	221	184.95	283	207.75	345	230.11	407	252.01
-88	64.50	-26	89.62	36	114.24	98	138.39	160	162.08	222	185.32	284	208.12	346	230.46	408	252.36
-87	64.91	-25	90.02	37	114.63	99	138.77	161	162.46	223	185.70	285	208.48	347	230.82	409	252.71
-86	65.32	-24	90.42	38	115.02	100	139.16	162	162.84	224	186.07	286	208.85	348	231.18	410	253.06
-85	65.73	-23	90.82	39	115.42	101	139.55	163	163.22	225	186.44	287	209.21	349	231.53	411	253.41
-84	66.14	-22	91.22	40	115.81	102	139.93	164	163.60	226	186.81	288	209.57	350	231.89	412	253.76
-83	66.55	-21	91.62	41	116.20	103	140.32	165	163.97	227	187.18	289	209.94	351	232.25	413	254.11
-82	66.96	-20	92.02	42	116.59	104	140.70	166	164.35	228	187.55	290	210.30	352	232.60	414	254.46
-81	67.36	-19	92.42	43	116.99	105	141.09	167	164.73	229	187.92	291	210.66	353	232.96	415	254.81
-80	67.77	-18	92.82	44	117.38	106	141.47	168	165.11	230	188.29	292	211.03	354	233.31	416	255.16
-79	68.18	-17	93.22	45	117.77	107	141.86	169	165.48	231	188.66	293	211.39	355	233.67	417	255.51
-78	68.59	-16	93.62	46	118.16	108	142.24	170	165.86	232	189.03	294	211.75	356	234.03	418	255.86
-77	69.00	-15	94.02	47	118.56	109	142.63	171	166.24	233	189.40	295	212.11	357	234.38	419	256.21
-76	69.41	-14	94.42	48	118.95	110	143.01	172	166.62	234	189.77	296	212.48	358	234.74	420	256.56
-75	69.81	-13	94.82	49	119.34	111	143.39	173	166.99	235	190.14	297	212.84	359	235.09	421	256.91
-74	70.22	-12	95.22	50	119.73	112	143.78	174	167.37	236	190.51	298	213.20	360	235.45	422	257.26
-73	70.63	-11	95.62	51	120.12	113	144.16	175	167.75	237	190.88	299	213.56	361	235.80	423	257.61
-72	71.04	-10	96.02	52	120.51	114	144.55	176	168.12	238	191.25	300	213.93	362	236.16	424	257.96
-71	71.44	-9	96.42	53	120.91	115	144.93	177	168.50	239	191.62	301	214.29	363	236.51	425	258.31
-70	71.85	-8	96.81	54	121.30	116	145.31	178	168.88	240	191.99	302	214.65	364	236.87	426	258.66
-69	72.26	-7	97.21	55	121.69	117	145.70	179	169.25	241	192.36	303	215.01	365	237.22	427	259.01
-68	72.66	-6	97.61	56	122.08	118	146.08	180	169.63	242	192.73	304	215.37	366	237.58	428	259.36
-67	73.07	-5	98.01	57	122.47	119	146.47	181	170.00	243	193.09	305	215.74	367	237.93	429	259.71
-66	73.48	-4	98.41	58	122.86	120	146.85	182	170.38	244	193.46	306	216.10	368	238.28	430	260.06
-65	73.88	-3	98.81	59	123.25	121	147.23	183	170.76	245	193.83	307	216.46	369	238.64	431	260.41
-64	74.29	-2	99.20	60	123.64	122	147.61	184	171.13	246	194.20	308	216.82	370	238.99	432	260.76
-63	74.70	-1	99.60	61	124.03	123	148.00	185	171.51	247	194.57	309	217.18	371	239.35	433	261.11
-62	75.10	0	100.00	62	124.42	124	148.38	186	171.88	248	194.94	310	217.54	372	239.70	434	261.46
-61	75.51	1	100.40	63	124.81	125	148.76	187	172.26	249	195.31	311	217.90	373	240.05	435	261.81
-60	75.91	2	100.80	64	125.20	126	149.15	188	172.63	250	195.67	312	218.26	374	240.41	436	262.16
-59	76.32	3	101.19	65	125.59	127	149.53	189	173.01	251	196.04	313	218.63	375	240.76	437	262.51
-58	76.72	4	101.59	66	125.98	128	149.91	190	173.38	252	196.41	314	218.99	376	241.11	438	262.86
-57	77.13	5	101.99	67	126.37	129	150.29	191	173.76	253	196.78	315	219.35	377	241.47	439	263.21
-56	77.53	6	102.38	68	126.76	130	150.67	192	174.13	254	197.14	316	219.71	378	241.82	440	263.56
-55	77.94	7	102.78	69	127.15	131	151.06	193	174.51	255	197.51	317	220.07	379	242.17	441	263.91
-54	78.34	8	103.18	70	127.54	132	151.44	194	174.88	256	197.88	318	220.43	380	242.53	442	264.26
-53	78.75	9	103.57	71	127.93	133	151.82	195	175.26	257	198.25	319	220.79	381	242.88	443	264.61
-52	79.15	10	103.97	72	128.32	134	152.20	196	175.63	258	198.61	320	221.15	382	243.23	444	264.96
-51	79.56	11	104.37	73	128.71	135	152.58	197	176.01	259	198.98	321	221.51	383	243.58	445	265.31
-50	79.96	12	104.76	74	129.09	136	152.96	198	176.38	260	199.35	322	221.87	384	243.94	446	265.66
-49	80.36	13	105.16	75	129.48	137	153.35	199	176.75	261	199.71	323	222.23	385	244.29	447	266.01
-48	80.77	14	105.56	76	129.87	138	153.73	200	177.13	262	200.08	324	222.59	386	244.64	448	266.36
-47	81.17	15	105.95	77	130.26	139	154.11	201	177.50	263	200.45	325	222.94	387	244.99	449	266.71
-46	81.58	16	106.35	78	130.65	140	154.49	202	177.88	264	200.81	326	223.30	388	245.35	450	267.06
-45	81.98	17	106.74	79	131.04	141	154.87	203	178.25	265	201.18	327	223.66	389	245.70	451	267.41
-44	82.38	18	107.14	80	131.42	142	155.25	204	178.62	266	201.55	328	224.02	390	246.05	452	267.76
-43	82.79	19	107.53	81	131.81	143	155.63	205	179.00	267	201.91	329	224.38	391	246.40	453	268.11
-42	83.19	20	107.93	82	132.20	144	156.01	206	179.37	268	202.28	330	224.74	392	246.75	454	268.46
-41	83.59	21	108.32	83	132.59	145	156.39	207	179.74	269	202.64	331	225.10	393	247.10	455	268.81
-40	83.99	22	108.72	84	132.98	146	156.77	208	180.12	270	203.01	332	225.46	394	247.46	456	269.16
-39	84.40	23	109.11	85	133.36	147	157.15	209	180.49	271	203.38	333	225.81	395	247.81	457	269.51

Z-255

Figure A.3: Temperature vs resistance table of PT100 thermocouple (TC) from [technitemp.com](http://technitemp.com).

## Appendix B

# Résumé en français

Ce travail de thèse visait à étendre notre compréhension de la physique des spins et des vallées excitoniques dans les Monocouches des Dichalcogénures des Métaux de Transition (TMD ML).

Les TMD ML ont été fabriqués par exfoliation mécanique, ce qui nous a permis de fabriquer des monocouches encapsulées de haute qualité optique. Nous avons donc pu isoler les ML TMD du désordre diélectrique induit par le substrat et supprimer l'élargissement inhomogène de la largeur de raie dans les spectres de Photoluminescence (PL).

Nous avons utilisé la technique de  $\mu$ -PL résolue en polarisation pour exciter sélectivement les vallées  $K^+$  et  $K^-$  et détecter la polarisation des vallées en PL grâce aux règles de sélection optique chirale dans les ML TMD. De plus, notre technique d'imagerie hyper spectrale permet d'étudier le transport par dérive de diffusion des espèces excitoniques. Avec ces méthodes, nous avons étudié divers TMD ML tels que  $WS_2$  (au chapitre 3),  $MoSe_2$  (au chapitre 4) et  $MoS_2$  (au chapitre 5).

Pour la monocouche  $WS_2$ , nous avons fabriqué un échantillon de haute qualité optique et observé les structures fines de trions chargés négativement ( $\sim 6$  meV) avec des largeurs de raie étroites (5 meV, FWHM) pour les trions intervallée ( $T_1$ ) et intravallée ( $T_2$ ) grâce à l'encapsulation avec des couches de Nitrure de Bor hexagonales (hBN). En utilisant à l'expérience de  $\mu$ -PL polarisée, nous avons démontré une polarisation de spin/vallée induite optiquement efficace. Sous excitation  $\sigma$ , nous avons observé que le  $T_1$  ( $T_2$ ) présente une polarisation circulaire maximale (minimale) de  $\sim 80\%$  ( $\sim 18\%$ ), là où le PL moyen présente une polarisation circulaire de  $\sim 40\%$ .

Notamment, nous avons révélé la présence d'une grande différence d'intensité de PL sous des polarisations d'excitation circulaires/linéaires pour le  $T_1$  (un rapport maximum de  $I^\sigma/I^\pi \sim 1,9$ ) provient d'un taux de formation de  $T_1$  différent sous des excitations  $\sigma/\pi$ . Ce mécanisme suppose qu'un apport continu de paires électron-trou photoexcitées dans une vallée sous excitation circulaire induit un déséquilibre des électrons résidents dans les vallées de sub-conduction, appelée polarisation dynamique spin-vallées des électrons résidents.

Nous avons démontré que cette polarisation de vallée dynamique est très sensible aux excitations résonnantes.

Nous avons proposé un modèle bi-moléculaire simple pour les trions et interprété le comportement de polarisation des  $T_1$  et  $T_2$  avec une polarisation maximale des électrons résidents estimée à - 40,7 %.

Pour la monocouche  $\text{MoSe}_2$ , nous avons étudié le transport excitonique à des fluences d'excitation élevées par la technique d'imagerie hyperspectrale de notre configuration  $\mu\text{-PL}$ . Nous avons révélé l'apparition d'un halo dans la distribution spatiale de la PL à des fluences d'excitation élevées et interprété l'origine du halo dans notre expérience en modélisant l'équation de dérive-diffusion en régime permanent, incluant un terme de dérive de Seebeck induite par un gradient thermique. La description suivante peut expliquer l'apparition d'un halo pour les trions : 1) L'excitation laser crée des paires électron-trou avec une énergie beaucoup plus élevée que le gap, générant des excitons chauds hors du cône de lumière. 2) ces excitons chauds diffusent hors du point d'excitation sur une distance caractéristique tout en se relaxant en trions et excitons. 3) Les excitons chauds émettent des phonons pendant le processus (2). Ce processus d'émission de phonons chauds génère un gradient thermique. 4) Aux puissances d'excitation élevées, le processus (3) est renforcé de sorte qu'un fort gradient thermique génère la dérive Seebeck, qui domine sur la diffusion. En revanche, la caractéristique de halo pour l'exciton est beaucoup moins prononcée, ce qui est un résultat cohérent basé sur le fait que la durée de vie de l'exciton est beaucoup plus courte que celle du trion. Nous avons reproduit avec succès le halo pour les trions en résolvant numériquement l'équation de dérive-diffusion en régime permanent du modèle.

Pour le dispositif monocouche  $\text{MoS}_2$ , nous avons effectué des expériences PL résolues en polarisation dans les différents régimes de dopage grâce à la réalisation d'un dispositif polarisable. En contrôlant le niveau de dopage, nous avons visualisé des espèces excitoniques neutres et chargées négativement mais aussi des espèces chargées positivement. Cette méthode nous permet d'étudier les détails de la dynamique des vallées excitoniques. Fait important, nous avons observé une polarisation circulaire de  $\sim 70\%$  pour les trions chargés négativement et discuté les mécanismes de relaxation de vallée possibles qui expliquent le degré élevé de polarisation circulaire observé. Nous avons également démontré que la polarisation de vallée induite optiquement des porteurs résidents est également possible dans les monocouches de  $\text{MoS}_2$ , et nous estimons une polarisation de vallée des trous  $P \sim 6,3\%$  sous excitation continue. Ces résultats démontrent que la polarisation dynamique de la vallée et l'émission PL dépendante du spin ne sont pas limitées aux monocouches TMD à base de tungstène.

En perspectives, à court terme, nous travaillons actuellement à l'amélioration de notre station expérimentale : 1) Un étage de chauffage pour les expériences dépendantes de la température, qui est disponible mais nécessite quelques modifications mineures. 2) Nous prévoyons de monter une étape de balayage haute résolution pour la cartographie 2D du spectre. Cela nous donnera des informations statistiques à basse température, ce qui améliorera la qualité de nos recherches. 3) Nous travaillons actuellement sur des expériences d'électroluminescence (EL) à balayage avec une configuration STM pour les S-TMD 2D, qui fournissent des informations de résolution atomique. De plus, les deux expériences avec des résolutions différentes ( $\mu\text{m}$ , échelle atomique) pourraient nous donner une corrélation non révélée pour la physique spin/vallée dans les matériaux 2D.

D'autres expériences sur  $\mu$ -PL en appliquant un champ magnétique seraient une amélioration intéressante pour l'étude de la polarisation dynamique des porteurs résidents. De plus, les ARPES résolus en temps ou en spin avec des dispositifs S-TMD 2D seraient prometteurs pour de futures expériences. Étant donné que la méthode expérimentale de  $\mu$ -PL est un moyen indirect d'étudier la physique des spins/vallées (principalement liée aux espèces excitoniques), la technique ARPES fournit une observation directe des états occupés de la structure de bande à une seule particule. Cette combinaison de méthodes d'observation indirecte/directe peut nous donner un aperçu plus clair du mécanisme de la polarisation dynamique de la vallée des porteurs résidents.

Enfin, le sujet de recherche se déplace lentement vers des investigations sur les hétérostructures verticales / horizontales, par exemple, l'exciton intercouche et les super-réseaux de moiré. Nous devrions développer notre configuration d'exfoliation mécanique pour empiler les hétérostructures en contrôlant l'angle de réseau de chaque monocouche.

Bien que ces questions restent ouvertes pour de futures investigations, nous tenons à souligner que ces études permettent de mieux comprendre la riche physique des excitons et des spins/vallées dans ces semi-conducteurs 2D, une étape cruciale pour les futures applications optoélectroniques et valleytroniques.



# List of Figures

1.1	Number of transistors on one integrated circuit (IC) chip. [ <a href="https://github.com/karlrupp/microprocessor-trend-data">https://github.com/karlrupp/microprocessor-trend-data</a> ] . . . . .	6
1.2	Table of 2D materials with depictions of a perspective view of their crystal structures [4]. . . . .	7
1.3	(a) atomic structure of a TMD monolayer (2H, hexagonal), where a transition metal is at the center, indicated by the eastern blue color, and chalcogen atoms are on both sides indicated by the yellow color. Atomic configurations of different TMD phases: (b) 1T, (c) 1T', and (d) 1T'' from the reference [31]. (e) a composition table for various TMD monolayers with stable structural phases [32]. . . . .	9
1.4	Calculated band structures of (a) bulk, (b) bilayer, and (c) monolayer MoS <sub>2</sub> . The solid arrows indicate the lowest energy transitions. [34]. . . . .	10
1.5	(a) Real-space representation of electrons and holes bound into excitons for the three-dimensional bulk and a two-dimensional monolayer. (b) Impact of the dimensionality on the optical absorption. The excited excitonic states and Coulomb corrections for the continuum absorption have been omitted for clarity. [45]. . . . .	11
1.6	Schematic illustration of the optical absorption of an ideal 2D semiconductor, including the series of bright exciton transitions. The inset shows the energy levels of the excited exciton states in analogy with the hydrogen series, the so-called excitonic Rydberg series [47]. (b) Schematic representation of electron-hole pairs forming 1s and 2s excitonic states in a nonuniform dielectric environment [45]. . . . .	12
1.7	(a) ARPES intensity map of WS <sub>2</sub> monolayer [50]. (b) Conduction band structures of MoS <sub>2</sub> and WS <sub>2</sub> monolayer at the vicinity of K point from DFT calculations [51]. . . . .	13
1.8	Schematic diagrams in a single-particle picture representing the lowest-energy optical transition of single layer (a) MoX <sub>2</sub> and (b) WX <sub>2</sub> in the vicinity of the K points. The arrows represent the electron spin along the axis perpendicular to the monolayer. $\sigma^+$ and $\sigma^-$ represent the helicity of the circularly polarized photon involved in each vertical transition. . . . .	14

1.9	(a) Circularly polarized micro-PL of monolayer MoS <sub>2</sub> at 83 K, along with the degree of circular polarization of the PL. The red and blue curves correspond to the intensities of $\sigma^+$ and $\sigma^-$ polarizations, respectively, in the luminescence spectrum. The black curve is the net degree of polarization [61]. (b) Polarization-resolved photoluminescence spectra of WSe <sub>2</sub> at selected gate voltages for horizontally (H, black curve) and vertically (V, red curve) polarized detection. Incident laser is horizontally polarized [62]. . . . .	15
1.10	(a) a schematic of the CVD chamber to synthesize MoSe <sub>2</sub> monolayer. (b) an optical image of monolayer triangles. (c) a schematic of the general CVD process in 2D TMDs. (d) an optical image of MoS <sub>2</sub> monolayers on 2-inches sapphire substrates by CVD. (e) a SEM image of monolayer WS <sub>2</sub> /WSe <sub>2</sub> superlattices by MOCVD. Images were taken from (a)-(b) [66], (c) [69], (d) [70], and (e) [71] . . . . .	18
1.11	Schematic description of the main liquid exfoliation mechanisms (a) ion intercalation. (b) ion exchange (c) sonication assisted exfoliation. [80] . . . . .	19
1.12	Deterministic transfer setup and process. (a) schematic diagram of the experimental setup. (b) diagram of the steps for the viscoelastic stamp and the deterministic transfer. [86] . . . . .	19
1.13	Typical disorder. (a) vacancy, anti-site, substitution, edges termination, grain boundary, and strain [93]. (b) Schematic illustration of the electron-electron and electron-hole interaction affected by environmental screening fluctuations due to the substrate roughness, impurities, and adsorbates [94]. . .	20
1.14	(a) a schematic of hBN encapsulated MoS <sub>2</sub> monolayer. (b) photoluminescence spectra of S-TMD monolayers (top) on SiO <sub>2</sub> /Si substrate (bottom) encapsulated by hBN at T= 4 K. [96] . . . . .	21
2.1	Required equipment for mechanical exfoliation. (Image was especially taken from outside of the glovebox for demonstration) . . . . .	24
2.2	Steps to prepare the scotch tape (a-c) and a small flake of TMD (e-f) for the exfoliation. (Images were especially taken from outside of the glovebox for demonstration) . . . . .	25
2.3	Process to thin down layers with the scotch tape (a-f). repeat (b-e) by taking different folding angles to get thinned flakes (f). (Images were especially taken from outside of the glovebox for demonstration)	26
2.4	(a) A small piece of PDMS is cut and placed onto the edge of the microscope glass. (b) Sometimes bubbles and dust can be trapped between the glass and the polymer stamp. (c-d) Procedure to remove the bubbles. (e) The goal is to achieve a clean interface between the PDMS and the glass. Here, we see dust that was not there before due to the unclean condition for the demonstration. (f) two possible choices for the PDMS size. (Images were especially taken from outside of the glovebox for demonstration) . . . . .	27
2.5	(a) The sticky side of the scotch tape is put on the PDMS piece. (b) TMD flakes stay preferentially on the PDMS piece. (Images were especially taken from outside of the glovebox for demonstration) . . .	27

2.6	(a-b) optical images of the stamping microscope setup inside a glovebox (c-d) schematics of the setup with difference side views indicated by the Cartesian coordinates. . . . .	28
2.7	Issues of difference sizes of PDMS on microscope glass. (a) the two possible configurations for taking different size of PDMS. <b>[A]</b> : using a small size of PDMS and <b>[B]</b> : using a relatively large size of PDMS. (b) Possible situations to transfer flakes to the edge of the substrate for <b>[A]</b> and <b>[A]</b> cases. (c) Possible situations to transfer flakes to the center of the substrate. The <b>[B]</b> case may have an issue since the edge of the substrate and PDMS may touch first so that a displacement may appear from the top view as shown in schematic (d). (e) A possible solution is that the flake to transfer on PDMS can be moved by cutting the PDMS and repositioning it. . . . .	29
2.8	Optical microscope images of stamping process for the bottom-hBN taken with the x10 objective. . . .	31
2.9	Optical microscope images of the stamping process for the TMD monolayer taken with the x10 objective.	31
2.10	Optical microscope images of stamping process for the top-hBN taken with the x10 objective. . . . .	32
2.11	(a) An optical image and (b) a side view schematic of the encapsulated WS <sub>2</sub> monolayer. (c) PL spectra and (d) Raman shifts of different layers from 1L to 3L at room temperature. The colors of the letter on the image correspond to the colors of Raman and PL spectra. . . . .	33
2.12	Histogram of the (a) exciton emission energy and (b) FWHM in the encapsulated (black), (c) the exciton emission energy, and (d) FWHM in half encapsulated (red) regions in the optical microscope image (e). . . . .	34
2.13	(a) an AFM image of the encapsulated WS <sub>2</sub> monolayer where is zoomed in bottom-left side of Fig. 2.11a. (b) line profile of the black line in the image (a). Transition points of layers are indicated as red and orange arrows. . . . .	35
2.14	(a) A schematic of the annealing chamber and (b) the optical image . . . . .	36
2.15	(a) An optical image of the patterned SiO <sub>2</sub> /Si substrate. AFM images on (b) Au electrode and (c) graphite. . . . .	37
2.16	A schematic of the polarization resolved micro-PL setup. . . . .	39
2.17	Optical images of (a) Rhodamine 6G Dye laser (Spectra-physics & Sirah) (b) Ti:Sapphire laser (Spectra-physics & Sirah) (c) 633 nm semiconductor laser (Oxxius). . . . .	40
2.18	Optical images of (a) PIXIS: 400 BR eXcelon and (b) IsoPlane SCT320. ( <a href="https://www.princetoninstruments.com/">https://www.princetoninstruments.com/</a> )	41
2.19	Optical images of (left) the helium compressor and (right) the cryostat. . . . .	42
2.20	Optical images of the inside of the vacuum chamber. The sample holder with xy piezo translations and the objective with z piezo translation are mounted on the cold plate. The objective and piezo translations are vacuum & low temperature compatible bought from Attocube. . . . .	43
2.21	A schematic for aligning CCD and spectrometer . . . . .	44
2.22	A schematic for an alignment of the laser polarization. . . . .	45

2.23 A schematic for an alignment of the PL polarization. . . . .	46
2.24 PL spectra and circular polarization of WS <sub>2</sub> monolayer at 20 K. $\sigma^{++}$ (or $\sigma^{--}$ ) corresponds to co-circular component of $\sigma^+$ laser excitation & $\sigma^+$ PL detection (or $\sigma^-$ laser excitation & $\sigma^-$ PL detection). The blue line exhibits circular polarization taken out from 2 components on $\sigma^-$ excitation basis. The dashed blue lines correspond to circular polarization by 4 components to take into account spurious effects of the optics. . . . .	47
2.25 Demonstration for obtaining and analyzing 0th order PL image of WS <sub>2</sub> monolayer at T = 20 K. . . . .	49
2.26 Demonstration for obtaining and analyzing first-order PL image of WS <sub>2</sub> monolayer at T = 20 K. . . . .	50
3.1 Photoluminescence spectrum (PL) under an excitation power of (a) 9 $\mu$ W and (b) 1.6 mW at T = 20 K of an hBN encapsulated WS <sub>2</sub> monolayer. The excitation wavelength of the laser was 570 nm (2.1754 eV). Several excitonic peaks are identified in the spectrum ( $X^0$ , $T_1$ , $T_2$ , $X^D$ , $XX$ , and $XX^-$ ). The dark exciton ( $X^D$ ) and localized (or phonon-related) states ( $L_1$ , $L_2$ , and $L_3$ ) are observable at (a) low excitation power. In contrast, bi-exciton ( $XX$ and $XX^-$ ) peaks dominate the emission at (b) high excitation power. The inset schematic of (a) describes $T_1$ and $T_2$ formations, which are the inter-valley trion singlet and intra-valley trion triplet, respectively. The red/blue colors indicate the spin (up/down) states of sub-valleys. The blue inset curve of (b) shows the PL spectrum at 10 $\mu$ W under the excitation energy 2.047 eV, below the $X^0$ energy. A PL peak appears at the energy below 5.5 meV from the $XX^-$ emission. This energy emission corresponds to the dark trion. . . . .	55
3.2 Power dependent (a) spectra and (b) peak intensity of power-dependent spectra (excitation power from 100 nW to 5 mW at 20 K). . . . .	56
3.3 Photoluminescence (PL) spectra and degree of circular/linear polarization (blue/gold circles) for a circularly/linearly-polarized excitation laser of wavelength 569.8 nm at 10 $\mu$ W. The black (red) line corresponds to $\sigma^+$ ( $\sigma^-$ ) detection under circularly polarized excitation. The inset shows the degree of circular polarization for the $T_1$ and $T_2$ as a function of the excitation power. The degree of circular polarization is calculated by $\frac{I^{\sigma^+} - I^{\sigma^-}}{I^{\sigma^+} + I^{\sigma^-}} \times 100$ (%), as well as the degree of linear polarization on a linear basis. . . . .	58
3.4 Total PL spectra and intensity ratio under circular/linear bases for an excitation laser of wavelength 569.8 nm at 10 $\mu$ W. The black (red) line corresponds to PL spectrum under $\sigma$ ( $\pi$ ) excitation. Purple circles correspond to the PL intensity ratio ( $I^\sigma/I^\pi$ ). The inset presents the $I^\sigma/I^\pi$ ratio for the $T_1$ and $T_2$ as a function of the excitation power. . . . .	60
3.5 Time-resolved photoluminescence (TRPL) of the trion triplet ( $T_1$ ) under circular (red) and linear excitations (black) at T = 5.1 K under the excitation laser power of 1 $\mu$ W. The experiment was performed by the collaboration group in Toulouse (LPCNO). . . . .	61

3.6	Sketch of the dynamic polarization of resident electrons for trions with $\sigma^+$ excitation. $\tau_{inter}$ ( $\tau_{intra}$ ) represents the inter-valley spin-conserving (intra-valley spin-flip) relaxation times of topmost electrons while $\tau_{sv}$ corresponds to the spin/valley relaxation time of resident electrons [100]. . . . .	63
3.7	Photoluminescence excitation spectroscopy (PLE) of $I^\sigma/I^\pi$ ratio for an excitation laser of wavelength 565 nm $\sim$ 605.8 nm at 10 $\mu$ W. The black curve indicates a normalized PL spectrum. The inset shows the neutral exciton ( $X^0$ ) intensity as a function of the excitation energy at a fixed excitation power of 10 $\mu$ W. One can observe that the $I^\sigma/I^\pi$ ratio increases for the two exciton resonances (neutral exciton ground state and first excited state of the trion). Note that we do not see the first excited state of the exciton resonance in PLE due to the maximum photon energy available with our laser source. (the red circle of the inset). . . . .	65
4.1	An optical image of the hBN encapsulated MoSe2 monolayer. [149] . . . . .	70
4.2	PL spectra of the hBN encapsulated MoSe2 monolayer under $\sigma^+$ laser excitation at T = 20 K (P = 9 $\mu$ W, $\lambda_{laser}$ = 633 nm). . . . .	71
4.3	Peak intensities (left axis) and circular polarization (right axis) of the exciton (black) and the trion (red) in photoluminescence excitation (PLE) experiments performed at T = 20 K with a laser power $P_{laser}$ = 5 $\mu$ W. The laser wavelength increased from 685 nm (1.8102 eV) to 753.5 nm (1.6456 eV) by 0.5 nm step. The emission intensity and circular polarization of the exciton from 1.661 eV to higher excitation were excluded from the graph due to the laser leak of the tunable longpass filter. Unfiltered laser light prevents us from acquiring precise spectra at the exciton emission energy when the laser energy goes close to the exciton resonance. The regular rise and decrease of the exciton circular polarization from 1.74 eV to 1.81 eV might originate from a parasitic issue due to the multiple filters and mirrors. . . . .	72
4.4	Gate-dependent PL splitting energy between $A_1^\pm$ , $A_2^\pm$ , $A_3^\pm$ and $A_{1s}$ , $A_{2s}$ , $A_{3s}$ , respectively (denoted by cyan, orange, and green squares, respectively). 1s, 2s, and 3s are the Rydberg states. The $A^+$ and $A^-$ represent the negatively and positively charged trions, respectively. [154] . . . . .	73
4.5	(a) Power dependent PL spectra (b) Integrated PL intensity of exciton and trion at T = 19 K ( $\lambda_{laser}$ = 570 nm). [149] . . . . .	76
4.6	Power dependent (a) peak position and (b) linewidth of the hBN encapsulated MoSe2 monolayer at T = 19 K ( $\lambda_{laser}$ = 570 nm). [149] . . . . .	76

4.7	(a) The exciton dispersion is shown in orange and photon dispersion in blue with exaggerated momentum, $\sim \times 200$ , to make the light cone visible. Only excitons within the light cone, $ p  < pc$ , can radiative decay. This population is highlighted in the narrow, delta function like region in the occupation number plot, which results in a Lorentzian shaped PL. (b) The Feynman diagram for trion radiative decay. One of the electrons recombines with the hole to emit a photon while the other electron is kicked out to conserve energy and momentum. (c) The trion dispersion is shown in purple with the zero-momentum and kinetic energies of a trion denoted. All trion states can radiatively decay, so all states in the occupation plot are allowed optical transitions. To convert from the occupation distribution to the PL, we must account for the energy of the recoil electron resulting in the long low-energy tail. [172]	78
4.8	The effective temperature of the trion and exciton gas extracted from power-dependent spectra of Fig. 4.5a.	79
4.9	(a) PL's spatial distribution of excitons and trions for selected excitation powers. The images have a lateral size of $14 \mu\text{m}$ . Measured PL's radial profile for trions (b) and excitons (c) for selected excitation powers. PL intensity is normalized by 1 at $r = 0$ where is the center of the excitation spot. Black is the laser profile and each color corresponds to the written excitation powers in the legend. [149]	81
4.10	(a) Normalized radial profile for excitons and trions at low excitation power in a logarithmic scale. Also shown is the laser profile and fits of the 2D diffusion equation. (b) Radial profiles at the highest excitation power, normalized to one at the center in a linear scale. Also shown is the trion temperature was extracted from the 1st order image which is the method described in chapter 2. [149]	82
4.11	Calculated profiles of trion and exciton obtained with a numerical solution of Eq.4.9 [149]	85
4.12	(a) Spatial dependence of the trion's luminescence spectrum at 20 mW when exciting resonantly the neutral exciton (b) Normalized trion profiles obtained from the figures in (a) by integrating the trion's spectrum at different distances from the excitation spot. (c) Trion's temperature as a function of position. The inset shows the measured temperature at the excitation spot, the continuous curve is a guide to the eye. (d) Trion's peak energy as a function of position. [149].	86
5.1	The MoS <sub>2</sub> charge tunable device. (a) schematic side view (the SiO <sub>2</sub> /Si substrate is not indicated here). (b) an optical microscope image [106].	90
5.2	PL spectra of the MoS <sub>2</sub> device under a 473 nm ( $10 \mu\text{W}$ ) laser excitation at $T = 300 \text{ K}$ . (a) PL spectra were taken from points A and B in Fig. 2d. The fitting was done by two Voigt functions. (b) A spatial map and (c) An histogram of the neutral exciton ( $X^0$ ) emission energy. (d) A spatial map and (e) An histogram of the FWHM of the experimental spectrum. The white lines in panels (b) and (d) indicate the MoS <sub>2</sub> monolayer with and without graphite contact on the monolayer.	92

5.3	Photoluminescence excitation (PLE) experiment at 100 $\mu$ W. T = 20 K and $V_g = 1.5$ V (neutral regime). (a) PL spectra (log scale). The spectra were normalized to 1 and multiplied arbitrary numbers to introduce vertical shift of the even distance in the log scale. (b) The exciton PL intensity. The spectrum color of (a) corresponds to the circle of (b), indicating the excitation laser energy. . . . .	93
5.4	(a) PL intensity on a logarithmic scale under cw laser excitation at 10 $\mu$ W as a function of photon emission energy and gate bias (b) PL spectra at selected gate voltages corresponding to the p-type (top), neutral (middle) and n-type doping regime (bottom). [106] . . . . .	95
5.5	(a) Monolayer MoS <sub>2</sub> is optically bright in a single-particle picture with $\Delta_{CB} > 0$ . (b) Local and non-local exchange interaction $U_{eh}$ reorders exciton spin configurations resulting in the lowest excitonic transition to be optically dark. This is schematically depicted as a flip of the conduction bands. (c) Trion fine structure in monolayer MoS <sub>2</sub> . [192] . . . . .	96
5.6	Density of states (left panel) and charge densities (right panel and inserts) of (a) perfect MoS <sub>2</sub> monolayer and monolayers with (b) Ad_S (sulfur adatoms) and (c) V_S (sulfur vacancies). Inserts show charge densities of the defect states. The right panel shows charge densities of band edge states. Ad_S has a shallow localized hole trap state next to the VB edge. V_S has two trap states: a shallow hole trap close to the VB edge and a deep localized electron trap 0.6 eV below the CB edge. The charge densities of the VB edge states are strongly perturbed by defects, while CB edge states remain unchanged. [193] . . . . .	97
5.7	(a) The difference in the exciton and trion energies, $\omega_A - \omega_{A^-}$ (symbols), as a function of Fermi energy $E_F$ . The red line is a linear fit to the $E_F$ dependence with a slope of 1.2 and an intercept of 18 meV. The latter determines the trion binding energy. Inset: representation of the dissociation of a trion into an exciton and an electron at the Fermi level [197]. (b) Evolution of the X <sup>+</sup> apparent binding energy measured in PL as a function of the applied gate bias. The continuous line is a guide to the eye [106].	98
5.8	Change in zone center phonons $\Delta\omega$ of (a) from experiment and (b) from DFT calculations as a function of electron concentration n. (c) Electron-phonon coupling of A <sub>1g</sub> and E <sub>2g</sub> <sup>1</sup> modes as a function of n. (d) Raman spectrum in the neutral regime, exhibiting the well-known E' and A'1 vibrational modes. (e) Peak position for both modes of the panel (d) as a function of gate bias. (a-c) Ref. [199]. (d-e) Data were taken from our charge tunable MoS <sub>2</sub> monolayer [106]. . . . .	100
5.9	Polarization-resolved photoluminescence (PL) emission under circularly polarized excitation and linearly polarized excitation for different gate voltages, + 3V (a), + 30 V (b) and - 20 V (c). Also shown is the energy-resolved degree of PL polarization (blue dots). [106] . . . . .	101
5.10	(a) Integrated intensity as a function of excitation power. (b) Degree of polarization as a function of excitation power. [106] . . . . .	102

5.11 The continuous (dashed) lines represent the ordering of the conduction bands in the excitonic (single-particle) picture. (a) Schematics of a negatively charged trion in the  $K^+$  valley corresponding to a spin-singlet state in which both electrons reside at opposite valleys. (b) State obtained after moving the exciton from the  $K^+$  to the  $K^-$  valley for the trion depicted in (a). This state is forbidden by the Pauli principle. (c) Negatively charged trion in the  $K^+$  valley corresponding to a spin-singlet state in which both electrons reside in the same valley  $K^+$ . (d) State obtained after moving the exciton from the  $K^+$  to the  $K^-$  valley for the trion depicted in (c). [106] . . . . . 103

5.12 (a) Total PL intensity under circular (black) and linear (red) excitation in the n-type regime for an excitation power of  $90 \mu\text{W}$  (top) and  $2 \mu\text{W}$  (bottom). (b) Total photoluminescence (PL) intensity under circular (black) and linear (red) excitation in the p-type regime at an excitation power of  $100 \mu\text{W}$  (top) and  $2 \mu\text{W}$  (bottom). Blue dots are the difference between these two curves. (c) Polarized PL emission under circular excitation and degree of circular polarization (blue dots) in the p-type regime at an excitation power of  $100 \mu\text{W}$ . [106] . . . . . 105

5.13 (a) Formation of a positively-charged trion in the  $K^+$  valley following right-handed circular polarization. (b) A trion in the  $K^+$  can either recombine radiatively or scatter to the opposite valley before recombination. (c) In a steady-state, the process (a) and (b) will lead to a spin and valley-polarization of the valence band. [106] . . . . . 106

A.1 PL spectrum ( $\text{MoSe}_2$  monolayer) under a continuous excitation before (black) and after (red) excitation with the same laser. (a) The first cycle for laser irradiation. A He-Ne laser ( $632.8 \text{ nm}$ ) of  $40 \mu\text{W}$  is used at  $T = 15 \text{ K}$ . (b) The same sample was exposed by the laser irradiation and cooling cycles from the RT to cryogenic. An excitation power of  $9 \text{ mW}$  under a wavelength of  $751 \text{ nm}$  is used at  $T = 20\text{K}$ . [149] . . . . . 113

A.2 Raman spectrum of the  $\text{MoS}_2$  monolayer upon excitation with a cw laser at  $473 \text{ nm}$  [106]. . . . . 114

A.3 Temperature vs resistance table of PT100 thermocouple (TC) from [technitemp.com](http://technitemp.com). . . . . 116

# List of Tables

2.1	Specifics of two tunable lasers from spectra-physics ( <a href="http://www.spectra-physics.com">www.spectra-physics.com</a> ) and sirah ( <a href="http://www.sirah.com">www.sirah.com</a> ) websites. . . . .	41
4.1	Parameters for the numerical calculation of trions and excitons profiles. . . . .	84

# Bibliography

- [1] W. H. Brattain and J. Bardeen. “Nature of the Forward Current in Germanium Point Contacts”. *Physical Review*, 74(2):231–232, 1948. doi:10.1103/PhysRev.74.231. URL <https://link.aps.org/doi/10.1103/PhysRev.74.231>, publisher: American Physical Society.
- [2] S. Ozdemir, Y. Yang, J. Yin, and A. Mishchenko. “Chapter 2 - Novel phenomena in two-dimensional semiconductors”. In D. Chi, K. E. J. Goh, and A. T. S. Wee, editors, “2D Semiconductor Materials and Devices”, *Materials Today*, pages 25–79. Elsevier, 2020. ISBN 978-0-12-816187-6. doi:10.1016/B978-0-12-816187-6.00002-9. URL <https://www.sciencedirect.com/science/article/pii/B9780128161876000029>.
- [3] T. Ochiai and M. Onoda. “Photonic analog of graphene model and its extension: Dirac cone, symmetry, and edge states”. *Physical Review B*, 80(15):155103, 2009. doi:10.1103/PhysRevB.80.155103. URL <https://link.aps.org/doi/10.1103/PhysRevB.80.155103>, publisher: American Physical Society.
- [4] A. Chaves, J. G. Azadani, H. Alsalman, D. R. da Costa, R. Frisenda, A. J. Chaves, S. H. Song, Y. D. Kim, D. He, J. Zhou, A. Castellanos-Gomez, F. M. Peeters, Z. Liu, C. L. Hinkle, S.-H. Oh, P. D. Ye, S. J. Koester, Y. H. Lee, P. Avouris, X. Wang, and T. Low. “Bandgap engineering of two-dimensional semiconductor materials”. *npj 2D Materials and Applications*, 4(1):1–21, August 2020. ISSN 2397-7132. doi:10.1038/s41699-020-00162-4. URL <https://www.nature.com/articles/s41699-020-00162-4>, number: 1 Publisher: Nature Publishing Group.
- [5] F. Bonaccorso, Z. Sun, T. Hasan, and A. C. Ferrari. “Graphene photonics and optoelectronics”. *Nature Photonics*, 4(9):611–622, September 2010. ISSN 1749-4893. doi:10.1038/nphoton.2010.186. URL <https://www.nature.com/articles/nphoton.2010.186>, number: 9 Publisher: Nature Publishing Group.
- [6] W. Choi, I. Lahiri, R. Seelaboyina, and Y. S. Kang. “Synthesis of Graphene and Its Applications: A Review”. *Critical Reviews in Solid State and Materials Sciences*, 35(1):52–71, 2010. ISSN 1040-8436. doi:10.1080/10408430903505036. URL <https://doi.org/10.1080/10408430903505036>, publisher: Taylor & Francis .eprint: <https://doi.org/10.1080/10408430903505036>.
- [7] A. G. Olabi, M. A. Abdelkareem, T. Wilberforce, and E. T. Sayed. “Application of graphene in energy storage device – A review”. *Renewable and Sustainable Energy Reviews*, 135:110026, 2021. ISSN

1364-0321. doi:10.1016/j.rser.2020.110026. URL <https://www.sciencedirect.com/science/article/pii/S1364032120303178>.

- [8] C. Si, Z. Sun, and F. Liu. "Strain engineering of graphene: a review". *Nanoscale*, 8(6):3207–3217, February 2016. ISSN 2040-3372. doi:10.1039/C5NR07755A. URL <https://pubs.rsc.org/en/content/articlelanding/2016/nr/c5nr07755a>, publisher: The Royal Society of Chemistry.
- [9] G. Jo, M. Choe, S. Lee, W. Park, Y. H. Kahng, and T. Lee. "The application of graphene as electrodes in electrical and optical devices". *Nanotechnology*, 23(11):112001, February 2012. ISSN 0957-4484. doi:10.1088/0957-4484/23/11/112001. URL <https://doi.org/10.1088/0957-4484/23/11/112001>, publisher: IOP Publishing.
- [10] Y. Cao, V. Fatemi, S. Fang, K. Watanabe, T. Taniguchi, E. Kaxiras, and P. Jarillo-Herrero. "Unconventional superconductivity in magic-angle graphene superlattices". *Nature*, 556(7699):43–50, April 2018. ISSN 1476-4687. doi:10.1038/nature26160. URL <https://www.nature.com/articles/nature26160>, number: 7699 Publisher: Nature Publishing Group.
- [11] W. Xu and T.-W. Lee. "Recent progress in fabrication techniques of graphene nanoribbons". *Materials Horizons*, 3(3):186–207, May 2016. ISSN 2051-6355. doi:10.1039/C5MH00288E. URL <https://pubs.rsc.org/en/content/articlelanding/2016/mh/c5mh00288e>, publisher: The Royal Society of Chemistry.
- [12] M. Autore, H. Engelkamp, F. D'Apuzzo, A. D. Gaspare, P. D. Pietro, I. L. Vecchio, M. Brahlek, N. Koirala, S. Oh, and S. Lupi. "Observation of Magnetoplasmons in Bi<sub>2</sub>Se<sub>3</sub> Topological Insulator". *ACS Photonics*, 2(9):1231–1235, September 2015. doi:10.1021/acsp Photonics.5b00036. URL <https://doi.org/10.1021/acsp Photonics.5b00036>, publisher: American Chemical Society.
- [13] Y. Hou, J. Kim, and R. Wu. "Magnetizing topological surface states of Bi<sub>2</sub>Se<sub>3</sub> with a CrI<sub>3</sub> monolayer". *Science Advances*, 5(5):eaaw1874. doi:10.1126/sciadv.aaw1874. URL <https://www.science.org/doi/10.1126/sciadv.aaw1874>, publisher: American Association for the Advancement of Science.
- [14] Q. Zhang, Z. Zhang, Z. Zhu, U. Schwingenschlögl, and Y. Cui. "Exotic Topological Insulator States and Topological Phase Transitions in Sb<sub>2</sub>Se<sub>3</sub>–Bi<sub>2</sub>Se<sub>3</sub> Heterostructures". *ACS Nano*, 6(3):2345–2352, March 2012. ISSN 1936-0851. doi:10.1021/nm2045328. URL <https://doi.org/10.1021/nm2045328>, publisher: American Chemical Society.
- [15] B. Monserrat and D. Vanderbilt. "Temperature Effects in the Band Structure of Topological Insulators". *Physical Review Letters*, 117(22):226801, 2016. doi:10.1103/PhysRevLett.117.226801. URL <https://link.aps.org/doi/10.1103/PhysRevLett.117.226801>, publisher: American Physical Society.

- [16] O. Breunig and Y. Ando. “Opportunities in topological insulator devices”. *Nature Reviews Physics*, pages 1–10, December 2021. ISSN 2522-5820. doi:10.1038/s42254-021-00402-6. URL <https://www.nature.com/articles/s42254-021-00402-6>, publisher: Nature Publishing Group.
- [17] J. Liu and T. Hesjedal. “Magnetic Topological Insulator Heterostructures: A Review”. *Advanced Materials*, n/a(n/a):2102427. ISSN 1521-4095. doi:10.1002/adma.202102427. URL <https://onlinelibrary.wiley.com/doi/abs/10.1002/adma.202102427>, \_eprint: <https://onlinelibrary.wiley.com/doi/pdf/10.1002/adma.202102427>.
- [18] X. Tan, Y. Liu, R. Liu, Z. Zhou, C. Liu, J.-L. Lan, Q. Zhang, Y.-H. Lin, and C.-W. Nan. “Synergistical Enhancement of Thermoelectric Properties in n-Type Bi<sub>2</sub>O<sub>2</sub>Se by Carrier Engineering and Hierarchical Microstructure”. *Advanced Energy Materials*, 9(31):1900354, 2019. ISSN 1614-6840. doi:10.1002/aenm.201900354. URL <https://onlinelibrary.wiley.com/doi/abs/10.1002/aenm.201900354>, \_eprint: <https://onlinelibrary.wiley.com/doi/pdf/10.1002/aenm.201900354>.
- [19] F. Yang, J. Wu, A. Suwardi, Y. Zhao, B. Liang, J. Jiang, J. Xu, D. Chi, K. Hippalgaonkar, J. Lu, and Z. Ni. “Gate-Tunable Polar Optical Phonon to Piezoelectric Scattering in Few-Layer Bi<sub>2</sub>O<sub>2</sub>Se for High-Performance Thermoelectrics”. *Advanced Materials*, 33(4):2004786, 2021. ISSN 1521-4095. doi:10.1002/adma.202004786. URL <https://onlinelibrary.wiley.com/doi/abs/10.1002/adma.202004786>, \_eprint: <https://onlinelibrary.wiley.com/doi/pdf/10.1002/adma.202004786>.
- [20] A. Patel, D. Singh, Y. Sonvane, P. B. Thakor, and R. Ahuja. “Bulk and monolayer As<sub>2</sub>S<sub>3</sub> as promising thermoelectric material with high conversion performance”. *Computational Materials Science*, 183:109913, 2020. ISSN 0927-0256. doi:10.1016/j.commatsci.2020.109913. URL <https://www.sciencedirect.com/science/article/pii/S0927025620304043>.
- [21] D. Ji, S. Cai, T. R. Paudel, H. Sun, C. Zhang, L. Han, Y. Wei, Y. Zang, M. Gu, Y. Zhang, W. Gao, H. Huyan, W. Guo, D. Wu, Z. Gu, E. Y. Tsymbal, P. Wang, Y. Nie, and X. Pan. “Freestanding crystalline oxide perovskites down to the monolayer limit”. *Nature*, 570(7759):87–90, June 2019. ISSN 1476-4687. doi:10.1038/s41586-019-1255-7. URL <https://www.nature.com/articles/s41586-019-1255-7>, number: 7759 Publisher: Nature Publishing Group.
- [22] P. Li, Y. Zhang, C. Liang, G. Xing, X. Liu, F. Li, X. Liu, X. Hu, G. Shao, and Y. Song. “Phase Pure 2D Perovskite for High-Performance 2D–3D Heterostructured Perovskite Solar Cells”. *Advanced Materials*, 30(52):1805323, 2018. ISSN 1521-4095. doi:10.1002/adma.201805323. URL <https://onlinelibrary.wiley.com/doi/abs/10.1002/adma.201805323>, \_eprint: <https://onlinelibrary.wiley.com/doi/pdf/10.1002/adma.201805323>.
- [23] X.-J. Hu, Y. Yang, C. Hou, and T.-X. Liang. “Thermodynamic and Electronic Properties of Two-Dimensional SrTiO<sub>3</sub>”. *The Journal of Physical Chemistry C*, 126(1):517–524, January 2022. ISSN 1932-7447. doi:10.

1021/acs.jpcc.1c07159. URL <https://doi.org/10.1021/acs.jpcc.1c07159>, publisher: American Chemical Society.

- [24] C. Gong, L. Li, Z. Li, H. Ji, A. Stern, Y. Xia, T. Cao, W. Bao, C. Wang, Y. Wang, Z. Q. Qiu, R. J. Cava, S. G. Louie, J. Xia, and X. Zhang. “Discovery of intrinsic ferromagnetism in two-dimensional van der Waals crystals”. *Nature*, 546(7657):265–269, June 2017. ISSN 1476-4687. doi:10.1038/nature22060. URL <https://www.nature.com/articles/nature22060>, number: 7657 Publisher: Nature Publishing Group.
- [25] M. Pizzochero and O. V. Yazyev. “Inducing Magnetic Phase Transitions in Monolayer CrI<sub>3</sub> via Lattice Deformations”. *The Journal of Physical Chemistry C*, 124(13):7585–7590, April 2020. ISSN 1932-7447. doi:10.1021/acs.jpcc.0c01873. URL <https://doi.org/10.1021/acs.jpcc.0c01873>, publisher: American Chemical Society.
- [26] R. M. Menezes, C. C. d. S. Silva, and M. V. Milošević. “Spin textures in chiral magnetic monolayers with suppressed nearest-neighbor exchange”. *Physical Review B*, 101(21):214429, 2020. doi:10.1103/PhysRevB.101.214429. URL <https://link.aps.org/doi/10.1103/PhysRevB.101.214429>, publisher: American Physical Society.
- [27] L. Jin, X. Zhang, Y. Liu, X. Dai, X. Shen, L. Wang, and G. Liu. “Two-dimensional Weyl nodal-line semimetal in a  $d^0$  ferromagnetic  $\mathcal{K}_{-2}\mathcal{N}$  monolayer with a high Curie temperature”. *Physical Review B*, 102(12):125118, 2020. doi:10.1103/PhysRevB.102.125118. URL <https://link.aps.org/doi/10.1103/PhysRevB.102.125118>, publisher: American Physical Society.
- [28] S. Wan, Y. Li, W. Li, X. Mao, C. Wang, C. Chen, J. Dong, A. Nie, J. Xiang, Z. Liu, W. Zhu, and H. Zeng. “Non-volatile Ferroelectric Memory Effect in Ultrathin  $\alpha$ -In<sub>2</sub>Se<sub>3</sub>”. *Advanced Functional Materials*, 29(20):1808606, 2019. ISSN 1616-3028. doi:10.1002/adfm.201808606. URL <https://onlinelibrary.wiley.com/doi/abs/10.1002/adfm.201808606>, eprint: <https://onlinelibrary.wiley.com/doi/pdf/10.1002/adfm.201808606>.
- [29] J. R. Schaibley, H. Yu, G. Clark, P. Rivera, J. S. Ross, K. L. Seyler, W. Yao, and X. Xu. “Valleytronics in 2D materials”. *Nature Reviews Materials*, 1(11):1–15, August 2016. ISSN 2058-8437. doi:10.1038/natrevmats.2016.55. URL <https://www.nature.com/articles/natrevmats201655>, number: 11 Publisher: Nature Publishing Group.
- [30] K.-A. N. Duerloo, Y. Li, and E. J. Reed. “Structural phase transitions in two-dimensional Mo- and W-dichalcogenide monolayers”. *Nature Communications*, 5(1):4214, July 2014. ISSN 2041-1723. doi:10.1038/ncomms5214. URL <https://www.nature.com/articles/ncomms5214>, number: 1 Publisher: Nature Publishing Group.

- [31] B. Ouyang, G. Lan, Y. Guo, Z. Mi, and J. Song. “Phase engineering of monolayer transition-metal dichalcogenide through coupled electron doping and lattice deformation”. *Applied Physics Letters*, 107(19):191903, November 2015. ISSN 0003-6951. doi:10.1063/1.4934836. URL <https://aip.scitation.org/doi/10.1063/1.4934836>, publisher: American Institute of Physics.
- [32] M. Bernardi, C. Ataca, M. Palummo, and J. C. Grossman. “Optical and Electronic Properties of Two-Dimensional Layered Materials”. *Nanophotonics*, 6(2):479–493, March 2017. ISSN 2192-8614. doi:10.1515/nanoph-2015-0030. URL <https://www.degruyter.com/document/doi/10.1515/nanoph-2015-0030/html>, publisher: De Gruyter.
- [33] K. F. Mak, C. Lee, J. Hone, J. Shan, and T. F. Heinz. “Atomically Thin  $\text{MoS}_2$ : A New Direct-Gap Semiconductor”. *Physical Review Letters*, 105(13):136805, 2010. doi:10.1103/PhysRevLett.105.136805. URL <https://link.aps.org/doi/10.1103/PhysRevLett.105.136805>, publisher: American Physical Society.
- [34] A. Splendiani, L. Sun, Y. Zhang, T. Li, J. Kim, C.-Y. Chim, G. Galli, and F. Wang. “Emerging Photoluminescence in Monolayer  $\text{MoS}_2$ ”. *Nano Letters*, 10(4):1271–1275, April 2010. ISSN 1530-6984. doi:10.1021/nl903868w. URL <https://doi.org/10.1021/nl903868w>, publisher: American Chemical Society.
- [35] K. F. Mak and J. Shan. “Photonics and optoelectronics of 2D semiconductor transition metal dichalcogenides”. *Nature Photonics*, 10(4):216–226, April 2016. ISSN 1749-4893. doi:10.1038/nphoton.2015.282. URL <https://www.nature.com/articles/nphoton.2015.282>, number: 4 Publisher: Nature Publishing Group.
- [36] S. M. Bahauddin, H. Robotjazi, and I. Thomann. “Broadband Absorption Engineering to Enhance Light Absorption in Monolayer  $\text{MoS}_2$ ”. *ACS Photonics*, 3(5):853–862, May 2016. doi:10.1021/acsp Photonics.6b00081. URL <https://doi.org/10.1021/acsp Photonics.6b00081>, publisher: American Chemical Society.
- [37] Y. You, X.-X. Zhang, T. C. Berkelbach, M. S. Hybertsen, D. R. Reichman, and T. F. Heinz. “Observation of biexcitons in monolayer  $\text{WSe}_2$ ”. *Nature Physics*, 11(6):477–481, June 2015. ISSN 1745-2481. doi:10.1038/nphys3324. URL <https://www.nature.com/articles/nphys3324>, number: 6 Publisher: Nature Publishing Group.
- [38] I. Epstein, B. Terrés, A. J. Chaves, V.-V. Pusapati, D. A. Rhodes, B. Frank, V. Zimmermann, Y. Qin, K. Watanabe, T. Taniguchi, H. Giessen, S. Tongay, J. C. Hone, N. M. R. Peres, and F. H. L. Koppens. “Near-Unity Light Absorption in a Monolayer  $\text{WS}_2$  Van der Waals Heterostructure Cavity”. *Nano Letters*, 20(5):3545–3552, May 2020. ISSN 1530-6984. doi:10.1021/acs.nanolett.0c00492. URL <https://doi.org/10.1021/acs.nanolett.0c00492>, publisher: American Chemical Society.

- [39] X. Huang, X. Feng, L. Chen, L. Wang, W. C. Tan, L. Huang, and K.-W. Ang. “Fabry-Perot cavity enhanced light-matter interactions in two-dimensional van der Waals heterostructure”. *Nano Energy*, 62:667–673, 2019. ISSN 2211-2855. doi:10.1016/j.nanoen.2019.05.090. URL <https://www.sciencedirect.com/science/article/pii/S2211285519305026>.
- [40] J. Frenkel. “On the Transformation of light into Heat in Solids. I”. *Physical Review*, 37(1):17–44, 1931. doi:10.1103/PhysRev.37.17. URL <https://link.aps.org/doi/10.1103/PhysRev.37.17>, publisher: American Physical Society.
- [41] D. C. Mattis and J. P. Gallinar. “What is the Mass of an Exciton?” *Physical Review Letters*, 53(14):1391–1393, 1984. doi:10.1103/PhysRevLett.53.1391. URL <https://link.aps.org/doi/10.1103/PhysRevLett.53.1391>, publisher: American Physical Society.
- [42] S. B. Nam, D. C. Reynolds, C. W. Litton, R. J. Almassy, T. C. Collins, and C. M. Wolfe. “Free-exciton energy spectrum in GaAs”. *Physical Review B*, 13(2):761–767, 1976. doi:10.1103/PhysRevB.13.761. URL <https://link.aps.org/doi/10.1103/PhysRevB.13.761>, publisher: American Physical Society.
- [43] G. Bastard, E. E. Mendez, L. L. Chang, and L. Esaki. “Exciton binding energy in quantum wells”. *Physical Review B*, 26(4):1974–1979, 1982. doi:10.1103/PhysRevB.26.1974. URL <https://link.aps.org/doi/10.1103/PhysRevB.26.1974>, publisher: American Physical Society.
- [44] I. Brener, W. H. Knox, K. W. Goossen, and J. E. Cunningham. “Shallow quantum well excitons: 2D or 3D?” *Physical Review Letters*, 70(3):319–322, 1993. doi:10.1103/PhysRevLett.70.319. URL <https://link.aps.org/doi/10.1103/PhysRevLett.70.319>, publisher: American Physical Society.
- [45] A. Chernikov, T. C. Berkelbach, H. M. Hill, A. Rigosi, Y. Li, O. B. Aslan, D. R. Reichman, M. S. Hybertsen, and T. F. Heinz. “Exciton Binding Energy and Nonhydrogenic Rydberg Series in Monolayer  $\text{WS}_2$ ”. *Physical Review Letters*, 113(7):076802, 2014. doi:10.1103/PhysRevLett.113.076802. URL <https://link.aps.org/doi/10.1103/PhysRevLett.113.076802>, publisher: American Physical Society.
- [46] T. C. Berkelbach, M. S. Hybertsen, and D. R. Reichman. “Theory of neutral and charged excitons in monolayer transition metal dichalcogenides”. *Physical Review B*, 88(4):045318, 2013. doi:10.1103/PhysRevB.88.045318. URL <https://link.aps.org/doi/10.1103/PhysRevB.88.045318>, publisher: American Physical Society.
- [47] G. Wang, A. Chernikov, M. M. Glazov, T. F. Heinz, X. Marie, T. Amand, and B. Urbaszek. “Colloquium: Excitons in atomically thin transition metal dichalcogenides”. *Reviews of Modern Physics*, 90(2):021001, 2018. doi:10.1103/RevModPhys.90.021001. URL <https://link.aps.org/doi/10.1103/RevModPhys.90.021001>, publisher: American Physical Society.

- [48] H. M. Hill, A. F. Rigosi, C. Roquelet, A. Chernikov, T. C. Berkelbach, D. R. Reichman, M. S. Hybertsen, L. E. Brus, and T. F. Heinz. “Observation of Excitonic Rydberg States in Monolayer MoS<sub>2</sub> and WS<sub>2</sub> by Photoluminescence Excitation Spectroscopy”. *Nano Letters*, 15(5):2992–2997, May 2015. ISSN 1530-6984. doi:10.1021/nl504868p. URL <https://doi.org/10.1021/nl504868p>, publisher: American Chemical Society.
- [49] E. Liu, J. van Baren, T. Taniguchi, K. Watanabe, Y.-C. Chang, and C. H. Lui. “Magnetophotoluminescence of exciton Rydberg states in monolayer  $\mathrm{WS}_2$ ”. *Physical Review B*, 99(20):205420, 2019. doi:10.1103/PhysRevB.99.205420. URL <https://link.aps.org/doi/10.1103/PhysRevB.99.205420>, publisher: American Physical Society.
- [50] C. Kastl, C. T. Chen, R. J. Koch, B. Schuler, T. R. Kuykendall, A. Bostwick, C. Jozwiak, T. Seyller, E. Rotenberg, A. Weber-Bargioni, S. Aloni, and A. M. Schwartzberg. “Multimodal spectromicroscopy of monolayer WS<sub>2</sub> enabled by ultra-clean van der Waals epitaxy”. *2D Materials*, 5(4):045010, July 2018. ISSN 2053-1583. doi:10.1088/2053-1583/aad21c. URL <https://doi.org/10.1088/2053-1583/aad21c>, publisher: IOP Publishing.
- [51] A. Kormányos, V. Zólyomi, N. D. Drummond, and G. Burkard. “Spin-Orbit Coupling, Quantum Dots, and Qubits in Monolayer Transition Metal Dichalcogenides”. *Physical Review X*, 4(1):011034, 2014. doi:10.1103/PhysRevX.4.011034. URL <https://link.aps.org/doi/10.1103/PhysRevX.4.011034>, publisher: American Physical Society.
- [52] H. Nakamura, A. Mohammed, P. Rosenzweig, K. Matsuda, K. Nowakowski, K. Küster, P. Wochner, S. Ibrahimkuty, U. Wedig, H. Hussain, J. Rawle, C. Nicklin, B. Stuhlhofer, G. Cristiani, G. Logvenov, H. Takagi, and U. Starke. “Spin splitting and strain in epitaxial monolayer  $\mathrm{WSe}_2$  on graphene”. *Physical Review B*, 101(16):165103, 2020. doi:10.1103/PhysRevB.101.165103. URL <https://link.aps.org/doi/10.1103/PhysRevB.101.165103>, publisher: American Physical Society.
- [53] W. Lee, Y. Lin, L.-S. Lu, W.-C. Chueh, M. Liu, X. Li, W.-H. Chang, R. A. Kaindl, and C.-K. Shih. “Time-resolved ARPES Determination of a Quasi-Particle Band Gap and Hot Electron Dynamics in Monolayer MoS<sub>2</sub>”. *Nano Letters*, 21(17):7363–7370, September 2021. ISSN 1530-6984. doi:10.1021/acs.nanolett.1c02674. URL <https://doi.org/10.1021/acs.nanolett.1c02674>, publisher: American Chemical Society.
- [54] Y. Zhang, T.-R. Chang, B. Zhou, Y.-T. Cui, H. Yan, Z. Liu, F. Schmitt, J. Lee, R. Moore, Y. Chen, H. Lin, H.-T. Jeng, S.-K. Mo, Z. Hussain, A. Bansil, and Z.-X. Shen. “Direct observation of the transition from indirect to direct bandgap in atomically thin epitaxial MoSe<sub>2</sub>”. *Nature Nanotechnology*, 9(2):111–115, February 2014. ISSN 1748-3395. doi:10.1038/nnano.2013.277. URL <https://www.nature.com/articles/nnano.2013.277>, number: 2 Publisher: Nature Publishing Group.
- [55] A. Kormányos, G. Burkard, M. Gmitra, J. Fabian, V. Zólyomi, N. D. Drummond, and V. Fal’ko. “ $k \cdot p$  theory for two-dimensional transition metal dichalcogenide semiconductors”. *2D Materials*, 2(2):022001, April

2015. ISSN 2053-1583. doi:10.1088/2053-1583/2/2/022001. URL <https://doi.org/10.1088/2053-1583/2/2/022001>, publisher: IOP Publishing.

- [56] J. P. Echeverry, B. Urbaszek, T. Amand, X. Marie, and I. C. Gerber. “Splitting between bright and dark excitons in transition metal dichalcogenide monolayers”. *Physical Review B*, 93(12):121107, 2016. doi: 10.1103/PhysRevB.93.121107. URL <https://link.aps.org/doi/10.1103/PhysRevB.93.121107>, publisher: American Physical Society.
- [57] G. Wang, C. Robert, A. Suslu, B. Chen, S. Yang, S. Alamdari, I. C. Gerber, T. Amand, X. Marie, S. Tongay, and B. Urbaszek. “Spin-orbit engineering in transition metal dichalcogenide alloy monolayers”. *Nature Communications*, 6(1):10110, December 2015. ISSN 2041-1723. doi:10.1038/ncomms10110. URL <https://www.nature.com/articles/ncomms10110>, number: 1 Publisher: Nature Publishing Group.
- [58] X.-X. Zhang, T. Cao, Z. Lu, Y.-C. Lin, F. Zhang, Y. Wang, Z. Li, J. C. Hone, J. A. Robinson, D. Smirnov, S. G. Louie, and T. F. Heinz. “Magnetic brightening and control of dark excitons in monolayer WSe<sub>2</sub>”. *Nature Nanotechnology*, 12(9):883–888, September 2017. ISSN 1748-3395. doi:10.1038/nnano.2017.105. URL <https://www.nature.com/articles/nnano.2017.105>, number: 9 Publisher: Nature Publishing Group.
- [59] M. R. Molas, C. Faugeras, A. O. Slobodeniuk, K. Nogajewski, M. Bartos, D. M. Basko, and M. Potemski. “Brightening of dark excitons in monolayers of semiconducting transition metal dichalcogenides”. *2D Materials*, 4(2):021003, January 2017. ISSN 2053-1583. doi:10.1088/2053-1583/aa5521. URL <https://doi.org/10.1088/2053-1583/aa5521>, publisher: IOP Publishing.
- [60] C. Robert, T. Amand, F. Cadiz, D. Lagarde, E. Courtade, M. Manca, T. Taniguchi, K. Watanabe, B. Urbaszek, and X. Marie. “Fine structure and lifetime of dark excitons in transition metal dichalcogenide monolayers”. *Physical Review B*, 96(15):155423, 2017. doi:10.1103/PhysRevB.96.155423. URL <https://link.aps.org/doi/10.1103/PhysRevB.96.155423>, publisher: American Physical Society.
- [61] T. Cao, G. Wang, W. Han, H. Ye, C. Zhu, J. Shi, Q. Niu, P. Tan, E. Wang, B. Liu, and J. Feng. “Valley-selective circular dichroism of monolayer molybdenum disulphide”. *Nature Communications*, 3(1):887, June 2012. ISSN 2041-1723. doi:10.1038/ncomms1882. URL <https://www.nature.com/articles/ncomms1882>, number: 1 Publisher: Nature Publishing Group.
- [62] A. M. Jones, H. Yu, N. J. Ghimire, S. Wu, G. Aivazian, J. S. Ross, B. Zhao, J. Yan, D. G. Mandrus, D. Xiao, W. Yao, and X. Xu. “Optical generation of excitonic valley coherence in monolayer WSe<sub>2</sub>”. *Nature Nanotechnology*, 8(9):634–638, September 2013. ISSN 1748-3395. doi:10.1038/nnano.2013.151. URL <https://www.nature.com/articles/nnano.2013.151>, number: 9 Publisher: Nature Publishing Group.

- [63] K. Hao, G. Moody, F. Wu, C. K. Dass, L. Xu, C.-H. Chen, L. Sun, M.-Y. Li, L.-J. Li, A. H. MacDonald, and X. Li. “Direct measurement of exciton valley coherence in monolayer WSe<sub>2</sub>”. *Nature Physics*, 12(7):677–682, July 2016. ISSN 1745-2481. doi:10.1038/nphys3674. URL <https://www.nature.com/articles/nphys3674>, number: 7 Publisher: Nature Publishing Group.
- [64] J. You, M. D. Hossain, and Z. Luo. “Synthesis of 2D transition metal dichalcogenides by chemical vapor deposition with controlled layer number and morphology”. *Nano Convergence*, 5(1):26, 2018. ISSN 2196-5404. doi:10.1186/s40580-018-0158-x. URL <https://doi.org/10.1186/s40580-018-0158-x>.
- [65] K. M. McCreary, A. T. Hanbicki, J. T. Robinson, E. Cobas, J. C. Culbertson, A. L. Friedman, G. G. Jernigan, and B. T. Jonker. “Large-Area Synthesis of Continuous and Uniform MoS<sub>2</sub> Monolayer Films on Graphene”. *Advanced Functional Materials*, 24(41):6449–6454, 2014. ISSN 1616-3028. doi:10.1002/adfm.201401511. URL <https://onlinelibrary.wiley.com/doi/abs/10.1002/adfm.201401511>, eprint: <https://onlinelibrary.wiley.com/doi/pdf/10.1002/adfm.201401511>.
- [66] X. Wang, Y. Gong, G. Shi, W. L. Chow, K. Keyshar, G. Ye, R. Vajtai, J. Lou, Z. Liu, E. Ringe, B. K. Tay, and P. M. Ajayan. “Chemical Vapor Deposition Growth of Crystalline Monolayer MoSe<sub>2</sub>”. *ACS Nano*, 8(5):5125–5131, May 2014. ISSN 1936-0851. doi:10.1021/nn501175k. URL <https://doi.org/10.1021/nn501175k>, publisher: American Chemical Society.
- [67] C. Lan, Z. Zhou, Z. Zhou, C. Li, L. Shu, L. Shen, D. Li, R. Dong, S. Yip, and J. C. Ho. “Wafer-scale synthesis of monolayer WS<sub>2</sub> for high-performance flexible photodetectors by enhanced chemical vapor deposition”. *Nano Research*, 11(6):3371–3384, June 2018. ISSN 1998-0000. doi:10.1007/s12274-017-1941-4. URL <https://doi.org/10.1007/s12274-017-1941-4>.
- [68] D. Zhu, H. Shu, F. Jiang, D. Lv, V. Asokan, O. Omar, J. Yuan, Z. Zhang, and C. Jin. “Capture the growth kinetics of CVD growth of two-dimensional MoS<sub>2</sub>”. *npj 2D Materials and Applications*, 1(1):1–8, May 2017. ISSN 2397-7132. doi:10.1038/s41699-017-0010-x. URL <https://www.nature.com/articles/s41699-017-0010-x>, number: 1 Publisher: Nature Publishing Group.
- [69] D. Li, Z. Li, P. Chen, L. Pi, N. Zuo, Q. Peng, X. Zhou, and T. Zhai. “Two-Dimensional Metal Chalcogenide Heterostructures: Designed Growth and Emerging Novel Applications”. *Advanced Materials Interfaces*, 8(15):2100515, 2021. ISSN 2196-7350. doi:10.1002/admi.202100515. URL <https://onlinelibrary.wiley.com/doi/abs/10.1002/admi.202100515>, eprint: <https://onlinelibrary.wiley.com/doi/pdf/10.1002/admi.202100515>.
- [70] H. Yu, M. Liao, W. Zhao, G. Liu, X. J. Zhou, Z. Wei, X. Xu, K. Liu, Z. Hu, K. Deng, S. Zhou, J.-A. Shi, L. Gu, C. Shen, T. Zhang, L. Du, L. Xie, J. Zhu, W. Chen, R. Yang, D. Shi, and G. Zhang. “Wafer-Scale Growth and

Transfer of Highly-Oriented Monolayer MoS<sub>2</sub> Continuous Films”. *ACS Nano*, 11(12):12001–12007, December 2017. ISSN 1936-0851. doi:10.1021/acs.nano.7b03819. URL <https://doi.org/10.1021/acs.nano.7b03819>, publisher: American Chemical Society.

- [71] S. Xie, L. Tu, Y. Han, L. Huang, K. Kang, K. U. Lao, P. Poddar, C. Park, D. A. Muller, R. A. DiStasio, and J. Park. “Coherent, atomically thin transition-metal dichalcogenide superlattices with engineered strain”. *Science*, 359(6380):1131–1136, March 2018. doi:10.1126/science.aao5360. URL <https://www.science.org/doi/10.1126/science.aao5360>, publisher: American Association for the Advancement of Science.
- [72] J. Park, N. Choudhary, J. Smith, G. Lee, M. Kim, and W. Choi. “Thickness modulated MoS<sub>2</sub> grown by chemical vapor deposition for transparent and flexible electronic devices”. *Applied Physics Letters*, 106(1):012104, January 2015. ISSN 0003-6951. doi:10.1063/1.4905476. URL <https://aip.scitation.org/doi/10.1063/1.4905476>, publisher: American Institute of Physics.
- [73] C. H. Naylor, W. M. Parkin, J. Ping, Z. Gao, Y. R. Zhou, Y. Kim, F. Streller, R. W. Carpick, A. M. Rappe, M. Drndić, J. M. Kikkawa, and A. T. C. Johnson. “Monolayer Single-Crystal 1T’-MoTe<sub>2</sub> Grown by Chemical Vapor Deposition Exhibits Weak Antilocalization Effect”. *Nano Letters*, 16(7):4297–4304, July 2016. ISSN 1530-6984. doi:10.1021/acs.nanolett.6b01342. URL <https://doi.org/10.1021/acs.nanolett.6b01342>, publisher: American Chemical Society.
- [74] X. Wang, H. Feng, Y. Wu, and L. Jiao. “Controlled Synthesis of Highly Crystalline MoS<sub>2</sub> Flakes by Chemical Vapor Deposition”. *Journal of the American Chemical Society*, 135(14):5304–5307, April 2013. ISSN 0002-7863. doi:10.1021/ja4013485. URL <https://doi.org/10.1021/ja4013485>, publisher: American Chemical Society.
- [75] P. Yang, S. Zhang, S. Pan, B. Tang, Y. Liang, X. Zhao, Z. Zhang, J. Shi, Y. Huan, Y. Shi, S. J. Pennycook, Z. Ren, G. Zhang, Q. Chen, X. Zou, Z. Liu, and Y. Zhang. “Epitaxial Growth of Centimeter-Scale Single-Crystal MoS<sub>2</sub> Monolayer on Au(111)”. *ACS Nano*, 14(4):5036–5045, April 2020. ISSN 1936-0851. doi:10.1021/acs.nano.0c01478. URL <https://doi.org/10.1021/acs.nano.0c01478>, publisher: American Chemical Society.
- [76] J. Li, S. Wang, Q. Jiang, H. Qian, S. Hu, H. Kang, C. Chen, X. Zhan, A. Yu, S. Zhao, Y. Zhang, Z. Chen, Y. Sui, S. Qiao, G. Yu, S. Peng, Z. Jin, and X. Liu. “Single-Crystal MoS<sub>2</sub> Monolayer Wafer Grown on Au (111) Film Substrates”. *Small*, 17(30):2100743, 2021. ISSN 1613-6829. doi:10.1002/sml.202100743. URL <https://onlinelibrary.wiley.com/doi/abs/10.1002/sml.202100743>, eprint: <https://onlinelibrary.wiley.com/doi/pdf/10.1002/sml.202100743>.
- [77] S. Balasubramanyam, M. J. M. Merckx, M. A. Verheijen, W. M. M. Kessels, A. J. M. Mackus, and A. A.

Bol. "Area-Selective Atomic Layer Deposition of Two-Dimensional WS<sub>2</sub> Nanolayers". *ACS Materials Letters*, 2(5):511–518, May 2020. doi:10.1021/acsmaterialslett.0c00093. URL <https://doi.org/10.1021/acsmaterialslett.0c00093>, publisher: American Chemical Society.

[78] S. Seo, S. Kim, H. Choi, J. Lee, H. Yoon, G. Piao, J.-C. Park, Y. Jung, J. Song, S. Y. Jeong, H. Park, and S. Lee. "Direct In Situ Growth of Centimeter-Scale Multi-Heterojunction MoS<sub>2</sub>/WS<sub>2</sub>/WSe<sub>2</sub> Thin-Film Catalyst for Photo-Electrochemical Hydrogen Evolution". *Advanced Science*, 6(13):1900301, 2019. ISSN 2198-3844. doi:10.1002/advs.201900301. URL <https://onlinelibrary.wiley.com/doi/abs/10.1002/advs.201900301>, eprint: <https://onlinelibrary.wiley.com/doi/pdf/10.1002/advs.201900301>.

[79] Q. Zhang, L. Mei, X. Cao, Y. Tang, and Z. Zeng. "Intercalation and exfoliation chemistries of transition metal dichalcogenides". *Journal of Materials Chemistry A*, 8(31):15417–15444, August 2020. ISSN 2050-7496. doi:10.1039/D0TA03727C. URL <https://pubs.rsc.org/en/content/articlelanding/2020/ta/d0ta03727c>, publisher: The Royal Society of Chemistry.

[80] V. Nicolosi, M. Chhowalla, M. G. Kanatzidis, M. S. Strano, and J. N. Coleman. "Liquid Exfoliation of Layered Materials". *Science*, 340(6139):1226419, June 2013. doi:10.1126/science.1226419. URL <https://www.science.org/doi/10.1126/science.1226419>, publisher: American Association for the Advancement of Science.

[81] C. Zhang, D.-F. Hu, J.-W. Xu, M.-Q. Ma, H. Xing, K. Yao, J. Ji, and Z.-K. Xu. "Polyphenol-Assisted Exfoliation of Transition Metal Dichalcogenides into Nanosheets as Photothermal Nanocarriers for Enhanced Antibiofilm Activity". *ACS Nano*, 12(12):12347–12356, December 2018. ISSN 1936-0851. doi:10.1021/acsnano.8b06321. URL <https://doi.org/10.1021/acsnano.8b06321>, publisher: American Chemical Society.

[82] R. J. Smith, P. J. King, M. Lotya, C. Wirtz, U. Khan, S. De, A. O'Neill, G. S. Duesberg, J. C. Grunlan, G. Moriarty, J. Chen, J. Wang, A. I. Minett, V. Nicolosi, and J. N. Coleman. "Large-Scale Exfoliation of Inorganic Layered Compounds in Aqueous Surfactant Solutions". *Advanced Materials*, 23(34):3944–3948, 2011. ISSN 1521-4095. doi:10.1002/adma.201102584. URL <https://onlinelibrary.wiley.com/doi/abs/10.1002/adma.201102584>, eprint: <https://onlinelibrary.wiley.com/doi/pdf/10.1002/adma.201102584>.

[83] A. Ciesielski and P. Samorì. "Graphene via sonication assisted liquid-phase exfoliation". *Chemical Society Reviews*, 43(1):381–398, December 2013. ISSN 1460-4744. doi:10.1039/C3CS60217F. URL <https://pubs.rsc.org/en/content/articlelanding/2014/cs/c3cs60217f>, publisher: The Royal Society of Chemistry.

[84] C. Huo, Z. Yan, X. Song, and H. Zeng. "2D materials via liquid exfoliation: a review on fabrication and applications". *Science Bulletin*, 60(23):1994–2008, 2015. ISSN 2095-9273. doi:10.1007/s11434-015-0936-3. URL <https://www.sciencedirect.com/science/article/pii/S2095927316302535>.

- [85] Y. Liu, N. O. Weiss, X. Duan, H.-C. Cheng, Y. Huang, and X. Duan. “Van der Waals heterostructures and devices”. *Nature Reviews Materials*, 1(9):1–17, July 2016. ISSN 2058-8437. doi:10.1038/natrevmats.2016.42. URL <https://www.nature.com/articles/natrevmats201642>, number: 9 Publisher: Nature Publishing Group.
- [86] A. Castellanos-Gomez, M. Buscema, R. Molenaar, V. Singh, L. Janssen, H. S. J. v. d. Zant, and G. A. Steele. “Deterministic transfer of two-dimensional materials by all-dry viscoelastic stamping”. *2D Materials*, 1(1):011002, April 2014. ISSN 2053-1583. doi:10.1088/2053-1583/1/1/011002. URL <https://doi.org/10.1088/2053-1583/1/1/011002>, publisher: IOP Publishing.
- [87] Y. Huang, Y.-H. Pan, R. Yang, L.-H. Bao, L. Meng, H.-L. Luo, Y.-Q. Cai, G.-D. Liu, W.-J. Zhao, Z. Zhou, L.-M. Wu, Z.-L. Zhu, M. Huang, L.-W. Liu, L. Liu, P. Cheng, K.-H. Wu, S.-B. Tian, C.-Z. Gu, Y.-G. Shi, Y.-F. Guo, Z. G. Cheng, J.-P. Hu, L. Zhao, G.-H. Yang, E. Sutter, P. Sutter, Y.-L. Wang, W. Ji, X.-J. Zhou, and H.-J. Gao. “Universal mechanical exfoliation of large-area 2D crystals”. *Nature Communications*, 11(1):2453, May 2020. ISSN 2041-1723. doi:10.1038/s41467-020-16266-w. URL <https://www.nature.com/articles/s41467-020-16266-w>, number: 1 Publisher: Nature Publishing Group.
- [88] M. Velický, G. E. Donnelly, W. R. Hendren, S. McFarland, D. Scullion, W. J. I. DeBenedetti, G. C. Correa, Y. Han, A. J. Wain, M. A. Hines, D. A. Muller, K. S. Novoselov, H. D. Abruña, R. M. Bowman, E. J. G. Santos, and F. Huang. “Mechanism of Gold-Assisted Exfoliation of Centimeter-Sized Transition-Metal Dichalcogenide Monolayers”. *ACS Nano*, 12(10):10463–10472, October 2018. ISSN 1936-0851. doi:10.1021/acsnano.8b06101. URL <https://doi.org/10.1021/acsnano.8b06101>, publisher: American Chemical Society.
- [89] F. He, Y. Zhou, Z. Ye, S.-H. Cho, J. Jeong, X. Meng, and Y. Wang. “Moiré Patterns in 2D Materials: A Review”. *ACS Nano*, 15(4):5944–5958, April 2021. ISSN 1936-0851. doi:10.1021/acsnano.0c10435. URL <https://doi.org/10.1021/acsnano.0c10435>, publisher: American Chemical Society.
- [90] P. Rivera, J. R. Schaibley, A. M. Jones, J. S. Ross, S. Wu, G. Aivazian, P. Klement, K. Seyler, G. Clark, N. J. Ghimire, J. Yan, D. G. Mandrus, W. Yao, and X. Xu. “Observation of long-lived interlayer excitons in monolayer MoSe<sub>2</sub>–WSe<sub>2</sub> heterostructures”. *Nature Communications*, 6(1):6242, February 2015. ISSN 2041-1723. doi:10.1038/ncomms7242. URL <https://www.nature.com/articles/ncomms7242>, number: 1 Publisher: Nature Publishing Group.
- [91] P. Nagler, G. Plechinger, M. V. Ballottin, A. Mitioglu, S. Meier, N. Paradiso, C. Strunk, A. Chernikov, P. C. M. Christianen, C. Schüller, and T. Korn. “Interlayer exciton dynamics in a dichalcogenide monolayer heterostructure”. *2D Materials*, 4(2):025112, June 2017. ISSN 2053-1583. doi:10.1088/2053-1583/aa7352. URL <https://doi.org/10.1088/2053-1583/aa7352>, publisher: IOP Publishing.

- [92] S. Pak, J. Lee, Y.-W. Lee, A.-R. Jang, S. Ahn, K. Y. Ma, Y. Cho, J. Hong, S. Lee, H. Y. Jeong, H. Im, H. S. Shin, S. M. Morris, S. Cha, J. I. Sohn, and J. M. Kim. “Strain-Mediated Interlayer Coupling Effects on the Excitonic Behaviors in an Epitaxially Grown MoS<sub>2</sub>/WS<sub>2</sub> van der Waals Heterobilayer”. *Nano Letters*, 17(9):5634–5640, September 2017. ISSN 1530-6984. doi:10.1021/acs.nanolett.7b02513. URL <https://doi.org/10.1021/acs.nanolett.7b02513>, publisher: American Chemical Society.
- [93] D. Rhodes, S. H. Chae, R. Ribeiro-Palau, and J. Hone. “Disorder in van der Waals heterostructures of 2D materials”. *Nature Materials*, 18(6):541–549, June 2019. ISSN 1476-4660. doi:10.1038/s41563-019-0366-8. URL <https://www.nature.com/articles/s41563-019-0366-8>, number: 6 Publisher: Nature Publishing Group.
- [94] A. Raja, L. Waldecker, J. Zipfel, Y. Cho, S. Brem, J. D. Ziegler, M. Kulig, T. Taniguchi, K. Watanabe, E. Malic, T. F. Heinz, T. C. Berkelbach, and A. Chernikov. “Dielectric disorder in two-dimensional materials”. *Nature Nanotechnology*, 14(9):832–837, September 2019. ISSN 1748-3395. doi:10.1038/s41565-019-0520-0. URL <https://www.nature.com/articles/s41565-019-0520-0>, number: 9 Publisher: Nature Publishing Group.
- [95] S. Feng, C. Cong, S. Konabe, J. Zhang, J. Shang, Y. Chen, C. Zou, B. Cao, L. Wu, N. Peimyoo, B. Zhang, and T. Yu. “Engineering Valley Polarization of Monolayer WS<sub>2</sub>: A Physical Doping Approach”. *Small*, 15(12):1805503, 2019. ISSN 1613-6829. doi:10.1002/smll.201805503. URL <https://onlinelibrary.wiley.com/doi/abs/10.1002/smll.201805503>, eprint: <https://onlinelibrary.wiley.com/doi/pdf/10.1002/smll.201805503>.
- [96] F. Cadiz, E. Courtade, C. Robert, G. Wang, Y. Shen, H. Cai, T. Taniguchi, K. Watanabe, H. Carrere, D. Lagarde, M. Manca, T. Amand, P. Renucci, S. Tongay, X. Marie, and B. Urbaszek. “Excitonic Linewidth Approaching the Homogeneous Limit in  $\text{MoS}_2$ -Based van der Waals Heterostructures”. *Physical Review X*, 7(2):021026, May 2017. doi:10.1103/PhysRevX.7.021026. URL <https://link.aps.org/doi/10.1103/PhysRevX.7.021026>, publisher: American Physical Society.
- [97] Y. Zhou, G. Scuri, J. Sung, R. Gelly, D. Wild, K. De Greve, A. Joe, T. Taniguchi, K. Watanabe, P. Kim, M. Lukin, and H. Park. “Controlling Excitons in an Atomically Thin Membrane with a Mirror”. *Physical Review Letters*, 124(2):027401, 2020. doi:10.1103/PhysRevLett.124.027401. URL <https://link.aps.org/doi/10.1103/PhysRevLett.124.027401>, publisher: American Physical Society.
- [98] P.-C. Shen, Y. Lin, H. Wang, J.-H. Park, W. S. Leong, A.-Y. Lu, T. Palacios, and J. Kong. “CVD Technology for 2-D Materials”. *IEEE Transactions on Electron Devices*, 65(10):4040–4052, October 2018. ISSN 0018-9383, 1557-9646. doi:10.1109/TED.2018.2866390. URL <https://ieeexplore.ieee.org/document/8452147/>.
- [99] M. Paur, A. J. Molina-Mendoza, R. Bratschitsch, K. Watanabe, T. Taniguchi, and T. Mueller. “Electroluminescence from multi-particle exciton complexes in transition metal dichalcogenide semiconductors”. *Na-*

- ture Communications*, 10(1):1709, April 2019. ISSN 2041-1723. doi:10.1038/s41467-019-09781-y. URL <https://www.nature.com/articles/s41467-019-09781-y>, number: 1 Publisher: Nature Publishing Group.
- [100] C. Robert, S. Park, F. Cadiz, L. Lombez, L. Ren, H. Tornatzky, A. Rowe, D. Paget, F. Sirotti, M. Yang, D. Van Tuan, T. Taniguchi, B. Urbaszek, K. Watanabe, T. Amand, H. Dery, and X. Marie. “Spin/valley pumping of resident electrons in WSe<sub>2</sub> and WS<sub>2</sub> monolayers”. *Nature Communications*, 12(1):5455, September 2021. ISSN 2041-1723. doi:10.1038/s41467-021-25747-5. URL <https://www.nature.com/articles/s41467-021-25747-5>, number: 1 Publisher: Nature Publishing Group.
- [101] S. Park, S. Arscott, T. Taniguchi, K. Watanabe, F. Sirotti, and F. Cadiz. “Efficient valley polarization of charged excitons and resident carriers in MoS<sub>2</sub> monolayers by optical pumping”. *arXiv:2110.07564 [cond-mat]*, October 2021. URL <http://arxiv.org/abs/2110.07564>, arXiv: 2110.07564.
- [102] H.-L. Tang, M.-H. Chiu, C.-C. Tseng, S.-H. Yang, K.-J. Hou, S.-Y. Wei, J.-K. Huang, Y.-F. Lin, C.-H. Lien, and L.-J. Li. “Multilayer Graphene–WSe<sub>2</sub> Heterostructures for WSe<sub>2</sub> Transistors”. *ACS Nano*, 11(12):12817–12823, December 2017. ISSN 1936-0851, 1936-086X. doi:10.1021/acsnano.7b07755. URL <https://pubs.acs.org/doi/10.1021/acsnano.7b07755>.
- [103] S. Bertolazzi, D. Krasnozhan, and A. Kis. “Nonvolatile Memory Cells Based on MoS<sub>2</sub>/Graphene Heterostructures”. *ACS Nano*, 7(4):3246–3252, April 2013. ISSN 1936-0851, 1936-086X. doi:10.1021/nn3059136. URL <https://pubs.acs.org/doi/10.1021/nn3059136>.
- [104] M. M. Benameur, B. Radisavljevic, J. S. Héron, S. Sahoo, H. Berger, and A. Kis. “Visibility of dichalcogenide nanolayers”. *Nanotechnology*, 22(12):125706, March 2011. ISSN 0957-4484, 1361-6528. doi:10.1088/0957-4484/22/12/125706. URL <https://iopscience.iop.org/article/10.1088/0957-4484/22/12/125706>.
- [105] H. Zhang, Y. Ma, Y. Wan, X. Rong, Z. Xie, W. Wang, and L. Dai. “Measuring the Refractive Index of Highly Crystalline Monolayer MoS<sub>2</sub> with High Confidence”. *Scientific Reports*, 5(1):8440, July 2015. ISSN 2045-2322. doi:10.1038/srep08440. URL <http://www.nature.com/articles/srep08440>.
- [106] S. Park, S. Arscott, T. Taniguchi, K. Watanabe, F. Sirotti, and F. Cadiz. “Efficient valley polarization of charged excitons and resident carriers in Molybdenum disulfide monolayers by optical pumping”. *Communications Physics*, 5(1):1–8, April 2022. ISSN 2399-3650. doi:10.1038/s42005-022-00850-1. URL <https://www.nature.com/articles/s42005-022-00850-1>, number: 1 Publisher: Nature Publishing Group.
- [107] M. M. Ugeda, A. J. Bradley, S.-F. Shi, F. H. da Jornada, Y. Zhang, D. Y. Qiu, W. Ruan, S.-K. Mo, Z. Hussain, Z.-X. Shen, F. Wang, S. G. Louie, and M. F. Crommie. “Giant bandgap renormalization and excitonic effects in

- a monolayer transition metal dichalcogenide semiconductor". *Nature Materials*, 13(12):1091–1095, December 2014. ISSN 1476-1122, 1476-4660. doi:10.1038/nmat4061. URL <http://www.nature.com/articles/nmat4061>.
- [108] S. Zhang, C.-G. Wang, M.-Y. Li, D. Huang, L.-J. Li, W. Ji, and S. Wu. "Defect Structure of Localized Excitons in a WSe<sub>2</sub> Monolayer". *Physical Review Letters*, 119(4):046101, July 2017. ISSN 0031-9007, 1079-7114. doi:10.1103/PhysRevLett.119.046101. URL <http://link.aps.org/doi/10.1103/PhysRevLett.119.046101>.
- [109] A. F. Rigosi, H. M. Hill, K. T. Rim, G. W. Flynn, and T. F. Heinz. "Electronic band gaps and exciton binding energies in monolayer Mo<sub>x</sub>W<sub>1-x</sub>S<sub>2</sub> transition metal dichalcogenide alloys probed by scanning tunneling and optical spectroscopy". *Physical Review B*, 94(7):075440, August 2016. ISSN 2469-9950, 2469-9969. doi:10.1103/PhysRevB.94.075440. URL <https://link.aps.org/doi/10.1103/PhysRevB.94.075440>.
- [110] H. Zeng, G.-B. Liu, J. Dai, Y. Yan, B. Zhu, R. He, L. Xie, S. Xu, X. Chen, W. Yao, and X. Cui. "Optical signature of symmetry variations and spin-valley coupling in atomically thin tungsten dichalcogenides". *Scientific Reports*, 3(1):1608, December 2013. ISSN 2045-2322. doi:10.1038/srep01608. URL <http://www.nature.com/articles/srep01608>.
- [111] A. Berkdemir, H. R. Gutiérrez, A. R. Botello-Méndez, N. Perea-López, A. L. Elías, C.-I. Chia, B. Wang, V. H. Crespi, F. López-Urías, J.-C. Charlier, H. Terrones, and M. Terrones. "Identification of individual and few layers of WS<sub>2</sub> using Raman Spectroscopy". *Scientific Reports*, 3(1):1755, December 2013. ISSN 2045-2322. doi:10.1038/srep01755. URL <http://www.nature.com/articles/srep01755>.
- [112] T. Jiang, R. Chen, X. Zheng, Z. Xu, and Y. Tang. "Photo-induced excitonic structure renormalization and broadband absorption in monolayer tungsten disulphide". *Optics Express*, 26(2):859, January 2018. ISSN 1094-4087. doi:10.1364/OE.26.000859. URL <https://www.osapublishing.org/abstract.cfm?URI=oe-26-2-859>.
- [113] C. Cong, J. Shang, X. Wu, B. Cao, N. Peimyoo, C. Qiu, L. Sun, and T. Yu. "Synthesis and Optical Properties of Large-Area Single-Crystalline 2D Semiconductor WS<sub>2</sub> Monolayer from Chemical Vapor Deposition". *Advanced Optical Materials*, 2(2):131–136, February 2014. ISSN 21951071. doi:10.1002/adom.201300428. URL <https://onlinelibrary.wiley.com/doi/10.1002/adom.201300428>.
- [114] K. Xu, Z. Wang, X. Du, M. Safdar, C. Jiang, and J. He. "Atomic-layer triangular WSe<sub>2</sub> sheets: synthesis and layer-dependent photoluminescence property". *Nanotechnology*, 24(46):465705, November 2013. ISSN 0957-4484, 1361-6528. doi:10.1088/0957-4484/24/46/465705. URL <https://iopscience.iop.org/article/10.1088/0957-4484/24/46/465705>.
- [115] R. Plougmann, M. Cowie, Y. Benkirane, L. Schué, Z. Schumacher, and P. Grütter. "How high is a MoSe<sub>2</sub>"

monolayer?" *arXiv:2109.05354 [cond-mat, physics:physics]*, September 2021. URL <http://arxiv.org/abs/2109.05354>, arXiv: 2109.05354.

- [116] Q. Song, T. L. Yu, X. Lou, B. P. Xie, H. C. Xu, C. H. P. Wen, Q. Yao, S. Y. Zhang, X. T. Zhu, J. D. Guo, R. Peng, and D. L. Feng. "Evidence of cooperative effect on the enhanced superconducting transition temperature at the FeSe/SrTiO<sub>3</sub> interface". *Nature Communications*, 10(1):758, December 2019. ISSN 2041-1723. doi:10.1038/s41467-019-08560-z. URL <http://www.nature.com/articles/s41467-019-08560-z>.
- [117] S. Han, K. M. Niang, G. Rughoobur, and A. J. Flewitt. "Effects of post-deposition vacuum annealing on film characteristics of p-type Cu<sub>2</sub>O and its impact on thin film transistor characteristics". *Applied Physics Letters*, 109(17):173502, October 2016. ISSN 0003-6951, 1077-3118. doi:10.1063/1.4965848. URL <http://aip.scitation.org/doi/10.1063/1.4965848>.
- [118] S. Niesar, A. R. Stegner, R. N. Pereira, M. Hoeb, H. Wiggers, M. S. Brandt, and M. Stutzmann. "Defect reduction in silicon nanoparticles by low-temperature vacuum annealing". *Applied Physics Letters*, 96(19):193112, May 2010. ISSN 0003-6951, 1077-3118. doi:10.1063/1.3428359. URL <http://aip.scitation.org/doi/10.1063/1.3428359>.
- [119] S.-W. Park, S. H. Jeong, J.-M. Choi, J. M. Hwang, J. H. Kim, and S. Im. "Rubrene polycrystalline transistor channel achieved through *in situ* vacuum annealing". *Applied Physics Letters*, 91(3):033506, July 2007. ISSN 0003-6951, 1077-3118. doi:10.1063/1.2756379. URL <http://aip.scitation.org/doi/10.1063/1.2756379>.
- [120] G. Zhou and J. C. Yang. "Reduction of Cu<sub>2</sub>O Islands Grown on a Cu(100) Surface through Vacuum Annealing". *Physical Review Letters*, 93(22):226101, November 2004. ISSN 0031-9007, 1079-7114. doi:10.1103/PhysRevLett.93.226101. URL <https://link.aps.org/doi/10.1103/PhysRevLett.93.226101>.
- [121] S. J. Haigh, A. Gholinia, R. Jalil, S. Romani, L. Britnell, D. C. Elias, K. S. Novoselov, L. A. Ponomarenko, A. K. Geim, and R. Gorbachev. "Cross-sectional imaging of individual layers and buried interfaces of graphene-based heterostructures and superlattices". *Nature Materials*, 11(9):764–767, September 2012. ISSN 1476-1122, 1476-4660. doi:10.1038/nmat3386. URL <http://www.nature.com/articles/nmat3386>.
- [122] A. V. Kretinin, Y. Cao, J. S. Tu, G. L. Yu, R. Jalil, K. S. Novoselov, S. J. Haigh, A. Gholinia, A. Mishchenko, M. Lozada, T. Georgiou, C. R. Woods, F. Withers, P. Blake, G. Eda, A. Wirsig, C. Hucho, K. Watanabe, T. Taniguchi, A. K. Geim, and R. V. Gorbachev. "Electronic Properties of Graphene Encapsulated with Different Two-Dimensional Atomic Crystals". *Nano Letters*, 14(6):3270–3276, June 2014. ISSN 1530-6984, 1530-6992. doi:10.1021/nl5006542. URL <https://pubs.acs.org/doi/10.1021/nl5006542>.
- [123] A. Jain, P. Bharadwaj, S. Heeg, M. Parzefall, T. Taniguchi, K. Watanabe, and L. Novotny. "Minimizing residues and strain in 2D materials transferred from PDMS". *Nanotechnology*, 29(26):265203, June 2018. ISSN 0957-

4484, 1361-6528. doi:10.1088/1361-6528/aabd90. URL <https://iopscience.iop.org/article/10.1088/1361-6528/aabd90>.

- [124] H. Zhu, Q. Wang, L. Cheng, R. Addou, J. Kim, M. J. Kim, and R. M. Wallace. "Defects and Surface Structural Stability of MoTe<sub>2</sub> Under Vacuum Annealing". *ACS Nano*, 11(11):11005–11014, November 2017. ISSN 1936-0851, 1936-086X. doi:10.1021/acsnano.7b04984. URL <https://pubs.acs.org/doi/10.1021/acsnano.7b04984>.
- [125] H.-J. Kim, D. Kim, S. Jung, M.-H. Bae, S. N. Yi, K. Watanabe, T. Taniguchi, S. K. Chang, and D. H. Ha. "Homogeneity and tolerance to heat of monolayer MoS<sub>2</sub> on SiO<sub>2</sub> and h-BN". *RSC Advances*, 8(23):12900–12906, April 2018. ISSN 2046-2069. doi:10.1039/C8RA01849A. URL <https://pubs.rsc.org/en/content/articlelanding/2018/ra/c8ra01849a>, publisher: The Royal Society of Chemistry.
- [126] L. Zhang, H. Yan, X. Sun, M. Dong, T. Yildirim, B. Wang, B. Wen, G. P. Neupane, A. Sharma, Y. Zhu, J. Zhang, K. Liang, B. Liu, H. T. Nguyen, D. Macdonald, and Y. Lu. "Modulated interlayer charge transfer dynamics in a monolayer TMD/metal junction". *Nanoscale*, 11(2):418–425, January 2019. ISSN 2040-3372. doi:10.1039/C8NR08728H. URL <https://pubs.rsc.org/en/content/articlelanding/2019/nr/c8nr08728h>, publisher: The Royal Society of Chemistry.
- [127] R. J. P. Román, Y. Auad, L. Grasso, F. Alvarez, I. D. Barcelos, and L. F. Zagonel. "Tunneling-current-induced local excitonic luminescence in p-doped WSe<sub>2</sub> monolayers". *Nanoscale*, 12(25):13460–13470, July 2020. ISSN 2040-3372. doi:10.1039/D0NR03400B. URL <https://pubs.rsc.org/en/content/articlelanding/2020/nr/d0nr03400b>, publisher: The Royal Society of Chemistry.
- [128] G. Froehlicher, E. Lorchat, and S. Berciaud. "Charge Versus Energy Transfer in Atomically Thin Graphene-Transition Metal Dichalcogenide van der Waals Heterostructures". *Physical Review X*, 8(1):011007, 2018. doi:10.1103/PhysRevX.8.011007. URL <https://link.aps.org/doi/10.1103/PhysRevX.8.011007>, publisher: American Physical Society.
- [129] G. Wang, Y. Kim, M. Choe, T.-W. Kim, and T. Lee. "A New Approach for Molecular Electronic Junctions with a Multilayer Graphene Electrode". *Advanced Materials*, 23(6):755–760, February 2011. ISSN 09359648. doi:10.1002/adma.201003178. URL <https://onlinelibrary.wiley.com/doi/10.1002/adma.201003178>.
- [130] X. Huang, Z. Zeng, Z. Fan, J. Liu, and H. Zhang. "Graphene-Based Electrodes". *Advanced Materials*, 24(45):5979–6004, November 2012. ISSN 09359648. doi:10.1002/adma.201201587. URL <https://onlinelibrary.wiley.com/doi/10.1002/adma.201201587>.
- [131] A. S. Lemine, M. M. Zagho, T. M. Altahtamouni, and N. Bensalah. "Graphene a promising electrode material

- for supercapacitors-A review". *International Journal of Energy Research*, 42(14):4284–4300, November 2018. ISSN 0363907X. doi:10.1002/er.4170. URL <https://onlinelibrary.wiley.com/doi/10.1002/er.4170>.
- [132] D. Xiao, G.-B. Liu, W. Feng, X. Xu, and W. Yao. "Coupled Spin and Valley Physics in Monolayers of MoS<sub>2</sub> and Other Group-VI Dichalcogenides". *Physical Review Letters*, 108(19):196802, May 2012. ISSN 0031-9007, 1079-7114. doi:10.1103/PhysRevLett.108.196802. URL <https://link.aps.org/doi/10.1103/PhysRevLett.108.196802>.
- [133] X. J. Wang, Y. Puttisong, C. W. Tu, A. J. Ptak, V. K. Kalevich, A. Y. Egorov, L. Geelhaar, H. Riechert, W. M. Chen, and I. A. Buyanova. "Dominant recombination centers in Ga(In)NAs alloys: Ga interstitials". *Applied Physics Letters*, 95(24):241904, December 2009. ISSN 0003-6951. doi:10.1063/1.3275703. URL <https://aip.scitation.org/doi/10.1063/1.3275703>, publisher: American Institute of Physics.
- [134] G. Plechinger, P. Nagler, J. Kraus, N. Paradiso, C. Strunk, C. Schüller, and T. Korn. "Identification of excitons, trions and biexcitons in single-layer WS<sub>2</sub>". *physica status solidi (RRL) – Rapid Research Letters*, 9(8):457–461, 2015. ISSN 1862-6270. doi:10.1002/pssr.201510224. URL <https://onlinelibrary.wiley.com/doi/abs/10.1002/pssr.201510224>, eprint: <https://onlinelibrary.wiley.com/doi/pdf/10.1002/pssr.201510224>.
- [135] G. Plechinger, P. Nagler, A. Arora, R. Schmidt, A. Chernikov, A. G. del Águila, P. C. M. Christianen, R. Bratschitsch, C. Schüller, and T. Korn. "Trion fine structure and coupled spin–valley dynamics in monolayer tungsten disulfide". *Nature Communications*, 7(1):12715, September 2016. ISSN 2041-1723. doi:10.1038/ncomms12715. URL <https://www.nature.com/articles/ncomms12715>, number: 1 Publisher: Nature Publishing Group.
- [136] M. Okada, Y. Miyauchi, K. Matsuda, T. Taniguchi, K. Watanabe, H. Shinohara, and R. Kitaura. "Observation of biexcitonic emission at extremely low power density in tungsten disulfide atomic layers grown on hexagonal boron nitride". *Scientific Reports*, 7(1):322, March 2017. ISSN 2045-2322. doi:10.1038/s41598-017-00068-0. URL <https://www.nature.com/articles/s41598-017-00068-0>, number: 1 Publisher: Nature Publishing Group.
- [137] M. R. Molas, K. Nogajewski, A. O. Slobodeniuk, J. Binder, M. Bartos, and M. Potemski. "The optical response of monolayer, few-layer and bulk tungsten disulfide". *Nanoscale*, 9(35):13128–13141, September 2017. ISSN 2040-3372. doi:10.1039/C7NR04672C. URL <https://pubs.rsc.org/en/content/articlelanding/2017/nr/c7nr04672c>, publisher: The Royal Society of Chemistry.
- [138] D. Vaclavkova, J. Wyzula, K. Nogajewski, M. Bartos, A. O. Slobodeniuk, C. Faugeras, M. Potemski, and M. R. Molas. "Singlet and triplet trions in WS<sub>2</sub> monolayer encapsulated in hexagonal boron nitride". *Nanotechnology*, 29(32):325705, June 2018. ISSN 0957-4484. doi:10.1088/1361-6528/aac65c. URL <https://doi.org/10.1088/1361-6528/aac65c>, publisher: IOP Publishing.

- [139] G. Plechinger, P. Nagler, A. Arora, A. Granados del Águila, M. V. Ballottin, T. Frank, P. Steinleitner, M. Gmitra, J. Fabian, P. C. M. Christianen, R. Bratschitsch, C. Schüller, and T. Korn. “Excitonic Valley Effects in Monolayer WS<sub>2</sub> under High Magnetic Fields”. *Nano Letters*, 16(12):7899–7904, December 2016. ISSN 1530-6984. doi:10.1021/acs.nanolett.6b04171. URL <https://doi.org/10.1021/acs.nanolett.6b04171>, publisher: American Chemical Society.
- [140] E. Courtade, M. Semina, M. Manca, M. M. Glazov, C. Robert, F. Cadiz, G. Wang, T. Taniguchi, K. Watanabe, M. Pierre, W. Escoffier, E. L. Ivchenko, P. Renucci, X. Marie, T. Amand, and B. Urbaszek. “Charged excitons in monolayer  $\text{WSe}_2$ : Experiment and theory”. *Physical Review B*, 96(8):085302, August 2017. doi:10.1103/PhysRevB.96.085302. URL <https://link.aps.org/doi/10.1103/PhysRevB.96.085302>, publisher: American Physical Society.
- [141] M. Zinkiewicz, A. O. Slobodeniuk, T. Kazimierczuk, P. Kapuściński, K. Oreszczuk, M. Grzeszczyk, M. Bartos, K. Nogajewski, K. Watanabe, T. Taniguchi, C. Faugeras, P. Kossacki, M. Potemski, A. Babiński, and M. R. Molas. “Neutral and charged dark excitons in monolayer WS<sub>2</sub>”. *Nanoscale*, 12(35):18153–18159, September 2020. ISSN 2040-3372. doi:10.1039/D0NR04243A. URL <https://pubs.rsc.org/en/content/articlelanding/2020/nr/d0nr04243a>, publisher: The Royal Society of Chemistry.
- [142] M. Zinkiewicz, T. Woźniak, T. Kazimierczuk, P. Kapuscinski, K. Oreszczuk, M. Grzeszczyk, M. Bartoš, K. Nogajewski, K. Watanabe, T. Taniguchi, C. Faugeras, P. Kossacki, M. Potemski, A. Babiński, and M. R. Molas. “Excitonic Complexes in n-Doped WS<sub>2</sub> Monolayer”. *Nano Letters*, 21(6):2519–2525, March 2021. ISSN 1530-6984. doi:10.1021/acs.nanolett.0c05021. URL <https://doi.org/10.1021/acs.nanolett.0c05021>, publisher: American Chemical Society.
- [143] Y. Yu, Y. Yu, C. Xu, A. Barrette, K. Gundogdu, and L. Cao. “Fundamental limits of exciton-exciton annihilation for light emission in transition metal dichalcogenide monolayers”. *Physical Review B*, 93(20):201111, May 2016. doi:10.1103/PhysRevB.93.201111. URL <https://link.aps.org/doi/10.1103/PhysRevB.93.201111>, publisher: American Physical Society.
- [144] S. D. Stranks, V. M. Burlakov, T. Leijtens, J. M. Ball, A. Goriely, and H. J. Snaith. “Recombination Kinetics in Organic-Inorganic Perovskites: Excitons, Free Charge, and Subgap States”. *Physical Review Applied*, 2(3):034007, September 2014. doi:10.1103/PhysRevApplied.2.034007. URL <https://link.aps.org/doi/10.1103/PhysRevApplied.2.034007>, publisher: American Physical Society.
- [145] A. T. Hanbicki, G. Kioseoglou, M. Currie, C. S. Hellberg, K. M. McCreary, A. L. Friedman, and B. T. Jonker. “Anomalous temperature-dependent spin-valley polarization in monolayer WS<sub>2</sub>”. *Scientific Reports*, 6(1):18885, January 2016. ISSN 2045-2322. doi:10.1038/srep18885. URL <https://www.nature.com/articles/srep18885>, number: 1 Publisher: Nature Publishing Group.

- [146] W.-H. Lin, W.-S. Tseng, C. M. Went, M. L. Teague, G. R. Rossman, H. A. Atwater, and N.-C. Yeh. “Nearly 90% Circularly Polarized Emission in Monolayer WS<sub>2</sub> Single Crystals by Chemical Vapor Deposition”. *ACS Nano*, 14(2):1350–1359, February 2020. ISSN 1936-0851. doi:10.1021/acsnano.9b05550. URL <https://doi.org/10.1021/acsnano.9b05550>, publisher: American Chemical Society.
- [147] M. He, P. Rivera, D. Van Tuan, N. P. Wilson, M. Yang, T. Taniguchi, K. Watanabe, J. Yan, D. G. Mandrus, H. Yu, H. Dery, W. Yao, and X. Xu. “Valley phonons and exciton complexes in a monolayer semiconductor”. *Nature Communications*, 11(1):618, January 2020. ISSN 2041-1723. doi:10.1038/s41467-020-14472-0. URL <https://www.nature.com/articles/s41467-020-14472-0>, number: 1 Publisher: Nature Publishing Group.
- [148] A. Arora, T. Deilmann, T. Reichenauer, J. Kern, S. Michaelis de Vasconcellos, M. Rohlfing, and R. Bratschitsch. “Excited-State Trions in Monolayer  $\text{WS}_2$ ”. *Physical Review Letters*, 123(16):167401, October 2019. doi:10.1103/PhysRevLett.123.167401. URL <https://link.aps.org/doi/10.1103/PhysRevLett.123.167401>, publisher: American Physical Society.
- [149] S. Park, B. Han, C. Boule, D. Paget, A. C. H. Rowe, F. Sirotti, T. Taniguchi, K. Watanabe, C. Robert, L. Lombez, B. Urbaszek, X. Marie, and F. Cadiz. “Imaging Seebeck drift of excitons and trions in MoSe<sub>2</sub> monolayers”. *2D Materials*, 8(4):045014, August 2021. ISSN 2053-1583. doi:10.1088/2053-1583/ac171f. URL <https://doi.org/10.1088/2053-1583/ac171f>, publisher: IOP Publishing.
- [150] F. Cadiz, D. Paget, A. C. H. Rowe, L. Martinelli, and S. Arscott. “Absence of carrier separation in ambipolar charge and spin drift in p+-GaAs”. *Applied Physics Letters*, 107(16):162101, October 2015. ISSN 0003-6951. doi:10.1063/1.4933189. URL <https://aip.scitation.org/doi/10.1063/1.4933189>, publisher: American Institute of Physics.
- [151] F. Cadiz, D. Paget, A. C. H. Rowe, T. Amand, P. Barate, and S. Arscott. “Effect of the Pauli principle on photoelectron spin transport in  $p^+$  GaAs”. *Physical Review B*, 91(16):165203, April 2015. doi:10.1103/PhysRevB.91.165203. URL <https://link.aps.org/doi/10.1103/PhysRevB.91.165203>, publisher: American Physical Society.
- [152] F. Cadiz, C. Robert, E. Courtade, M. Manca, L. Martinelli, T. Taniguchi, K. Watanabe, T. Amand, A. C. H. Rowe, D. Paget, B. Urbaszek, and X. Marie. “Exciton diffusion in WSe<sub>2</sub> monolayers embedded in a van der Waals heterostructure”. *Applied Physics Letters*, 112(15):152106, April 2018. ISSN 0003-6951. doi:10.1063/1.5026478. URL <https://aip.scitation.org/doi/10.1063/1.5026478>, publisher: American Institute of Physics.
- [153] F. Cadiz, S. Gerl, T. Taniguchi, and K. Watanabe. “Enhancement of valley polarization at high photoexcited

densities in MoS2 monolayers”. *arXiv:2110.15791 [cond-mat, physics:physics]*, October 2021. URL <http://arxiv.org/abs/2110.15791>, arXiv: 2110.15791.

- [154] E. Liu, J. van Baren, Z. Lu, T. Taniguchi, K. Watanabe, D. Smirnov, Y.-C. Chang, and C. H. Lui. “Exciton-polaron Rydberg states in monolayer MoSe<sub>2</sub> and WSe<sub>2</sub>”. *Nature Communications*, 12(1):6131, October 2021. ISSN 2041-1723. doi:10.1038/s41467-021-26304-w. URL <https://www.nature.com/articles/s41467-021-26304-w>, number: 1 Publisher: Nature Publishing Group.
- [155] S.-Y. Seo, G. Moon, O. F. N. Okello, M. Y. Park, C. Han, S. Cha, H. Choi, H. W. Yeom, S.-Y. Choi, J. Park, and M.-H. Jo. “Reconfigurable photo-induced doping of two-dimensional van der Waals semiconductors using different photon energies”. *Nature Electronics*, 4(1):38–44, January 2021. ISSN 2520-1131. doi:10.1038/s41928-020-00512-6. URL <https://www.nature.com/articles/s41928-020-00512-6>, number: 1 Publisher: Nature Publishing Group.
- [156] Y. Kang and S. Han. “An origin of unintentional doping in transition metal dichalcogenides: the role of hydrogen impurities”. *Nanoscale*, 9(12):4265–4271, March 2017. ISSN 2040-3372. doi:10.1039/C6NR08555E. URL <https://pubs.rsc.org/en/content/articlelanding/2017/nr/c6nr08555e>, publisher: The Royal Society of Chemistry.
- [157] F. Ceballos, Q. Cui, M. Z. Bellus, and H. Zhao. “Exciton formation in monolayer transition metal dichalcogenides”. *Nanoscale*, 8(22):11681–11688, June 2016. ISSN 2040-3372. doi:10.1039/C6NR02516A. URL <https://pubs.rsc.org/en/content/articlelanding/2016/nr/c6nr02516a>, publisher: The Royal Society of Chemistry.
- [158] A. Singh, G. Moody, K. Tran, M. E. Scott, V. Overbeck, G. Berghäuser, J. Schaibley, E. J. Seifert, D. Pleskot, N. M. Gabor, J. Yan, D. G. Mandrus, M. Richter, E. Malic, X. Xu, and X. Li. “Trion formation dynamics in monolayer transition metal dichalcogenides”. *Physical Review B*, 93(4):041401, January 2016. doi:10.1103/PhysRevB.93.041401. URL <https://link.aps.org/doi/10.1103/PhysRevB.93.041401>, publisher: American Physical Society.
- [159] F. Gao, Y. Gong, M. Titze, R. Almeida, P. M. Ajayan, and H. Li. “Valley trion dynamics in monolayer  $\text{MoSe}_2$ ”. *Physical Review B*, 94(24):245413, December 2016. doi:10.1103/PhysRevB.94.245413. URL <https://link.aps.org/doi/10.1103/PhysRevB.94.245413>, publisher: American Physical Society.
- [160] P. Steinleitner, P. Merkl, P. Nagler, J. Mornhinweg, C. Schüller, T. Korn, A. Chernikov, and R. Huber. “Direct Observation of Ultrafast Exciton Formation in a Monolayer of WSe<sub>2</sub>”. *Nano Letters*, 17(3):1455–1460, March 2017. ISSN 1530-6984. doi:10.1021/acs.nanolett.6b04422. URL <https://doi.org/10.1021/acs.nanolett.6b04422>, publisher: American Chemical Society.

- [161] C. Trovatiello, F. Katsch, N. J. Borys, M. Selig, K. Yao, R. Borrego-Varillas, F. Scotognella, I. Kriegel, A. Yan, A. Zettl, P. J. Schuck, A. Knorr, G. Cerullo, and S. D. Conte. “The ultrafast onset of exciton formation in 2D semiconductors”. *Nature Communications*, 11(1):5277, October 2020. ISSN 2041-1723. doi:10.1038/s41467-020-18835-5. URL <https://www.nature.com/articles/s41467-020-18835-5>, number: 1 Publisher: Nature Publishing Group.
- [162] G. Wang, E. Palleau, T. Amand, S. Tongay, X. Marie, and B. Urbaszek. “Polarization and time-resolved photoluminescence spectroscopy of excitons in MoSe<sub>2</sub> monolayers”. *Applied Physics Letters*, 106(11):112101, March 2015. ISSN 0003-6951. doi:10.1063/1.4916089. URL <https://aip.scitation.org/doi/10.1063/1.4916089>, publisher: American Institute of Physics.
- [163] H. Fang, B. Han, C. Robert, M. Semina, D. Lagarde, E. Courtade, T. Taniguchi, K. Watanabe, T. Amand, B. Urbaszek, M. Glazov, and X. Marie. “Control of the Exciton Radiative Lifetime in van der Waals Heterostructures”. *Physical Review Letters*, 123(6):067401, August 2019. doi:10.1103/PhysRevLett.123.067401. URL <https://link.aps.org/doi/10.1103/PhysRevLett.123.067401>, publisher: American Physical Society.
- [164] G. Wang, I. C. Gerber, L. Bouet, D. Lagarde, A. Balocchi, M. Vidal, T. Amand, X. Marie, and B. Urbaszek. “Exciton states in monolayer MoSe<sub>2</sub> : impact on interband transitions”. *2D Materials*, 2(4):045005, November 2015. ISSN 2053-1583. doi:10.1088/2053-1583/2/4/045005. URL <https://doi.org/10.1088/2053-1583/2/4/045005>, publisher: IOP Publishing.
- [165] H. Tornatzky, A.-M. Kaulitz, and J. Maultzsch. “Resonance Profiles of Valley Polarization in Single-Layer  $\text{MoS}_2$  and  $\text{MoSe}_2$ ”. *Physical Review Letters*, 121(16):167401, October 2018. doi:10.1103/PhysRevLett.121.167401. URL <https://link.aps.org/doi/10.1103/PhysRevLett.121.167401>, publisher: American Physical Society.
- [166] F. Mahmood, Z. Alpichshev, Y.-H. Lee, J. Kong, and N. Gedik. “Observation of Exciton–Exciton Interaction Mediated Valley Depolarization in Monolayer MoSe<sub>2</sub>”. *Nano Letters*, 18(1):223–228, January 2018. ISSN 1530-6984. doi:10.1021/acs.nanolett.7b03953. URL <https://doi.org/10.1021/acs.nanolett.7b03953>, publisher: American Chemical Society.
- [167] M. Yang, C. Robert, Z. Lu, D. Van Tuan, D. Smirnov, X. Marie, and H. Dery. “Exciton valley depolarization in monolayer transition-metal dichalcogenides”. *Physical Review B*, 101(11):115307, March 2020. doi:10.1103/PhysRevB.101.115307. URL <https://link.aps.org/doi/10.1103/PhysRevB.101.115307>, publisher: American Physical Society.
- [168] N. Kumar, Q. Cui, F. Ceballos, D. He, Y. Wang, and H. Zhao. “Exciton-exciton annihilation in MoSe<sub>2</sub> monolayers”. *Physical Review B*, 89(12):125427, March 2014. doi:10.1103/PhysRevB.89.125427. URL <https://link.aps.org/doi/10.1103/PhysRevB.89.125427>, publisher: American Physical Society.

- [169] J. Zipfel, M. Kulig, R. Perea-Causín, S. Brem, J. D. Ziegler, R. Rosati, T. Taniguchi, K. Watanabe, M. M. Glazov, E. Malic, and A. Chernikov. “Exciton diffusion in monolayer semiconductors with suppressed disorder”. *Physical Review B*, 101(11):115430, March 2020. doi:10.1103/PhysRevB.101.115430. URL <https://link.aps.org/doi/10.1103/PhysRevB.101.115430>, publisher: American Physical Society.
- [170] C. Robert, M. A. Semina, F. Cadiz, M. Manca, E. Courtade, T. Taniguchi, K. Watanabe, H. Cai, S. Tongay, B. Lassagne, P. Renucci, T. Amand, X. Marie, M. M. Glazov, and B. Urbaszek. “Optical spectroscopy of excited exciton states in  $\text{MoS}_2$  monolayers in van der Waals heterostructures”. *Physical Review Materials*, 2(1):011001, January 2018. doi:10.1103/PhysRevMaterials.2.011001. URL <https://link.aps.org/doi/10.1103/PhysRevMaterials.2.011001>, publisher: American Physical Society.
- [171] S. Shree, M. Semina, C. Robert, B. Han, T. Amand, A. Balocchi, M. Manca, E. Courtade, X. Marie, T. Taniguchi, K. Watanabe, M. M. Glazov, and B. Urbaszek. “Observation of exciton-phonon coupling in  $\text{MoSe}_2$  monolayers”. *Physical Review B*, 98(3):035302, July 2018. doi:10.1103/PhysRevB.98.035302. URL <https://link.aps.org/doi/10.1103/PhysRevB.98.035302>, publisher: American Physical Society.
- [172] J. W. Christopher, B. B. Goldberg, and A. K. Swan. “Long tailed trions in monolayer  $\text{MoS}_2$ : Temperature dependent asymmetry and resulting red-shift of trion photoluminescence spectra”. *Scientific Reports*, 7(1):14062, October 2017. ISSN 2045-2322. doi:10.1038/s41598-017-14378-w. URL <https://www.nature.com/articles/s41598-017-14378-w>, number: 1 Publisher: Nature Publishing Group.
- [173] Y. V. Zhumagulov, A. Vagov, D. R. Gulevich, P. E. Faria Junior, and V. Perebeinos. “Trion induced photoluminescence of a doped  $\text{MoS}_2$  monolayer”. *The Journal of Chemical Physics*, 153(4):044132, July 2020. ISSN 0021-9606. doi:10.1063/5.0012971. URL <https://aip.scitation.org/doi/abs/10.1063/5.0012971>, publisher: American Institute of Physics.
- [174] D. F. Cordovilla Leon, Z. Li, S. W. Jang, and P. B. Deotare. “Hot exciton transport in  $\text{WS}_2$  monolayers”. *Physical Review B*, 100(24):241401, December 2019. doi:10.1103/PhysRevB.100.241401. URL <https://link.aps.org/doi/10.1103/PhysRevB.100.241401>, publisher: American Physical Society.
- [175] J. Madéo, M. K. L. Man, C. Sahoo, M. Campbell, V. Pareek, E. L. Wong, A. Al-Mahboob, N. S. Chan, A. Karmakar, B. M. K. Mariserla, X. Li, T. F. Heinz, T. Cao, and K. M. Dani. “Directly visualizing the momentum-forbidden dark excitons and their dynamics in atomically thin semiconductors”. *Science*, 370(6521):1199–1204, December 2020. doi:10.1126/science.aba1029. URL <https://www.science.org/doi/10.1126/science.aba1029>, publisher: American Association for the Advancement of Science.

- [176] S. Z. Uddin, H. Kim, M. Lorenzon, M. Yeh, D.-H. Lien, E. S. Barnard, H. Htoon, A. Weber-Bargioni, and A. Javey. “Neutral Exciton Diffusion in Monolayer MoS<sub>2</sub>”. *ACS Nano*, 14(10):13433–13440, October 2020. ISSN 1936-0851. doi:10.1021/acsnano.0c05305. URL <https://doi.org/10.1021/acsnano.0c05305>, publisher: American Chemical Society.
- [177] M. Palummo, M. Bernardi, and J. C. Grossman. “Exciton Radiative Lifetimes in Two-Dimensional Transition Metal Dichalcogenides”. *Nano Letters*, 15(5):2794–2800, May 2015. ISSN 1530-6984. doi:10.1021/nl503799t. URL <https://doi.org/10.1021/nl503799t>, publisher: American Chemical Society.
- [178] M. Kulig, J. Zipfel, P. Nagler, S. Blanter, C. Schüller, T. Korn, N. Paradiso, M. M. Glazov, and A. Chernikov. “Exciton Diffusion and Halo Effects in Monolayer Semiconductors”. *Physical Review Letters*, 120(20):207401, May 2018. doi:10.1103/PhysRevLett.120.207401. URL <https://link.aps.org/doi/10.1103/PhysRevLett.120.207401>, publisher: American Physical Society.
- [179] R. Perea-Causín, S. Brem, R. Rosati, R. Jago, M. Kulig, J. D. Ziegler, J. Zipfel, A. Chernikov, and E. Malic. “Exciton Propagation and Halo Formation in Two-Dimensional Materials”. *Nano Letters*, 19(10):7317–7323, October 2019. ISSN 1530-6984. doi:10.1021/acs.nanolett.9b02948. URL <https://doi.org/10.1021/acs.nanolett.9b02948>, publisher: American Chemical Society.
- [180] Y. Lee, T. T. Tran, Y. Kim, S. Roy, T. Taniguchi, K. Watanabe, J. I. Jang, and J. Kim. “Enhanced Radiative Exciton Recombination in Monolayer WS<sub>2</sub> on the hBN Substrate Competing with Nonradiative Exciton–Exciton Annihilation”. *ACS Photonics*, 9(3):873–879, March 2022. doi:10.1021/acsp Photonics.1c01584. URL <https://doi.org/10.1021/acsp Photonics.1c01584>, publisher: American Chemical Society.
- [181] B. Han, C. Robert, E. Courtade, M. Manca, S. Shree, T. Amand, P. Renucci, T. Taniguchi, K. Watanabe, X. Marie, L. Golub, M. Glazov, and B. Urbaszek. “Exciton States in Monolayer  $\text{MoSe}_2$  and  $\text{MoTe}_2$  Probed by Upconversion Spectroscopy”. *Physical Review X*, 8(3):031073, September 2018. doi:10.1103/PhysRevX.8.031073. URL <https://link.aps.org/doi/10.1103/PhysRevX.8.031073>, publisher: American Physical Society.
- [182] E. J. Sie, A. Steinhoff, C. Gies, C. H. Lui, Q. Ma, M. Rösner, G. Schönhoff, F. Jahnke, T. O. Wehling, Y.-H. Lee, J. Kong, P. Jarillo-Herrero, and N. Gedik. “Observation of Exciton Redshift–Blueshift Crossover in Monolayer WS<sub>2</sub>”. *Nano Letters*, 17(7):4210–4216, July 2017. ISSN 1530-6984. doi:10.1021/acs.nanolett.7b01034. URL <https://doi.org/10.1021/acs.nanolett.7b01034>, publisher: American Chemical Society.
- [183] F. Cadiz, C. Robert, G. Wang, W. Kong, X. Fan, M. Blei, D. Lagarde, M. Gay, M. Manca, T. Taniguchi, K. Watanabe, T. Amand, X. Marie, P. Renucci, S. Tongay, and B. Urbaszek. “Ultra-low power threshold for laser induced changes in optical properties of 2D molybdenum dichalcogenides”. *2D Materials*, 3(4):045008, October

2016. ISSN 2053-1583. doi:10.1088/2053-1583/3/4/045008. URL <https://doi.org/10.1088/2053-1583/3/4/045008>, publisher: IOP Publishing.

- [184] J. Wierzbowski, J. Klein, F. Sigger, C. Straubinger, M. Kremser, T. Taniguchi, K. Watanabe, U. Wurstbauer, A. W. Holleitner, M. Kaniber, K. Müller, and J. J. Finley. “Direct exciton emission from atomically thin transition metal dichalcogenide heterostructures near the lifetime limit”. *Scientific Reports*, 7(1):12383, September 2017. ISSN 2045-2322. doi:10.1038/s41598-017-09739-4. URL <https://www.nature.com/articles/s41598-017-09739-4>, number: 1 Publisher: Nature Publishing Group.
- [185] J. Klein, A. Hötger, M. Florian, A. Steinhoff, A. Delhomme, T. Taniguchi, K. Watanabe, F. Jahnke, A. W. Holleitner, M. Potemski, C. Faugeras, J. J. Finley, and A. V. Stier. “Controlling exciton many-body states by the electric-field effect in monolayer  $\text{MoS}_2$ ”. *Physical Review Research*, 3(2):L022009, April 2021. doi:10.1103/PhysRevResearch.3.L022009. URL <https://link.aps.org/doi/10.1103/PhysRevResearch.3.L022009>, publisher: American Physical Society.
- [186] C. Robert, B. Han, P. Kapuscinski, A. Delhomme, C. Faugeras, T. Amand, M. R. Molas, M. Bartos, K. Watanabe, T. Taniguchi, B. Urbaszek, M. Potemski, and X. Marie. “Measurement of the spin-forbidden dark excitons in  $\text{MoS}_2$  and  $\text{MoSe}_2$  monolayers”. *Nature Communications*, 11(1):4037, August 2020. ISSN 2041-1723. doi:10.1038/s41467-020-17608-4. URL <https://www.nature.com/articles/s41467-020-17608-4>, number: 1 Publisher: Nature Publishing Group.
- [187] D. Vaquero, V. Clericò, J. Salvador-Sánchez, A. Martín-Ramos, E. Díaz, F. Domínguez-Adame, Y. M. Meziani, E. Diez, and J. Quereda. “Excitons, trions and Rydberg states in monolayer  $\text{MoS}_2$  revealed by low-temperature photocurrent spectroscopy”. *Communications Physics*, 3(1):1–8, October 2020. ISSN 2399-3650. doi:10.1038/s42005-020-00460-9. URL <https://www.nature.com/articles/s42005-020-00460-9>, number: 1 Publisher: Nature Publishing Group.
- [188] D. J. Clark, V. Senthilkumar, C. T. Le, D. L. Weerawarne, B. Shim, J. I. Jang, J. H. Shim, J. Cho, Y. Sim, M.-J. Seong, S. H. Rhim, A. J. Freeman, K.-H. Chung, and Y. S. Kim. “Strong optical nonlinearity of CVD-grown  $\text{MoS}_2$  monolayer as probed by wavelength-dependent second-harmonic generation”. *Physical Review B*, 90(12):121409, September 2014. doi:10.1103/PhysRevB.90.121409. URL <https://link.aps.org/doi/10.1103/PhysRevB.90.121409>, publisher: American Physical Society.
- [189] C. T. Le, D. J. Clark, F. Ullah, J. I. Jang, V. Senthilkumar, Y. Sim, M.-J. Seong, K.-H. Chung, J. W. Kim, S. Park, S. H. Rhim, G. Kim, and Y. S. Kim. “Impact of Selenium Doping on Resonant Second-Harmonic Generation in Monolayer  $\text{MoS}_2$ ”. *ACS Photonics*, 4(1):38–44, January 2017. doi:10.1021/acsp Photonics.6b00530. URL <https://doi.org/10.1021/acsp Photonics.6b00530>, publisher: American Chemical Society.

- [190] S. Shree, D. Lagarde, L. Lombez, C. Robert, A. Balocchi, K. Watanabe, T. Taniguchi, X. Marie, I. C. Gerber, M. M. Glazov, L. E. Golub, B. Urbaszek, and I. Paradisanos. “Interlayer exciton mediated second harmonic generation in bilayer MoS<sub>2</sub>”. *Nature Communications*, 12(1):6894, November 2021. ISSN 2041-1723. doi:10.1038/s41467-021-27213-8. URL <https://www.nature.com/articles/s41467-021-27213-8>, number: 1 Publisher: Nature Publishing Group.
- [191] S. Shree, A. George, T. Lehnert, C. Neumann, M. Benelajla, C. Robert, X. Marie, K. Watanabe, T. Taniguchi, U. Kaiser, B. Urbaszek, and A. Turchanin. “High optical quality of MoS<sub>2</sub> monolayers grown by chemical vapor deposition”. *2D Materials*, 7(1):015011, November 2019. ISSN 2053-1583. doi:10.1088/2053-1583/ab4f1f. URL <https://doi.org/10.1088/2053-1583/ab4f1f>, publisher: IOP Publishing.
- [192] J. Klein, M. Florian, A. Hötger, A. Steinhoff, A. Delhomme, T. Taniguchi, K. Watanabe, F. Jahnke, A. W. Holleitner, M. Potemski, C. Faugeras, A. V. Stier, and J. J. Finley. “Trions in  $\mathrm{MoS}_2$  are quantum superpositions of intra- and intervalley spin states”. *Physical Review B*, 105(4):L041302, January 2022. doi:10.1103/PhysRevB.105.L041302. URL <https://link.aps.org/doi/10.1103/PhysRevB.105.L041302>, publisher: American Physical Society.
- [193] L. Li, R. Long, T. Bertolini, and O. V. Prezhdo. “Sulfur Adatom and Vacancy Accelerate Charge Recombination in MoS<sub>2</sub> but by Different Mechanisms: Time-Domain Ab Initio Analysis”. *Nano Letters*, 17(12):7962–7967, December 2017. ISSN 1530-6984. doi:10.1021/acs.nanolett.7b04374. URL <https://doi.org/10.1021/acs.nanolett.7b04374>, publisher: American Chemical Society.
- [194] P. Vancsó, G. Z. Magda, J. Pető, J.-Y. Noh, Y.-S. Kim, C. Hwang, L. P. Biró, and L. Tapasztó. “The intrinsic defect structure of exfoliated MoS<sub>2</sub> single layers revealed by Scanning Tunneling Microscopy”. *Scientific Reports*, 6(1):29726, July 2016. ISSN 2045-2322. doi:10.1038/srep29726. URL <https://www.nature.com/articles/srep29726>, number: 1 Publisher: Nature Publishing Group.
- [195] E. Ponomarev, n Pásztor, A. Waelchli, A. Scarfato, N. Ubrig, C. Renner, and A. F. Morpurgo. “Hole Transport in Exfoliated Monolayer MoS<sub>2</sub>”. *ACS Nano*, 12(3):2669–2676, March 2018. ISSN 1936-0851. doi:10.1021/acsnano.7b08831. URL <https://doi.org/10.1021/acsnano.7b08831>, publisher: American Chemical Society.
- [196] S. Mignuzzi, A. J. Pollard, N. Bonini, B. Brennan, I. S. Gilmore, M. A. Pimenta, D. Richards, and D. Roy. “Effect of disorder on Raman scattering of single-layer  $\mathrm{MoS}_2$ ”. *Physical Review B*, 91(19):195411, May 2015. doi:10.1103/PhysRevB.91.195411. URL <https://link.aps.org/doi/10.1103/PhysRevB.91.195411>, publisher: American Physical Society.
- [197] K. F. Mak, K. He, C. Lee, G. H. Lee, J. Hone, T. F. Heinz, and J. Shan. “Tightly bound trions in monolayer

MoS<sub>2</sub>". *Nature Materials*, 12(3):207–211, March 2013. ISSN 1476-4660. doi:10.1038/nmat3505. URL <https://www.nature.com/articles/nmat3505>, number: 3 Publisher: Nature Publishing Group.

- [198] K. Xiao, T. Yan, Q. Liu, S. Yang, C. Kan, R. Duan, Z. Liu, and X. Cui. "Many-Body Effect on Optical Properties of Monolayer Molybdenum Diselenide". *The Journal of Physical Chemistry Letters*, 12(10):2555–2561, March 2021. doi:10.1021/acs.jpcclett.1c00320. URL <https://doi.org/10.1021/acs.jpcclett.1c00320>, publisher: American Chemical Society.
- [199] B. Chakraborty, A. Bera, D. V. S. Muthu, S. Bhowmick, U. V. Waghmare, and A. K. Sood. "Symmetry-dependent phonon renormalization in monolayer MoS<sub>2</sub> transistor". *Physical Review B*, 85(16):161403, April 2012. doi:10.1103/PhysRevB.85.161403. URL <https://link.aps.org/doi/10.1103/PhysRevB.85.161403>, publisher: American Physical Society.
- [200] T. Sohler, E. Ponomarev, M. Gibertini, H. Berger, N. Marzari, N. Ubrig, and A. F. Morpurgo. "Enhanced Electron-Phonon Interaction in Multivalley Materials". *Physical Review X*, 9(3):031019, August 2019. doi:10.1103/PhysRevX.9.031019. URL <https://link.aps.org/doi/10.1103/PhysRevX.9.031019>, publisher: American Physical Society.
- [201] J. G. Roch, G. Froehlicher, N. Leisgang, P. Makk, K. Watanabe, T. Taniguchi, and R. J. Warburton. "Spin-polarized electrons in monolayer MoS<sub>2</sub>". *Nature Nanotechnology*, 14(5):432–436, May 2019. ISSN 1748-3395. doi:10.1038/s41565-019-0397-y. URL <https://www.nature.com/articles/s41565-019-0397-y>, number: 5 Publisher: Nature Publishing Group.
- [202] J. Zipfel, K. Wagner, M. A. Semina, J. D. Ziegler, T. Taniguchi, K. Watanabe, M. M. Glazov, and A. Chernikov. "Electron recoil effect in electrically tunable MoSe<sub>2</sub> monolayers". *Physical Review B*, 105(7):075311, February 2022. doi:10.1103/PhysRevB.105.075311. URL <https://link.aps.org/doi/10.1103/PhysRevB.105.075311>, publisher: American Physical Society.
- [203] E. J. Sie, T. Rohwer, C. Lee, and N. Gedik. "Time-resolved XUV ARPES with tunable 24–33 eV laser pulses at 30 meV resolution". *Nature Communications*, 10(1):3535, August 2019. ISSN 2041-1723. doi:10.1038/s41467-019-11492-3. URL <https://www.nature.com/articles/s41467-019-11492-3>, number: 1 Publisher: Nature Publishing Group.
- [204] K. Fukutani, R. Stania, C. Il Kwon, J. S. Kim, K. J. Kong, J. Kim, and H. W. Yeom. "Detecting photoelectrons from spontaneously formed excitons". *Nature Physics*, 17(9):1024–1030, September 2021. ISSN 1745-2481. doi:10.1038/s41567-021-01289-x. URL <https://www.nature.com/articles/s41567-021-01289-x>, number: 9 Publisher: Nature Publishing Group.

**Titre:** Micro luminescence polarisée dans les hétéro-structures de van der Waals

**Mots clés:** 2D semiconductors, spin/valley physics, quantum physics, TMD, polarization-resolved photoluminescence

**Résumé:** Les monocouches de dichalcogénures de métaux de transition (TMD, formule chimique de  $MX_2$  où  $M = Mo, W$  ;  $X = S, Se, Te$ ) sont des semi-conducteurs 2D avec une bande interdite directe qui sont très prometteurs dans le domaine de la spin/valleytronique. Dans les monocouches de TMD, les effets de confinement quantique bidimensionnels, et le faible écrantage diélectrique, conduisent à une énergie de liaison d'exciton extraordinaire d'environ 500 meV. La bande interdite se trouve aux points K de la zone de Brillouin hexagonale, appelés également "les vallées". Le fort couplage spin-orbite (SOC) brise la dégénérescence des vallées de valence et de conduction, créant ainsi un couplage spin-vallée. Les monofeuillets TMD sont donc sensibles à la polarisation de l'excitation optique. Les règles de sélection optique chirales sont valides et efficaces dans les monofeuillets de TMD et nous permettent d'exciter sélectivement les vallées  $K^+$  /  $K^-$  par pompage optique, simplement en contrôlant l'hélicité de la lumière.

Dans cette thèse, nous réalisons des études de photoluminescence (PL) résolue en polarisation à des températures cryogéniques sur des monofeuillets de

TMD. Nous avons démontré une très grande polarisation spin/vallée dynamique des porteurs résidents induite par la lumière polarisée circulairement, jusqu'à présent elle avait été mesurée seulement par des expériences de rotation de Kerr résolues en temps. Nous avons étudié le transport excitonique grâce à la PL en utilisant une technique d'imagerie hyperspectrale à des fluences d'excitation élevées. Nous avons révélé l'apparition d'un halo dans la distribution de la PL du trion et construit un modèle pour interpréter la formation du halo en modélisant l'équation de dérive-diffusion en régime permanent incluant un terme Seebeck lié à la présence d'un gradient thermique. En outre, nous avons étudié de la PL des excitons chargées positivement et négativement à différents régimes de dopage. Pour cela, nous avons appliqué des champs électriques dans des dispositifs et nous avons étudié la polarisation et la cohérence spin/vallée des émissions excitoniques. Ces études permettent de mieux comprendre la riche physique des excitons et des spins et des vallées dans ces semi-conducteurs 2D, une étape cruciale pour les futures applications optoélectroniques et valleytroniques.

**Title:** Polarization resolved photoluminescence in van der Waals heterostructures

**Keywords:** 2D semiconductors, spin/valley physics, quantum physics, TMD, polarization-resolved photoluminescence

**Abstract:** Transition metal dichalcogenide (TMD, chemical formula of  $MX_2$  where  $M=Mo, W$ ;  $X=S, Se, Te$ ) monolayers (MLs) are promising 2D direct bandgap semiconductors for applications in spin/valleytronics and the study of many-body physics. In a monolayer limit, the bandgap occurs at the K points, where a strong spin-orbit coupling (SOC) splits the valence and conduction sub-bands. Because of this, a unique spin-polarized band structure appears at the two non-equivalent K points, also called valleys. This makes chiral optical selection rules valid and effective in TMD MLs so that one can selectively excite  $K^+/K^-$  valleys by optical pumping controlling the helicity of light. Also, in TMD MLs 2D quantum confinement effects and low dielectric screening lead to extraordinary exciton binding energies of  $\sim 500$  meV, and the chiral optical selection rules also apply for the exciton transitions.

In this thesis, we perform polarization-resolved photoluminescence (PL) studies at cryogenic temper-

atures on TMD MLs. We have demonstrated in PL a very large dynamical spin/valley polarization of resident carriers induced by circularly polarized light, so far only probed through time-resolved Kerr rotation experiments. We have investigated the excitonic transport through PL by using an hyperspectral imaging technique at high excitation fluences. We revealed an appearance of a halo in the trion PL distribution and built a model to interpret the halo formation by considering a steady-state drift-diffusion equation, including the Seebeck drift induced by a thermal gradient. Also, by applying electric fields in gate-tunable devices, we investigated positively/negatively charged excitonic species at different doping regimes and studied their spin/valley polarization and coherence. These studies provide a further understanding of the rich exciton and spin/valley physics in these 2D semiconductors, a crucial step for future optoelectronic and valleytronic applications.